The Identification of Stable Reaction Intermediates on Aluminum Oxide Surfaces with Inelastic Electron Tunneling Spectroscopy

Thesis by
Michael Karpovich Templeton

In Partial Fulfillment
of the Requirements for the Degree of
Doctor of Philosophy

California Institute of Technology
Pasadena, California

1984
(Submitted April 24)

ACKNOWLEDGEMENTS

It is unfortunate that I cannot mention everyone who contributed measurably to my personal growth and to the enjoyment of my sojourn in Southern California. Those that I wish to especially acknowledge are my advisor Henry Weinberg, and the present and past members of the Weinberg Research Group. You have all contributed with friendship, sound advice, and moral support. I still remember well the day when so many of you appeared as familiar faces for my talk at the AIChE Conference. I will long reminisce grading exams for so many semesters of ChE 164 with Charles Sobrero.

I also wish to express my thanks to John Lambe for giving generously of his wisdom and time during the critical first years that I became engaged in tunneling spectroscopy. Several other colleagues have been influential in my thinking. Jim Gleason was an exemplary surface chemist and a good friend; more than anyone else he expanded my horizons in applying spectroscopic techniques other than tunneling to my research. Kurt Fickie was a continual source of information; in the "early" days, our runs to Cheli Warehouse were a special boon. Other friends have made the years bearable: Jeff Koller, Jim Kralik, Dave Chang, Herman Yee, and Nadeem Tufail, to whom I also owe special thanks for his uncomplaining and exacting help with experimental work during one summer and fall. Jack, Libby, Brad and Gregg Collin have been like a second family. Since the first day that I arrived in the Southland, they have generously opened their home to me. Bill Kath has been a friend and roommate for nearly ten years, and has always acted unselfishly.

Most of all, my family has been a continual source of encouragement, and, appropriately, I dedicate this thesis to them.

ABSTRACT

The stable surface intermediates that were formed in several heterogeneous reactions on aluminum oxide films were identified with inelastic electron tunneling spectroscopy. The heterogeneous reactions included associative and dissociative adsorption, nucleophilic substitution, surface catalyzed elimination, hydrolysis and hydrogenolysis. Primarily two chemisorption systems are discussed. These are cyclopropane carboxylic acid on aluminum oxide and phosphonate esters on aluminum oxide. In conjunction with the temperature and exposure dependence of the stable reaction intermediates, the nature of these reactions and the aluminum oxide surface are discussed.

The temperature and exposure dependent interaction of cyclopropane carboxylic acid with alumina surfaces has been studied with inelastic electron tunneling spectroscopy. Cyclopropane carboxylate and n-butane carboxylate were the only adsorbed species formed, as determined by a comparison with tunneling spectra of n-butane carboxylic acid and cyclopropane carboxylic acid coadsorbed on alumina. The n-butane carboxylate results from hydrogenolysis of the cyclopropyl ring of the adsorbed cyclopropane carboxylate with hydrogen supplied by surface hydroxyl groups. The relative populations of the two surface species are strongly dependent upon coverage and temperature.

The adsorption of gaseous dimethyl methyl phosphonate (DMMP) on aluminum oxide film surfaces has been investigated with inelastic electron tunneling spectroscopy. Surface temperatures ranged between 200 K and 673 K, and exposures ranged between 3×10^{-4} and 10 Torr-s. Tunneling spectra of deuterium labeled DMMP, perdeutero methyl alcohol, methyl methyl phosphonic acid, methyl phosphonic acid and trimethyl phosphine oxide, all adsorbed on aluminum oxide surfaces, were used to clarify the structures of the species resulting from the adsorption and decomposition of DMMP. At 200 K, DMMP is adsorbed molecularly with high surface coverages. At surface temperatures above 295 K,

DMMP is adsorbed dissociatively in low coverages. Surface temperatures above 473 K lead to the dealkylation of the dissociatively adsorbed adspecies, which results in the formation of adsorbed methyl phosphonate.

Inelastic electron tunneling spectroscopy was used to examine comparatively the adsorption and reaction of three phosphonate esters on aluminum oxide surfaces which were synthesized by the plasma oxidation of aluminum metal films. The phosphonate esters were diisopropyl methyl phosphonate (DIMP), dimethyl methyl phosphonate (DMMP) and diphenyl methyl phosphonate (DPMP). The adsorption temperatures ranged from 200 to 673 K. The exposures of gaseous DIMP and DMMP were 1.0 Torr-s, while DPMP was exposed to the surface as a 0.025 M solution in hexane. DIMP was found to adsorb associatively in low coverages at 295 K, whereas at 373 K, DIMP was found to adsorb dissociatively in low coverages as isopropyl methyl phosphonate. Above 373 K the isopropyl methyl phosphonate decomposed to the metastable hydroxy methyl phosphonate, which, in turn, decomposed completely to the methy phosphonate above 573 K. Although the dissociative adsorption temperature was lower (295 K), adsorbed DMMP decomposed similarly through the hydroxy methyl phosphonate to form the methyl phosphonate. However, in this case the hydroxy methyl phosphonate was a short-lived intermediate. DPMP was found to adsorb dissociatively at 295 K, and the adsorbed species formed is stable through 673 K. Consistent with these observations, mechanisms for the adsorption and decomposition of phosphonate esters on aluminum oxide are proposed that involve P-O bond cleavage upon adsorption but O-C bond cleavage upon decomposition of the adspecies.

A versatile tunnel junction fabrication system is described. A temperature controller which resistively heats the aluminum oxide films by passing a current through the underlying aluminum film is presented. Computer software for spectral analysis is discussed.

Contents

Chapter I

The Identification of Stable Reaction Intermediates on Aluminum Oxide Surfaces with Inelastic Electron Tunneling Spectroscopy

1 Introduction

In such diverse areas as corrosion, lubrication, microelectronics, heterogeneous catalysis and adhesion, the important influence of surface properties is without question. Of particular interest to us are the chemical properties of surfaces. That is, not merely the elemental composition of a surface but, more importantly, its tendencies toward chemical combination and reaction with other molecules accidentally or intentionally present at the interface. In virtually all nonstructural applications, these surface chemical properties are exceedingly important.

With this motivation, we were led to investigate several aspects of the surface chemistry of aluminum oxide films. This was accomplished primarily by determining the structure of stable reaction intermediates on aluminum oxide surfaces with inelastic electron tunneling spectroscopy (IETS), which is a promising vibrational spectroscopy [1-6]. Aluminum oxide was chosen since it is a ubiquitous material that is often found in applications where its surface properties are of technological importance, and because tunneling spectroscopy easily adapts to the study of this surface. Section 2 emphasizes further the importance of aluminum oxide surface chemistry. Then, in Section 3, the phenomenology of tunneling spectroscopy and the reasons for employing this particular spectroscopy are discussed. Finally, in Section 4, the major goals and accomplishments of this thesis are presented.

2. Aluminum Oxide Surfaces

Sales of heterogeneous catalysts alone constituted a 1.3 billion dollar industry in 1983 [7]. Since the value of chemicals processed by these catalysts exceeds by several orders of magnitude the net worth of the catalysts themselves, the science of heterogeneous catalysis is economically critical to the

functioning of our technological society. Within the confines of heterogeneous catalysis, the surface chemistry of Al_2O_3 is of paramount importance since Al_2O_3 powders, particularly the γ and η forms, are used extensively as supports for these catalysts. For example, typical hydrodesulfurization catalysts consist of Co, Ni and Mo oxides supported on Al_2O_3 [8], reforming catalysts consist of metallic Pt and Rh supported on high surface area γ–Al_2O_3 [7], ethylene oxidation catalysts consist of metallic Ag supported on Al_2O_3 [7,9], and catalysts for the selective oxidation of butene to butadiene consist of Bi_2O_3-MoO_3 supported on Al_2O_3 [10].

It is especially significant that Al_2O_3 does not function as a completely inert component of the catalyst formulations. An extreme example of this is the reforming catalyst, where the Pt is active for hydrogenation/dehydrogenation, while the Al_2O_3 is active for isomerization [11]. However, cooperative functioning of metal and support is not necessarily limited to interactions through the gas phase, as recent work has demonstrated "spillover" effects [12]. In some cases, the effect of the support is more subtle, as when changing the support alters the activity and/or the selectivity. For example, when SiO_2 is used in place of Al_2O_3 for supporting Bi_2O_3-MoO_3, the catalyst is more suitable for selective oxidation of propene to 2-propene aldehyde, rather than selective oxidation of butene to butadiene [10]. Sometimes Al_2O_3 is added in small amounts as a structural promoter for heterogeneous catalysts, as in, for example, the NH_3 synthesis catalyst, which consists mostly of Fe_2O_3 before reduction [13]. Often, however, the function of the Al_2O_3 support is not well understood, as in, for example, the hydrodesulfurization catalyst [14].

In pure form, or treated with small amounts of halogen promoters [11], Al_2O_3 catalyzes a wide assortment of hydrocarbon transformations. These range from exchange between gaseous H_2 and alkanes [15,16], alkenes [17] or aryls [10] to

cis-trans isomerization, double bond migration, and skeletal isomerization for alkenes [18]. Furthermore, Al_2O_3 powders, sometimes promoted with small amounts of alkali metals [20], are both selective and active for catalytic dehydration of alcohols to alkenes and/or ethers and for catalytic dehydration of carboxylic acids to ketones [18-20]. From studying reactions such as the above, profiles for the active sites on Al_2O_3 have been developed [18,19,21], and, although a great deal is known, still much more remains to be determined.

Aluminum metal is a very important structural material. Although the thin, natural Al_2O_3 film that forms on the bare metal surface is sufficient protection for most applications, sometimes it is desirable to further improve the corrosion or abrasion resistance. This is commonly done by either applying a coating such as paint, or creating an unnaturally thick Al_2O_3 surface coating via electrochemical means. In both of these instances, to maximize the efficacy of such coatings, it is essential to understand the chemical means by which Al_2O_3 interacts and reacts with other materials.

3. Tunneling Spectroscopy

The surface scientist has several hundred techniques at his disposal for examining the chemical and physical nature of surfaces. The theory and application of the most common ones have been widely discussed in the literature [22]. One class of especially powerful techniques probes surfaces through vibrational spectroscopy and is thus capable of providing detailed structural information about adsorbate/surface complexes, and hence stable reaction intermediates [23,24]. Such information can be directly utilized in studies of adsorption and reaction which determine, for example, the corrosion resistance of a material's surface. In addition, the structure of stable surface species as determined by vibrational spectroscopy has enormously influenced mechanisms pro-

posed for catalytic reactions on oxide surfaces [19,20,26]. However, vibrational spectroscopic results must be applied cautiously to this latter area. For example, poisoning experiments estimate the number of active sites for catalytic isomerization on Al_2O_3 to be on the order of 1% of the total number of surface sites [19]. Thus, if an alkene is found to be adsorbed on Al_2O_3, it is not necessarily adsorbed at an isomerization site. Additionally, there is the possibility of a catalytic reaction proceeding through an adsorbate-surface complex in which the adsorbate is held in loose association with the surface. For example, in the Al_2O_3 catalyzed dehydration of formic acid to CO, in addition to surface hydroxyls, the only adspecies observed was a surface formate, and this was determined not to be an active intermediate in catalytic dehydration [25]. Accordingly, the mechanisms proposed for catalytic dehydration of alcohols and carboxylic acids invoke hydrogen bonded adsorbate-surface complexes [19,20].

Inelastic electron tunneling spectroscopy (IETS) is one vibrational spectroscopy that is ideally suited for the study of low area aluminum oxide surfaces and aluminum oxide supported materials. This technique was discovered less than 20 years ago [1] during the measurements of the density of electronic states in superconductors via metal-insulator-metal tunneling. In the interim, a promising but incomplete picture of this technique has emerged. This has been presented in a number of review articles [2,3,6] and books [4,5], some of which emphasize the comparison of IETS with other vibrational spectroscopies [3] or the applications of IETS [4-6].

Inelastic electron tunneling spectroscopy is carried out by measuring the electrical characteristics of metal-insulator-metal tunnel junctions. Since the results of this thesis are exclusively obtained with tunneling spectroscopy, it is appropriate to discuss the phenomenology of IETS in some detail. The technique can be divided conveniently into two steps: *(1)* synthesis of the metal-insulator-

metal tunnel junction, and *(2)* measurement of its current-voltage characteristics. Shown in Fig. 1 is a cross section of a typical metal-insulator-metal tunnel junction consisting of Al-Al_2O_3-Pb. Synthesis of this device is as follows (see Chapter III, Section 2.2 for more specific fabrication details). One electrode of the metal-insulator-metal tunnel junction is formed by evaporating a thin aluminum film (approximately 1000 Angstroms thick) onto a glass substrate. The surface of this aluminum film is oxidized in an oxygen plasma to form an insulating aluminum oxide layer that is estimated to be 30 Angstroms (Å) thick.

Since the composition of aluminum oxides can vary from tri-hydrates to perfectly ordered aluminum oxides of stoichiometric composition Al_2O_3 [27] and since the exposed surface of this aluminum oxide layer becomes the surface under study, it is important to know the precise nature of this oxide layer. [1] Aluminum oxide films grown thermally on aluminum metal have been related to commercial γ–Al_2O_3 by catalytic studies [28]. Furthermore, XPS measurements of aluminum oxide films grown under various conditions have been able to show similarities between thermally synthesized aluminum oxides and oxygen plasma synthesized aluminum oxide [29]. Unfortunately, the data in this latter study are not complete enough to be directly related to a recent broad survey of similar data given for many different phases of aluminum oxide and aluminum oxide hydrates [30]. However, as discussed in the following chapters, the surface reactions undergone by cyclopropane carboxylic acid and by phosphonate esters are consistent with reactions observed on γ–Al_2O_3 powders. The observed hydrogenolysis of the former compound may indicate, however, differences between the aluminum oxide films and γ–Al_2O_3 powders, as discussed further in Chapter II. In any event, the bulk of the Al_2O_3 barrier does not appear to contain any partially hydrated phases of Al_2O_3, as determined recently by the absence of a

[1] To ensure that the surface is well characterized in the sense of being clean, most of our work is done in a clean, bakable fabrication system.

contribution from the bulk to the O-H vibrational mode of the tunneling spectrum [31].

Once the oxide barrier has been synthesized, it is exposed to the adsorbate as either a vapor or a dilute solution. Consequently, the adsorption, chemisorption or reaction between the aluminum oxide surface and the adsorbate occurs during this phase of the tunnel junction synthesis. In some cases the aluminum oxide surface is heated [32] or cooled during or following this step to promote adsorption and/or reaction. The net result of this step is that the surface now contains associatively adsorbed molecules and/or dissociatively adsorbed molecular fragments, which are indicated schematically by the dipoles in Fig. 1.

To complete the tunnel junction synthesis, a 1000 to 2000 Å thick counter electrode is evaporated over the exposed surface. The ideal material for this would be one that immeasurably perturbs the adsorbate/surface complex. It is not clear that such a material exists. Different counter electrodes of Pb, Tl, Sn, In and Ag gave qualitatively different spectra for CO adsorbed on Al_2O_3 supported Fe clusters [33]. On the other hand, vibrational modes of adsorbed hydrocarbon groups were shifted by less than 1% from the values found by infrared spectroscopy [33]. In practice, Pb is found to be the most nearly ideal material since it combines inertness with a low melting point and a large ionic radius. Consequently, Pb is exclusively used in this work.

The physical principles behind tunneling spectroscopy can be understood with the aid of the energy diagram in Fig. 2. This indicates the important energy levels across the metal-insulator-metal structure. These are the conduction band of the insulator (denoted Φ) and the fermi levels of the metal electrodes on either side of the barrier (denoted $E_{F_{Al}}$ and $E_{F_{Pb}}$ for the Al and Pb, respectively).[2] The fermi level of the aluminum ($E_{F_{Al}}$) is biased with respect to the fermi level of

the Pb ($E_{F_{Pb}}$) by an applied potential of magnitude V. Since the electrons in the metal lack sufficient energy to attain the conduction band of the insulator, current flow through the metal-insulator-metal device is classically forbidden. However, quantum mechanically, there is a finite probability for an electron in one metal to tunnel through the barrier into the other metal. Furthermore, the tunneling can occur either elastically or inelastically. Elastic tunneling occurs if there exists on the other side of the barrier an empty electronic state into which the electron can tunnel without losing energy. Thus, electron tunneling from the Al to the Pb is allowed when $E_{F_{Al}}$ is greater than $E_{F_{Pb}}$ or when the applied potential V is less than zero. Elastic tunneling accounts for approximately 99% of the observed current flow in tunnel junctions. Inelastic tunneling accounts for the remaining 1%. This process can occur if an electron is able to give up a fraction of its kinetic energy through excitation of a molecular vibration and can still access an empty electronic state in the other metal. Thus, the inelastic process is allowed if

$$eV > \bar{h}\omega \qquad (1)$$

where $\bar{h}$ is the Planck constant divided by 2π, and ω is the angular frequency of the excited vibration.

With Eq. (1) it is possible to understand the phenomenological picture of inelastic electron tunneling spectroscopy shown in Fig. 3. The I-V, $\partial I/\partial V$ and $\partial^2 I/\partial V^2$ characteristics of an ideal tunnel junction containing only one molecular vibrator of fundamental frequency ω are shown in Figs. 3(a), (b) and (c), respectively. As long as the magnitude of the bias voltage (V) is such that the kinetic energy gained by the electron in transit across the barrier is less than

[2] For our purposes, the fermi level can be thought of as the delineation between filled and unfilled electronic states in the metal. Strictly speaking, this is true only at a temperature of absolute zero, but since tunneling spectra are typically measured at 4 K, this is a reasonable approximation.

the vibrational energy, elastic tunneling is the only allowed process. Thus the current-voltage characteristic rises approximately linearly at a rate that reflects both the differential increase in the number of states in the Pb counter electrode with increasing energy, as well as changes in the barrier shape [34]. However, as soon as the magnitude of the bias voltage (V) is such that the kinetic energy gained by the electron in transit across the barrier exceeds the vibrational energy, then the inelastic tunneling process is allowed, in addition to the elastic tunneling process. The net result is another path by which electrons can flow through the metal-insulator-metal tunnel junction, and consequently is evidenced as an abrupt increase in the conductance of the device. This is manifested as an increase in slope of the I-V characteristic at the vibrational energy hbarω as shown in Fig. 3(a). Here, the change in slope is exaggerated dramatically; typically, the increase in conductance is less than 1% and would be difficult to locate precisely on an I-V characteristic. Usually, this difficulty is overcome by detecting a derivative characteristic such as $\partial^2 I/\partial V^2$, where the increases in conductance now appear as a peak superimposed on a sloping background, as shown in Fig. 3(c). Detection of a second derivative is accomplished easily by means of a "harmonic" detection scheme. There are a good number of these described in the literature, all employing the same basic principle of operation [35]. The particular scheme employed by us is shown in Fig. 4 and has been described previously [3]. This scheme measures $\partial^2 I/\partial V^2$, which is equal to $-(\partial I/\partial V)^{-3}\partial^2 I/\partial V^2$. Often, $\partial I/\partial V$ is approximately constant over the spectral range, and thus the former quantity is linearly proportional to $\partial^2 I/\partial V^2$.

A typical tunneling spectrum of a clean aluminum oxide surface is shown in Fig. 5. The spectrum is usually recorded beginning at 30 meV, since below this there are inelastic losses due to excitations of phonons in the superconducting Pb counter electrode that are orders of magnitude larger than the vibrational

losses. The vibrational assignments of the modes observed in the tunneling spectrum are also indicated in Fig. 5. The major modes include the Al-phonon mode at 260 cm^{-1}, the Al-O stretching mode at approximately 940 cm^{-1} and the (Al)O-H stretching mode at 3600 cm^{-1}. This latter is due exclusively to surface hydroxyls [31]. The assignments of other less important modes have been recently clarified. These include the Al-H bending mode (600 and 725 cm^{-1}), the (Al)O-H bending mode (930 cm^{-1}) and the Al-H stretching mode (1850 cm^{-1}). Note that the aluminum hydride modes have been localized to the Al-Al_2O_3 interfacial region, while the Al_2O_3-vacuum interface is likely to be free of such species [31]. The upward sloping background, which is superimposed upon the vibrational peaks in Fig. 5, has been to a large extent removed from all of the tunneling spectra subsequently presented. This was done by digitally subtracting a linear function of energy from the recorded spectrum, as detailed in Appendix A. However, since the background is not strictly linear, the resulting spectrum most often shows some curvature.

4. Objectives and Accomplishments

Like all instrumental techniques, inelastic electron tunneling spectroscopy has both advantages and disadvantages over other vibrational spectroscopies. Although these have been dealt with in the literature [3,36], it is appropriate to mention some of them. In comparison with infrared spectroscopy, the advantages of tunneling spectroscopy are primarily a high sensitivity to CH stretching vibrations, and an extremely wide spectral window (0-4000 cm^{-1}) in connection with Al_2O_3 and Al_2O_3 supported systems.

Traditionally, infrared studies have emphasized carbonyl related vibrations because of their intense infrared coupling [23], and conversely, deemphasized C-H vibrations. However, the C-H stretching region provides a wealth of informa-

tion about the transformation of adsorbed hydrocarbons, and tunneling spectroscopy may provide new insights into this important class of reactions because of its higher sensitivity to C-H stretching vibrations. Often, the sensitivity of tunneling spectroscopy to both infrared and Raman type modes is cited as another one of its principal advantages. However, in our opinion this is of lesser advantage since in many cases the presence of the surface perturbs the adspecies sufficiently so that other wise infrared inactive modes are commonly observed with infrared spectroscopy [37]. On the other hand, the inherent disadvantages of tunneling spectroscopy seem to be an inability to observe surface reactions kinetically, the presence of perturbations in the adsorbate vibrations induced by the top metal electrode, poorer quantitative measurement, and, in connection with Al_2O_3 systems, pretreatment temperature limitations (700 K appears to be the maximum attainable surface temperature for the Al/Al_2O_3 system with IETS, whereas Al_2O_3 powders are commonly treated to 1100 K in many infrared experiments [38]). Although these disadvantages seem rather formidable, in practice they do not severely limit the utility of IETS. For example, although observing high temperature surface reactions kinetically can provide additional insight [25,39], most commonly spectroscopic observation is done at 295 K after cooling the sample which had been treated at high temperature. Furthermore, even though the effects of the top metal electrode are understood incompletely [33], the adsorbate/surface complex remains remarkably unperturbed.

Only the "theoretical" advantages and limitations of IETS are mentioned above. Unfortunately, there were also a good many practical limitations that had not been solved when work on this thesis was begun. As a consequence, most of the reported work with tunneling spectroscopy lacked an overall sophistication that is characteristic of state-of-the-art research in surface science.

Thus, this promising technique was ignored by all but an adventurous few. Appropriately, this brings us to a discussion of the goals of this research, which can be stated as two interrelated objectives:

1. To advance the development of IETS to where it can be applied to study adsorption and reaction on surfaces over a wide range of conditions; and
2. To show the utility of IETS as a tool for investigating such problems by using it to contribute to the understanding of the surface chemistry of aluminum oxide.

If a technique is too time-consuming to apply compared to similar techniques, it becomes an alternative of last resort. Although it is generally far easier to prepare one tunneling sample than, say, one supported infrared sample, with some exceptions the tunneling sample can be used only once, whereas the infrared sample can be used for a series of experiments. Thus, in order for tunneling spectroscopy to be a successful endeavor, it must be possible to fabricate tunneling samples routinely within about two hours. This does not mean merely going through the motions, but that a "successful" junction should be produced. Thus the success rate for tunnel junctions should approach, say, 70%. In regard to both of these considerations, the original equipment in our tunneling laboratory performed unsatisfactorily.

Consequently, a considerable effort was invested into designing a new fabrication system. The resulting instrument is quite versatile and considerably easier to operate than the previous model (see Appendix C). In addition a significant simplification of surface temperature control during experiments was instituted with a feedback temperature controller (Appendix B).

Clean room temperature junctions can now be synthesized with practically 100% success, whereas no successful clean junctions have been made with the

older system. This tremendous improvement in the yield of good quality tunnel junctions was accomplished through a concerted effort on several fronts. Other things being equal, the three most important factors affecting yield are device size (area), thickness of the Al film and the plasma oxidation parameters, in that order. Overall size critically affects yields of semiconductor devices. Unsurprisingly, decreasing the tunnel junction area significantly improves yield. Currently, masks are employed that produce junctions with areas of between 1/4 and 1/16 of the former size (i.e., between 0.6 and 0.16 mm^2). At the same time, it is also possible to keep junction resistances near their previous values by decreasing the thickness of the Al_2O_3 barrier. Thus, the signal-to-noise ratio of these smaller devices remains equivalent to the larger devices. Of course, the device size cannot be continually decreased without impunity. At some point, the tunneling current density causes line width increases due to heating and to voltage nonuniformities across the junction [40].

The thickness of the aluminum film is another important device parameter. Although it seems to be relatively unimportant in unheated devices, it is especially important to control the film thickness of devices that will be heated above approximately 373 K. That is, if the aluminum film thickness is kept below approximately 1000 Å, then the device yield is two to three times higher. Unfortunately, with the higher current densities in small devices there are more serious peak shifts associated with inaccuracies in the voltage measurement. One method to avoid this involves doing the measurements at the temperature where aluminum becomes superconducting (T_c = 1.196 K). Unfortunately, our laboratory is not presently equipped to achieve these temperatures. However, in George Walmsley's laboratory, temperatures of 1.2 to 2 K are used routinely [41].

The plasma oxidation parameters also have a significant impact on the device quality. As an extreme example, acceptable devices could not be produced when a completely water-free environment was maintained during the plasma oxidation. For our purposes, the oxidation parameters were optimized by making sets of clean junctions under various conditions and adopting those changes which improved the yield of successful devices.

Thus, the yield of successful devices was improved considerably. The aspiring "tunneler" would do well to consider these factors if he has not already done so.

An instrumental technique capable of routinely providing physical insights must possess three important attributes: *(1)* versatility, *(2)* sensitivity, and *(3)* quantifiability. As has been made clear from the literature, IETS appears to be a very versatile tool. In addition, to specialized applications [4,5], it is also capable of examining a large variety of surfaces, from Al_2O_3-supported metal clusters [42] to chemically [43] and epitaxially deposited materials [44], to barriers of different materials such as magnesium oxide [41] and aluminum nitride [45]. In addition, there are three principal ways in which adsorbates can be contacted with the surface: *(1)* vapor phase, *(2)* solution [46] and *(3)* infusion through the metal overlayer [47]. However, virtually all of the studies reported in the literature have been done at room temperature. Using the technique developed by Bowser and Weinberg [32], and used by Evans and Weinberg [48] to attain surface temperatures of 573 K in the preparation of aluminum oxide tunnel junctions, we have studied adsorption and reaction of phosphonate esters at temperatures of up to 700 K (Chapters III and IV). In connection with Al_2O_3 and Al_2O_3-supported systems, temperatures above 573 K take on special significance because substantial weight loss of Al_2O_3 powders occurs at these temperatures [18]. In fact, the tunneling study of Chapter III is able to demonstrate quantitatively the occurrence of Al_2O_3 surface dehydroxylation.

The sensitivity of tunneling spectroscopy can be assessed in a number of ways. For example, studies with benzoic acid indicate that tunneling spectroscopy is capable of detecting 3% of a monolayer [49]. Furthermore, in mixtures of deuterium labeled and unlabeled benzoic acids, it was possible to detect as little as 1% of deuterium [50]. Although these measurements are important in themselves, the ability to distinguish between closely related adspecies is also essential. In spite of limited resolution (16-25 cm^{-1}), tunneling spectroscopy also performs well in this area as demonstrated by the ability to distinguish between two isomers of butane carboxylate (isobutane carboxylate and n-butane carboxylate) within a considerable background of cyclopropane carboxylate (Chapter II), and between a series of very closely related methyl phosphonic acid derivatives (Chapters III and IV). It would be misleading to say that tunneling spectroscopy is infallible in this regard. Rather, one difficulty noticed during the course of work with phosphonate esters was the extremely weak electron-vibration coupling constant of P-O vibrations (Chapter III). This made it exceedingly difficult to distinguish between a molecularly adsorbed species and a dissociatively adsorbed species and was quite surprising in view of the reasonable sensitivity demonstrated for carboxylate modes. Perhaps, more importantly, it emphasizes the need for a better theory for understanding intensities in IETS.

Tunneling spectroscopy performs weakest in the area of quantitative comparisons. Present theories cannot determine adequately the absolute surface coverage represented in a tunneling spectrum. Furthermore, a rigorous theory does not even exist to relate relative coverages among different spectra. To some degree, it is possible to circumvent this latter problem by using the intensity of the Al-O stretching mode as an internal normalization. This technique was used extensively in Chapter III, and gives quite reasonable results. In order to use this technique effectively, some means of removing the sloping

background from the tunneling spectrums is desirable. Accordingly, software was developed to perform this function as well as to automate the analysis of the data (Appendix A). However, there is no reason to suspect that a more adequate theoretical basis for performing such calculations could not be developed, and thus the poor quantitative performance of the technique does not seem to be an insurmountable problem.

At this point, it should be clear that tunneling spectroscopy is reasonably versatile, sensitive and quantitative. Why then has it remained so neglected? To bring about a change to new methods, it is not enough to demonstrate that the new methods are as good as the old ones. Rather the new methods must be shown to be superior to the old ones. In the case of a new instrumental technique, this is most effectively done by providing heretofore unobtained insights into physical systems. Unfortunately, the majority of the literature employing tunneling spectroscopy does not bring home this point. For example, many studies could be classified simply as survey type studies of chemisorption at room temperature; e.g., a group of related compounds is adsorbed on aluminum oxide at 245 K. This has been done ad nauseum with carboxylic acids. Usually this type of study furnishes only an all too cursory view, rather than providing a penetrating insight. Some imaginative studies of alumina supported transition metals [42] and alumina supported organometallic complexes [51] were done, but, with the exception of $Zr(BH_4)_4$ [52], the poor quality spectra obtained for these systems were especially disparaging in relation to previous infrared work of CO adsorption on supported transition metals [53], where CO is an intense infrared scatterer. Together these factors provided little incentive for others to invest in tunneling spectroscopy.

Consequently, the second goal of this thesis was to remedy this. That is, we hoped to stimulate interest in IETS by using it to genuinely contribute to the

understanding of the surface chemistry of aluminum oxide. Accordingly, we undertook several detailed investigations of adsorption and reaction on aluminum oxide films. The results of these investigations are presented in Chapters II through IV.

Chapter II investigates the adsorption and reaction of cyclopropane carboxylic acid (1)

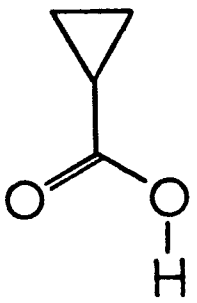

1

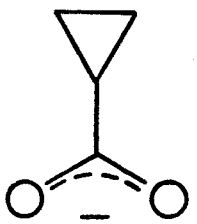

2

with aluminum oxide films. Carboxylic acids were known to chemisorb as carboxylates [3]. Consequently, cyclopropane carboxylic acid was expected to adsorb as cyclopropane carboxylate (**2**), and thus bring the three-membered cyclopropyl ring into intimate contact with the surface. Prior to this work, the only hydrocarbon transformations observed on Al_2O_3 with IETS were carbon-carbon double and carbon-carbon triple bond hydrogenation [54,55]. Therefore, this particular molecule was used in the hope of observing other hydrocarbon transformations; namely, the cyclopropyl ring might be easily coaxed into isomerizing due to its high strain energy. Indeed, we found that the adsorbed cyclopropane carboxylate reacts further with the aluminum oxide surface. However, nature being who she is, rather than undergoing the expected isomerization reaction, the adsorbed cyclopropane carboxylate underwent hydrogenolysis; to form exclusively n-butane carboxylate (**3**). Furthermore, isotopic labeling of the surface hydroxyls showed clearly that these groups were supplying the hydrogen for the hydrogenolysis. Chapter II discusses these observations and

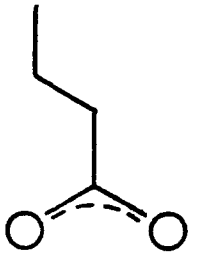

3

further relates them to reactions observed on Al_2O_3 powders. However, the important point about this work is that, even though a detailed mechanism for the hydrogenolysis reaction could not be proposed, tunneling spectroscopy nevertheless proves to be quite adequate for conclusively identifying all of the stable reaction intermediates present during the course of this reaction on the aluminum oxide surface.

Chapter III examines the adsorption and reaction of dimethyl methyl phosphonate (**4**)

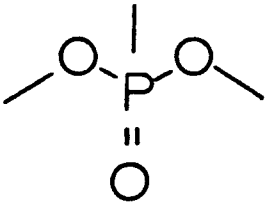

4

with aluminum oxide films. This compound is capable of interacting with the aluminum oxide surface in several ways. For example, it might either *(1)* associatively adsorb, *(2)* dissociatively adsorb, and/or *(3)* modify the surface properties of the Al_2O_3. By identifying the course of reaction, we will learn about relative reaction rates, and therefore clarify the surface chemistry of aluminum oxide. In subsequent experiments, tunneling spectroscopy again proves very successful in identifying and distinguishing among a series of closely related

adsorbed species, and thus provides substantial insight into the reactivity of aluminum oxide surfaces for these types of compounds.

In a continuation of our work with phosphonate esters, Chapter IV presents a comparative study of the adsorption and reaction of dimethyl methyl phosphonate (**4**), diisopropyl methyl phosphonate (**5**) and diphenyl methyl phosphonate (**6**).

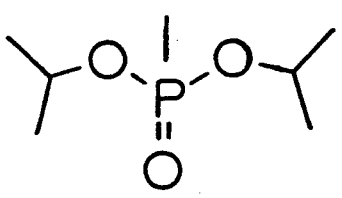

5

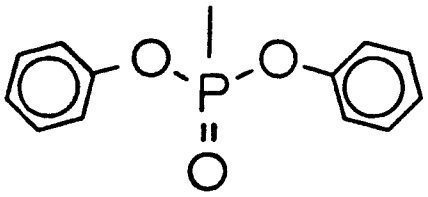

6

In these compounds, the nature of the ester group exerts a pronounced influence on the homogeneous chemistry of these compounds. Unsurprisingly, a comparative analysis of the tunneling spectra for these compounds adsorbed over a wide temperature range leads to a reaction mechanism for the adsorption and decomposition of phosphonate esters on aluminum oxide.

Together, the force of Chapters II through IV is to provide remarkably detailed insight into hydrogenolysis, hydrolysis and nucleophilic substitution on aluminum oxide surfaces. Thus, this work is certain to stimulate further interest in using tunneling spectroscopy as a probe for surface chemistry.

The conclusions to this this thesis are presented in Chapter V. Following this, Appendices A, B and C, respectively, provide documentation on the spectral analysis and plotting programs, the temperature controller used in heating the aluminum oxide films, and the versatile tunnel junction fabrication system used in making all of the tunnel junctions discussed in this thesis.

References

1. J. Lambe, R. C. Jaklevic, Phys. Rev. **165**, 821; R. C. Jaklevic, J. Lambe, Phys. Rev. Lett **17**, 1139 (1966).

2. P. K. Hansma, Physics Reports **30**, 145 (1977).

3. W. H. Weinberg, Ann. Rev. Phys. Chem. **29**, 115 (1978).

4. T. Wolfram, ed., *Inelastic Electron Tunneling Spectroscopy*, Springer Verlag, New York (1978).

5. P. K. Hansma, ed., *Tunneling Spectroscopy Capabilities, Applications and New Techniques*, Plenum Press, New York (1982).

6. S. K. Khanna, J. Lambe, Science **220** (1983).

7. S. C. Stinson, Chem. Eng. News, 19, Dec. 5 (1983).

8. F. E. Massoth, G. Murali Dhar, in Proc. 4th Int. Conf. on the *Chemistry and Uses of Molybdenum*, P. C. M. Mitchell, Ed., Climax Molybdenum Co., Ann Arbor, MI, p. 343 (1982).

9. H. E. Evans, W. M. Bowser, W. H. Weinberg, Surface Sci. **85**, L497 (1979).

10. D. B. Dadyburjor, S. S. Jewur, E. Ruckenstein, Catal. Rev. Sci. Eng. **19**, 293 (1979).

11. T. Edmonds, in *Catalysis and Chemical Processes*, R. Pearce, W. R. Patterson, eds., John Wiley, p. 91 (1981).

12. R. Kramer, J. Catal. **58**, 287 (1979).

13. G. Ertl, J. Vac. Sci. Technol. A **1**, 1247 (1983).

14. W. K. Hall, in *Proc. 4th Int. Conf. Chemistry and Molybdenum*, H. F. Barry, P. C. H. Mitchell, eds., Climax Molybdenum Co., Ann Arbor, MI, p. 224 (1982).

15. P. J. Robertson, M. S. Scurrell, C. Kemball, J. C. S. FTAR I **71**, 9023 (1975).

16. B. T. Hughes, J. K. Tyler, C. Kemball, J. C. S. FTAR I, **71**, 1285 (1975).

17. A. Corado, A. Kiss, H. Knozinger, H. D. Muller, J. Catal. **37**, 68 (1975).

18. H. Knozinger, P. Ratnasamy, Catal. Rv. Sci. Eng. **17**, 31 (1978).

19. C. S. John, M. S. Scurrell, in *Catalysis*, Vol. 2, The Chemical Society, London, p. 136 (1978).

20. W. H. Saunders, A. F. Cocerkill, *Mechanisms of Elimination Reactions*, John Wiley, New York, p. 256, (1973).

21. H. Noller, J. M. Parera, J. Res. Inst. Catalysis **29**, 95 (1981).

22. *Methods of Surface Analysis*, A. W. Czanderna, ed., Elsevier, New York (1975); *Chemistry and Physics of Solid Surfaces IV*, R. Vanselow, R. Howe, eds., Springer-Verlag (1982); G. Ertl, J. Kuppers, *Low Energy Electrons and Surface Chemistry*, Verlag Chemie, Germany (1974); W. N. Delegass, G. L. Haller, R. Kellerman, J. H. Lunsford, *Spectroscopy in Heterogeneous Catalysis*, Academic Press, New York (1979).

23. L. H. Little, *Infrared Spectra of Adsorbed Species*, Academic Press (1966); F. M. Hoffmann, Surface Sci. Reports **3**, 107 (1983).

24. H. Ibach, D. L. Mills, *Electron Energy Loss Spectroscopy and Surface Vibrations*, Academic Press, New York (1982).

25. Y. Noto, K. Fukuda, T. Onishi, K. Tamaru, J. C. S. FTAR **63**, 2300 (1967).

26. O. V. Krylov, *Catalysis by Non-Metals*, Academic Press (1970).

27. B. C. Lippens, J. J. Steggerda, in *Physical and Chemical Aspects of Adsorbents and Catalysts*, B. G. Linsen, ed., Academic Press, New York, p. 171 (1970).

28. P. K. Hansma, D. A. Hickson, J. A. Schwartz, J. Catal. **48**, 237 (1977).

29. H. E. Evans, W. H. Weinberg, Applications of Surface Sci. **5**, 258 (1980).

30. C. D. Wagner, D. E. Passoja, H. F. Hillery, T. G. Kinisky, H. A. Six, W. T. Jansen, J. A. Taylor, J. Vac. Sci. Tech. **21**, 933 (1982).

31. S. Gauthier, S. De Cherveigne, J. Klein, M. Belin, Phys. Rev (1983), submitted.

32. W. M. Bowser, W. H. Weinberg, Rev. Sci. Instrum. **47**, 583 (1976).

33. A. Buyman, P. K. Hansma, Phys. Rev. Abst., 12 (1981).

34. C. B. Duke, in *Tunneling Phenomena in Solids*, E. Burnstein, S. Lundqvist, eds., Plenum Press, New York, p. 31 (1969).

35. M. Altwein, H. Finkenrath, J. Phys. E **6** (1973); J. G. Adler, J. E. Jackson, Rev. Sci. Instrum. **36**, 1301 (1965); S. Colley, P. K. Hansma, Rev. Sci. Instrum. **48**, 1192 (1977);

36. L. H. Dubois, in *Tunneling Spectroscopy*, P. K. Hansma, ed., Plenum Press, New York, p. 153 (1982).

37. D. R. Taylor, K. H. Ludlum, J. Phys. Chem. **76**, 2882 (1972).

38. J. B. Peri, J. Phys. Chem. **69**, 231 (1965).

39. S. T. King, E. J. Strojny, J. Cat. **76**, 274 (1982).

40. I. Giaever, in *Tunneling Phenomena in Solids*, E. Burnstein, S. Lundqvist, eds., Plenum Press, New York, p. 19 (1969).

41. D. G. Walmsley, W. J. Nelson, in *Tunneling Spectroscopy*, Plenum Press, New York, p. 311 (1982).

42. R. M. Kroeker, in *Tunneling Spectroscopy*, P. K. Hansma, ed., Plenum Press, p. 393 (1982).

43. U. Mazur, K. W. Hipps, J. Phys. Chem. **85**, 2244 (1981).

44. J. S. Modera, R. Meservey, P. M. Tedrow, App. Phys. Lett. **41**, 488 (1982).

45. O. I. Shklyarevskii, I. K. Yanson, V. D. Zaporozhskii, Solid State Comm. **14**, 327 (1974).

46. K. W. Hipps, U. Mazur, in *Tunneling Spectroscopy*, P. K. Hansma, ed., Plenum Press, p. 229 (1982).

47. R. C. Jaklevic, in *Tunneling Spectroscopy*, P. K. Hansma, ed., Plenum Press, New York, p. 451 (1982).

48. H. E. Evans, W. H. Weinberg, J. Chem. Phys. **71**, 1537 (1979).

49. J. D. Langan, P. K. Hansma, Surface Sci. **52**, 211 (1975).

50. M. Kroeker, P. K. Hansma, Surface Sci. **67**, 362 (1977).

51. W. M. Bowser, W. H. Weinberg, J.A.C.S. **102**, 4720 (1980); **103**, 1453 (1981).

52. H. E. Evans, W. H. Weinberg, J.A.C.S. **102**, 872 (1980).

53. J. T. Yates, Jr., T. M. Duncan, S. D. Worley, R. W. Vaughan, J. Chem. Phys. **70**, 1219 (1979).

54. D. E. McBride, J. T. Hall, J. Cat. **58**, 320 (1979).

55. R. C. Jaklevic, App. Surface Sci. **4**, 174 (1980).

Figure Captions

Figure 1: Cross section of an $Al/Al_2O_3/Pb$ tunnel junction depicting the physical morphology.

Figure 2: Cross section of an $Al/Al_2O_3/Pb$ tunnel junction depicting the energy levels and the elastic and inelastic tunneling processes.

Figure 3: Various current (I) voltage (V) characteristics of an idealized metal-insulator-metal tunnel junction containing an adsorbed species at the Al_2O_3/Pb interface. The adsorbed species has only one vibration with an angular frequency of ω: *(a)* I vs. V, *(b)* $\partial I/\partial V$, *(c)* $\partial^2 I/\partial V^2$ vs. V.

Figure 4: Harmonic detection scheme used for measuring the $\partial^2 V/\partial I^2$ vs. V characteristics of tunnel junctions.

Figure 5: Inelastic electron tunneling spectrum of an $Al/Al_2O_3/Pb$ tunnel junction that is free of impurities adsorbed at the Al_2O_3/Pb interface.

PHYSICAL PICTURE

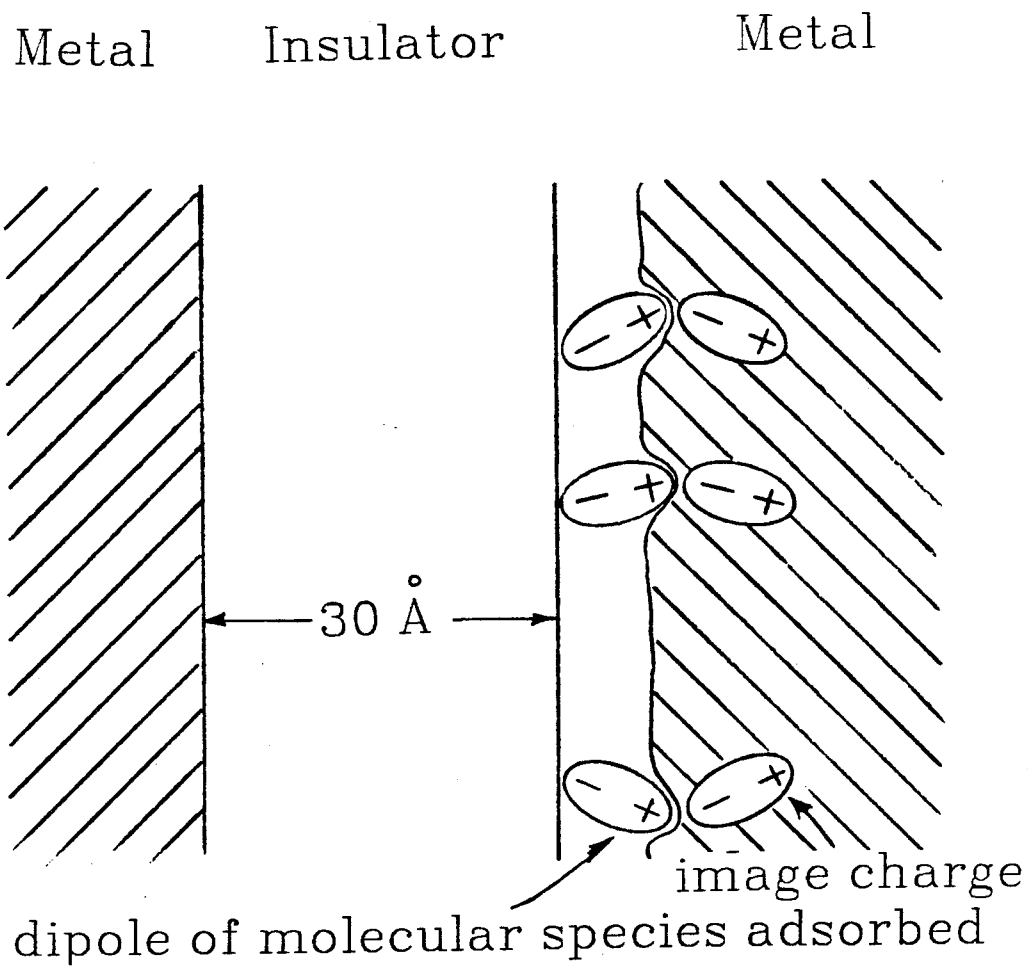

Figure I-1

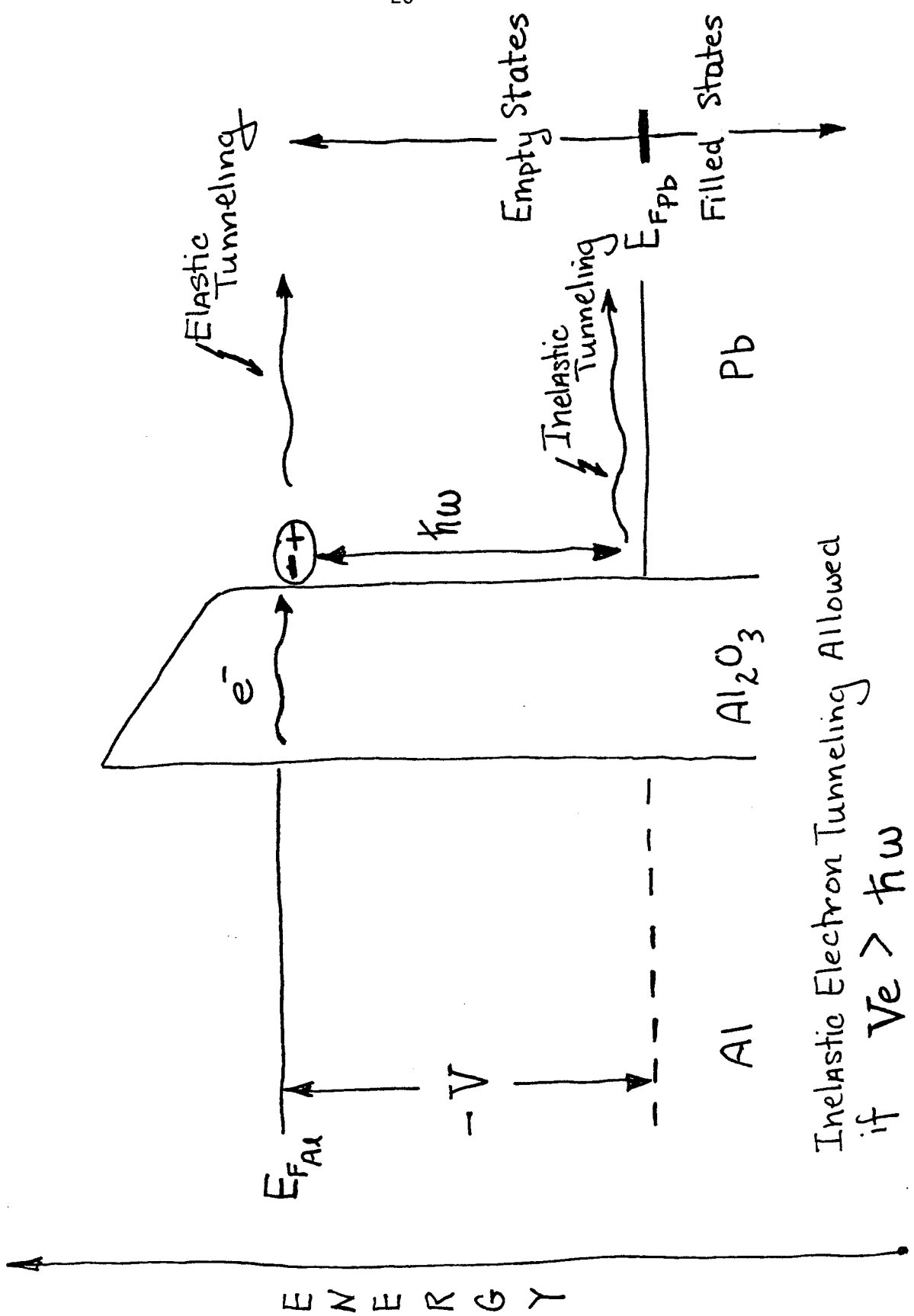
Elastic Tunneling
Empty States
Filled States
$E_{F_{Pb}}$
Inelastic Tunneling
Pb
$\hbar\omega$
e^-
Al_2O_3
Al
$-V$
$E_{F_{Al}}$
ENERGY
Inelastic Electron Tunneling Allowed
if $Ve > \hbar\omega$

Figure I-2

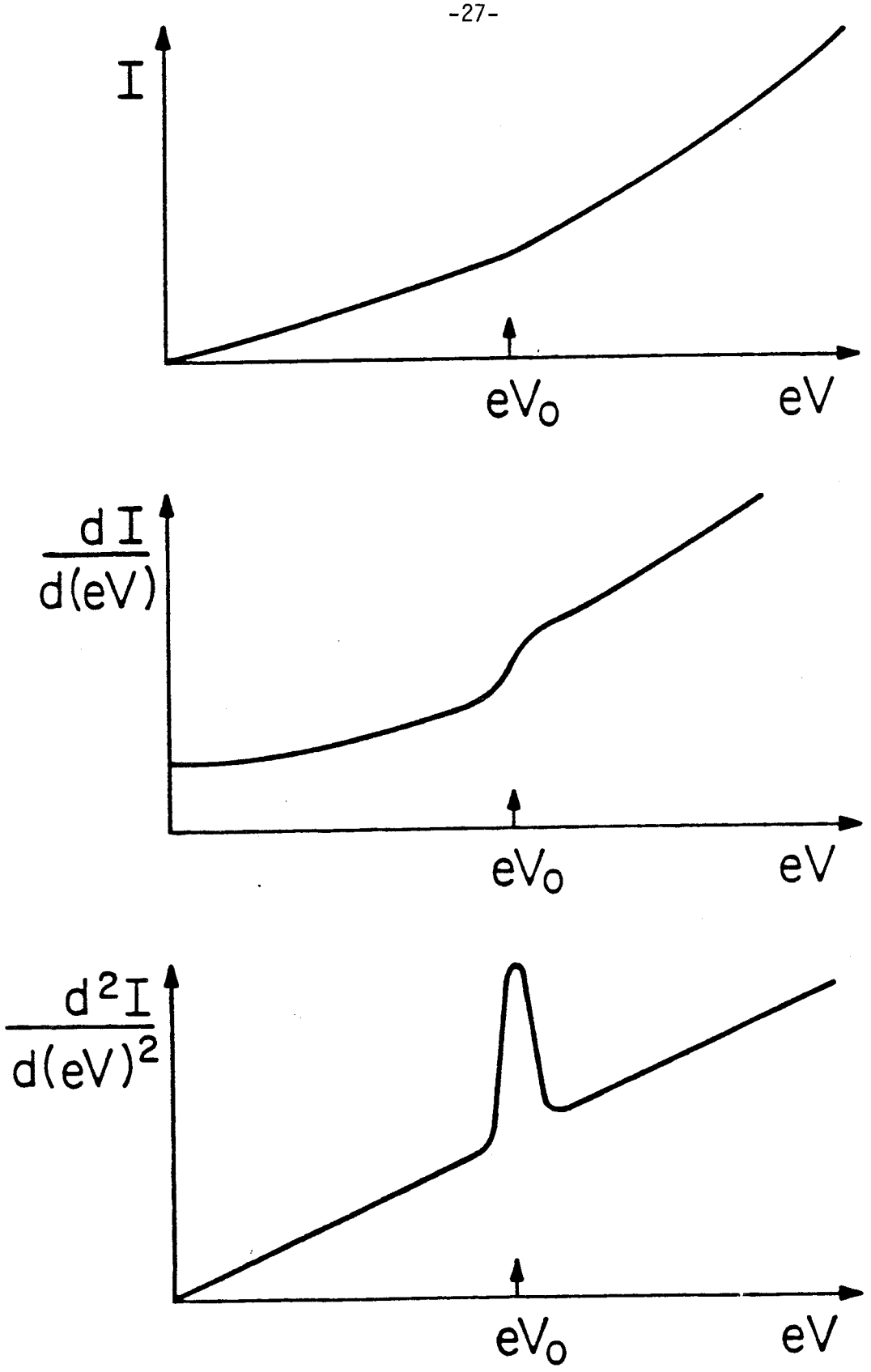

Figure I-3

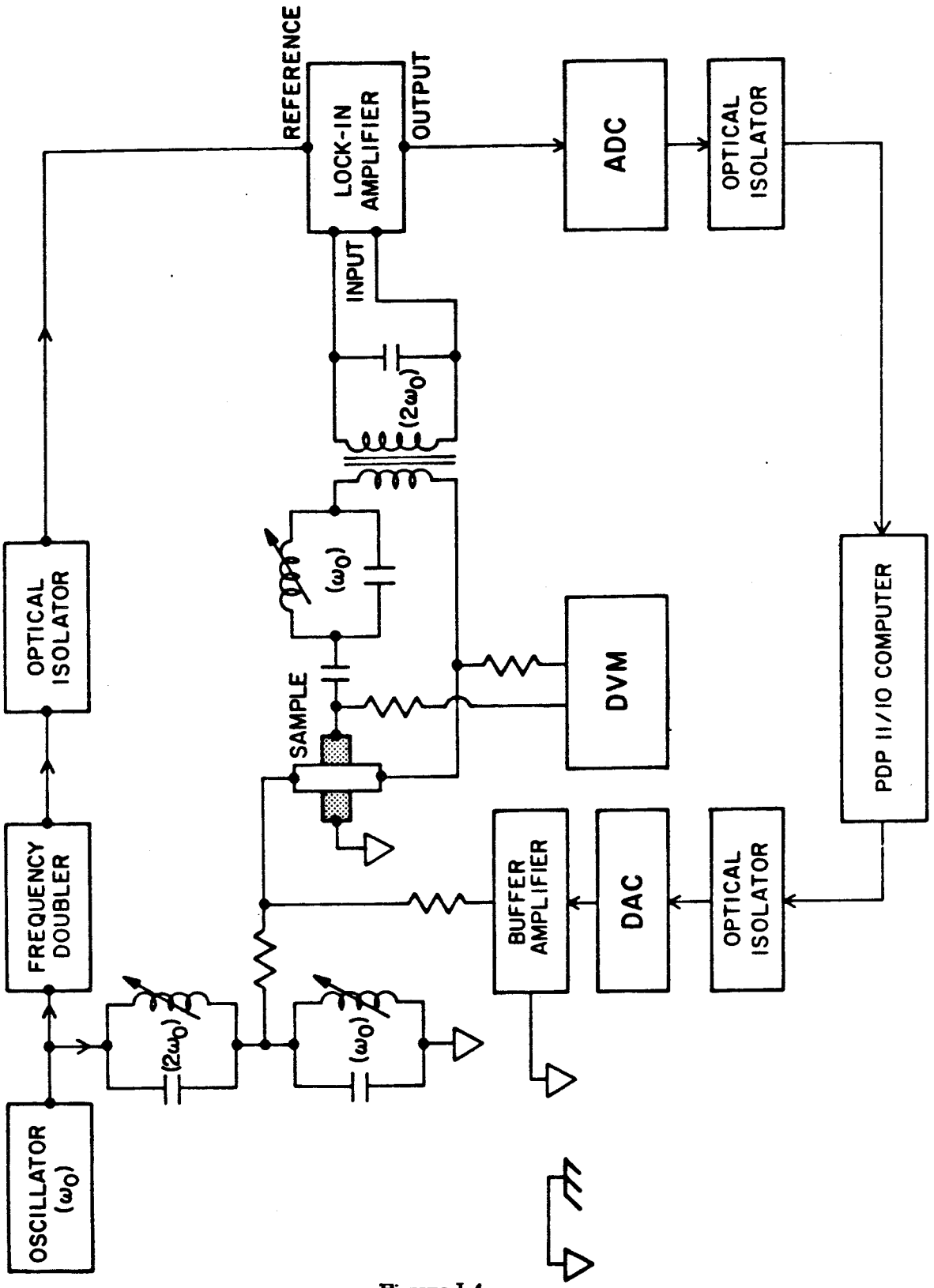
REFERENCE
LOCK-IN AMPLIFIER
OUTPUT
ADC
OPTICAL ISOLATOR
INPUT
$(2\omega_0)$
(ω_0)
OPTICAL ISOLATOR
SAMPLE
DVM
PDP 11/10 COMPUTER
FREQUENCY DOUBLER
BUFFER AMPLIFIER
DAC
OPTICAL ISOLATOR
$(2\omega_0)$
(ω_0)
OSCILLATOR (ω_0)

Figure I-4

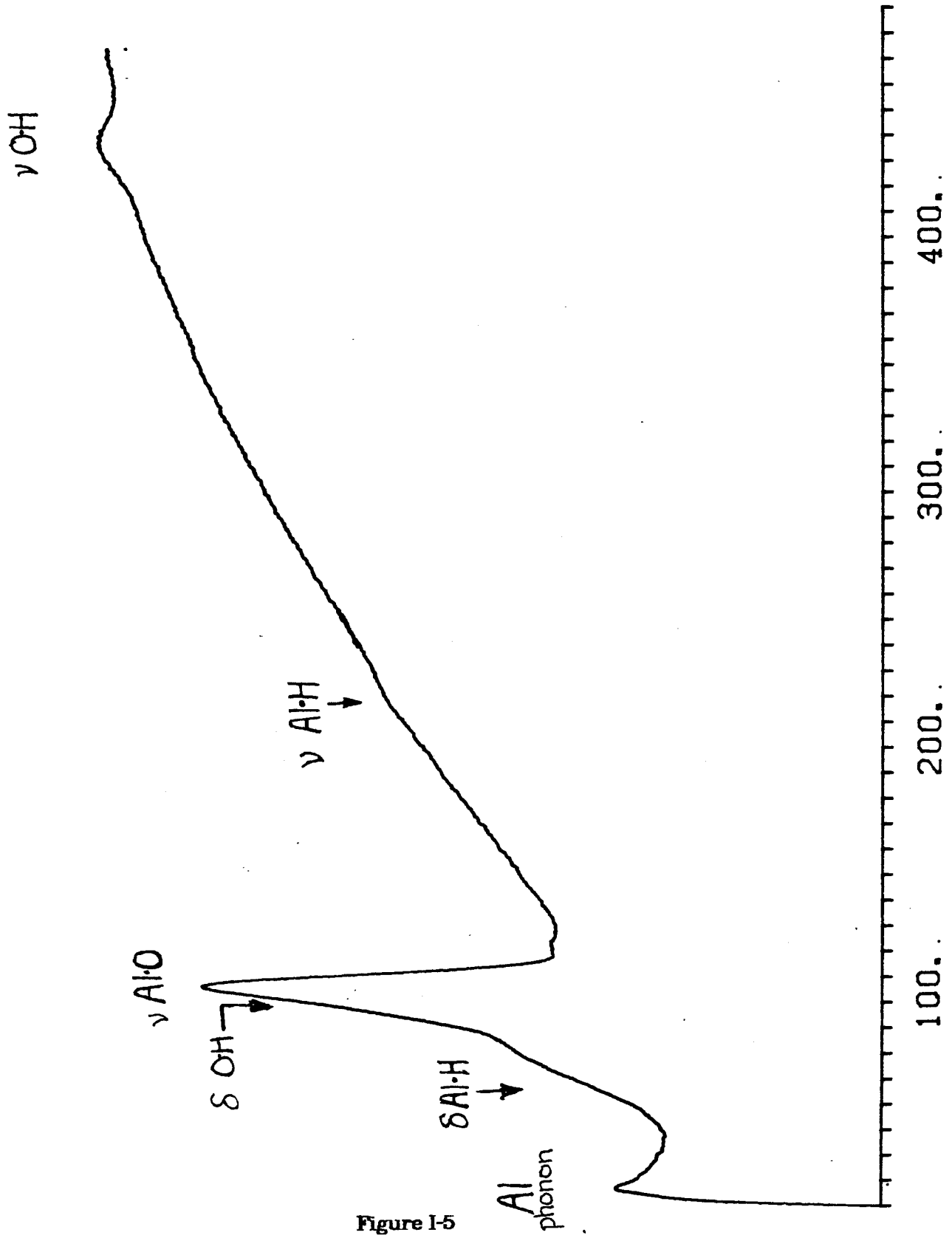

Figure I-5

Chapter II:

The Adsorption and Hydrogenolysis of Cyclopropane Carboxylic Acid on Aluminum Oxide

Abstract

The temperature and exposure dependent interaction of cyclopropane carboxylic acid with alumina surfaces has been studied with inelastic electron tunneling spectroscopy. Cyclopropane carboxylate and n-butane carboxylate were the only adsorbed species formed, as determined by a comparison with tunneling spectra of n-butane carboxylic acid and cyclopropane carboxylic acid coadsorbed on alumina. The n-butane carboxylate results from hydrogenolysis of the cyclopropyl ring of the adsorbed cyclopropane carboxylate with hydrogen supplied by surface hydroxyl groups. The relative populations of the two surface species are strongly dependent upon coverage and temperature.

1. Introduction

Tunneling spectroscopy has been employed to characterize a variety of surface reactions from the chemisorption of carboxylic acids on Al_2O_3 **(1-6)** to the reaction of acetylene with the polymerization catalyst $Zr(BH_4)_4$ supported on Al_2O_3 **(7)**. Tunneling spectroscopy has several advantages over conventional infrared spectroscopy in dealing with catalytic alumina and alumina supported systems. Among these advantages are submonolayer sensitivity in connection with low area surfaces, a large electron-vibration cross section for carbon-hydrogen modes, the observation of dipolar and induced dipolar allowed modes, and an excellent vibrational window extending well below 1000 cm^{-1}.

In this study, tunneling spectroscopy is used to examine the adsorption and hydrogenolysis of cyclopropane carboxylic acid (C_3H_5COOH) on alumina surfaces. Molecular carboxylic acid adsorbs dissociatively on alumina, resulting in an adspecies that is bound to the surface through the two carboxylate oxygens as the symmetrical bidentate cyclopropane carboxylate ion, probably of the bridging rather than the chelating type **(2)**. Consequently, for cyclopropane carboxylic acid, the surface bond through the carboxylate moiety serves to constrain the three-membered ring in close proximity to the surface, allowing subsequent reaction and/or fragmentation. In this way, C_3H_5COOH affords the opportunity to study the interaction of a strained ring having properties similar to unsaturated π electron systems **(8)** with the Al_2O_3 surface.

In a similar manner, unsaturated carboxylic acids adsorbed on alumina have been used to study the hydrogenation of carbon-carbon multiple bonds by the alumina surface. McBride and Hall **(9)** advantageously used the bicarboxylic acid muconate (HOOC-HC=CH-HC=CH-COOH) to study the hydrogenation of carbon-carbon double bonds on plasma grown Al_2O_3 by tunneling spectroscopy.

Similiarly, Jaklevic **(10)** studied the hydrogenation of the carbon-carbon triple bond of propiolic acid ($HC{\equiv}CCOOH$) by tunneling spectroscopy. Unlike these simple hydrogenation reactions, however, adsorbed cyclopropane carboxylic acid undergoes a skeletal rearrangement that involves the breaking of a carbon-carbon bond.

There has been no prior work concerning the adsorption or reaction of C_3H_5COOH with Al_2O_3. However, γ–Al_2O_3 (dehydroxylated at 723 K in vacuuo) catalyzed the exchange between D_2 and various alkanes, including cyclopropane and methyl cyclopropane at temperatures as low as 250 K **(11)**. On the other hand, the rates of γ–Al_2O_3 catalyzed isomerization of cyclopropane to propene, and methyl cyclopropane to trans-2-butene were measurable only above 358 K and 355 K, respectively **(11)**. Note that exchange and isomerization are perceived to be catalyzed by different active sites **(12)**. The isomerization of methyl cyclopropane over SiO_2–Al_2O_3 also produced strictly n-butenes **(13)**. However, the isomerization mechanisms over SiO_2–Al_2O_3 and Al_2O_3 are probably quite different, the former proceeding via a carbenium ion intermediate **(13)** and the latter proceeding via a carbanion intermediate **(11,12)**. In contrast, thermal cracking of methyl cyclopropane yields a nearly uniform distribution of structural isomers, and is thought to proceed via radical intermediates **(14)**. Al_2O_3 is not normally perceived as a hydrogenation catalyst on account of its low activity for such reactions. However, pure γ–Al_2O_3 (dehydroxylated at 923 K in vacuuo) was active for the hydrogenation of adsorbed ethylene **(15)**, and a composite Al_2O_3 consisting of γ–Al_2O_3 and bohemite (AlOOH) was active for the hydrogenation and isomerization of pent-1ene **(16)**. Although hydrogenolysis of cyclopropane and alkylcyclopropanes is observed in catalytic hydrocracking, the catalysts used in hydrocracking combine metal centers for catalytic hydrogenation on a SiO_2-Al_2O_3 support that functions for isomerization and catalytic

cracking **(17,18)**. However, it should be noted that while n-butanes are the dominant product (100%) in ring opening hydrogenolysis of methyl cyclopropane over SiO_2–Al_2O_3 supported platinum metal, iso-butanes (94-97%) are the products over SiO_2 supported platinum metal **(19)**.

The major results presented here are the identification of two stable intermediates in the reaction of cyclopropane carboxylic acid with a plasma grown aluminum oxide surface and a characterization of the reactivity pattern of the oxide for this particular reaction. For cyclopropane carboxylic acid, adsorption initially results in the formation of the cyclopropane carboxylate surface species. This species may interact with surface hydroxyls to form a new surface species, an n-butane carboxylate, by hydrogenolysis of the cyclopropyl ring. The hydrogenolysis reaction is more likely to take place at room temperatures if the coverage of the cyclopropane carboxylate is low, thereby maximizing the number of available hydroxyls per adsorbed cyclopropane carboxylate, or on an alumina surface that is heated above 500 K, thereby mobilizing the surface hydrogen.

To demonstrate the above ideas the paper proceeds as follows. Section 2 puts forth experimental details and tunnel junction fabrication procedures. Section 3 identifies the adsorbed cyclopropane carboxylate as the principal chemisorbed species formed when the plasma grown alumina is exposed to 0.4 Torr-s of cyclopropane carboxylic acid at 295 K. Here, the identification is by means of a comparison between the tunneling spectrum of this surface and the optical spectra of the sodium salt of cyclopropane carboxylic acid. Hence, under these conditions (low surface temperature and high coverage), the cyclopropane carboxylate adspecies is stable and likely to undergo hydrogenolysis. In Section 4 it is shown that cyclopropane carboxylic acid can form a second surface species, the n-butane carboxylate adspecies, upon adsorption and reaction with the

aluminum oxide surface. This is done by a comparison of two tunneling spectra, one of which was prepared by heating the alumina to 550 K during exposure to cyclopropane carboxylic acid and the other by exposing the alumina at 295 K to both cyclopropane carboxylic acid and n-butane carboxylic acid vapors. As noted above, the cyclopropane carboxylate surface species is unstable on the alumina surface temperatures above 500 K and reacts to form the n-butane carboxylate. Hence, the alumina heated to 550 K while exposed to the cyclopropane carboxylic acid should show a larger percentage of the n-butane carboxylate in its total adspecies population. Similarly, when n-butane carboxylate acid and cyclopropane carboxylic acid are coadsorbed on Al_2O_3 at 295 K, the relative population of the n-butane carboxylate surface species is "artificially" increased. Tunneling spectra of these two junctions should be very similar if n-butane carboxylate is indeed the reacted form of the cyclopropane carboxylate. In Section 5, the mechanism and energetics of the surface reaction are discussed. Isotopic labeling experiments (Fig. 3) are analyzed for information pertinent to these two topics. Finally, the paper is concluded with a summary in Section 6.

2. Experimental Procedures

The cyclopropane carboxylic acid (C_3H_5COOH) (95% purity), the n-butane carboxylic acid ($CH_3CH_2CH_2COOH$) (> 99%), the iso-butane carboxylic acid [$(CH_3)_2CHCOOH$] (> 99%), and the deuterium oxide (D_2O) (> 99%) were obtained from Aldrich Chemical and were used without further purification. Deuterium labeled cyclopropane carboxylic acid (C_3H_5COOD) was synthesized from the unlabeled reagent by an acid catalyzed exchange with D_2O: 5 ml C_3H_5COOH, 5 ml D_2O, and one drop of HCl were mixed and allowed to equilibrate for 30 min. in a water bath at 30°C. The mixture was vacuum distilled to leave the deuterium enriched cyclopropane carboxylic acid. This sequence was repeated three additional

times using the deuterium enriched cyclopropane carboxylic acid from the previous sequence as the starting material for the current sequence. An NMR spectrum of the final product showed that the deuterium enrichment of the acid proton was greater than 99%. In addition, the IR spectrum showed no absorption at 1178 cm^{-1}, indicating that residual amounts of D_2O were negligible.

Typically, junction fabrication was begun by the evaporation of 800 Angstroms (Å) of an Al film from a W coil through a mask onto a borosilicate glass substrate 2.5 cm x 1 cm x 1 mm in dimension. The base pressure prior to evaporation was below 1×10^{-8} Torr, and the film thickness was monitored by a quartz crystal microbalance. The Al film was annealed by resistive heating. The temperature was correlated with the film resistance, and, following Bowser and Weinberg **(20)**, this technique was used to control the substrate temperature in all subsequent steps in the synthesis of the junction. A cohesive oxide was then grown on the Al film by an oxygen plasma discharge. To grow a suitable oxide barrier in the UHV environment, water was required in the oxygen plasma atmosphere. [Brown and Walmsley **(3)** have also noted problems with rigorously dried O_2]. Pumpdown was followed by exposure to the adsorbate from the vapor phase. During this step, the oxide temperature was controlled carefully as described above, and the pressure was monitored by Varian UHV or Millitorr ionization gauges. In some cases, the oxide was held at room temperature during exposure and then heated following the evacuation of the belljar. For the cyclopropane carboxcyclic acid, typical pressures during exposure were between 0.1 and 0.5 micron.

After exposure to the adsorbate, 2000 Å of Pb were evaporated at a pressure below 1×10^{-5} Torr, in a cross strip pattern to form the completed junction. Junctions were removed from the vacuum system and mounted for immersion in liquid He. All measurements were carried out at 4.2 K with PDP 11/10

digitally controlled electronics **(21)**. The spectra were accumulated through multiple scan averaging, typically on the order of several hundred separate scans. The data were then processed as follows: (1) The spectra were first smoothed by a cubic convolute **(22)**; (2) An attempt was made at background removal (only linear functions of voltage were used to fit the background); (3) The peaks were located by a least-squares fit of the first derivative, followed by an interpolated location of the first derivative zero crossings; and (4) Peak energies were corrected for the Pb superconducting band gap and for modulation effects on the band gap width **(23)**.

For the isotopic labeling experiments, special procedures were required to produce a fully deuteroxylated alumina surface. Since surface hydroxyls exchange rapidly with D_2O or H_2O vapor, it was necessary to exchange the H_2O in the bell jar completely with D_2O. This was done by heating the bell jar to 75°C and then performing three successive cycles of evacuation to 10^{-5} Torr and exposure to several Torr of D_2O vapor for approximately one hour. A quadrupole mass spectrometer monitored the residual gas spectrum in the bell jar, and the degree of isotopic exchange could be evaluated from the ratio of mass peaks 20 (D_2O) to 19 (HDO). Following the third exposure to D_2O vapor, the bell jar was cooled and evacuated to approximately 1×10^{-7} Torr, and the aluminum evaporation was performed. The molar ratio of D_2O to HDO was greater than 7:1 at this point. For the plasma oxidation, an O_2/D_2O mixture was used, but following the plasma oxidation, the D_2O to HDO ratio decreased slightly. To insure nearly complete exchange of deuteroxyl groups for hydroxyl groups, the alumina surfaces were subjected to a high pressure "beam dose" of D_2O. From this point, the tunnel junctions were completed in the conventional manner described above.

The infrared sample was prepared by spraying a CaF_2 disk with Degussa Aluminum Oxide C, following the procedures of Yang & Garland **(24)**. The IR cell

was evacuated and exposed to approximately 300 microns of C_3H_5COOH for 500 s at room temperature, then evacuated for several hours.

3. The Cyclopropane Carboxylate Surface Species

A peak-by-peak comparison of the modes in the tunneling spectrum of Fig. 1(f) below 2000 cm^{-1} shows excellent agreement with the IR and Raman spectroscopic data of Maillols **(25)** for sodium cyclopropane carboxylate (see Table 1). This suggests that under the conditions of Fig. 1(f) (295 K and 0.4 Torr-s exposure), cyclopropane carboxylic acid adsorbs on the plasma grown Al_2O_3 predominantly as the cyclopropane carboxylate anion. This is consistent with nearly all of the investigations of the chemisorption of carboxylic acids on Al_2O_3 surfaces to date, where it has been concluded that the adsorbed species is the carboxylate anion of the acid. Using Raman depolarization, Maillols **(25)** identified mode symmetries, and, aided by theoretical and gas phase spectra of cyclopropane and its derivatives, proposed consistent mode assignments.

A tunneling spectrum of the clean alumina surface is shown in Fig. 1(a). This spectrum shows characteristic modes at 3600 cm^{-1} (due to surface hydroxyl O-H vibrations) and at 940 cm^{-1} and 650 cm^{-1} (due to bulk Al-O vibrations). If the clean alumina surface is exposed to increasing amounts of cyclopropane carboxylic acid, then Fig 1(b) through (f) result, with Fig. 1(f) being a near saturation exposure.

The point group symmetry for the free cyclopropane carboxylate anion is C_s. The symmetry element is the plane that is perpendicular to the plane containing the cyclopropyl ring and that bisects the cyclopropane ring through the tertiary carbon center. In the gaseous carboxylic acid, the O=C-OH group lies entirely in the symmetry plane **(26)**. Maillols **(25)** was able to assign 24 of the 27 possible vibrational modes of the free anion. The modes that were not assigned

correspond to the A" CH_2 scissoring mode [A" $\delta_S(CH_2)$], two deformation modes [A' and A" δ (C-C)]. The similarity between the tunneling spectra on the one hand and the IR and Raman spectra on the other hand has made it possible to confidently assign nearly 24 vibrational modes of the adsorbed species in direct analogy. From the close correspondence between the CH_2 stretching and deformation modes in the free anion and in the adsorbed species, it is apparent that the C_s symmetry classification is also valid for the CH_2 groups on the cyclopropyl ring of the adsorbed species. However, the orientation of the OCO group with respect to the symmetry plane is unclear. In addition to the 27 free anion vibrational modes, six additional modes - three frustrated translations and three frustrated rotations - are expected at low frequencies [for the cyclopropane carboxylate ($C_3H_5COO^-$) adsorbed on Al_2O_3]. These modes would be associated with deformation and stretching vibrations of Al-O type bonds, and hence, in conjunction with the strong vibrational signals from the Al-O modes of the alumina barrier, would be extremely difficult to detect. Thus, the six additional modes could not be assigned with confidence, but this does not mitigate any of the arguments to be made subsequently. However, as mentioned above, the adsorbate spectrum is almost, but not completely analogous to the free carboxylate anion spectrum . Hence, there are a number of mode assignments which shall be discussed individually.

3.1 Spectral Modes Below 800 cm^{-1}

For a surface acetate species, identified as the adsorbed species after acetic acid chemisorption on Al_2O_3, the COO^- rocking, wagging and scissoring modes appear as well defined modes of weak to moderate intensity near 475, 610, and 680 cm^{-1}, respectively **(2)**. The adsorption of propenoic acid (CH_2=CHCOOH) on Al_2O_3 results in a surface species with low frequency modes at 511, 630, and 684

cm^{-1} **(4)**. To be consistent with these data, it is necessary to assign the peaks in Fig. 1(f) at 490, 565 and 680 cm^{-1} to the COO^- rocking [$\rho(COO^-)$], the COO^- wagging [$\omega(COO^-)$] and COO^- scissoring modes [$\delta_s(COO^-)$], respectively (cf. Table 1) **(27)**. The in-plane CH deformation mode [A'δ(CH)] is assigned as the peak at 764 cm^{-1}. This switches Maillols' assignment of the COO^- scissoring mode and the in-plane CH deformation mode. Our proposed assignment, however, is also more consistent with the observed line shapes. The COO^- rocking, wagging and scissoring modes are observed to be broad and weak. For these modes, there are two possible effects responsible for this. (1) Lifetime broadening of the modes since vibrational energy transfer to the substrate lattice may be rapid for bonds adjacent to the surface; and (2) Since the cyclopropane carboxylate anion is chemisorbed through the carboxylate oxygen atoms, the COO^- wagging, twisting and rocking modes would be especially sensitive to adsorption site heterogeneity. On the other hand, for the CH in-plane deformation mode there is no a priori reason for expecting peak broadening or shifting, and the intensity and sharpness of the peak at 764 cm^{-1} would be in line with this.

3.2 The Spectral Mode at 955 cm^{-1}

It is logical to associate the peak at 951 cm^{-1} in the tunneling spectrum with the ring deformation mode observed at 945/946 cm^{-1} (IR/Raman) by Maillols **(25)**. However, electron coupling to Al-O longitudinal stretching modes contributes additional energy losses near this frequency. In junctions without an adsorbate on the oxide surface, this coupling yields a broad, intense peak characteristic of the tunneling spectrum of the Al_2O_3 barrier [cf. Fig. 1(a)]. This peak appears consistently in our unheated Al_2O_3 barriers at approximately 940 cm^{-1}. Traditionally, this Al-O mode assignment follows from polarized IR studies of electrochemically grown Al_2O_3 **(28)**. The observation by DeCheveigne, et al. **(6)**

concerning the sensitivity in the Al-O longitudinal phonon mode to perturbations by ^{18}O isotopically labeled carboxylic acid adsorbates indicates that the Al-O bonds of the adsorbate-surface complex furnish a significant fraction of the peak intensity of the Al-O mode. The 945 cm^{-1} ring deformation mode is intensely IR active, and the sharp adsorbate peak appears superimposed on the broad Al-O band. This implies that the 951 and 901 cm^{-1} peaks [due to the A" $r(CH_2)$ modes] are shifted down and up, respectively, in frequency from their true, deconvoluted values. As a consequence, the frequencies observed in tunneling spectroscopy are shifted slightly further away from the spectroscopic data for the free anion.

3.3 The A' $\delta(CH_2)$ and $\nu_s(COO^-)$ Modes

The assignment of the symmetric COO^- stretching mode [$\nu_s(COO^-)$], the CH_2 scissoring (symmetrical in plane deformation) mode [$\delta_s(CH_2)$], and the CH_3 asymmetric deformation mode [$\delta_a(CH_3)$] in carboxylic acids adsorbed on Al_2O_3 has been disputed in the literature. Recently with $CH_3C^{18}O^{18}OH$, DeCheveigne, et al. **(6)** have established firmly, however, the identification of the $\nu_s(COO^-)$ mode at 1470 cm^{-1} in the acetate adspecies. In the adsorbed cyclopropane carboxylic acid, the symmetric COO^- stretching mode and the CH_2 scissoring mode appear as a very strong peak at 1465 cm^{-1}, with a prominent low-frequency shoulder [Fig. 1(f)]. Analogy with the acetate adspecies suggests that the 1465 cm^{-1} peak in the spectrum of adsorbed C_3H_5COOH is due to the $\nu_s(COO^-)$ vibrational mode, and the prominent low-frequency shoulder results from the CH_2 scissoring mode. Without performing a detailed peak deconvolution, an estimate of 1450 cm^{-1} is deduced for the vibrational frequency of the CH_2 scissoring mode that gives rise to the shoulder. This frequency correlates well with the A' $\delta_s(CH_2)$ mode of the cyclopropane carboxylate sodium salt observed by Maillols at 1445

and 1453 cm^{-1} in the IR and Raman, respectively **(25)**.

Shifts in the COO^- asymmetric and symmetric stretching frequencies of the adsorbed carboxylate from the corresponding sodium salt frequencies infer much about bonding between the carboxylate and the surface. For cyclopropane carboxylate, the $\nu_s(COO^-)$ and $\nu_a(COO^-)$ modes are upshifted from 1429 and 1537 cm^{-1} in the Raman spectrum of the sodium salt to 1479 and 1579 cm^{-1} in the tunneling spectrum: shifts of 36 and 45 cm^{-1}, respectively. This is comparable to shifts in the acetate adspecies on Al_2O_3. The $\nu_s(COO^-)$ and $\nu_a(COO^-)$ modes in the acetate anion shift from 1413 and 1556 cm^{-1} [Raman spectrum of the sodium salt **(29)**] to 1470 cm^{-1} and 1598 cm^{-1} in the tunneling spectrum **(2)**: shifts of 57 and 42 cm^{-1}, respectively. Therefore, by analogy to the surface acetate species **(2)**, the bonding of cyclopropane carboxylate to the surface is bidentate, symmetrical bridging through the carboxylate moiety.

3.4 The $\nu(CH_2)$ and $\nu(CH_2)$ Modes above 3000 cm^{-1}

The C-H stretching modes of the sodium salt of cyclopropane carboxylic acid all lie above 3000 cm^{-1}. Hence, it is convenient to consider first those bands in the tunneling spectrum above 3000 cm^{-1}, which, in direct analogy to the sodium salt, are due to a cyclopropane carboxylate adspecies.

The free anion has five CH stretching modes (cf. Table 1). These are A' and A'' $\nu_s(CH_2)$, the A' and A'' $\nu_a(CH_2)$, and the A' $\nu(CH)$ modes. However, the Raman spectrum of the free anion shows only four peaks, the two lowest lying CH stretching modes [A'$\nu(CH)$ and A'$\nu_s(CH_2)$] being unresolved.

The two highest lying modes (the two CH_2 asymmetric stretching modes), are only split by 12 cm^{-1} in the Raman spectrum. Since the instrumental broadening function of the tunneling spectrometer is approximately 14 cm^{-1} in the best scans of this spatial region, two Lorentzian functions would be unresolved.

Hence, the tunneling peak at 3084 cm^{-1} (FWHM = 50 cm^{-1}) is assigned to this combination of modes (cf. Table 1). Comparing the tunneling peak at 3084 cm^{-1} to the Raman center of mass for these two asymmetric stretching modes (of nearly equal Raman intensity), a shift of approximately -5 cm^{-1} is found. This is in good agreement, for example, with the results of Evans and Weinberg who found shifts ranging from -6 to -15 cm^{-1} between tunneling and optical spectra of CH stretching modes of ethanol chemisorbed on Al_2O_3 **(2)**.

The two lowest lying CH stretching modes of the free anion are the the A'' $\nu_s(CH_2)$ mode and the composite of the A' $\nu_s(CH_2)$ mode and A' ν(1-CH) modes, occurring at 3048 and 3018 cm^{-1}, respectively, in the Raman spectrum. However, the corresponding region in the tunneling spectra shows only one peak at 3001 cm^{-1} (FWHM M = 50 cm^{-1}). This would reasonably correspond to the lowest frequency CH stretching mode of the free anion. For the free anion, the Raman bands for these two modes are split by approximately 30 cm^{-1}, and this should be resolvable in the tunneling spectrum. The conspicuous absence of the A'' $\nu_s(CH_2)$ modes required further investigation. Consequently, IR measurements with C_3H_5COOH adsorbed on Al_2O_3 were carried out in order to confirm the tunneling spectroscopic findings. As may be seen in Fig. 4, four $\nu(CH_2)$ modes were visible corresponding closely (within ± 2 cm^{-1}) to the Raman spectrum of the sodium salt. The A' $\nu_s(CH_2)$ mode, the strongest IR mode, has a full-width at half-maximum (FWHM) of approximately 20 cm^{-1}. The A'' $\nu_a(CH_2)$, and A' $\nu_a(CH_2)$ modes were observed as a less intense peak (FWHM $\approx$ 16 cm^{-1}) with a small shoulder. Curiously, the A'' $\nu_s(CH_2)$ mode was barely visible. Hence, the "absence" of the corresponding mode in the tunneling spectrum is probably due to its being only a weakly active mode that is buried between the remaining two intense C-H stretching modes.

The broad line width (> 40 cm^{-1}) of the two $\nu(CH_2)$ modes in the tunneling spectrum may be explained by considering that in reality two modes are responsible for the intensity of each peak. Hence, different downshifts in frequency due to image dipole interactions for each mode may increase the frequency splitting, broadening the peaks **(30)**. It is apparent that the distance between the CH_2 groups and the Pb overlayer may vary substantially from molecule to molecule, giving a distribution of frequency shifts. The shape of the ring breathing mode supports this idea. It is the narrowest spectral line, and because its dipole derivative is most remote from the Pb overlayer (without suffering lifetime broadening), it experiences only weak image-dipole shifts.

3.5 The $\nu(CH_n)$ Modes below 3000 cm^{-1}

There are clearly no vibrational modes of the adsorbed cyclopropane carboxylate anion that would reasonably yield the observed low frequency peaks at 2950-2800 cm^{-1} in Fig. 1(f). Therefore, to explain the existence of these peaks, it is necessary to postulate the existence of another surface species in addition to the cyclopropane carboxylate anion.

4. The n-Butane Carboxylate Surface Species

For the majority of carboxylic acids studied (e.g., saturated hydrocarbons), at room temperature the Al_2O_3 surface exhibits little affinity or reactivity for the hydrocarbon group, as evidenced by little or no perturbation in the carbon-hydrogen stretching vibrations. This is true also for cyclopropane carboxylic acid in the sense that [as we have identified in Fig. 1(f)] there are CH stretching modes present in the tunneling spectrum that correspond closely to the CH stretching frequencies of the sodium salt of this acid. However, there is also a moderately strong CH stretching band in the tunneling spectrum that is not present in the IR or Raman spectrum of the sodium salt. Furthermore, this CH

stretching band is present (with undiminished intensity) in the other tunneling spectra of Fig. 1, as well as in Fig. 2(c) where C_3H_5COOH is exposed to an alumina surface heated to 550 K. In the latter, the intensity of this CH stretching band has increased markedly.

The appearance of the strong carbon-hydrogen stretching bands at 2962, 2908, and a shoulder (sh) at 2860-2870 cm^{-1} with intensity comparable to the $\nu(CH_2)$ modes of the adsorbed cyclopropane carboxylate anion is certain evidence for the existence of a second adsorbed hydrocarbon species (cf. Fig. 2c). The spectral regions where the $\delta_s(CH_2)$ and $\nu_s(COO^-)$ modes of adsorbed $C_3H_5COO^-$ appear also show new vibrational modes. It is clear that the surface species responsible for these additional modes is a carboxylate anion; modes corresponding to $\nu_a(COO^-)$ and $\tau(C\text{-}COO^-)$ remain strong despite significant reduction in the $C_3H_5COO^-$ surface population.

Bearing in mind that the chemical transformation undergone by the $C_3H_5COO^-$ is probably some form of ring opening, a list of likely reaction products is readily enumerable:

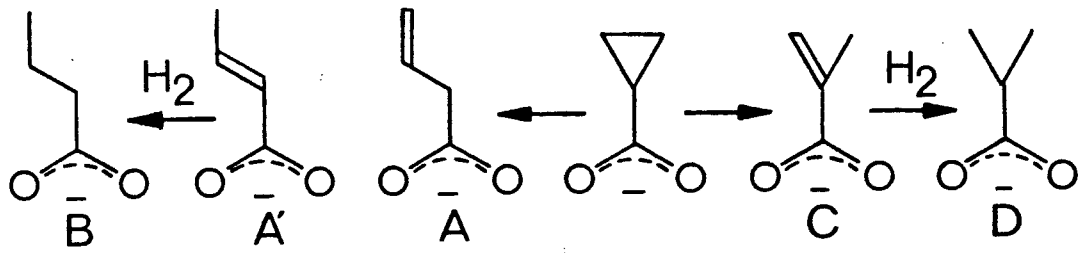

In Fig. 2(c), the absence of carbon-carbon multiple bond stretching modes, coupled with the paraffinic character of the unidentified carbon-hydrogen stretching modes, is compelling evidence that the second surface species is a paraffinic hydrocarbon. In fact, the tunneling spectrum of adspecies A', crotonate, has

been reported **(1)** and shows a carbon-carbon double bond stretching mode and other modes that are absent in our spectra. These arguments eliminate the unsaturated species (A, A' and C) shown above, in favor of either saturated species (B and/or D). Vibrational modes attributable to the $\nu_a(CH_3)$ (2940 cm^{-1}), the $\nu_s(CH_3)$ (2880-2860 cm^{-1},sh) and the $\delta_s(CH_3)$ (1380 cm^{-1}) identify a methyl group; while modes attributable to the $\nu_a(CH_2)$ (2908 cm^{-1}), and the $\nu_s(CH_2)$ (2870-2860 cm^{-1},sh) indicate the presence of a methylene group **(39)**. Other strong stretching modes characteristic of these groups [$\delta_a(CH_3)$ (1480-1430 cm^{-1}) and $\delta_s(CH_2)$ (1490-1450 cm^{-1}) **(31)**] most certainly occur, but they are unresolved in the broad loss (FWHM $\approx$ 80 cm^{-1}) at 1450 cm^{-1} that also contains another mode for this species [$\nu_s(COO^-)$], plus modes from the unreacted $C_3H_5COO^-$ [($\nu_s(COO^-)$ and $\delta(CH_2)$]. These observations argue in favor of n-butane carboxylate (species B) as a product of reaction. However, the existence of the isobutane carboxylate surfaces species (D) cannot be ruled out. Because of the broad line widths intrinsic to tunneling spectroscopy it is impossible to find modes, such as skeletal vibrations, unique to species B or D and yet still free from interfering bands of other surface species. Nevertheless, it has been possible to reduce the number of candidate surface species to either n-butane carboxylate (B) and/or isobutane carboxylate (D).

To provide positive identification, isobutane carboxylic acid and n-butane carboxylic acid were adsorbed independently on Al_2O_3. The resulting tunneling spectra for alumina exposed to 0.21 Torr-s of isobutane carboxylic acid at 295 K, and for alumina exposed to 0.21 Torr-s of n-butane carboxylic acid at 295 K are shown in Figs. 2(a,e), respectively **(32)**. To reproduce closely the expected distribution of surface species from C_3H_5COOH adsorbed on alumina heated above 500 K [Fig. 2(c)], n-butane carboxylic acid and cyclopropane carboxlic acid were coadsorbed on alumina at 295 K [Fig. 2(d)]. Isobutane carboxylic acid and

cyclopropane carboxylic acid were also coadsorbed on alumina [Fig. 2(b)] at 295 K to check for the other possible combination of surface species (i.e., isobutane carboxylate and cyclopropane carboxylate). A comparison of the tunneling spectrum of alumina exposed to 0.4 Torr-s of C_3H_5COOH at 550 K [Fig. 2(c)] and the tunneling spectrum of alumina exposed to n-C_3H_7COOH and C_3H_5COOH at 295 K [Fig. 2(d)] gives an exceedingly close match, except for intensity differences due to the imperfect match in the relative populations of n-$C_3H_7COO^-$ and $C_3H_5COO^-$ on each surface. On the other hand, a comparison of the tunneling spectrum of alumina exposed to 0.4 Torr-s C_3H_5COOH at 550 K [Fig. 2(c)] and the tunneling spectrum of alumina exposed to 150-C_3H_5COOH and C_3H_5COOH at 295 K [Fig. 2(b)] is an obvious mismatch. The twin peak structure of the combination of the $\delta(CH_2)$, $\delta_a(CH_3)$, δ_s(ch3) and $\nu_s(COO^-)$ modes apparent in Fig. 2(b) is absent from Fig. 2(c), nor is the structure of the CH stretching region in Fig. 2(b) reproduced in Fig. 2(c). Thus, within the detectability limit, isobutane carboxylate is not present on the surface. Hence, it can be concluded that cyclopropane carboxylic acid chemisorbs on plasma-grown alumina as either the cyclopropane carboxylate anion or the n-butane carboxylate anion, depending upon the surface temperature and surface coverage.

Surface hydroxyls on TiO_2 reportedly add across the carbon-carbon double bond of cyclohexene to form a surface cyclohexanolate **(33)**. Homogeneous analogues of this reaction, such as the acid catalyzed hydration of a carbon-carbon double bond, have been studied extensively **(34)**. These reactions suggest that, acidic or electrophilic, surface hydroxyls must be responsible for the observed hydrations on TiO_2. Although measurements indicate the surface acidity of Al_2O_3 is substantially less than TiO_2 **(35)**, in light of the unprecedented observation of hydrogenolysis that is reported herein, it would be important to verify that we are not in fact observing a hydration reaction. This is especially

important in view of the expected close similarity in spectra between the n-butane carboxylate and the possible hydration product of cyclopropane carboxylate, which would be the 2-hydroxy n-butane carboxylate. This latter isomer is to be the preferred product, based on the acid catalyzed isomerization of methy cyclopropane over SiO_2–Al_2O_3 where the acid proton attacks one of the vinyl carbons **(13)**. Therefore, an aluminum oxide surface was exposed to a 0.016 M solution of 2-hydroxy n-butane carboxylic acid in H_2O. The resulting tunneling spectrum is shown in Fig. 2(f). The C-H stretching in this spectrum [Fig. 2(f)] compares unfavorably with the aliphatic C-H stretching region in the spectrum of cyclopropane carboxylic acid adsorbed at 550 K; in the former spectrum, the C-H stretching region does not show the distinct shoulder at 2860 cm^{-1} that is visible in the latter spectrum. This difference was not an experimental artifact. Consequently, the products of a hydration reaction are absent on the surface of Al_2O_3 exposed to C_3H_5COOH above 550 K, and this further strengthens our earlier identification of n-butane carboxylate as the only reaction product.

5. The Surface Hydrogenolysis Reaction

5.1. Isotopic Studies

To gain further insight into the reaction mechanism whereby the adsorbed cyclopropane carboxylate is converted to the n-butane carboxylate, isotopic labeling experiments were performed. These experiments consisted of producing a plasma grown alumina surface that had surface deuteroxyl groups (OD) rather than surface hydroxyl groups (OH). The deuterium labeled alumina surface was then exposed to 0.036 Torr-s of deuterium labeled cyclopropane carboxylic acid (C_3H_5COOD) at 295 K. The exposed surface was then heated to 573 K in vacuum. Tunneling spectra from junctions completed after each of these

three steps are shown, respectively, in Figs. 3(a), (b) and (c). These spectra are similar to the analogous spectra of the unlabeled surface exposed to the unlabeled acid with the exception of two features. These are the OD stretching mode at 2666 cm^{-1} [Fig. 3(a)] rather than OH stretching mode at 3600 cm^{-1} (for clean plasma grown alumina surfaces), and the broad ($\sim$ 120 cm^{-1} FWHM) carbon-deuterium stretching mode centered at 2172 cm^{-1}. Comparing the tunneling spectrum of C_3H_5COOD adsorbed on the surface before heating [Fig. 3(b)] to the tunneling spectrum of C_3H_5COOD adsorbed on the surface after heating to 573 K [Fig. 3(c)], it is apparent that several significant changes have taken place. The intensity of the OD stretching mode at 2698 cm^{-1} has decreased, and, concomitantly, the intensity of the CD stretching mode has increased. Clearly, deuterium has been transferred from OD groups to form carbon-deuterium bonds. The carbon-deuterium modes are almost certainly not the result of exchange between the deuteroxyls and the hydrogen in the adsorbed cyclopropane carboxylate species. If this were the case, the OH stretching mode would show an increase in intensity comparable to the OD decrease in intensity (assuming reasonably equivalent cross sections for deuterium and hydrogen). However, within experimental error, the intensity of the OH mode remains unchanged. Hence, it can be concluded that the hydrogenolysis of cyclopropane carboxylate adsorbed on Al_2O_3 involves the transfer of hydrogen from the surface hydroxyls to form additional carbon-hydrogen bonds. If the integrated intensity of the C-D stretching mode is compared with the integrated intensity of the aliphatic C-H stretching mode, a ratio of 2.2 to 5.0 is found. This is very close to the predicted ratio of 2:5 if it is assumed that C-D and C-H vibrations have identical cross sections. This confirms that hydrogen from two surface hydroxyls is transferred to the cyclopropane carboxylate to form the n-butane carboxylate surface species.

The final point of interest concerning the carbon-deuterium stretching mode is its FWHM of ~ 120 cm^{-1}. This is apparently the same as the FWHM of the combined aliphatic C-H stretching modes. Infrared studies have shown the carbon-deuterium stretching frequency to shift from 2169 cm^{-1} to 2154 cm^{-1} as the deuterium location shifts from the methyl group in 1-deuteropropane to the methylene group in 2-deuteropropane. This indicates that as the adsorbed cyclopropane carboxylate undergoes hydrogenolysis to form the n-butane carboxylate adspecies, the deuterium that is effecting hydrogenolysis is incorporated onto different carbon centers in the hydrogenolysis products.

5.2. The Coverage Dependent and Temperature Reactivity of the Al_2O_3 Surface

At constant temperature (295 K), the coverage dependence of the n-butane carboxylate and cyclopropane carboxylate adspecies populations yield information concerning the coverage dependent reactivity of the Al_2O_3 surface (cf. Fig. 1). The stretching modes associated with the n-butane carboxylate species (2935-2830 cm^{-1}) are the first CH modes to appear after low exposures of the Al_2O_3 surface to C_3H_5COOH (cf. Fig. 1b). With increasing exposure, these modes subsequently stop growing in intensity (or grow little), while the CH modes of the cyclopropane carboxylate species (3001-3081 cm^{-1}) continue to increase dramatically in intensity [cf. Figs. 1(c-f)]. This implies that cyclopropane carboxylate undergoes a hydrogenolysis reaction on the alumina surface at low coverages. As the surface coverage increases, the differential amount of adsorbed cyclopropane carboxylic acid is significantly less likely to undergo hydrogenolysis. An estimate of the number of reacted molecules on the Al_2O_3 surface at 295 K can be made by calculating the relative areas of the CH modes below 3000 cm^{-1} compared to those above 3000 cm^{-1}. This assumes that the electron-

vibrational coupling constant of CH modes is independent of symmetry and chemical species. On this basis, one concludes that 25% of the chemisorbed molecules undergo hydrogenolysis.

At fixed exposure of 0.4 Torr-s, the temperature dependence of the hydrogenated species population gives distinct clues concerning its formation. As judged by the spectral band between 2800 and 2980 cm^{-1}, the surface population of the n-butane carboxylate remains small and nearly constant, independent of temperature, until approximately 460 K. (Although not shown here, tunneling spectra of alumina exposed to C_3H_5COOH at temperatures below 500 K are virtually identical to their unheated counterparts shown in Fig. 1.) Between 460 and 500 K, the population of adsorbed n-butane carboxylate increases as shown in Fig. 2(c). However, a further increase in the surface temperature results in little increase in the amount of cyclopropane carboxylate hydrogenolysis product. The motion of protons on bare Al_2O_3 had been explored only by NMR at temperatures below 400 K **(36)**. Consequently, calculations of the rate of thermal diffusion of protons cannot be made for this surface since thermal spin diffusion is not the dominant mechanism of relaxation over this temperature regime. However, studies of protons on decationized zeolites indicate that the proton diffusion coefficient, expressed in terms of a jump frequency, increases from 0.2 sec^{-1} at 300 K, 2.2 x 10^4 sec^{-1} at 473 K, to 1.5 x 10^5 sec^{-1} at 525 K, where the jump distance is approximately 4.4 Å **(37)**. Presumably, the significantly enhanced rate of proton diffusion at high temperatures is largely responsible for the observed rapid increase in the population of the n-butane carboxylate.

Diffusion, however, is an activated process, and if solely responsible for surface hydrogenation, the surface population of hydrogenated species would show an exponential temperature dependence. This is not the case, however. Rather,

above 500 K at constant coverage, the ratio of hydrogenated to unreacted surface populations remains remarkably invariant, increasing only slightly between 500 and 700K, indicative of a rate limiting process other than proton diffusion. Certainly the reaction is not hydrogen limited: a moderate hydroxyl stretching mode attests to the availability of surface hydrogen [cf. Fig. 3(c)]. On the other hand, possible hydroxyl sites around an adsorbate molecule could be statistically blocked on a nearly saturated surface. Since the carboxylate is immobile, this would effectively limit the $C_3H_5COO^-$ available for reaction.

5.3 The Mechanism of the Hydrogenolysis Reaction

Tunneling spectroscopy has been previously used to investigate the hydrogenation of carbon-carbon double and triple bonds on Al_2O_3 surfaces produced by plasma oxidation of an evaporated Al film. Brown, et al. **(4)** observed a mixture of hydrogenated products and parent molecules on Al_2O_3 barriers of tunnel junction exposed to HC≡CCOOH, H_2C=CHCOOH and 3-methyl but-2-enoic acid at room temperature. McBride and Hall **(9)** investigated the temperature dependent incorporation of deuterium from D_2O vapor into muconic acid (HOOC-HC=CH-HC=CH-COOH) adsorbed on Al_2O_3 barriers of tunnel junctions. The deuterium was incorporated by deuteration of the double bonds to form adipate, the corresponding saturated hydrocarbon. Jaklevic **(10)** has examined the hydrogenation and deuteration of HC≡CCOOH in tunnel junctions exposed to this acid at room temperature. In all cases, the source of hydrogen was concluded to be surface hydroxyl groups. The present work, however, is the first observation of ring hydrogenolysis where carbon-carbon bonds are broken, and the hydrocarbon skeletal structure is changed.

Since isomerization is intrinsically faster than hydrogenation, and since identical sites on dehydroxylated Al_2O_3 powders catalyzed both isomerization (1-

butene) and hydrogenation (ethylene) **(15)**, it may be fundamentally correct to view the hydrogenolysis as an isomerization followed by a hydrogenation. Then, the observed selectivity of the hydrogenolysis of cyclopropane carboxylate to n-butane carboxylate may be a consequence of the selectivity of Al_2O_3 powders to isomerize methyl cyclopropane to trans-2-butene **(38)**. Certainly this is not a completely fortuitous result since thermal isomerization of methyl cyclopropane yields a uniform distribution of isomers **(14)** and hydrogenolysis of methyl cyclopropane by Pt metal on an inactive support (SiO_2) yields isobutanes **(19)**. Although the isomerization of methyl cyclopropane over SiO_2–Al_2O_3 also yields strictly n-butenes **(13)**, the isomerization mechanism over these catalysts involves proton transfer *from the surface* to the hydrocarbon to form the carbocation **(13)**, whereas the isomerization mechanism over Al_2O_3 involves proton transfer *to the surface* to form the carbanion **(11,12)**. Although the hydrogenolysis product distribution is well in accord with dehydroxylated Al_2O_3 powders, there are a number of important distinctions between these catalytically active materials and the aluminum oxide film. In particular, on Al_2O_3 powders, the active sites, which are thought to be created by dehydroxylation at very high temperatures, have an extremely low density, which is estimated to be on the order of 1.4×10^{13} sites cm^{-2} for hydrogenation below 333 K and as low as 1.6×10^{12} sites cm^{-2} for hydrogenation above 333 K **(15)**. In contrast, these numbers are to be compared with the number of active sites for hydrogenolysis on the aluminum oxide films which were not produced by high temperature pretreatment and which, from the number of adsorbed cyclopropane carboxylates that underwent hydrogenolysis in Fig. 2(c) is estimated to be 1.1×10^{14} sites; several very reasonable assumptions were made to arrive at this figure: (1) the (100) surface of plane of γ–Al_2O_3 is preferentially exposed **(39)**, (2) adsorption sites consist of pairs of octahedrally coordinated aluminum ions of the (100) surface,

(3) the surface in Fig. 2(c) is saturated, and (4) the relative coverage of the cyclopropane carboxylate to the n-butane carboxylate is 2:1. Furthermore, on the Al_2O_3 powder, the experimental evidence strongly supported a hydrogenation mechanism involving adsorbed ethylene and molecularly adsorbed H_2 **(15)**; whereas on the aluminum oxide films, the surface hydroxyls provide hydrogen and there is no source of gaseous hydrogen. Thus, the hydrogenation mechanisms for Al_2O_3 powders would not fully explain the hydrogenation **(4,9,10)** and hydrogenolysis results observed on aluminum oxide films.

However, a boehmite/γ–Al_2O_3 prepared from Al_2O_3 powder exhibits behavior that is remarkably similar to what has been reported here **(11)**. For example, the number of active sites was measured (by HCl poisoning) to be between 1 x 10^{14} and 0.42 x 10^{14} sites cm^{-2} for different preparations. Furthermore, high temperature activation was unnecessary and, in fact, the deactivated material was regenerated with steam. The material was active for both isomerization and hydrogenation of 1-pentane and 1,3-butadiene to butenes. Although the material was referred to as a "catalyst," in our opinion it exhibited a stochiometric behavior. In most instances, during the hydrogenation of 1-pentene, the activity of the material decreased slowly with time. Furthermore, the turnover number (number of 1-pentene molecules hydrogenated per site per hour) calculated for the most active material was 0.2. Thus to substantiate "catalytic" activity, the catalysts must necessarily be run for at least five hours, whereas typical run times were no longer than one hour. Unfortunately, the behavior of the "catalyst" in the absence of hydrogen was not mentioned. As detailed above, the aluminum oxide films also suggest morphological similarities. From X-ray diffraction and differential thermal analysis, a γ-alumina core covered by 0.2 to 0.7 monolayer of bohemite was the hypothesized structure for the active material. The active region may consist of the interface between the bohemite

and the γ–Al_2O_3 surface. Supporting this view was the complete inactivity of pure bohemite for any hydrocarbon transformations.

However, there is no spectroscopic evidence for the presence of bohemite on our aluminum oxide films. In the concentrations necessary for the observed behavior, the bohemite would be detectable easily by the presence of a mode at 1070 cm^{-1}, as reported in the infrared spectrum of bohemite powders **(40)**, whereas the clean aluminum oxide film does not have a mode in this vicinity.

Although metal oxides such as ZnO and MgO are active for hydrogenation/dehydrogenation, the active site in these materials is thought to involve a metal hydride. Though there is evidence for Al-H at the Al/Al_2O_3 interface of Al/Al_2O_3/Pb tunnel junctions **(41)**, because of the rapid gettering action of low valent aluminum with residual H_2O, this type of structure is not likely to be present at the Al_2O_3/vacuum interface.

6. Synopsis

The temperature and coverage dependent interaction of cyclopropane carboxylic acid with aluminum oxide surfaces has been studied with tunneling spectroscopy. The coverage dependent work was carried out at room temperature, while the temperature dependent work was done at constant coverage with the temperature varied between 295 and 700 K. The Al_2O_3 surface was synthesized by plasma oxidation of Al films. Two species were formed upon adsorption, the relative populations of which were a function of coverage and temperature. A comparison of the IR and Raman spectra of sodium cyclopropane carboxylate and the tunneling spectra of the acid adsorbed on Al_2O_3 indicates that one of the two surface species is cyclopropane carboxylate coordinated to the surface through the carboxylate group as a symmetrical bidentate ion. The population

of the cyclopropane carboxylate species was dominant at high coverages on Al_2O_3 surfaces held at room temperature. At low coverages and room temperature, the second surface species, an n-butane carboxylate, was predominant. If the Al_2O_3 surface was exposed to cyclopropane carboxylic acid at room temperature and subsequently heated above 500 K, the intensity of the carbon-hydrogen stretching modes due to the n-butane carboxylate increased at least threefold. Coadsorption of n-butyric acid and cyclopropane carboxylic acid on the Al_2O_3 surface at room temperature resulted in spectra that closely matched the tunneling spectra of cyclopropane carboxylic acid adsorbed on Al_2O_3 at temperatures above 500 K, verifying the identification of n-butane carboxylate coordinated to the surface through the carboxylate group. Isotopic labeling of the surface hydroxyls with deuterium, followed by adsorption of the cyclopropane carboxylic acid, resulted in a surface species with carbon-deuterium stretching vibrations. Thus, the n-butane carboxylate must be the product of a hydrogenolysis reaction in which the hydrogen atoms are supplied by hydroxyl groups present on the Al_2O_3 surface. No stable intermediates were found prior to the formation of the n-butane carboxylate surface species. Coadsorption of cyclopropane carboxylic acid and isobutyric acid on Al_2O_3 at room temperature resulted in spectra that correlated poorly with the spectra of cyclopropane carboxylic acid adsorbed on Al_2O_3 at temperatures above 500 K. Consequently, the other possible species resulting from ring opening and hydrogenation, isobutane carboxylate, is not formed.

Acknowledgment

The generous assistance of Dr. J. W. Gleeson in preparing the infrared sample was greatly appreciated.

References and Notes

1. J. T. Hall and P. K. Hansma, Surface Sci. **76**, 61 (1978).

2. H. E. Evans and W. H. Weinberg, J. Chem. Phys. **71**, 4789 (1979).

3. N. M. D. Brown, R. B. Floyd and D. G. Walmsley, J. Chem. Soc. Faraday II **75**, 17 (1979).

4. N. M. D. Brown, W. J. Nelson and B. G. Walmsley, J. Chem. Soc. Faraday II **75**, 32 (1979).

5. N. M. D. Brown, R. B. Floyd and D. G. Walmsley, J. Chem. Soc. Faraday II **75**, 261 (1979);

6. S. De Cheveigne, S. Gauthier, J. Klein, A. Leger, C. Guinet, M. Belin and D. Defourneau, Surface Sci. **105**, 377 (1981).

7. H. E. Evans and W. H. Weinberg, J. Am. Chem. Soc. **102**, 2548 (1980).

8. A. Greenberg and J. F. Liebman, *Strained Organic Molecules*, Academic Press, N.Y., 1978.

9. D. E. McBride and J. T. Hall, J. Catal. **58**, 320 (1979).

10. R. C. Jaklevic, Appl. Surface Sci. **4**, 174 (1980).

11. P. J. Robertson, M. S. Scurrell, C. Kemball, J.C.S. FTAR I **71**, 903 (1975).

12. C. S. John, M. S. Scurrell, in *Catalysis*, Vol. 2, The Chemical Society, London, 1978, p. 136.

13. J. W. Hightower and W. K. Hall, J. Amer. Chem. Soc. **90**, 851 (1968).

14. D. W. Setser and B. S. Rabonivitch, J. Amer. Chem. Soc. **86**, 567 (1964).

15. Y. Amenomiya, J. H. B. Chenier, R. J. Cvetanovic, J. Catal. **9**, 28 (1967); **12**, 198 (1968).

16. P. A. Sermon, G. C. Bond, J.C.S. FTAR I **1978**, 395.

17. G. E. Langlois and R. F. Sullivan, p. 38, Advances in Chemistry Series Vol. 97, American Chemical Society, Washington, D. C., 1970.

18. P. A. Compagnon, C. Hoang-Van, S. J. Teichner, p. 117, Proceedings of Sixth International Congress on Catalysis, The Chemical Society, Burlington House, London, 1977.

19. J. C. Slater, M. Boudart, J. Catal. **25**, 93 (1972).

20. W. M. Bowser and W. H. Weinberg, Rev. Sci. Inst. **47**, 583 (1976).

21. B. F. Lewis, M. Mossesman and W. H. Weinberg, Surface Sci. **41**, 142 (1974).; W. M. Bowser, PhD Thesis, California Institute of Technology, Pasadena, CA, 1980.

22. A. Savitzky and M. J. E. Golay, Analytical Chem. **36**, 1627 (1964).

23. J. Kirtley and P. K. Hansma, Phys. Rev. B **13**, 2910 (1976).

24. A. C. Yang and C. N. Garland, J. Phys. Chem. **61**, 1504 (1957).

25. J. Maillols, J. Molec. Struct. **14**, 171 (1972).

26. J. Maillols, V. Tabacik and S. Sportouch, J. Molec. Struct. **32**, 173 (1976).

27. The Notation is after Maillols and M. St. C. Flett; M. St. C. Flett, *An Introduction to Spectroscopic Methods for the Identification of Organic Compounds*, Pergamon Press, Oxford, 1970.

28. A. J. Maeland, R. Rittenhouse, W. Lahar and P. V. Romano, Thin Solid Films **21**, 67 (1974).

29. K. Ito and H. J. Bernstein, Canad. J. Chem. **34**, 170 (1956).

30. J. R. Kirtley and P. K. Hansma, Phys. Rev. B **12**, 531 (1975).

31. D. Dolphin and A. Wick, *Dolphin Tabulation of & Wick Infrared Spectral Data*, John Wiley & Sons, New York, 1977; L. J. Bellamy, *The Infrared Spectra of Complex Molecules*, John Wiley & Sons, New York, 1956; L. M. Sverdlov, M. A. Kovner and E. P. Krainov, *Vibrational Spectra of Polyatomic Molecules*, John Wiley & Sons, New York, 1974.

32. Brown, et al. (see ref. 5) have published the spectrum of C_3H_7COOH/Al_2O_3 and peak positions and intensities reported there correspond very well with our work.

33. H. P. Boem, H. Knözinger, in *Catalysis Science and Technology*, Vol. 4, J. R. Anderson, M. Boudart, Eds., Springer-Verlag, 1983, p. 177.

34. T. H. Lowry, K. Richardson, *Mechanism and Theory in Organic Chemistry*, Harper and Row, New York, 1976.

35. K. Tanabe, in *Catalysis Science and Technology*, Vol. 2, J. R. Anderson, M. Boudart, Eds., Springer-Verlag, 1981, p. 231.

36. B. Stubner, H. Knözinger, J. Conard and J. J. Fripiat, J. Phys. Chem. **82**, 1811 (1978).

37. "Nuclear Magnetic Resonance Spectroscopy," Ch. 7 in *Spectroscopy in Heterogeneous Catalysis*, W. N. Delegass, G. L. Haller, R. Kellerman and J. H. Lunsford, Academic Press, 1979.

38. Y. Amenomiya, J. Catal. **46**, 326 (1977).

39. H. Knozinger and P. Ratnasamy, Catal. Rev. Sci. Eng. **17**, 31 (1976).

40. L. D. Frederickson, Analytical Chem. **12**, 1883 (1954).

41. S. Gauthier, S. DeCherveigne, J. Klein, M. Belin, Phys. Rev. (1983), submitted.

Figure Captions

Figure 1: Inelastic electron tunneling spectra of alumina at 295 K exposed to increasing amounts of cyclopropane carboxylic acid vapor. (a) Clean Al_2O_3 surface; (b) 0.025 Torr-s; (c) 0.05 Torr-s; (d) 0.1 Torr-s; (e) 0.2 Torr-s; (f) 0.4 Torr-s.

Figure 2: Inelastic electron tunneling spectra of (a) Al_2O_3 at 295 K exposed to 0.21 Torr-s iso-butyric acid; (b) Al_2O_3 at 295 K exposed to 0.09 Torr-s cyclopropane carboxylic acid followed by exposure to 0.18 Torr-s iso-butyric acid; (c) Al_2O_3 heated to 550 K while exposed to 0.4 Torr-s of cyclopropane carboxylic acid; (d) Al_2O_3 at 295 K exposed to 0.09 Torr-s cyclopropane carboxylic acid followed by exposure to 0.18 Torr-s n-butyric acid; (e) Al_2O_3 at 295 K exposed to 0.18 Torr-s n-butyric acid; (f) Al_2O_3 at 295 K exposed to a 0.0016 M solution of 2-hydroxy n-butric acid in H_2O.

Figure 3: Inelastic electron tunneling spectra of a deuterated exposed to cyclopropane carboxylic acid: (a) Tunneling spectrum of clean Al_2O_3 junction showing nearly complete exchange of surface OH groups with OD groups; (b) As in (a) except that surface was exposed to 0.038 Torr-s cyclopropane carboxylic acid-OD at 295 K; (c) as in (b) except that surface was subsequently heated in vacuo to 573 K.

Fig. 4: Infrared spectrum of Al_2O_3 powder exposed to cyclopropane carboxylic acid vapor.

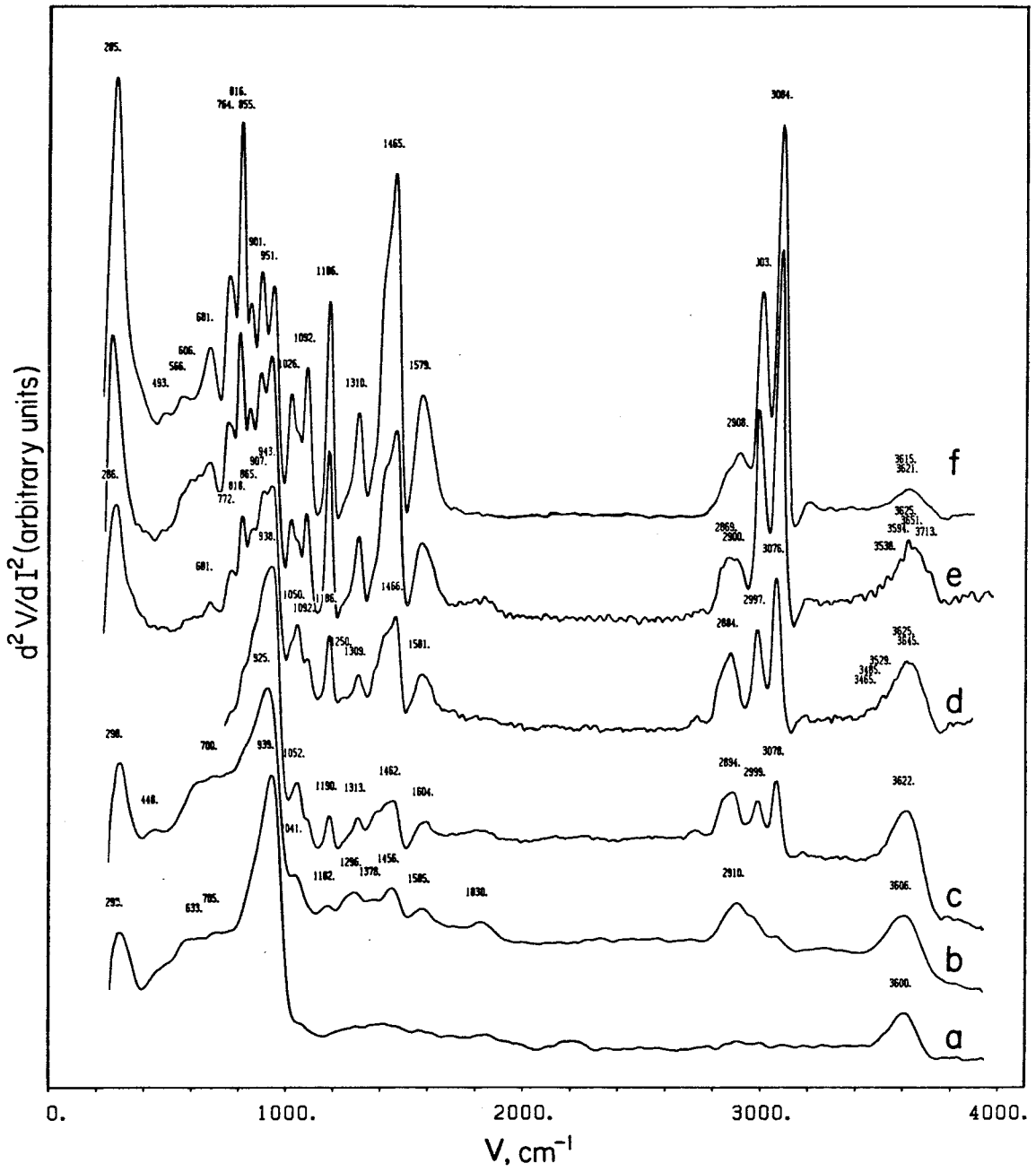

Figure II-1

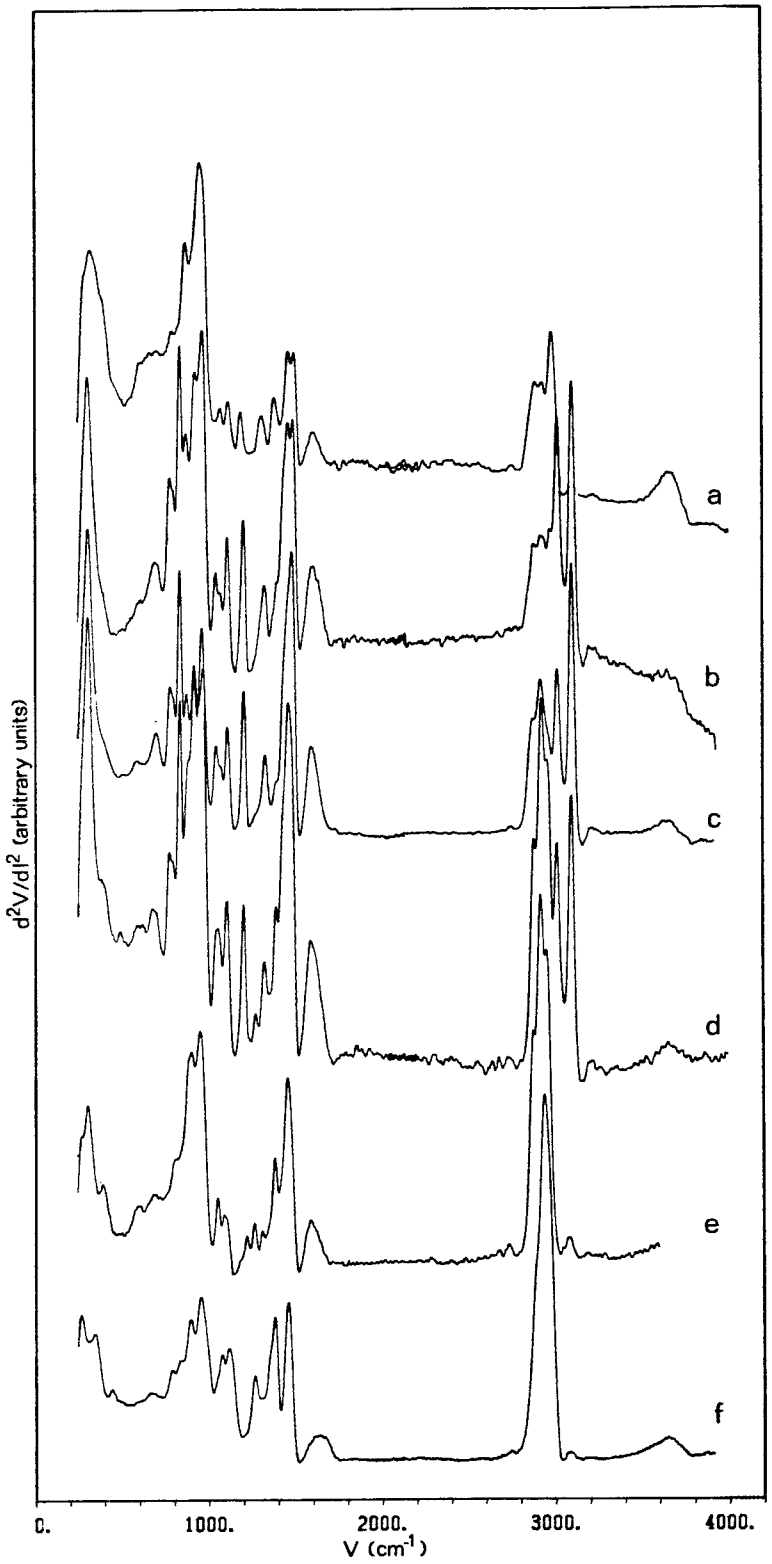

Figure II-2

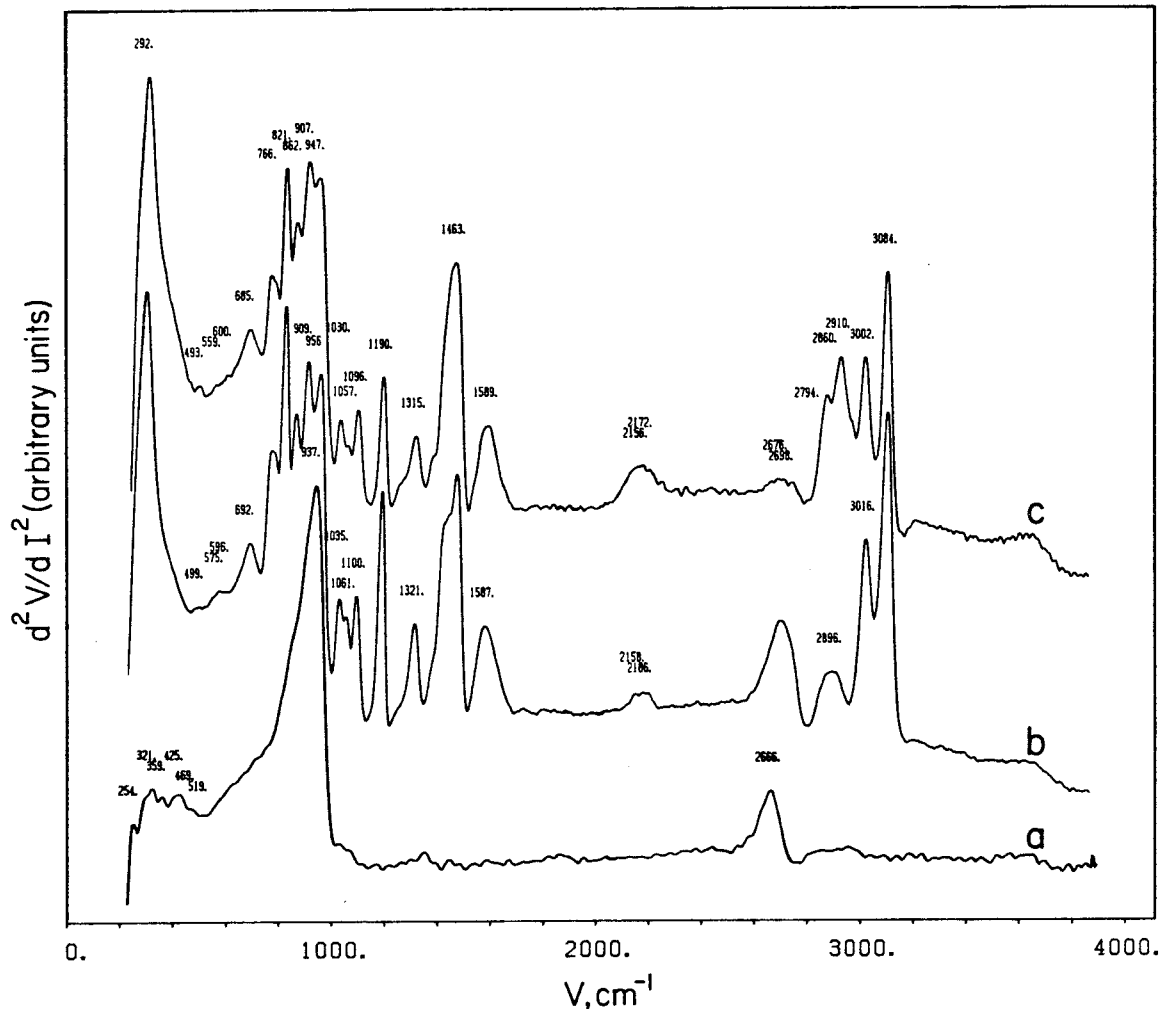
292.
821.
907.
766.
862.
947.
1463.
3084.
685.
600.
559.
493.
909.
956
1030.
1190.
2910.
2860.
3002.
1096.
1057.
1315.
1589.
2794.
2172.
2156.
2678.
2698.
937.
692.
3016.
595.
575.
499.
1095.
1100.
1061.
1321.
1587.
2896.
2158.
2186.
425.
359.
321.
468.
519.
254.
2686.
c
b
a
d²V/d I² (arbitrary units)
0.
1000.
2000.
3000.
4000.
V, cm⁻¹

Figure II-3

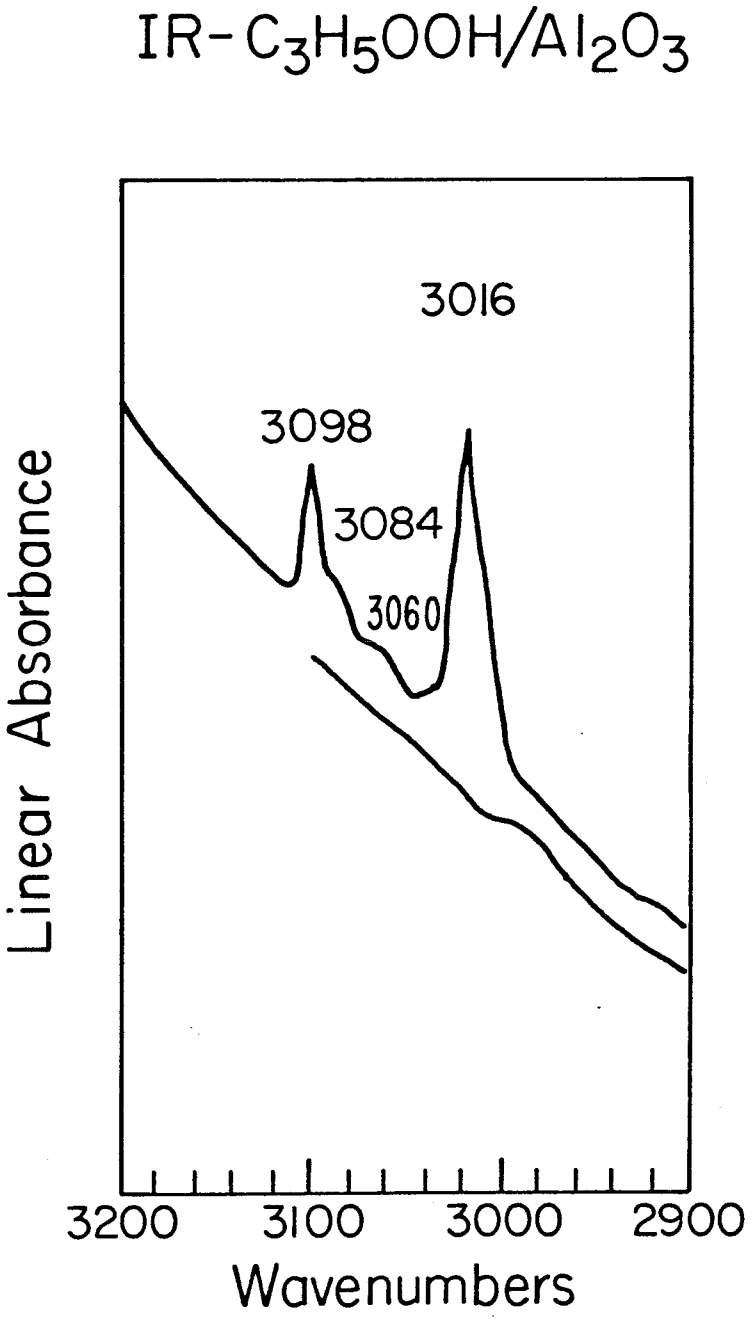
IR-C3H5OOH/Al2O3
3016
3098
3084
3060
Linear Absorbance
3200
3100
3000
2900
Wavenumbers

Figure II-4

$C_3H_5COO^-$ Approximate Assignments	$C_3H_5COO^-Na^+$ Maillols IR/Raman	IETS 295 K, 0.4 Torr-s	IETS 550 K, 0.4 Torr-s	$n\text{-}C_3H_7COOH/Al_2O_3$ IETS 300 K		$n\text{-}C_3H_7COO^-$ Approximate Assignments
$A''\nu_a(CH_2)$	3100/3095					
$A'\nu_a(CH_2)$	3083	3084	3084			
$A''\nu_s(CH_2)$	3050/3048					
$A'\nu_s(CH_2)$,ν(CH)	3015/3018	3003	3005			
				2962	2942	$\nu_a(CH_3)$
		2840-2920 *(sh)		2908	2904	$\nu_a(CH_2)$
				2970-2960(sh)	2861	$\nu_s(CH_2)\nu_s(CH_3)$
		1830				
$\nu_a(CO_2^-)$	1555/1537	1582		1588	1583	$\nu_a(CO_2^-)$
$\nu_s(CO_2^-)$		1470	1470(sh)			$\delta_s(CH_2)$ $\delta_a(CH_3)$
$\delta_s(CH_2)$	1445/1453	1440-1450(sh)	+	1450	1448	$\delta_s(CH_2)$,$\nu_s(CO_2^-)$
$\nu_s(CO_2^-)$	1418/1429					
				1382	1375	$\delta_s(CH_3)$
$A''\tau(CH_2)$	1305/1309	1317	1309			
					1297	
				1258	1256	δCH_2 progression
					1200	
$A'\tau(CH_2)$	1225/1232 (f)					
ring breathing	1190/1198	1186	1187			
ν(C-COO^-)	1083-1090/1095	1092	+	1091	1082	
			+	1051	1044	ν(C-C)
$A'w(CH_2)$	1040/1034	1034				
$A''w(CH_2)$	1020	1026				
ring deformation	945/946	951	940-960 (sh)			
$A''\rho(CH_2)$	910/914	901	901			
					892	$\rho(CH_3)$
					872	
$A'\rho(CH_2)$	850/853	855	862			
ring deformation	820/826	816	818			
δ(1-CH) out of plane	791					
$\delta_s(CO_2^-)$	758/772	764				
				720(sh)		
δ(1-CH) in plane	648/645	690				
$w(CO_2^-)$	550			652	670	
$\rho(CO_2^-)$	492					
					378	
τ(C-CO_2^-)	285/282	294	+	290	290	

Chapter III

The Adsorption and Decomposition of Dimethyl Methyl Phosphonate on an Aluminum Oxide Surface...

Abstract

The adsorption of gaseous dimethyl methyl phosphonate (DMMP) on aluminum oxide film surfaces has been investigated with inelastic electron tunneling spectroscopy. Surface temperatures ranged between 200 K and 673 K, and exposures ranged between 3 x 10^{-4} and 10 Torr-s. Tunneling spectra of deuterium labeled DMMP, perdeutero methyl alcohol, methyl methyl phosphonic acid, methyl phosphonic acid and trimethyl phosphine oxide, all adsorbed on aluminum oxide surfaces, were used to clarify the structures of the species resulting from the adsorption and decomposition of DMMP. At 200 K, DMMP is adsorbed molecularly with high surface coverages. At surface temperatures above 295 K, DMMP is adsorbed dissociatively in low coverages. Surface temperatures above 473 K lead to the dealkylation of the dissociatively adsorbed adspecies, which results in the formation of adsorbed methyl phosphonate.

1. Introduction

The interaction between aluminum oxide surfaces and phosphonate esters is important in two contexts. Not only does it elucidate the surface chemistry of phosphorus/metal oxide systems, but it also serves to clarify the chemical nature of the aluminum oxide surface itself.

Industrially, phosphorus is used in the treatment of metal surfaces; phosphoric acid is used in the application of protective and anti-friction coating [1], while phosphonic acids find use as corrosion inhibitors in heat exchangers [2]. In these applications, the interaction of phosphorus with the oxidized metal surface and with the bare metal surface are of equal importance. However, in the defloculation of slurries of mixed metal oxides with tripolyphosphate, the interaction between phosphorus and the metal oxide surface are of paramount interest [3]. Attention has also been focused specifically on the metal oxide surface chemistry of phosphonate esters. The anti-wear properties of phosphonate esters when used as lubricating oil addititives have been studied [4]. A recent concept in catalyst design uses phosphonates as bridges to anchor transition metal atoms to metal oxide surfaces [5]. Finally, phosphonate esters serve as models of pesticides and chemical warfare agents; there has been a small but steady interest in the use of physical adsorbents, such as carbon [6], and decontaminating adsorbents, such as aluminum oxide [7] for protection of personnel.

Perhaps the foremost method for probing surface properties of oxides is through the use of adsorbates. The adsorption of Lewis and Brönsted bases, such as pyridine and ammonia, were among the first methods used to probe the acid/base properties of aluminum oxide surfaces [8]. However, adsorption studies are by no means limited to examining acid/base properties. For example, the adsorption of alcohols, aldehydes and ketones has been used for some time

to demonstrate the nucleophilic character of oxygen atoms at aluminum oxide surfaces [9-11]. The adsorption of phosphonate esters can potentially add to our view of surface chemical properties and their interrelation since these esters can serve as Lewis bases, modifiers of surface acidity, and/or centers for nucleophilic substitution. For example, the phosphonate ester might react with the aluminum oxide surface in at least three ways: (1) The electron rich phosphoryl oxygen could simply form an adduct with a Lewis acid surface site; (2) The adsorbed phosphonate ester might modify the surface acidity as is observed with other phosphorous compounds [12]; and/or (3) The phosphorus center of the phosphonate ester might be subject to nucleophilic attack by the surface oxygens. Although this is an incomplete list, it serves to show that by determining the type of interactions and, when they occur, important information concerning the dominant chemical processes on the aluminum oxide surface will be learned.

1.1 Previous Studies of Phosphonate Ester Adsorption

Previous infrared spectroscopic studies of the adsorption of phosphonate esters suggest two forms of adsorption: molecular and dissociative [7,13]. These are shown, respectively, in Schemes 1(a) and 1(b). Here, the simplified surface is depicted to consist of two types of sites, S and $\overline{S}$. In addition, note that the dissociative adsorption reaction [Scheme 1(b)] is depicted arbitrarily to occur through cleavage of the phosphorus-oxygen bond, but this will depend in general on the specific nature of the surface. In the infrared studies, the structural determination is usually made on the basis of the observed vibrational frequencies for the phosphoryl stretching mode and/or the phosphorus oxygen stretching vibrations, since these shift characteristically upon complex formation [14-16]. The adsorption of diisopropyl methyl phosphonate,

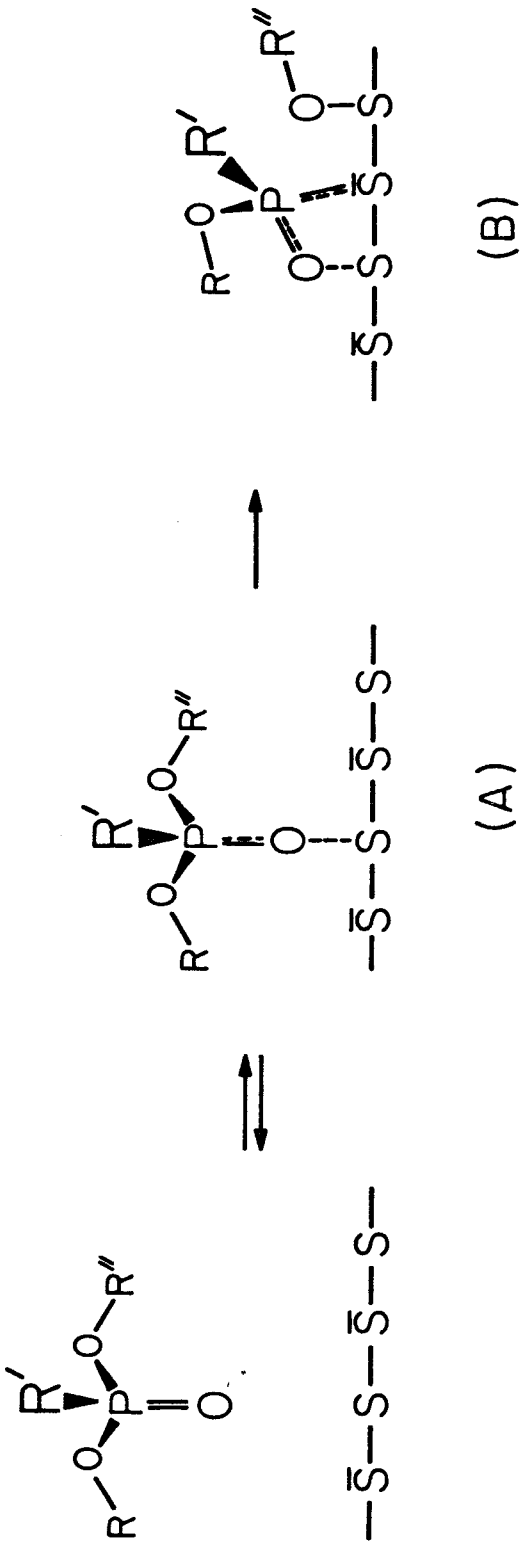

Scheme III-1

$[(CH_3)_2CHO]_2(CH_3)P(O)$, and dimethyl methyl phosphonate, $(CH_3O)_2(CH_3)P(O)$, onto powdered $FeCl_3$ at 295 K was found to produce only a molecularly adsorbed species [Scheme 1(a)] [13]. Similarly, adsorption of diisopropyl methyl phosphonate (DIMP) onto undehydroxylated alumina powders at 295 K was found to produce a molecularly adsorbed species [7]. However, in addition, a low concentration of the dissociatively adsorbed species was also present on this surface [Scheme 1(b)].

Homogenous analogues to the molecular and dissociatively adsorbed species have been isolated [14-16]. Here, since we are specifically interested in aluminum oxide surfaces and dimethyl methyl phosphonate (DMMP), two of these homogeneous analogies are worth mentioning. In the $[Al^{3+}(DMMP)_6](ClO_4^-)_3$ complex [14], the phosphonate ester molecule is weakly bound to the aluminum cation via a Lewis acid/Lewis base bond between the metal cation and the phosphoryl oxygen (the oxygen of the O=P bond). Thus, this complex embodies the type of coordination analogous to Scheme 1(a) that might be observed on the aluminum oxide surface.

On the other hand, when DMMP is added to anhydrous $AlCl_3$, a violent reaction ensues, which produces polymeric $Al(CH_3O)(CH_3)PO_2$ and liberates gaseous $ClCH_3$, as indicated in Scheme 2 [15,16]: The bonding in this complex exhibits the type of coordination analogous to Scheme 1(b) that might be observed on the aluminum oxide surface.

2. Experimental Procedures

2.1 Adsorbates

Dimethyl methyl phosphonate $[(CH_3O)_2(CH_3)P(O)]$ (97+%) and perdeutero methanol (CD_3OD) (99+%) were obtained from Aldrich Chemical Company. Methyl phosphonic acid $[CH_3P(O)(OH)_2]$ (98%) was obtained from Alfa Products.

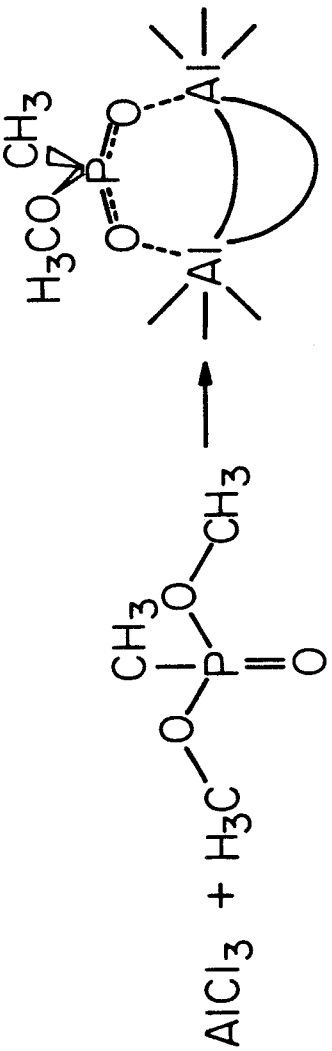

Scheme III-2

Trimethyl phosphine oxide [$(CH_3)_3P(O)$] was obtained from Strem Chemicals. Except for the dimethyl methyl phosphonate, to which a minute amount of sodium carbonate was added to remove any traces of formic acid, all were used without further purification.

Deuterated dimethyl methyl phosphonate [$(CD_3O)_2(CH_3)P(O)$] was synthesized by a standard procedure from CD_3OD and methyl phosphonic dichloride [$CH_3P(O)Cl_2$] [17,18]. The methyl phosphonic dichloride was obtained from Alfa Products and used without further purification. The synthesis was initiated by dissolving the $CH_3P(O)Cl_2$ in anhydrous diethyl ether. Two equivalents of dry distilled pyridine were added, and the CD_3OD was added dropwise while the reaction mixture was stirred and maintained at room temperature. After 24 hours, the liquid was decanted and the ether flash evaporated to give the crude $(CD_3O)_2(CH_3)P(O)$, which was then purified further by distillation under an aspirator-produced vacuum. The purity of the final product was confirmed with ^1H NMR (Fig. P-1). Depolarized Raman spectra were taken of labeled (Fig. P-2) and unlabeled (Fig. P-3) neat samples of the dimethyl methyl phosphonate esters in order to characterize the vibration modes of the molecular species.

Methyl methyl phosphonic acid $(CH_3O)(CH_3)P(O)(OH)$ was synthesized by partial hydrolysis of dimethyl methyl phosphonate in an aqueous sodium hydroxide solution [18,19]. The preparation method was a modified version of previously published procedures for monoester synthesis and methyl methyl phosphonic acid synthesis. To 150 ml of a 10% base solution (0.375 mole NaOH), 0.140 mole of dimethyl methyl phosphonate was added. The mixture was refluxed gently for five hours. The cooled solution was acidified to pH $\approx$ 2 and vacuum distilled until NaCl strongly precipitated. This mixture was then heavily acidified with concentrated HCl (total HCl added up to this point = 0.375 moles). The concentrated acid/salt solution was then "extracted" several times with reagent grade

acetone, the salt was filtered out, and the extract was dried several hours over anhydrous $CaSO_4$. The acetone extract was then flash evaporated, and the concentrated product was distilled under vacuum at 143°C to give the purified product. Yields of this procedure were approximately 20%, and ^1H NMR (Fig. P-4) [18] and IR (Fig. P-5) indicated purity to be greater than 95%. The methyl methyl phosphonic acid was stored in a freezer until needed. An alternate and simpler method for synthesis of this compound would be to start with $(CH_3O)(CH_3)P(O)Cl$ (Alfa Products) and simply hydrolyze this compound and distill.

2.2 Tunnel Junction Fabrication Procedures

Typically, junction fabrication was begun by the evaporation of an 800 Angstrom (Å) thick Al film from a W coil onto a Corning 7059 borosilicate glass substrate. The base pressure prior to evaporation was below 10^{-6} Torr, and the film thickness was monitored by a quartz crystal microbalance. Deposition rates were approximately 10 Å/s. A cohesive oxide barrier was then grown on the Al film by an oxygen-water plasma discharge (O_2:H_2O –wig 100:1) with pressures during the discharge of approximately 200 microns. The oxygen plasma was formed by an ionizing field of 100 kV/M and oxidation time was on the order of 350 s. Tunneling barriers with acceptable current-voltage characteristics could not be grown in the UHV environment without the presence of small concentrations of water in the oxygen plasma atmosphere. Pumpdown was followed by exposure to the vapor phase of the adsorbate. During this step, the technique developed by Bowser and Weinberg [20] for simultaneous heating and temperature measurement was used to heat the aluminum film and thus also the thin aluminum oxide film. Briefly, this method of temperature control employs the temperature dependence of the resistance of the aluminum film to provide the temperature measurement. In order to obtain reproducible results, it was

necessary first to anneal the aluminum film at moderate temperatures (~500 K), and this was done prior to growth of the oxide barrier. Typical exposures for heated and room temperature work ranged from 1 x 10^{-4} Torr for 1000 s to 1 x 10^{-3} Torr for 1000 s.

In most cases, the adsorbate vapor was exposed to the aluminum oxide surface after the latter had attained the desired temperature. However, some experiments were done by dosing the surface at room temperature, and subsequently heating the surface in a vacuum of approximately 5 x 10^{-6} Torr. Junctions prepared by different methods were qualitatively similar, although apparent differences are discussed below.

Following exposure to the adsorbate the substrates were cooled to 295 K, and 2000 Å of Pb were evaporated at a pressure below 1 x 10^{-6} Torr in a cross strip pattern to form the completed junction. In order to measure their current voltage characteristics, junctions were removed from the vacuum system and mounted for immersion in liquid He. All measurements were carried out in liquid He at 4.2 K with PDP 11/10 digitally controlled electronics [21]. The spectra were accumulated through multiple scan averaging, typically on the order of several hundred separate scans. The data were then processed as follows: (1) The spectra were first smoothed by a cubic convolute [22]; (2) An attempt was made at background removal (only linear functions of voltage were used to fit the background); (3) The peaks were located by a least-squares fit of the first derivative, followed by an interpolated location of the first derivative zero crossings; and (4) Peak energies were corrected for the Pb superconducting band gap and for modulation effects on the band gap width [23].

In some instances, adsorption was done on substrates at temperatures of approximately 200 K. These temperatures were attained by using LN_2 to cool the

cold fingers to which the substrate holders were attached. Special precautions were taken to insure that the cooled aluminum oxide surfaces were not exposed to other readily condensible gases, and typical base pressures before dosing the surface were below 2 x 10^{-8} Torr. Exposures to the vapor of the adsorbate ranged between 100 and 2000 L for the phosphorus compounds to 20,000 L for perdeutero methanol [1 Langmuir (L) equals 1 x 10^{-6} Torr-s]. In most of the low temperature adsorption experiments, the Pb counter electrode was evaporated while the substrates were still at low temperature. The junctions were then allowed to warm to room temperature prior to removal from the vacuum chamber. Subsequent mounting and measurement of these junctions was identical to that described above.

The methyl methyl phosphonic acid and methyl phosphonic acid possessed such low vapor pressures that they were unsuitable for vapor phase dosing of the aluminum oxide surface. Consequently, it was necessary to contact the aluminum oxide with a solution of the adsorbate dissolved in an appropriate solvent. To accommodate this, the fabrication procedure outlined above was modified in the following way. After the aluminum oxide barrier was formed, the vacuum chamber was vented to atmospheric pressure with high purity N_2, and a small drop of the adsorbate solution was placed on the aluminum oxide surface. Then, the vacuum chamber was sealed and evacuated with cryosorption pumps followed by a liquid nitrogen trapped diffusion pump [24]. The remaining steps of the fabrication procedure were carried out normally. The modified adsorption procedure kept contamination by airborne materials to a minimum since the vacuum chamber remained open to atmosphere for only five to seven minutes. During this time, the solvent would evaporate either completely or partially. A slightly more controlled version of this procedure has been used routinely in several laboratories for studying adsorption on aluminum oxide

surfaces [25]. Furthermore, studies have indicated that several common solvents can be used that will insignificantly perturb the tunneling spectrum of the chemisorbed species as compared to the spectrum obtained by vapor exposure [26]. For studying methyl phosphonic acid adsorption, a dilute solution was prepared with distilled H_2O. For methyl methyl phosphonic acid, spectroscopic grade hexane was the preferred solvent. Clean junctions dosed with either solvent showed unappreciable amounts of contamination.

3.1 Identification of the Adsorbed Species

Section 3.1 deals with the identification of the surface species resulting from the adsorption of DMMP on aluminum oxide. Accordingly, Section 3.1.1 examines the adsorption of methyl methyl phosphonic acid (MMPA) since the adsorbed form of this compound, the methyl methyl phosphonate, is identical with what would be produced by the dissociative adsorption of DMMP. Consequently, the tunneling spectrum of adsorbed MMPA will give the spectral signatures to identify the dissociatively adsorbed form of DMMP. In Section 3.1.2 the tunneling spectrum of adsorbed MMPA is compared with the tunneling spectrum of DMMP adsorbed at 200 K. Although the comparison suggests that DMMP is molecularly adsorbed at 200 K, due to the weak electron-vibration coupling constant of the phosphorus-oxygen bond, further work is needed. Therefore, as will be discussed in Section 3.1.3, isotopically labeled DMMP is used in further adsorption experiments. These experiments lead to the definitive conclusion that DMMP adsorbs molecularly at 200 K, probably by formation of an acid-base adduct with a surface hydroxyl. On the other hand, as discussed in Section 3.1.4, it is also evident that between 295 K and 473 K the adsorption of DMMP is dissociative. Adsorption experiments with trimethyl phosphine oxide (TMPO) are of help in ascertaining this, as also discussed in Section 3.1.4. The identification

of other fragments of dissociative adsorption (primarily a surface methoxide) is undertaken in Section 3.1.5. In Section 3.2, the discussion will focus on the temperature and exposure dependent interrelations among these surface species.

3.1.1 A Model for the Dissociatively Adsorbed Species: Adsorbed Methyl Methyl Phosphonic Acid

In order to determine whether DMMP adsorbs dissociatively on the aluminum oxide surface, it is essential to know the spectral signatures of the dissociatively adsorbed adspecies. Although good estimates of these could be obtained, for example, from the infrared spectrum of the analogous homogeneous organometallic complexes, it would be far better to take a "model" compound that is known to adsorb as the species in question and to prepare a tunneling spectrum of this adsorbed "model" compound. Methyl methyl phosphonic acid is such a model compound, as may be determined most simply by analogy with the adsorption chemistry of carboxylic acids on aluminum oxide.

The chemisorption of carboxylic acids on aluminum oxide surfaces has been studied extensively both with infrared spectroscopy [27] and with tunneling spectroscopy [28-30]. Chemisorption proceeds dissociatively at 295 K, and the resulting adspecies has been identified as the symmetrical bidentate bridging carboxylate anion of the corresponding carboxylic acid [30]. The chemisorption reaction is thought to proceed via the following scheme: There are two parameters of obvious importance in Scheme 3. First, the geometrical match between the oxygen-to-oxygen distance of the carboxylate group and the oxygen-to-oxygen distance of the aluminum oxide lattice, and, second, the dissociation constant of the acid. Since the dissociation constant for methyl methyl phosphonic acid ($pK_a \approx 2.37$ [18]) exceeds the dissociation constant for carboxylic acids ($pK_a \approx 4.5$ [31]), and the oxygen-to-oxygen distance of the phosphonate

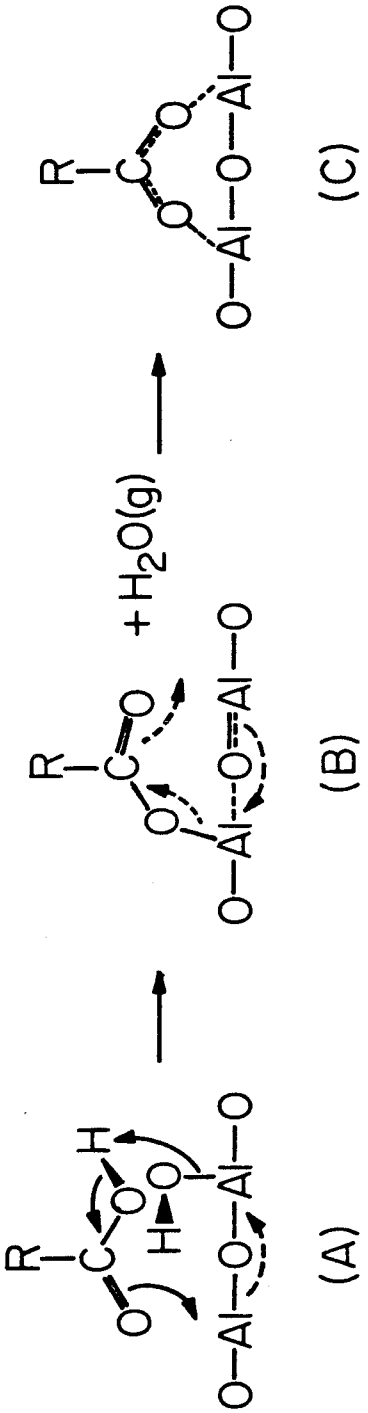

Scheme III-3

anion (2.44 Å [32]) is comparable to the oxygen-to-oxygen distance of the carboxylate anion (2.20 Å [33]), then it is entirely plausible that the chemisorption of MMPA proceeds in a fashion analogous to the chemisorption of carboxylic acids: Accordingly, MMPA adsorbs dissociatively on aluminum oxide with the loss of a proton and the formation of the symmetrical bidentate bridging methyl methyl phosphonate adspecies [Scheme 4(c)]. The dissociated proton either combines with a surface hydroxyl to form water (as shown in Scheme 4), or attaches to an oxygen anion to form a surface hydroxyl.

Spectroscopic evidence supports a reaction such as Scheme 4, where methyl methyl phosphonate (MMP) is the predominant surface species. From the tunneling spectrum of MMPA adsorbed on aluminum oxide [see Fig. 1(a) and Table 1], it is apparent that both the (CH_3)-P and the (CH_3)-O-P linkages of the adsorbate remain intact following adsorption. At the same time, the near negligible intensity of the (P)O-H stretching mode is indicative of a broken (P)O-H bond in the adsorbate. The incomplete disappearance of the (P)O-H mode is unsurprising in view of the high adsorbate coverage and indicates the presence of a small amount of molecularly adsorbed MMPA. Unfortunately, the expected appearance of the PO_2^- grouping is impossible to confirm spectroscopically from Fig. 1(a). Although the ν_s(O-P-O) and ν_a(O-P-O) of this group are expected near 1058 cm^{-1} and 1185 cm^{-1}, respectively (these estimates are based on the observed positions of these modes in polymeric $Al(MMP)_3$ [15]), unlike their carbon counterparts, phosphorus-oxygen vibrations have weak electron-vibration coupling constants (this will be discussed in more detail in Section 3.1.3). Consequently, these modes are eclipsed by other intense modes falling in the same spectral region. However, when the isopropyl analogue of MMPA, isopropyl methyl phosphonic acid $\{[(CH_3)_2CHO](CH_3)P(O)(OH)\}$, is adsorbed on unpretreated alumina powder, modes at 1090 cm^{-1} and 1180 cm^{-1} are observed with infrared

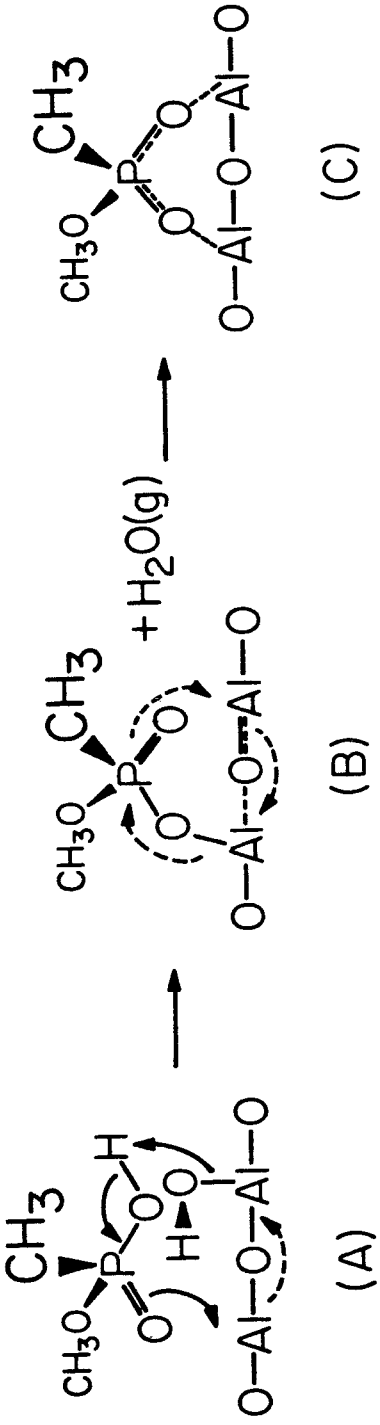

Scheme III-4

spectroscopy [7]. No modes attributable to a down shifted phosphoryl mode are observed. Thus, dissociative adsorption for the isopropoxy analog of MMPA is conclusive, and this suggests that MMPA will adsorb also dissociatively.

Kinetic parameters confirm the mechanistic similarity between carboxylic acid chemisorption and MMPA chemisorption; i.e., adsorption probabilities for carboxylic acids and for MMPA are similar. The tunneling spectrum of Fig. 1(a) was prepared by contacting a 0.005 M solution of MMPA with the aluminum oxide surface. Contacting a carboxylic acid solution of similar concentration with an aluminum oxide surface gives a tunneling spectrum showing similar surface coverage [26]. In contrast, more than a 250-fold increase in concentration is necessary before solutions of DMMP produce surface coverages similar to Fig. 1(a). (Presumably, this indicates the very different mechanistic nature of chemisorption between these two compounds.)

In summary, spectroscopic and kinetic data point to the similarity between carboxylic acid and MMPA chemisorption. Consequently, the spectrum of an aluminum oxide surface exposed to MMPA [Fig. 1(a)] reflects the spectral signature of the methyl methyl phosphonate adspecies.

3.1.2 Comparison Between Adsorbed DMMP and Adsorbed Methyl Methyl Phosphonic Acid

Figure 1(b) presents the spectrum of DMMP adsorbed on the aluminum oxide surface at 200 K. Table 1 compares the vibrational frequencies between this spectrum [Fig. 1(b)] and the spectrum of adsorbed MMPA [Fig. 1(a)]. Several small discrepancies between these two spectra are observed. Among these are the following [see Table 1]. The C-P stretching mode and the (C)O-P stretching mode appear as doublets in the spectrum of adsorbed DMMP but only as singlets in the spectrum of adsorbed MMPA. The C-P mode is downshifted approximately

30 cm^{-1} in the spectrum of adsorbed DMMP from where it appears in the spectrum of adsorbed MMPA. The region between 550 and 400 cm^{-1} appears as three distinct modes in the spectrum of adsorbed DMMP while as only a single very broad mode in the spectrum of adsorbed MMPA. It is felt that these differences are unlikely to be manifestations of the difference in surface coverages between Figs. 1(a) and (b).

The reason that a definitive assessment cannot be made is due apparently to the insensitivity of the tunneling spectrum for discriminating between a molecularly adsorbed species and a dissociatively adsorbed species. This is expected for the following two reasons. First, the P-O vibrations, which allow one to discern between molecular adsorption and dissociative adsorption, have weak electron-vibration coupling constants and are therefore eclipsed by other intense modes. Second, aside from the P-O vibrations, the remaining vibrational modes of the molecularly adsorbed DMMP would be very similar to the vibrational modes of the dissociatively adsorbed DMMP. This point is also demonstrated in Table 1: neglecting P-O modes, the Raman spectrum of liquid DMMP agrees quite well with the tunneling spectrum of adsorbed MMPA.

3.1.3 Molecular Chemisorption: The Adsorption of Deuterium Labeled DMMP at 200 K

When deuterium labeled DMMP [$(CD_3O)_2(CH_3)P(O)$] is used as the adsorbate, the strong modes occluding the phosphoryl region are isotopically shifted clear of this region. This is shown in Fig. 2(a), which is the tunneling spectrum of an aluminum oxide surface exposed to 2100 L of deuterium labeled dimethyl methyl phosphonate (DDMMP) at 200 K. (Note that saturation coverage is reached with exposures of less than 300 L at this temperature.)

The important feature in the spectrum of adsorbed DDMMP [Fig. 2(a)] is the mode at 1217 cm^{-1}. This mode is now clearly visible because the intense methoxy rocking modes $\rho[(O)CH_3]$ appearing at 1166 cm^{-1} and 1177 cm^{-1} in the spectrum of adsorbed, unlabeled DMMP are isotopically shifted clear of the phosphoryl stretching region in the spectrum of adsorbed DDMMP [see Table 1]. The phosphoryl stretching mode appears in the spectrum of $[Al^{3+}(DMMP)_6](ClO_4^-)_3$ at 1212 cm^{-1} [14] and in the spectrum of $DIMP/Al_2O_2$ at 1220 cm^{-1} [7]. Furthermore, although the phosphoryl mode at 1217 extends below 1160 cm^{-1}, the contribution from the region near 1185 cm^{-1}, which would characterize the ν_a (O-P-O) vibrational mode of the dissociatively adsorbed DDMMP, is small in comparison to the entire phosphoryl mode. Thus, most of DDMMP is chemisorbed molecularly at 200 K.

It is important to distinguish between two possible adsorption sites: surface hydroxyls or coordinately unsaturated aluminum atoms. Schemes 5(a) and (b) depict DMMP that is adsorbed molecularly to these respective sites.

The nonlinear Lewis acid/O-P bond is suggested by an X-ray crystallographic study of a similar Lewis acid/Lewis base adduct, $(CH_3)_3PO{\cdot}SbCl_5$, where the P-O-Sb bond angle is 139° [34].

An important distinction between adsorption sites 5(a) and (b) can be made in terms of the binding energy or heat of adsorption which should be considerably lower for the surface hydroxyl site than for the coordinately unsaturated aluminum site. This is suggested by calorometic determinations of the heat of formation of Lewis acid/Lewis base complexes similar to Schemes 5(a) and (b): an adduct similar to site 5(a), $(C_6H_5)_3PO{\cdot}HOC_6H_5$, has a heat of formation of 7.0 kcal/mole [35], while the corresponding adduct similar to site 5(b), $(C_6H_5)_3PO{\cdot}Al(CH_3)_3$, has a heat of formation of 28.6 kcal/mole [36]. Contrary to

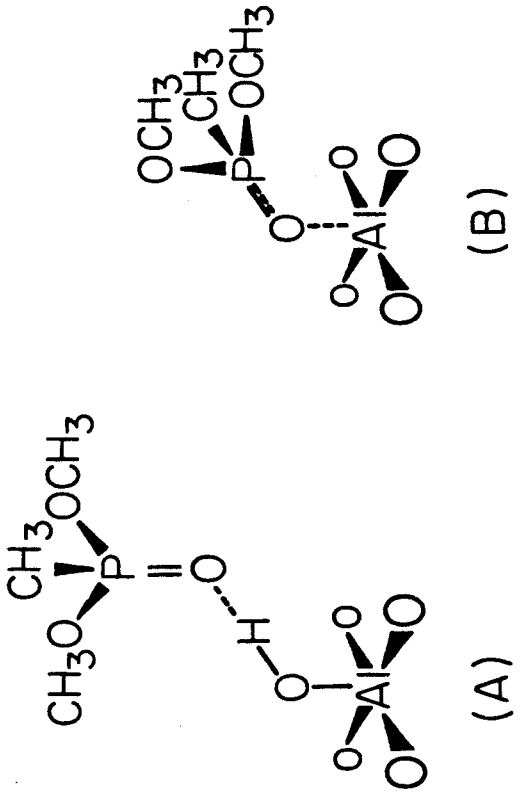

Scheme III-5

expectations, it is impossible to determine the difference between these sites based on the stretching frequency of the phosphoryl bond since the adducts similar to sites 5(a) and (b) have phosphoryl stretching frequencies of 1164 cm^{-1} and 1167 cm^{-1}, respectively — a difference of only three wavenumbers [35,36] — whereas the phosphoryl mode in Fig. 2(a) has a full width at half maximum of 70 cm^{-1}. However, the adduct formed with the hydroxyl site will downshift the OH stretching mode by approximately 430 cm^{-1} [36]. Although a small mode at 415 cm^{-1} below the normal hydroxyl stretching mode appears in the spectrum of adsorbed DDMMP in Fig. 2(a), it is most likely due to a combination band rather than a downshifted hydroxyl.

To distinguish between these two structures, the following experiment was carried out. The aluminum oxide surface was cooled to 200 K and exposed to DDMMP. However, rather than evaporating the Pb counter electrode at this point as in Fig. 2(a), the aluminum oxide was warmed to 295 K, and then cooled to 200 K before the Pb counter electrode was evaporated. The purpose of the intermediate warming to 295 K was to allow any weakly chemisorbed molecules to desorb. On the other hand, temperatures of 410 K are necessary for the desorption of molecules bound by approximately 25 kcal/mole (this assumes a preexponential of 500 cm^{-1}). The resulting spectrum is shown in Fig. 2(b). *From a comparison between Figs. 2(a) and (b), it is apparent that virtually all of the DDMMP exists in a weakly chemisorbed state on the aluminum oxide surface at 200 K.* Thus, the adsorbate is probably chemisorbed through the hydroxyl as indicated in Scheme 5(a), in accordance with the much lower binding energy expected for this type of site. Since the surfaces of undehydroxylated alumina powders are terminated with a monolayer of surface hydroxyls, this is exactly what would be expected [37].

3.1.4 Dissociative Chemisorption: The Adsorption of Deuterium Labeled DMMP at 295 K and Above

Note, however, a small but significant amount of adsorbed DDMMP remains on the aluminum oxide surface after warming to 295 K [Fig. 2(b)]. This could be due either to the existence of some strongly chemisorbed molecular DDMMP [as in Scheme 5(b)], or the existence of a small amount of dissociatively chemisorbed DDMMP.

To investigate these possibilities, DDMMP was exposed [1.0 Torr-s] to the aluminum oxide surface at 295 K and 473 K. The resulting tunneling spectra are displayed in Figs. 3(a) and (b), respectively. The tunneling spectrum of DDMMP adsorbed at 200 K is displayed in Fig. 3(c) for comparison.

There are two small but important distinctions to be made between the spectra of DMMP adsorbed above 295 K [Figs. 3(a) and (b)] and the spectrum of DDMMP adsorbed at 200 K [Fig. 3(c)]. First, the C-P stretching vibration that occurs at 695 cm^{-1} in DDMMP adsorbed at 200 K [Figs. 3(c)] is upshifted substantially to 740 cm^{-1} in DDMMP adsorbed above 295 K [Figs. 3(a) and (b)]. This upshifted position corresponds closely to the position of the C-P stretching vibration that is observed in adsorbed MMPA, namely 750 cm^{-1} (the 10 cm^{-1} discrepancy is attributed to an isotopic shift). Presumably, this upshift represents a strengthening of the C-P bond due to a negative charge gain at the phosphorus caused by dissociative adsorption, since the molecularly adsorbed DMMP is similar to a neutral species, whereas the dissociatively adsorbed species is more similar to the methyl methyl phosphonate anion. The second important difference between the spectrum of DDMMP adsorbed at 200 K [Fig. 3(c)] and the spectra of DDMMP adsorbed above 295 K [Figs. 3(a) and (b)] is seen in the position of the P-O stretching vibration: from a position of 1217 cm^{-1} in the former,

it is downshifted to 1190 cm^{-1} in the latter. This new position corresponds closely with the position of the asymmetric O-P-O stretching vibration observed in $Al(MMP)_3$ at 1185 cm^{-1} [15], and with the position of the corresponding mode observed in isopropoxy methyl phosphonic acid $[(CH_3)_2CHO(CH_3)P(O)OH]$ adsorbed on alumina at 1180 cm^{-1} [7]. These observations strongly suggest that DDMMP adsorbs dissociatively on the aluminum oxide surface above 295 K.

In order to rule out the possibility that these observations could rather be due to a difference in charge transfer between DDMMP molecularly adsorbed as in Scheme 5(a) and DMMP molecularly adsorbed as in Scheme 5(b), adsorption experiments were performed with trimethylphosphine oxide $[(CH_3)_3PO]$. Trimethylphosphine oxide (TMPO) differs from DMMP in that the former has methyl groups in place of the methoxy groups found in the latter. Although C-P bonds are thermodynamically weaker than P-O bonds, they are not so easily subject to heterolytic cleavage as are the latter. Consequently, TMPO can only chemisorb molecularly on the aluminum oxide surface through its phosphoryl oxygen. For example, TMPO forms Lewis base/Lewis acid adducts with phenol, $(CH_3)_3PO \rightarrow HOC_6H_5$ [36]. In addition, TMPO forms molecular Lewis base/Lewis acid adducts with $Al(CH_3)_3$, $(CH_3)_3PO \rightarrow Al(CH_3)_3$ [36], and also with $\{Al[OSi(CH_3)_3]_3\}_2$, $2\{(CH_3)_3PO \rightarrow Al[OSi(CH_3)_3]_3\}$ [36]. These two classes of adducts are excellent analogues for the two types of molecular adsorption depicted in Schemes 5(a) and (b), respectively. As discussed previously, a large difference is expected in the heats of adsorption between Schemes 5(a) and 5(b): the heat of formation of the TMPO-phenol adduct is estimated at 8.0 kcal/mole, while the heat of formation of the TMPO-$Al(CH_3)_3$ adduct is measured calormetrically to be 32.0 kcal/mole [36].

The tunneling spectra of TMPO adsorbed on the aluminum oxide surface at 473 K and at 200 K are shown in Figs. 4(a) and (b), respectively. As evidenced by

the strong change in spectral intensities between adsorption at 473 K [Fig. 4(a)] and adsorption at 200 K [Fig. 4(b)], the extreme temperature dependence of the surface coverage is suggestive of the two different adsorption sites depicted in Schemes 5(a) and (b). Again, this behavior is quite similar to what was observed for DDMMP in Fig. 3, with one extremely important exception: *C-P and P-O stretching vibrations in the spectra of adsorbed TMPO remain unchanged in going from adsorption at 473 K [Fig. 4(a)] to adsorption at 200 K [Fig. 4(b)]*. This suggests that the shifts experienced by these modes in the spectra of adsorbed DDMMP for adsorption above 295 K [Figs. 3(a) and (b)] and adsorption at 200 K [Fig. 3(c)] are not produced by a change in adsorption site for a molecularly adsorbed species. Therefore, this supports the earlier conclusion that DDMMP is adsorbed dissociatively on the aluminum oxide surface above 295 K, giving rise to the methyl methyl phosphonate (MMP) adspecies.

This is not to say that only one type of site participates in the adsorption of DDMMP. Rather, two types of sites participate. However, the hydroxyl site is capable only of molecular adsorption [as in Scheme 5(a)], while the coordinately unsaturated site adsorbs DDMMP dissociatively. This is due probably to the destabilizing amount of electron transfer experienced by the DDMMP following coordination as in Scheme 5(b). Thus the sequence of events for the dissociative adsorption might be depicted as follows (Scheme 6): Note that the adsorption may proceed via the well-known pena-coordinate transition state of phosphorus [39] as in Scheme 6(b).

Other spectroscopic assignments make us confident of the dissociative nature of adsorption above 295 K. While modes associated with a surface methoxide (these will be identified in the next section) appear and disappear between 295 K and 473 K, the relative intensities of the MMP modes are completely invariant. This indicates strongly that some process other than the

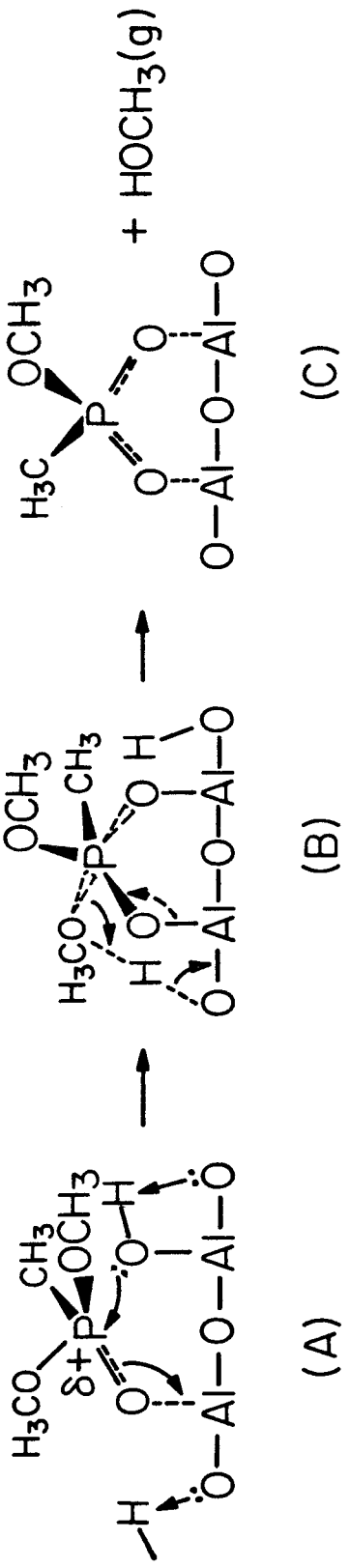

Scheme III-6

decomposition of the MMP adspecies gives rise to a surface methoxide. Presumably, the process would be dissociative adsorption of DDMMP where both the MMP and the methoxy fragments are chemisorbed.

Related chemistry also suggests the dissociative adsorption of DDMMP at 295 K. The reaction between unsolvated $AlCl_3$ and DMMP is instantaneously violent at 295 K and produces polymeric $Al(MMP)_3$. In particular, $AlCl_3$ is expected to have properties similar to the coordinately unsaturated aluminum site. In addition, carboxylic acid esters have been shown recently to adsorb dissociatively at 295 K on aluminum oxide surfaces that are quite similar to ours [40].

An infrared spectroscopic study of the adsorption of diisopropyl methyl phosphonate $[(CH_3)_2HCO]_2(CH_3)P(O)$, a phosphonate ester similar to DMMP, concluded that adsorption onto pressed disks of unpretreated, high area aluminas was largely molecular at 295 K [17], although some dissociative adsorption was evidenced by weak bands in the appropriate spectral regions. We explain these observations by noting that typical exposures for these experiments were 10^4 times the exposures used in our experiments. In addition, in our case, the partial pressure of DDMMP was below 10^{-6} Torr above the aluminum oxide surface, assuring complete removal of all weakly adsorbed species.

3.1.5 Other Fragments of Dissociative Adsorption: The Surface Methoxides

Dissociative adsorption produces two molecular fragments. Thus far, attention has been focused on the identification of the fragment that forms the MMP adspecies. Scheme 6 tentatively indicates that the other fragment, the methoxy moiety, combines with a surface proton and is subsequently desorbed as methyl alcohol. However, some spectroscopic evidence for or against this would be desirable. Such evidence is virtually impossible to obtain when DMMP is used as the adsorbate since the resolution of the tunneling spectrum is insufficient to

distinguish among the several types of methyl groups that are present.

However, the reaction pathway of the methoxy group can be investigated if DDMMP is used as the adsorbate because these difficulties are to some extent alleviated. In DDMMP [$(CD_3O)_2(CH_3)P(O)$], the deuterium selectively labels the methoxy groups. This increases the splitting between the asymmetric and symmetric stretching vibration of the methoxy group, and also shifts them to a region of the spectrum that is free from otherwise interfering C-H stretching vibrations. The only difficulty then is in knowing the vibrational signatures of a surface methoxide in order to distinguish it from the methoxy that remains attached to the phosphorus in the MMP adspecies. To determine these signatures unequivocally, it is necessary to prepare the tunneling spectrum of adsorbed perdeutero methyl alcohol (CD_3OD).

The chemisorption of methyl alcohol and perdeutero methyl alcohol on aluminum oxide has been studied extensively with infrared spectroscopy [9]. Chemisorption has been determined to occur dissociatively at 295 K on γ-alumina that was pretreated in vacuum at temperatures above 573 K [9]. This results in a surface methoxide species that is bound through its oxygen to a surface aluminum ion. Consequently, a comparison between the tunneling spectrum of chemisorbed perdeutero methyl alcohol and the tunneling spectrum of molecularly adsorbed DDMMP will determine which bands can be used to identify a surface methoxide.

The tunneling spectrum of perdeutero methyl alcohol chemisorbed on the aluminum oxide surface is shown in Fig. 5(a). This spectrum was prepared by exposing the aluminum oxide surface to 21,000 L of CD_3OD at 200 K, which is close to a saturation exposure under these conditions. For comparison, the spectrum of DDMMP adsorbed at 200 K is displayed again in Fig. 5(b). Unfor-

tunately, a direct comparison between Figs. 5(a) and (b) is impossible since there are a significant number of modes in the spectrum of chemisorbed CD_3OD [Fig. 5(a)] that are not due to the labeled surface methoxide species.

These additional adspecies result when surface reactions transform the chemisorbed methoxide species into additional surface products. In particular, nucleophilic attack of the surface methoxide by the lattice oxygen produces a surface formate, and hydrogen-deuterium exchange via the surface hydroxyls is responsible for the carbon-hydrogen stretching modes of the methoxide and the formate. Fortunately, there have been several studies of the adsorption of formic acid [29,41-44] and deuterium-labeled formic acid [29] on aluminum oxide with tunneling spectroscopy. With the aid of these, it is possible to make the proper peak assignments (see Table 2). There are several unusual issues concerning the spectrum of adsorbed CD_3OD [Fig. 5(a)]. First, previous infrared spectroscopic results indicate that adsorbed methoxide is converted to a formate only at temperatures above 450 K [9]. Consequently, it is surprising that surface formate is observed on this surface which was not heated above 295 K. Second, although it is unsurprising that the proton of the surface formate can readily exchange with the protons from surface hydroxyls, it seems quite unusual to observe the exchange of surface methoxide protons with surface hydroxyls, since this reaction has not been heretofore reported. It is quite possible that the explanation for these observations lies in the sample preparation procedure.

Since the strongest C-D stretching mode of the surface methoxide occurs at 2200 cm^{-1} (see Table 2), and since the spectrum of DDMMP, molecularly adsorbed at 200 K, has its weakest C-D stretching mode here (~2195 cm^{-1}) (see Table 1), it follows that the amount of surface methoxide in the spectrum of dissociatively adsorbed DDMMP [for example, Fig. 3(a)] will be proportional to the

intensity of the mode at 2200 cm^{-1} (provided there is a sufficient surface methoxide concentration to allow the mode to rise above its nonzero baseline value). Unfortunately, because the electron-vibration coupling constants are poorly understood, it is futile to attempt to relate the surface methoxide coverage to the dissociatively adsorbed DDMMP coverage. Nonetheless, having some independent indication of the surface methoxide coverage will be useful (e.g., Section 3.2).

3.2 Adsorption of $(CD_3O)_2(CH_3)P(O)$ Between 295 K and 673 K

Thus far, identification of the various surface species taking part in the adsorption of dimethyl methyl phosphonate on aluminum oxide has been emphasized. Now that the spectral signatures for these species have been identified clearly, we have the ability to assess the ways in which temperature and exposure affect the interaction between the aluminum oxide surface and gaseous dimethyl methyl phosphonate.

For adsorption between 295 K and 473 K, there are only three surface species present: MMP, surface methoxides and surface hydroxyls. However, as the adsorption temperature is increased from 295 K to 473 K, the relative surface coverages of these three adspecies change. These changes are discussed quantitatively in Section 3.2.1. Increasing the temperature of adsorption further to 573 and above leads to the formation of a new surface species, a methyl phosphonate (MP). Therefore, Section 3.2.2 discusses adsorption at these temperatures separately. Finally, in Section 3.2.3 the exposure dependence and temperature dependence of the surface coverage of MMP are compared in various ways. This leads to conclusions concerning the nature of the adsorption sites and the mechanism for adsorption. In particular, the surface consists of a small number of sites that are highly active for the dissociative adsorption of

DDMMP, and activated adsorption is responsible for the temperature dependence of the surface coverage of the MMP at constant exposure.

Displayed in Fig. 6 are the tunneling spectra of aluminum oxide surfaces that are exposed to 1.0 Torr-s of DDMMP at progressively higher temperatures: 295 K [Fig. 6(a)], 373 K [Fig. 6(b)], 473 K [Fig. 6(c)], 573 K [Fig. 6(d)] and 673 K [Fig. 6(e)]. In the following, we report changes in surface coverage based on comparisons among peak areas in the different spectra of Fig. 6 and among other similarly scaled sets of spectra. It is important to emphasize the approximate nature of these comparisons. The uncertainty arises because each of these spectra is recorded from a different tunnel junction, and a reliable theory does not exist to relate absolute coverages measured on different tunnel junctions. The following steps are taken in an attempt to accomplish this. The sloping background of each spectrum is removed by subtracting a linear function of energy until a flat mid-region is obtained. The spectra are then scaled so that the magnitude of the Al-O bulk stretching mode at approximately 940 cm^{-1} is uniform. The Al-O bulk stretching mode was chosen as the constant of scaling on the following basis. If the adsorbate coverage is ϑ, then the aluminum oxide surface coverage is $1-\vartheta$. If the adsorbate coverage is small, then variations δ in this coverage cause the adsorbate mode intensity to increase as δ/ϑ relative to its former intensity. On the other hand, the Al-O mode intensity decreases only as $\delta + \delta\vartheta + \ldots$ relative to its former intensity, and it is therefore less sensitive to variations in the adsorbate surface coverage. Thus when the surface coverage is small, for moderate variations in the surface coverage (on the order of the adsorbate coverage itself), the Al-O mode intensity represents a feature of approximately constant coverage. Obviously, this procedure is hardly rigorously correct. Nonetheless, judging from Fig. 6, it seems to be efficacious; the nonlinear background has the same shape and magnitude on each spectrum in Fig.

6, even though the resistances of the tunnel junctions varied substantially (50-300 ohms). In general, a variation in resistance is attributable to any factor that changes the shape of the tunneling barrier. That is, changes in the barrier height are equally important to changes in the barrier width. Changes in the barrier height are largely manifest by changes in the adsorbate surface coverage and the adsorbate species. For example, Coleman, et al. [45] examined the very influential effects of the hydroxyl layer on the barrier shape.

3.2.1 Adsorption Between 295 K and 473 K at Exposures of 1.0 Torr-s

The tunneling spectra of aluminum oxide surfaces exposed to 1.0 Torr-s of DDMMP at 295 K, 373 K and 473 K are shown, respectively, in Figs. 6(a), (b) and (c). Comparisons among Figs. 6(a), (b) and (c) are facilitated by recognizing the three distinct surface species that appear in these spectra. These are the surface hydroxyls, the surface methoxides and the MMP adspecies, each of which has distinct vibrational modes. The surface hydroxyls account for the very broad mode at approximately 3630 cm^{-1}. Of the four distinct C-D stretching peaks observed, the surface methoxides best account for the central two modes at 2200 and 2130 cm^{-1}. The MMP adspecies account for many distinct modes, and we will focus arbitrarily on the most intense C-D and C-H stretching modes at 2250 and 2915 cm^{-1}, respectively. Thus, the relative surface coverage of each adspecies can be assessed independently by following the relative changes in the intensities of these three groups of modes.

3.2.1a The Surface Hydroxyls

The hydroxyl surface coverage decreases substantially as the temperature of the exposed surface is increased from 295 K to 473 K. A comparison among the relative peak areas of the surface hydroxyl stretching mode at approximately

3630 cm^{-1} quantifies this statement; the hydroxyl surface coverage falls from 1.0 at 295 K, to 0.73 at 373 K, and to 0.46 at 473 K (to 0.42 at 573 K). In this estimate, the bulk aluminum oxide surface is assumed to be terminated by a monolayer of surface hydroxyls at 295 K, and the intensity of the mode is assumed to be proportional to the surface coverage raised to the 1.4 power [46]. Normally, surfaces of bulk aluminas have physically adsorbed H_2O in addition to a monolayer of surface hydroxyls. However, physically adsorbed water has seldom been observed on the low area aluminum oxide surfaces used in tunneling spectroscopy. Indeed, the agreement is surprisingly good between gravametric studies of the dehydroxylation of bulk aluminas and the crude measurements for our low area alumina. On bulk aluminas, the surface hydroxyl coverage decreases from 0.87 at 373 K, to 0.61 at 473 K (to 0.50 at 573 K) [37].

3.2.1b The Surface Methyl Methyl Phosphonate

The MMP adspecies is stable on the aluminum oxide surface to 473 K, based on the following experimental observations. Two aluminum oxide surfaces are exposed to 1.0 Torr-s of DDMMP at 373 K [as in Fig. 6(b)]. One of these is subsequently heated in vacuuo to 473 K. Since the intensities of the modes of the MMP adspecies between the resulting spectra are identical, the surface coverage of the MMP is unaffected by heating to 473 K, and thus the MMP does not decompose into other surface species or gaseous products below 473 K.

On the other hand, at a constant exposure, the surface coverage of the MMP increases markedly as the temperature of the exposed aluminum oxide surface is increased from 295 K to 473 K. A manifestation of this is the overall increase in intensity of the MMP modes in going from 295 K to 473 K. Based on a comparison of the integrated intensity of the C-H stretching modes, the surface coverage of MMPA increases by 16% at 373 K [Fig. 6(b)], and by 22% at 473 K [Fig.

6(c)]. (Note that judgments based solely on peak amplitudes are misleading; the amplitude of the 2915 cm^{-1} peak at 295 K increases by 68% at 373 K.)

An activated process for the adsorption of DDMMP is responsible for the increase in MMP surface coverage with temperature. Contrary to expectations, dehydroxylation of the aluminum oxide surface at higher temperatures does not create additional adsorption sites. Experiments demonstrating this are discussed in Section 3.2.3.

3.2.1c The Surface Methoxide

The amount of surface methoxide formed per dissociatively adsorbed DDMMP decreases substantially as the adsorption temperature is increased from 295 K to 473 K. This follows from the decrease in the intensity of the mode at 2200 cm^{-1} relative to the mode at 2250 cm^{-1} as the adsorption temperature is increased. The former is characteristic of the surface methoxide while the latter is characteristic of the MMP adspecies [$\nu_a(CD_3)$]. Two concerted effects are responsible for this; namely, any surface methoxide formed during the dissociative adsorption of DDMMP would be transformed to a surface formate above 450 K [9], and the dissociative adsorption reaction appears to produce less surface methoxide at higher adsorption temperatures. Of these two processes, we feel the latter is most responsible for the decrease in the surface methoxide coverage.

The transformation of the surface methoxide into the surface formate above 450 K necessarily implies that formate bands should increase in intensity when the adsorption temperature is increased from 373 K [Fig. 6(b)] to 473 K [Fig. 6(c)]. An examination of the appropriate spectra [Figs. 6(b) and (c)] indicates that this is not the case. Although modes of the surface methoxide decrease markedly in going from adsorption at 373 K [Fig. 6(b)] to adsorption at 473 K

[Fig. 6(c)], a concomitant increase in formate modes fails to occur. Of course, interfering modes from the neighboring C-H stretching region might mask this small increase.

On the other hand, the methoxide conversion to formate cannot explain the substantial decrease in the ratio of surface methoxide to MMP in going from adsorption at 295 K [Fig. 6(a)] to adsorption at 373 K [Fig. 6(b)]. Thus, it tentatively appears that a substantial decrease in the adsorption probability of the methoxy fragment occurs as the adsorption temperature is increased.

3.2.2 Adsorption of $(CD_3O)_2(CH_3)P(O)$ Between 573 K and 673 K

Adsorption of DDMMP on aluminum oxide at 573 K produces a new surface species. This is apparent from the subtle changes taking place in the tunneling spectra as the adsorption temperature is increased from 473 K [Fig. 6(c)] to 573 K [Fig. 6(d)]. In particular, the mode at 800 cm^{-1}, which occurs on the low-energy shoulder of the Al-O stretching mode, appears with much higher intensity at 573 K [Fig. 6(d)]. In addition, the relative intensity between the mode at 1418 cm^{-1} [$\delta_a CH_3(-P)$] and the mode at 1308 cm^{-1} [$\delta_s CH_3(-P)$] changes significantly; at 473 K [Fig. 6(c)], the former is much stronger than the latter, while the reverse is true at 573 K [Fig. 6(d)]. Finally, the intensity of the $\nu_a(PO)CD_3$ mode declines relative to the intensity of the $\nu_a(P)CH_3$ mode, suggesting that a methoxy is being lost from the MMP.

The new surface species is adsorbed methyl phosphonate (MP). This identification is made by a comparison between the tunneling spectrum of DDMMP adsorbed at 573 K [Fig. 6(d)] and the tunneling spectrum of methyl phosphonic acid (MPA) adsorbed on aluminum oxide at 295 K [Fig. 7]. The spectrum of adsorbed methyl phosphonic acid [Fig. 7] reproduces nicely the new features that appear in the spectrum of adsorbed DDMMP when the adsorption

temperature is increased to 573 K [Fig. 6(d)].

Relative to the surface coverage of the MMP, the surface coverage of the MP increases as the adsorption temperature is increased from 573 K to 673 K. This is apparent from the decrease in the ratio of the mode at 2250 cm^{-1} to the mode at 2915 cm^{-1} as the adsorption temperature is increased, since the former mode is proportional to the surface coverage of the MMP, and the latter mode is proportional to the combined surface coverage of the MMP and MP. A properly scaled ratio of these two modes will be proportional to $\vartheta_{MMP}/(\vartheta_{MMP} + \vartheta_{MP})$, assuming a weak dependence of mode intensity upon orientation. Such a ratio decreases from 1 at 473 K to 0.6 at 573 K to 0.4 at 673 K. Note that the MMP still represents 40% of the total phosphorus containing surface population at the highest temperature examined in this study (673 K).

The MP is a product of the decomposition of the MMP. This is made clear from the following experiment. If DDMMP is adsorbed at 373 K and subsequently heated in vacuuo to 573 K, then the MP adspecies again appears.

Before discussing the decomposition mechanisms giving rise to the MP adspecies, it is useful to discuss the structure of the adsorbed MP. To obtain the spectrum of adsorbed methyl phosphonic acid (Fig. 7), an aluminum oxide surface was contacted with a 0.0033 M solution of methyl phosphonic acid (MPA) in water. By analogy to the adsorption mechanism for methyl methyl phosphonic acid (see Section 3.1.1), the first step in the chemisorption of methyl phosphonic acid is the transfer of one proton to the aluminum oxide surface and the formation of the bidentate hydroxy methyl phosphonate adspecies, as shown in Scheme 7(a). In Scheme 7, the substrate depicted is one of the (100) γ-alumina planes. The (100) planes are low-energy cleavage planes and possibly represent the actual surface that is synthesized [37,47]. This surface contains aluminum

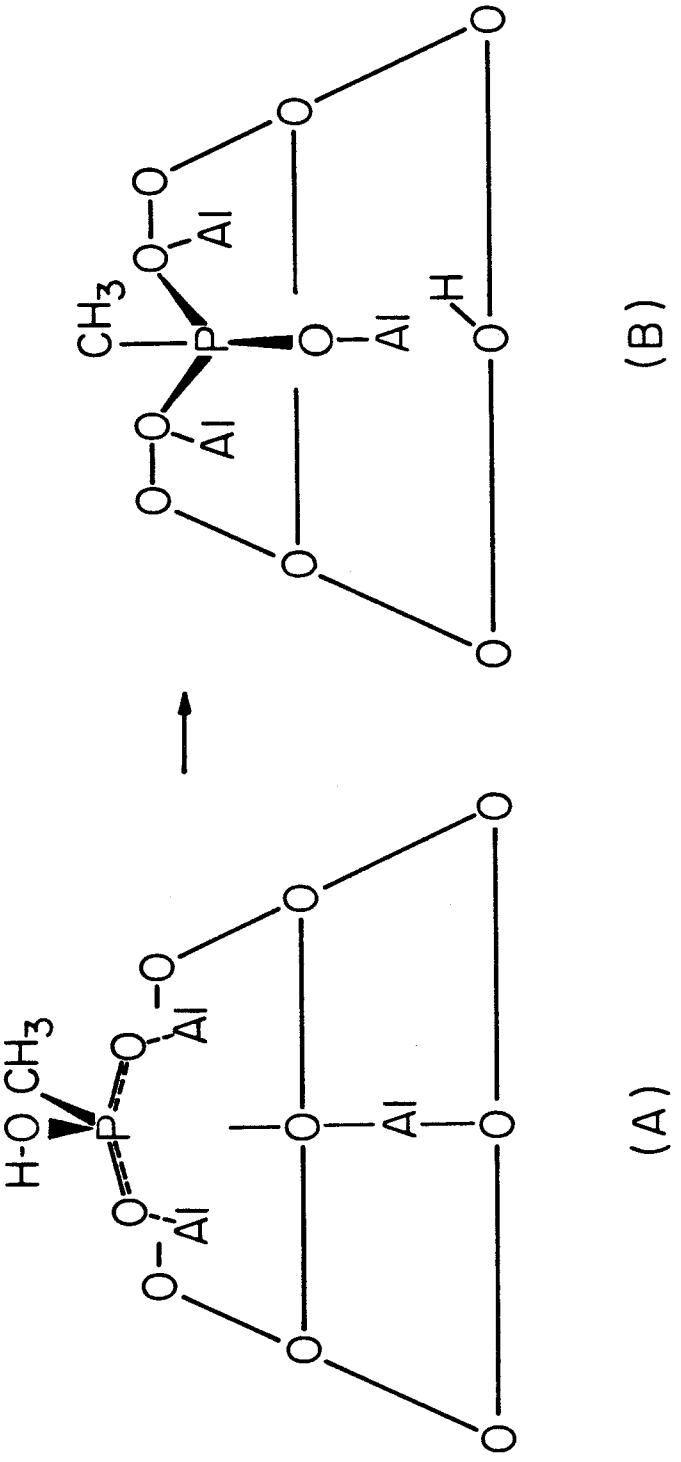

Scheme III-7

in both octahedral and tetrahedral coordinations. Scheme 7(a) depicts the MP adspecies anchored to the surface through two octahedral aluminum atoms. These sites were chosen because they bind the surface hydroxyls most weakly and, consequently, they are likely to be exposed for chemisorption most easily. In going from the bidentate species in 7(a) to the tridentate species in 7(b), the hydroxy methyl phosphonate has transferred another proton to the surface. Table 3 compares results from the tunneling spectrum of adsorbed MPA with results from the infrared spectrum of powdered $CH_3P(O)_2Na$, the monobasic salt of MPA [48]. It is clear from the presence of the (P)O-H stretching mode in the tunneling spectrum that some of the bidentate species is stable on the surface. However, the PO_3 stretching modes of metal complexes, analogous to the tridentate species, are characterized by a very broad absorption band between 1200 cm^{-1} and 1000 cm^{-1}, with its maximum located between 1120 cm^{-1} and 1030 cm^{-1} [16]. This information together with other spectra of the MP species showing negligible (P)OH modes, leads us to conclude that the tridentate form represents the dominant form of the MP adspecies in Fig. 7 in spite of the fortuitous match between the tunneling spectrum and the IR spectrum of the monobasic salt.

This interpretation can also explain the observed change in the relative intensity between the δ_a(P-)CH_3 mode [at 1408 cm^{-1}] and the δ_s(P-)CH_3 mode [at 1308 cm^{-1}] as the adsorption temperature is increased from 473 K [Fig. 6(c)] to 573 K [Fig. 6(d)]. The dipole derivatives of the δ_s(P-)CH_3 mode changes from 54.6° off normal to the surface with the bidentate adspecies, which prevails in the spectrum of DDMMP adsorbed at 473 K [Fig. 6(c)], to nearly normal in the tridentate adspecies, which prevails in the spectrum of DDMMP adsorbed at 573 K [Fig. 6(d)]. Since vibrational modes more normal to the surface are less attenuated by interaction with their image dipoles in the Pb overlayer, the intensity of the

δ_s(P-)CH_3 mode increases in going from Fig. 6(c) to Fig. 6(d). The opposite is true for the δ_a(P-)CH_3 mode.

The decomposition mechanism of the MMP is the topic of more extensive discussion in a related publication, and therefore we do not dwell on it here [49]. However, some of the pertinent conclusions are the following. Although the initial dissociative adsorption of the phosphonate ester to form the MMP proceeds by attack at the phosphorus by a nucleophilic surface oxygen (as shown in Scheme 6), an identical reaction is not responsible for the subsequent decomposition of the MMP at 573 K. Rather, in all probability, the decomposition of the MMP proceeds via attack at the methoxy carbon by a nucleophilic surface oxygen and simultaneous protonation of the methoxy oxygen by a hydroxyl [Scheme 8(a)]. This results in cleavage of the C-O methoxy bonds and the formation of a surface methoxide and a hydroxy methyl phosphonate [Scheme 8(b)]. The hydroxy methyl phosphonate reacts rapidly with the surface methoxide to eliminate gaseous methyl alcohol and to form the tridentate MP [Scheme 8(c)]. A detailed discussion of the evidence for this mechanism is presented elsewhere [49]. The MP is expected to decompose further only above 750 K, which is an unattainable temperature in our experiments [50].

3.2.3 Dependence of the Surface Coverage on Exposure and Temperature

Only a modest increase in the surface coverage of MMP results when the aluminum oxide surface is held at 295 K and exposed to progressively larger fluxes of DDMMP. A comparison among the tunneling spectra in Fig. 8 supports this statement. These spectra correspond to aluminum oxide surfaces that were held at 295 K and exposed to the following fluxes of DDMMP: 0.10 Torr-s [Fig. 8(a)], 1.0 Torr-s [Fig. 8(b)] and 10 Torr-s [Fig. 8(c)]. While the exposure to DDMMP increases by a hundredfold in going from Fig. 8(a) to Fig. 8(c), there is

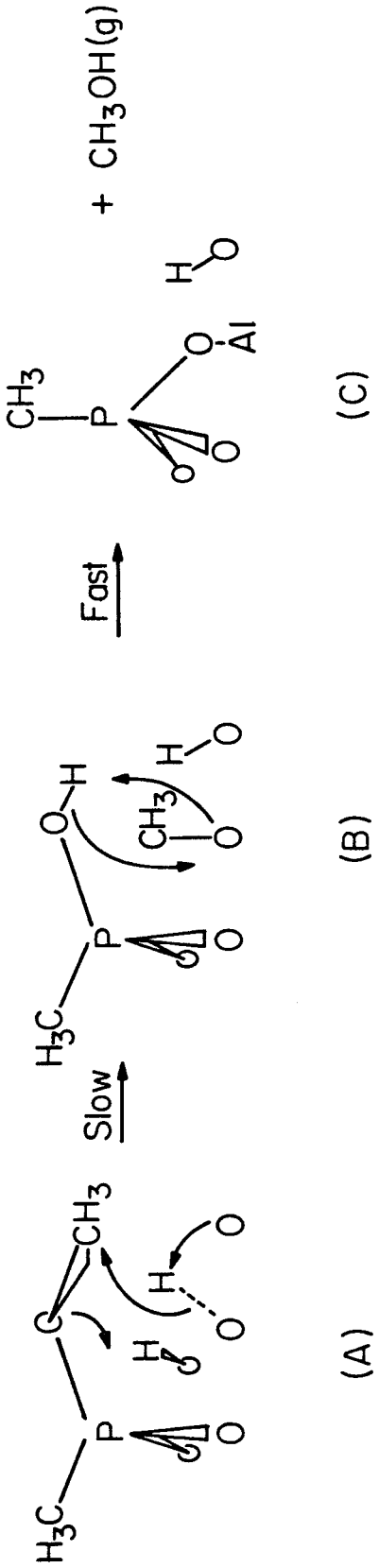

Scheme III-8

only a twofold increase in the concentration of dissociatively adsorbed DDMMP. Thus, the aluminum oxide surface is highly active for the dissociative adsorption of DDMMP at exposures below 0.1 Torr-s, and much less active for the dissociative adsorption of DDMMP at exposures higher than this.

Whereas saturation coverage is unattained with exposures of 0.1 Torr-s at 295 K, Fig. 9 indicates that saturation coverage is already attained at 0.1 Torr-s when the adsorption temperature is increased to 373 K. Since the integrated intensity of the C-H stretching modes in the spectrum of aluminum oxide exposed to 0.1 Torr-s of DDMMP at 373 K [Fig. 9(a)] is nearly identical to the integrated intensity of the C-H stretching modes in the spectra of aluminum oxide exposed to 10.0 Torr-s of DDMMP at 373 K [Fig. 9(b)], the surface coverages are nearly the same.

Thus, a 78° increase in the adsorption temperature (from 295 K to 373 K) at a constant exposure of 0.10 Torr-s leads to a greater increase in surface coverage of MMP than a hundredfold increase in the exposure (from 0.1 Torr-s to 10 Torr-s) at 295 K. This is clear from a comparison between the spectrum of aluminum oxide exposed to 0.1 Torr-s of DDMMP at 373 K [Fig. 9(a)] and the spectrum of aluminum oxide exposed to 10.0 Torr-s of DDMMP at 295 K [Fig. 8(c)]; the surface coverage is clearly greater in Fig. 9(a) since the C-H mode intensities are greater.

There are two possible explanations for this strong dependence of the surface coverage on the temperature that is maintained during the exposure. One is that the dissociative adsorption reaction is slightly activated. The other explanation is that the dehydroxylation of the aluminum oxide surface, which results from the increase in surface temperature, produces coordinately unsaturated sites that are active for the dissociative adsorption of DDMMP. The dehydroxyla-

tion of aluminum oxide surfaces is well documented. Studies of alumina powders indicate that the surface hydroxyl density will decrease by 30% when the temperature is increased from 373 K to 473 K. To decide between these two explanations, the following experiment was performed. An aluminum oxide surface was dehydroxylated at 295 K (in a vacuum of 1 x 10^{-7} Torr) prior to exposure to 1.0 Torr-s of DDMMP at 295 K. The tunneling spectrum of this surface is shown in Fig. 10(b). Unpretreated surfaces were also exposed to 1.0 Torr-s of DDMMP at 473 K [Fig. 10(a)] and 473 K [Fig. 10(c)]. Since the surface coverages of MMP are more similar between the pretreated surface exposed at 295 K [Fig. 10(b)] and the unpretreated surface exposed at 295 K [Fig. 10(a)] than between the pretreated surface exposed at 295 K [Fig. 10(b)] and the unpretreated surface exposed at 473 K [Fig. 10(c)], the dehydroxylation pretreatment did not appreciably influence the surface coverage. Hence, an activated adsorption reaction is the proper explanation for the observed dependence of the surface coverage of MMP on the temperature of exposure.

Although this result is somewhat surprising, it is consistent. The intensities of the hydroxyl stretch on the pretreated surface [Fig. 10(b)] and the surface exposed at 473 [Fig. 10(c)] compare favorably. Thus, the thermal pretreatment did dehydroxylate the surface, and the experiment compared the proper variables. It also indicates that the observed dehydroxylation is due principally to a thermal effect and not to chemical effects associated with dissociative adsorption. It is entirely possible that thermal pretreatment temperatures of 473 K are inadequate to produce the type of adsite necessary for dissociative adsorption.

4. Conclusions

In this investigation, the extremely high sensitivity and wide spectral range

inherent to tunneling spectroscopy have been used successfully to study the chemisorption of dimethyl methyl phosphonate (DMMP) and a number of related phosphorus compounds on aluminum oxide surfaces at coverages ranging from submonolayer to saturation, and over a temperature range from 200 K to 673 K. Together, this information has led to a number of important conclusions concerning the adsorption of dimethyl methyl phosphonate on aluminum oxide. These can be summarized as follows (all conclusions refer to gaseous DMMP adsorbed on Al_2O_3):

1. At 200 K, dimethyl methyl phosphonate adsorbs molecularly with exposures as low as 300 L producing saturation coverage. For molecular adsorption, the adsorbate/surface complex is thought to consist of a Lewis base/Lewis acid adduct between DMMP and a surface hydroxyl.

2. With exposures of less than 10 Torr-s between 295 K and 473 K, DMMP adsorbs dissociatively to form the methyl methyl phosphonate (MMP) adspecies through cleavage of a phosphorus-oxygen bond. The dissociative adsorption sites are thought to consist of coordinately unsaturated aluminum. The methoxy fragment formed during the dissociative adsorption reaction appears to be more likely to remain on the surface at lower adsorption temperatures.

3. Saturation coverage is unattained at 295 K with exposures of 10 Torr-s. However, saturation coverage is achieved at 373 K with exposures below 0.10 Torr-s. An activated adsorption reaction appears to be responsible for the strong temperature dependence of the surface coverage. Although significant surface dehydroxylation occurs upon increasing the surface temperature from 295 K to 473 K, this influences the surface coverage of MMP only slightly.

4. Above 573 K, the methyl methyl phosphonate adspecies decomposes to yield the tridentate methyl phosphonate adspecies. The other fragment of decomposition was not identified but presumably consists of gaseous methyl alcohol. The surface coverage consists of approximately equal concentrations of MP and MMP when DMMP is adsorbed at 673 K. The total surface coverage is estimated to be less than 20% of a monolayer.

Acknowledgments

We would like to thank Nadeem Tufail for his competent and exacting preparation of many of the tunnel junctions used in this study. In addition, we are indebted to Steve Buchwald for synthesizing the deuterated dimethyl methyl phosphonate, and we also thank Steve Blair for taking the Raman spectra of the phosphonate esters. This work was supported by the Army Research Office under grant number

References

1. J. R. Van Wazer, in *Phosphorous and Its Compounds, Vol. II. Technology, Biological Functions and Applications*, Ch. 30, Interscience, p. 1857, New York, 1961.

2. A. Harris and A. Marshall, Corrosion Prev. Control **27**, 17 (1980).

3. J. W. Lyons, Ch. 13 in *Environmental Phosphorous Handbook*, J. Wiley & Sons, New York, 1973.

4. V. L. Lashkhi, Khim. Tekhnol. Topl. Masel. **1977**, 59 (1977).

5. M. B. Dines, P. M. Digiacomo, K. P. Callahan, P. C. Griffith, R. H. Lane, R. E. Cooksey, ACS Symposium Series 192, p. 223, 1982.

6. L. A. Jonas, Carbon **16**, 47 (1978).

7. A. E. T. Kuiper and J. J. G. M. van Bokhoven, J. Medema J. Catal. **43**, 154 (1976).

8. L. H. Little, in *Infrared Spectra of Adsorbed Species*, Ch. 7, Academic Press, p. 180, 1966, and references therein.

9. R. G. Greenler, J. Chem. Phys. **37**, 2094 (1962).

10. H. E. Evans and W. H. Weinberg, J. Chem. Phys. **71**, 1537 (1979).

11. A. V. Deo, T. T. Chuang and I. G. Dalla Lana, J. Phys. Chem. **75**, 234 (1971).

12. P. Fink, W. Pohle and A. Kohler, Z. Chem. **12**, 117 (1972).

13. G. G. Guibault and E. Scheide, J. Das, Spectroscopy Letters **1**, 167 (1968).

14. N. M. Karayannis, C. M. Mikulski, M. J. Strocko, L. L. Pytlewski and M. M. Labes, Inorganica Chemica Acta **8**, 91 (1974).

15. C. M. Mikulsi, N. M. Karayannis and L. L. Pytlewski, J. Inorg. Nucl. Chem. **36**, 971 (1974).

16. N. M. Karayannis, C. M. Mikulski and L. L. Pytlewski, Inorg. Chemica Acta Rev. **5**, 69 (1971).

17. K. H. Worms and M. Schmidt-Dunker, in *Organic Phosphorous Compounds*, Vol. 17, John Wiley, 1976, p. 22.

18. H. Christol, M. Levy and C. Marty, J. Organometallic Chem. **12**, 459 (1968).

19. R. Rabinowitz, J. Am. Chem. Soc. **82**, 4564 (1960).

20. W. M. Bowser and W. H. Weinberg, Rev. Sci. Instrum. **47**, 583 (1976).

21. B. F. Lewis, M. Mossesman and W. H. Weinberg, Surface Sci. **41**, 142 (1974); W. M. Bowser, PhD Thesis, California Institute of Technology, Pasadena, CA, 1980.

22. A. Savitzky and M. J. E. Golay, Anal. Chem. **36**, 1627 (1964).

23. J. Kirtley and P. K. Hansma, Phys. Rev. B **13**, 2910 (1976).

24. M. K. Templeton, PhD Thesis, California Institute of Technology, Pasadena, CA, 1984.

25. K. W. Hipps and U. Mazur, in *Tunneling Spectroscopy*, Ch. 8, Plenum Press, 1982, p. 229.

26. A. Bayman and P. K. Hansma, Nature **285**, 97 (1980).

27. K. Hirota, K. Fueki, K. Shindi and Y. Nakai, Bull. Chem. Soc. Japan **32**, 1261 (1959).

28. J. T. Hall and P. K. Hansma, Surface Sci. **76**, 61 (1978).

29. N. M. D. Brown, R. B. Floyd and D. G. Walmsley, J.C.S. Faraday II **75**, 17 (1979).

30. H. E. Evans and W. H. Weinberg, J. Chem. Phys. **71**, 4789 (1979).

31. J. B. Hendrickson, D. J. Cram and G. S. Hammond, *Organic Chemistry*, 3rd Ed., p. 306, McGraw-Hill, 1970.

32. B. J. Van der Veken and M. A. Herman, J. Molec. Structure **15**, 225,237 (1973).

33. V. Amirthalingam and V. M. Padmanabhan, Acta Cryst. **11**, 896 (1958).

34. C. Bränden and Lindqvist, Acta Chem. Scand. **15**, 167 (1961).

35. E. I. Matrosov and I. Kabachnik, Dokl. Akad. Nauk SSSR **232**, 89 (1977).

36. K. M. Nykerk and D. P. Eyman, Inorg. Nucl. Chem. Letters **4**, 253 (1968).

37. H. Knözinger and P. Ratnasamy, Catal. Rev. Sci. Eng. **17**, 31 (1978).

38. F. Schindler and H. Schmidbaur, Chem. Ber. **101**, 1656 (1968).

39. J. Emsley and D. Hall, *The Chemistry of Phosphorus*, Harper & Row Ltd., London, 1976, p. 319.

40. A. Bayman, P. K. Hansma and L. H. Gale, Surface Sci. **125**, 613 (1983).

41. S. De Cheveigne, S. Gauthier, J. Kline, A. Leger, C. Gurnet, M. Belin and D. Deforneau, Surface Sci. **105**, 377 (1981).

42. B. F. Lewis, M. Mosesman and W. H. Weinberg, Surface Sci. **41**, 142 (1974).

43. O. I. Shklyarevskii, A. A. Lysykh and I. K. Yanson, Sov. J. Low Temp. Phys. **2**, 328 (1976).

44. R. Magno and J. G. Adler, J. Appl. Phys. **49**, 4465 (1978).

45. R. A. Dragosset, E. S. Phillips and R. V. Coleman, Phys. Rev. B **26**, 5333 (1982).

46. J. D. Lagan and P. K. Hansma, Surface Sci. **52**, 211 (1967); A. A. Cederberg, Surface Sci. **103**, 148 (1981).

47. B. C. Lippens and J. J. Steggerda, in *Physical and Chemical Aspects of Adsorbents and Catalysts*, Ch. 4, p. 171, Academic Press, 1970; B. C. Lippens, PhD, Delft University of Technology, The Netherlands, 1961.

48. B.Dupuy and C. Garrigou-Lagrange, J. Chemie Physique **65**, 632 (1968).

49. M. K. Templeton and W. H. Weinberg, in preparation.

50. E. E. Flagg and D. L. Schmidt, J. Polymer Sci. A-1, **8**, 1 (1970).

Figure Captions

Figure 1: (a) Inelastic electron tunneling spectrum of an aluminum oxide surface exposed at 295 K to a 0.005 M solution of methyl methyl phosphonic acid in hexane. (b) Inelastic electron tunneling spectrum of an aluminum oxide surface subjected to a saturation exposure of DMMP at 200 K. The Pb counter electrode was evaporated onto this surface at 200 K.

Figure 2: Inelastic electron tunneling spectra of aluminum oxide exposed to 2100 L of DDMMP at 200 K. (a) Immediately following exposure, the Pb counter electrode was evaporated onto the cold surface. (b) Following exposure the surface was warmed to 295 K and then cooled to 200 K before the Pb counter electrode was evaporated.

Figure 3: Inelastic electron tunneling spectra of aluminum oxide exposed to 1.0 Torr-s of DDMMP at various temperatures: (a) 295 K. (b) 473 K. (c) same as Fig. 2(a).

Figure 4: Inelastic electron tunneling spectra of aluminum oxide exposed to trimethyl phosphine oxide at various temperatures: (a) 0.061 Torr-s at 473 K. (b) 1000 L at 200 K. For spectrum (b), the Pb counter electrode was evaporated onto the cold surface.

Figure 5: (a) Inelastic electron tunneling spectrum of aluminum oxide exposed to 2.1×10^4 L of CD_3OD at 200 K. The Pb counter electrode was evaporated onto the cold surface. (b) Same as Fig. 2(a).

Figure 6: Inelastic electron tunneling spectra of aluminum oxide exposed to 1.0 Torr-s of DDMMP at various temperatures: (a) 295 K. (b) 373 K. (c) 473 K. (d) 573 K. (e) 673 K.

Figure 7: Inelastic electron tunneling spectrum of aluminum oxide exposed at 295 K to a 0.0033 M solution of methyl phosphonic acid in H_2O.

Figure 8: Inelastic electron tunneling spectra of aluminum oxide subjected to increasing exposures of DDMMP at 295 K: (a) 0.1 Torr-s. (b) 1.0 Torr-s. (c) 10 Torr-s.

Figure 9: Inelastic electron tunneling spectra of aluminum oxide subjected to increasing exposures of DDMMP at 373 K: (a) 0.1 Torr-s. (b) 1.0 Torr-s. (c) 10 Torr-s.

Figure 10: Inelastic electron tunneling spectra of aluminum oxide surfaces exposed to 1.0 Torr-s of DDMMP at various temperatures: (a) 295 K. (b) as in (a) except prior to exposure, surface was heated in vacuuo to 473 K. (c) 473 K.

Procedure Figure Captions

Figure P-1: ^1H NMR spectrum of $(CD_3O)_2(CH_3)P(O)$.

Figure P-2: Depolarized Raman spectrum of $(CD_3O)_2(CH_3)P(O)$.

Figure P-3: Depolarized Raman spectrum of $(CH_3O)_2(CH_3)P(O)$.

Figure P-4: ^1H NMR spectrum of $(CH_3O)(CH_3)P(O)(OH)$.

Figure P-5: Infrared spectrum of $(CH_3O)(CH_3)P(O)(OH)$.

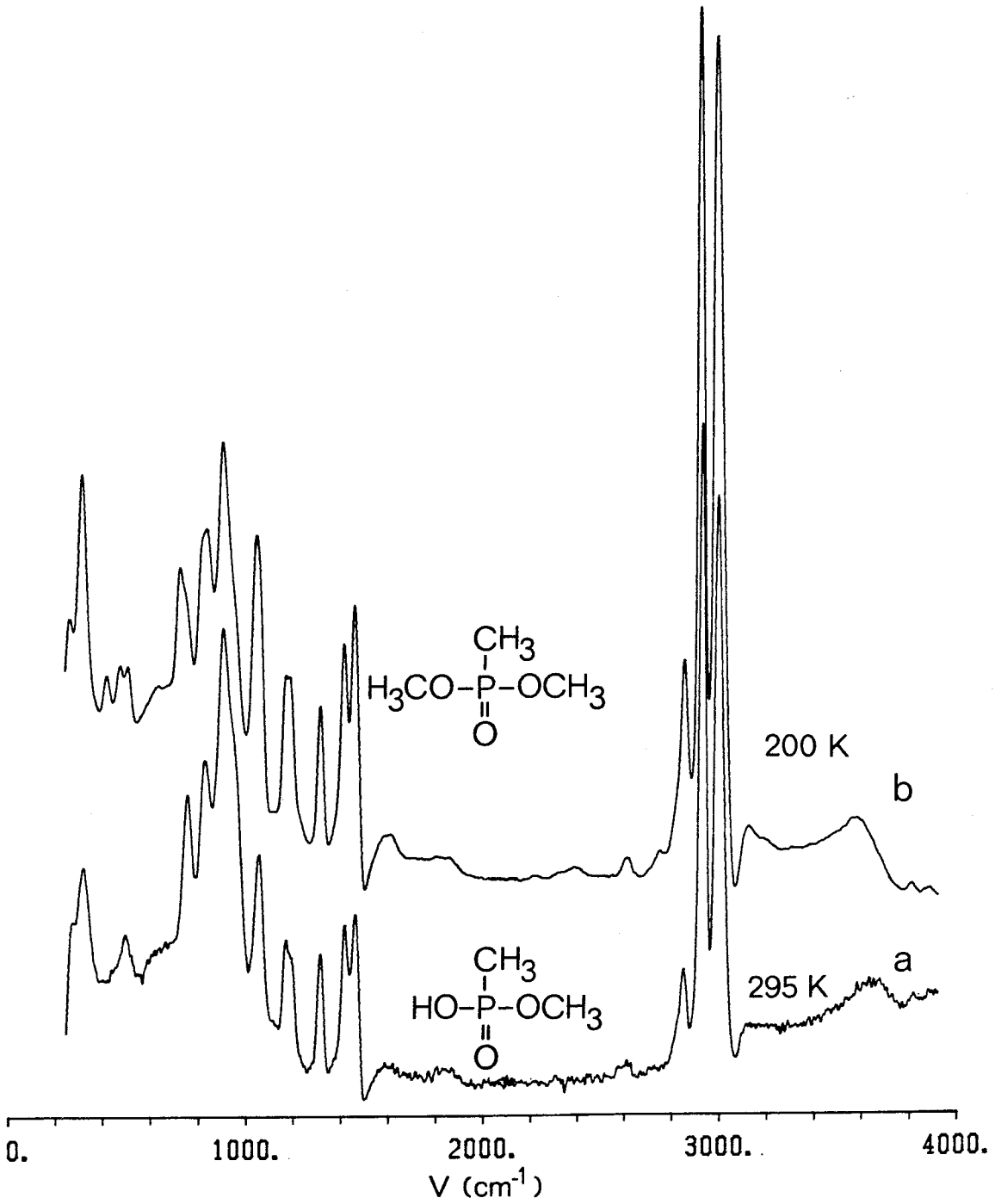
CH3
H3CO–P–OCH3
O
200 K
b
CH3
HO–P–OCH3
O
295 K
a
0.
1000.
2000.
3000.
4000.
V (cm-1)

Figure III-1

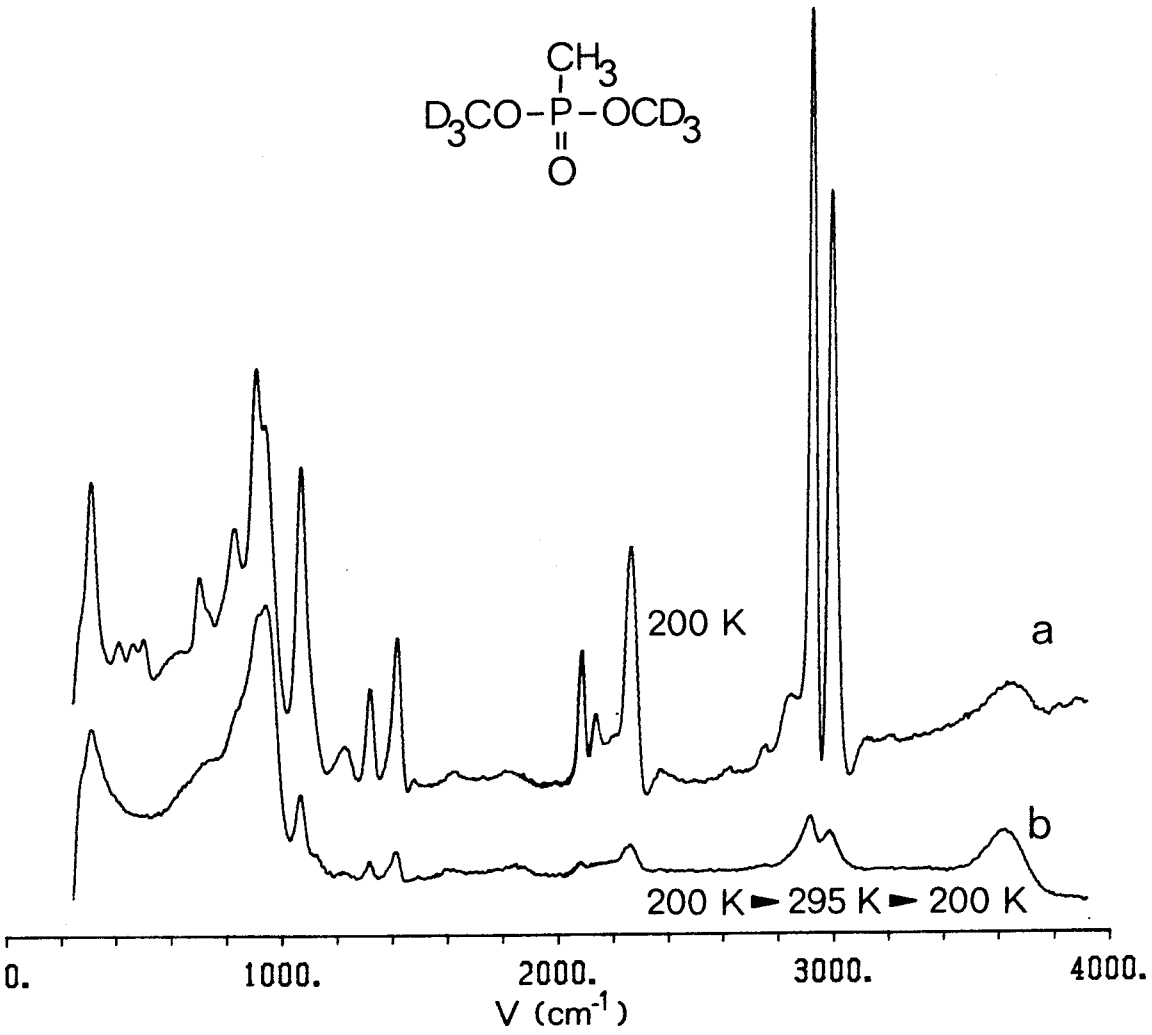
CH3
D3CO-P-OCD3
O
200 K
a
b
200 K ► 295 K ► 200 K
0.
1000.
2000.
3000.
4000.
V (cm-1)

Figure III-2

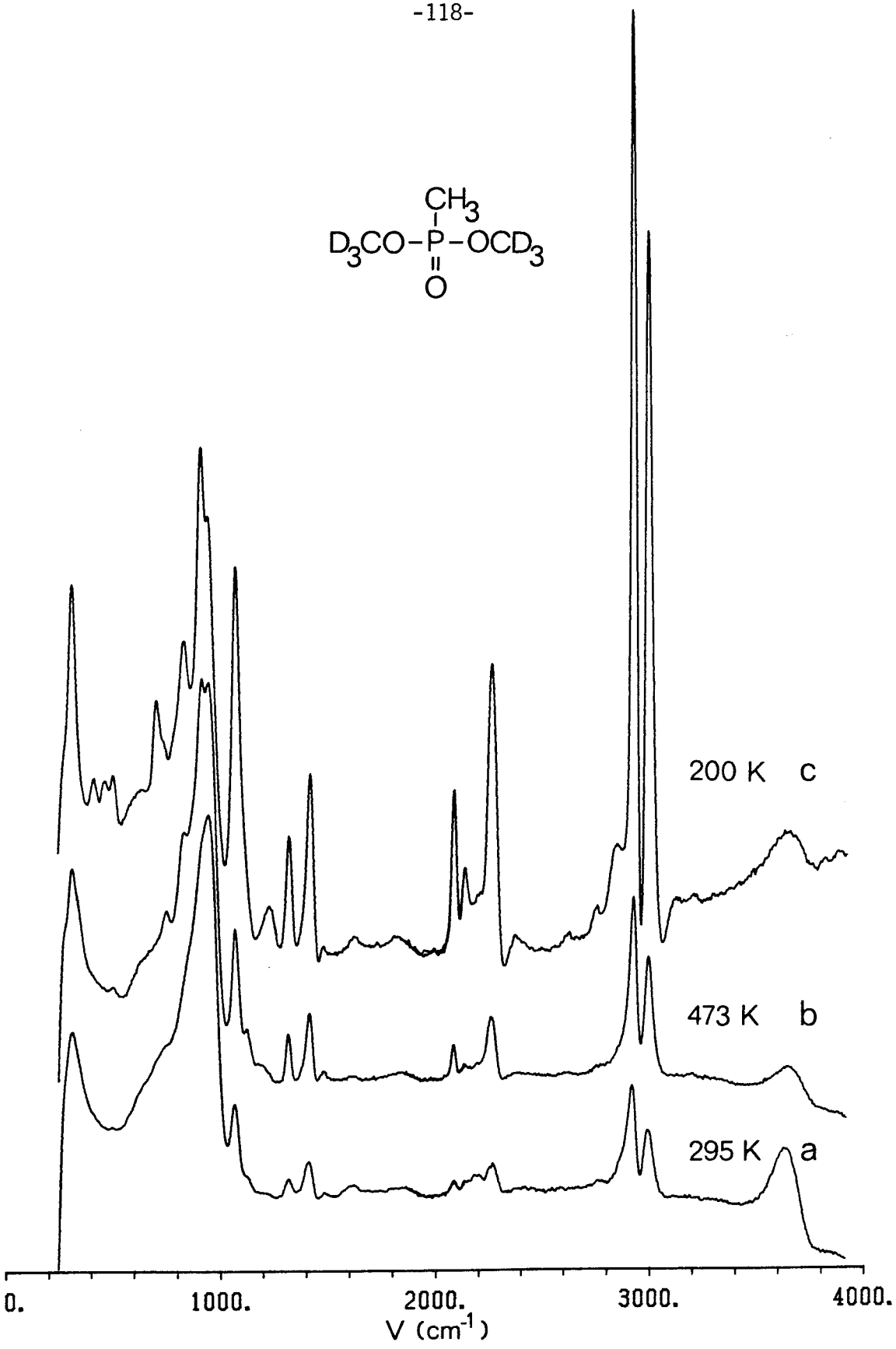

Figure III-3

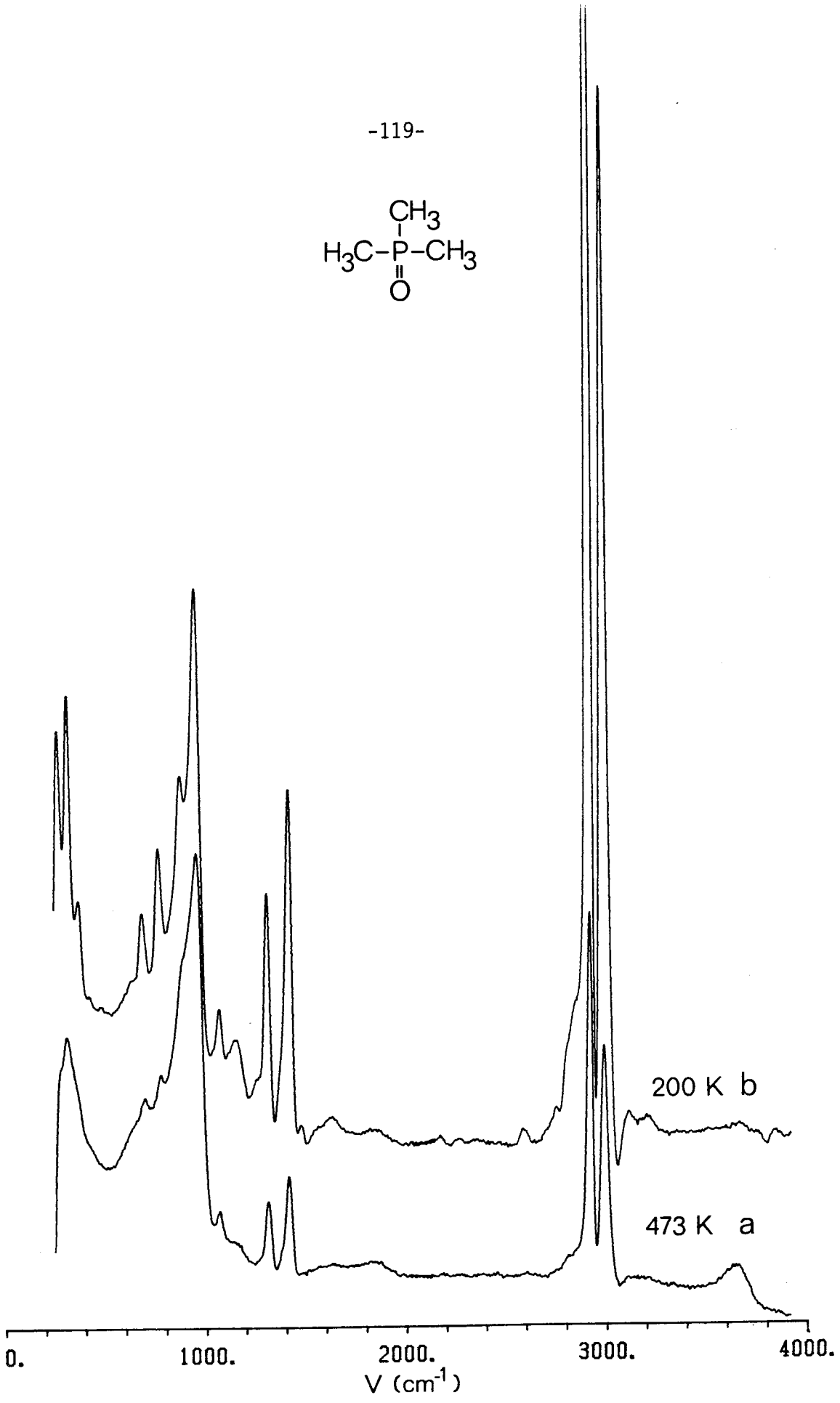

Figure III-4

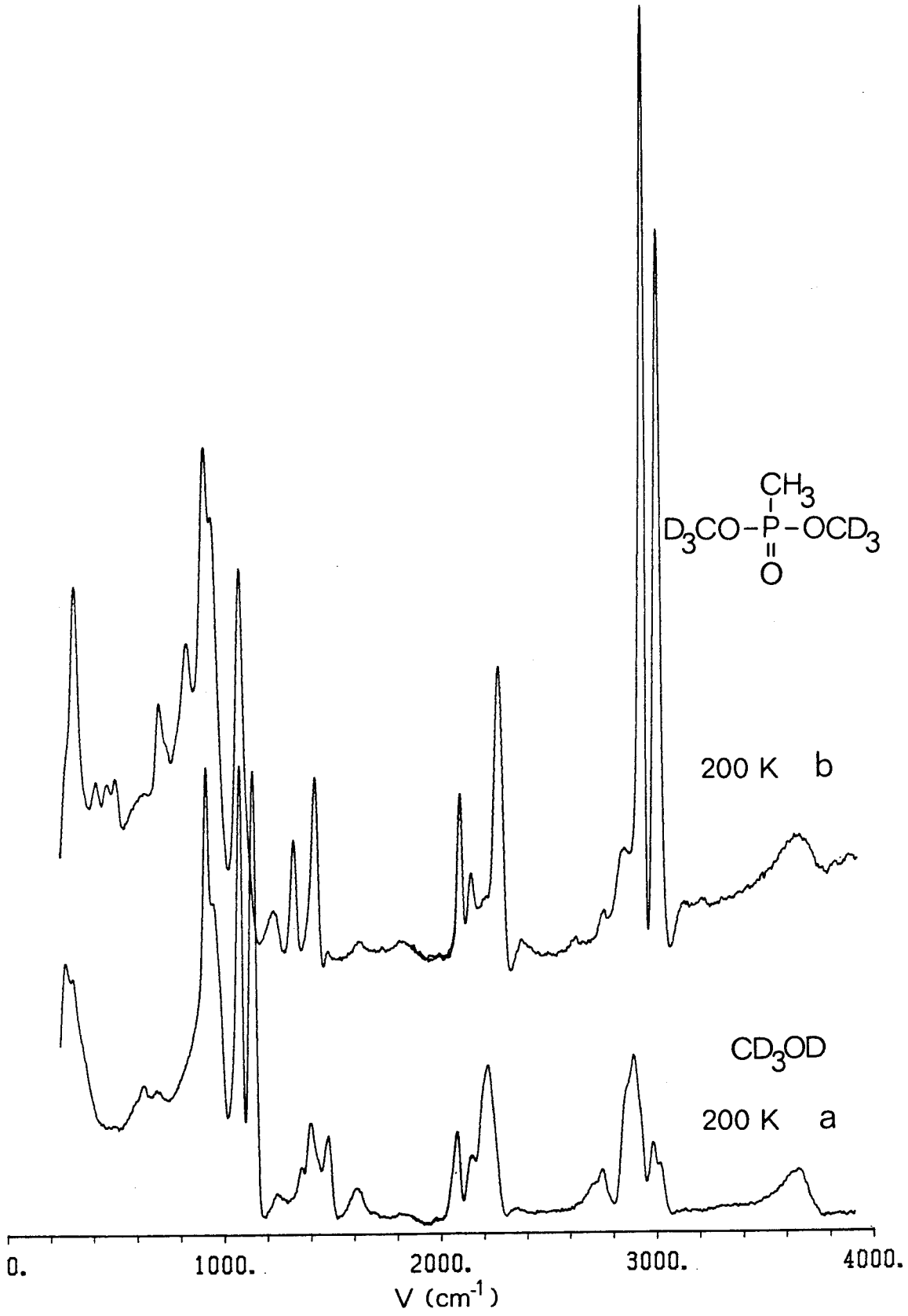

Figure III-5

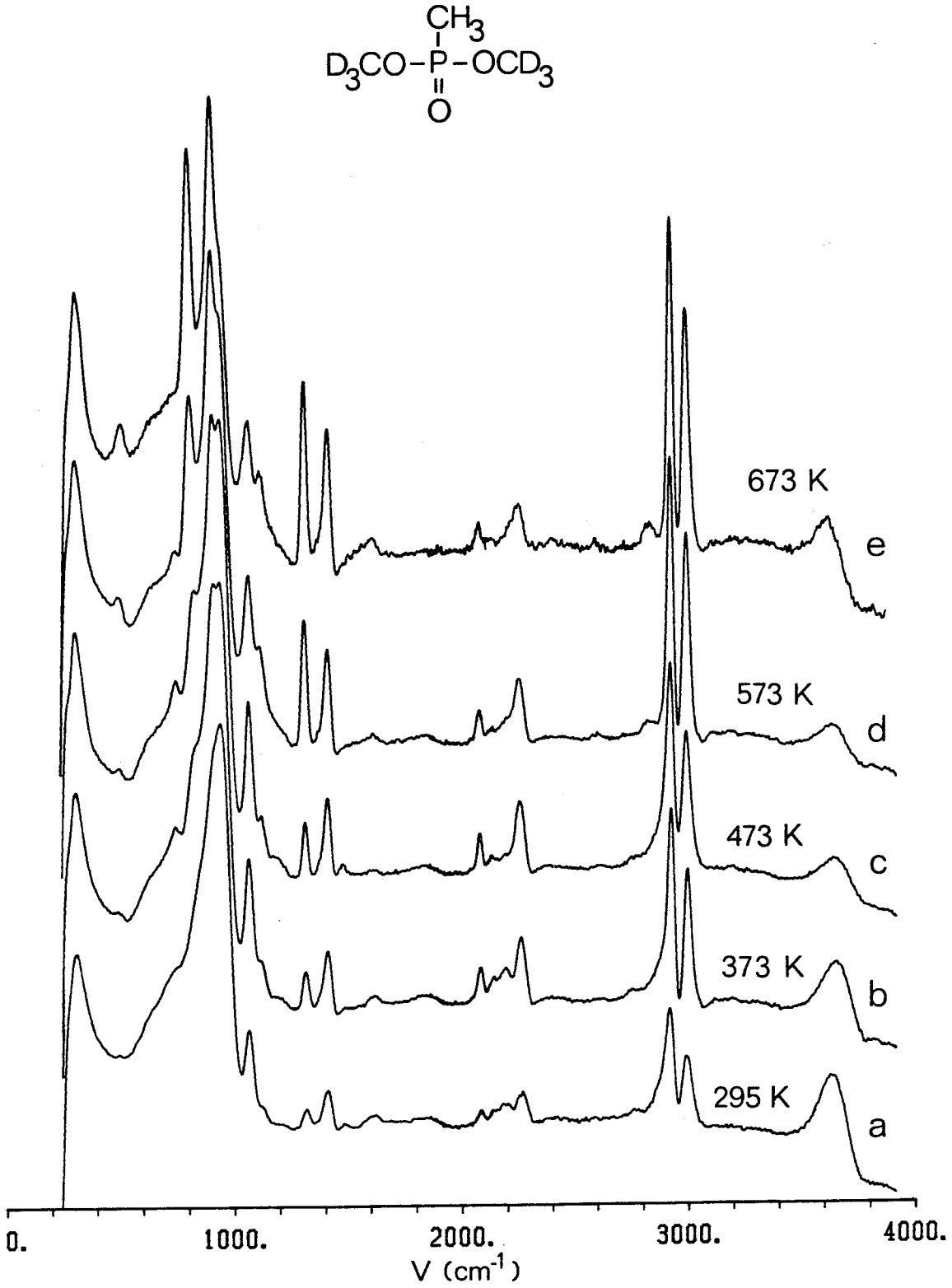
CH3
D3CO-P-OCD3
O
673 K
e
573 K
d
473 K
c
373 K
b
295 K
a
0.
1000.
2000.
3000.
4000.
V (cm-1)

Figure III-6

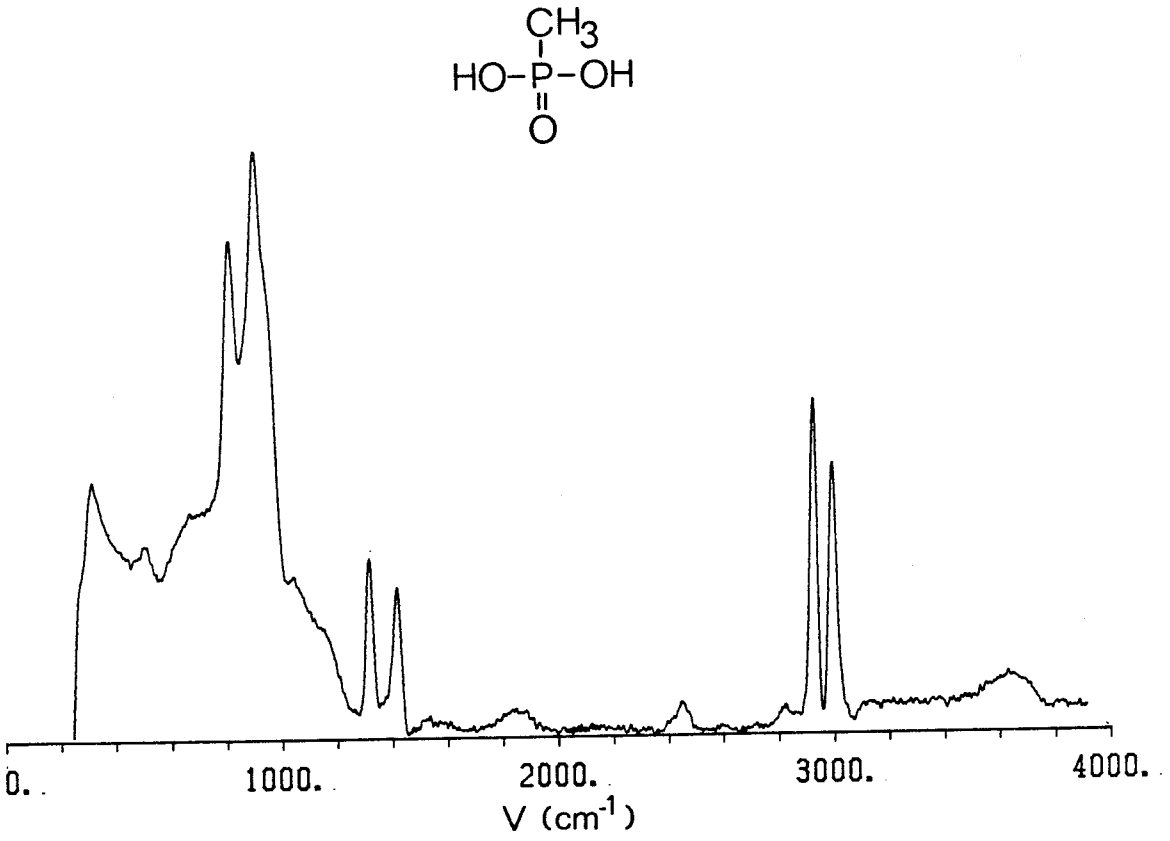

Figure III-7

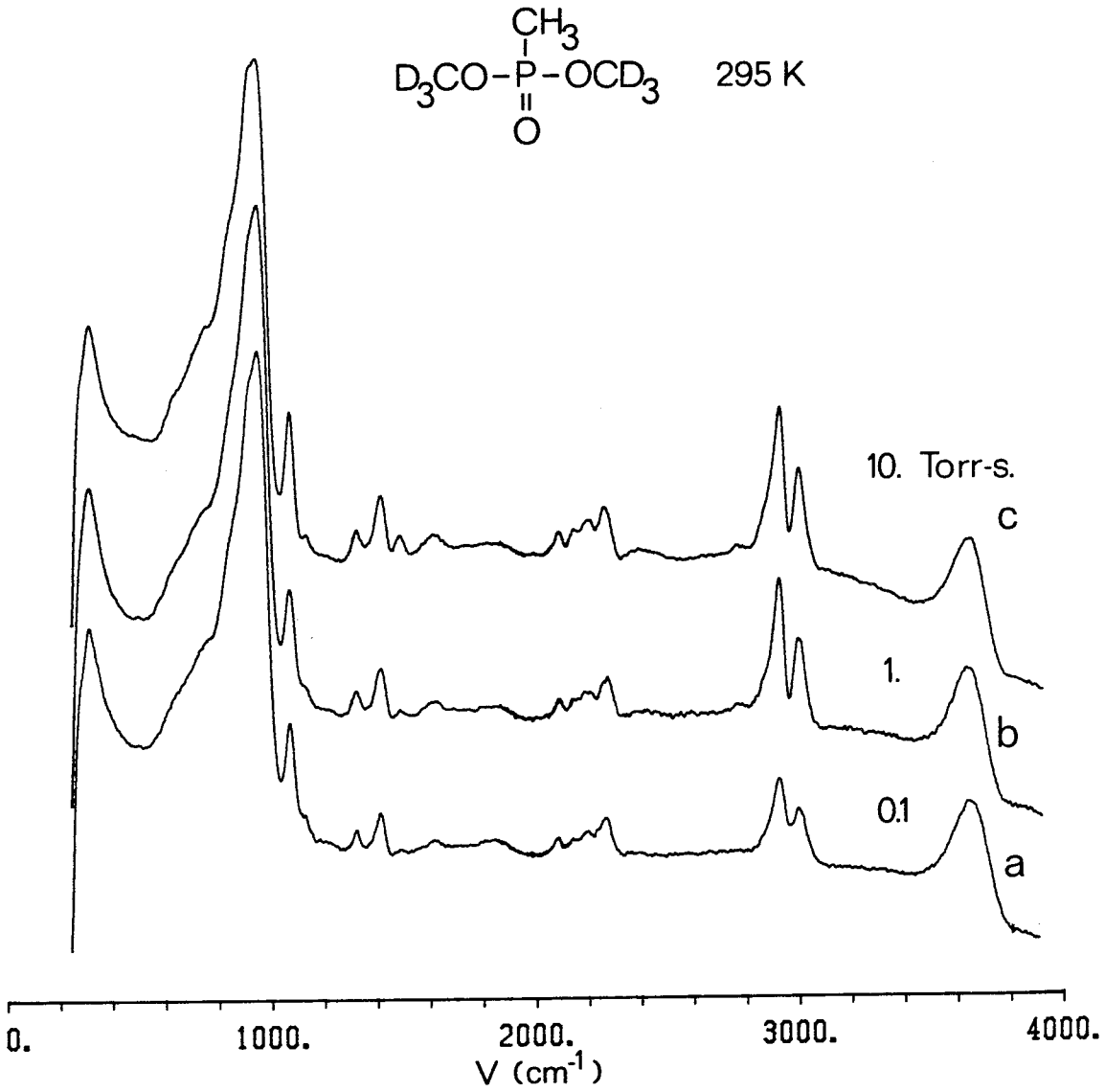
CH3
D3CO-P-OCD3
O
295 K
10. Torr-s.
c
1.
b
0.1
a
0.
1000.
2000.
3000.
4000.
V (cm-1)

Figure III-8

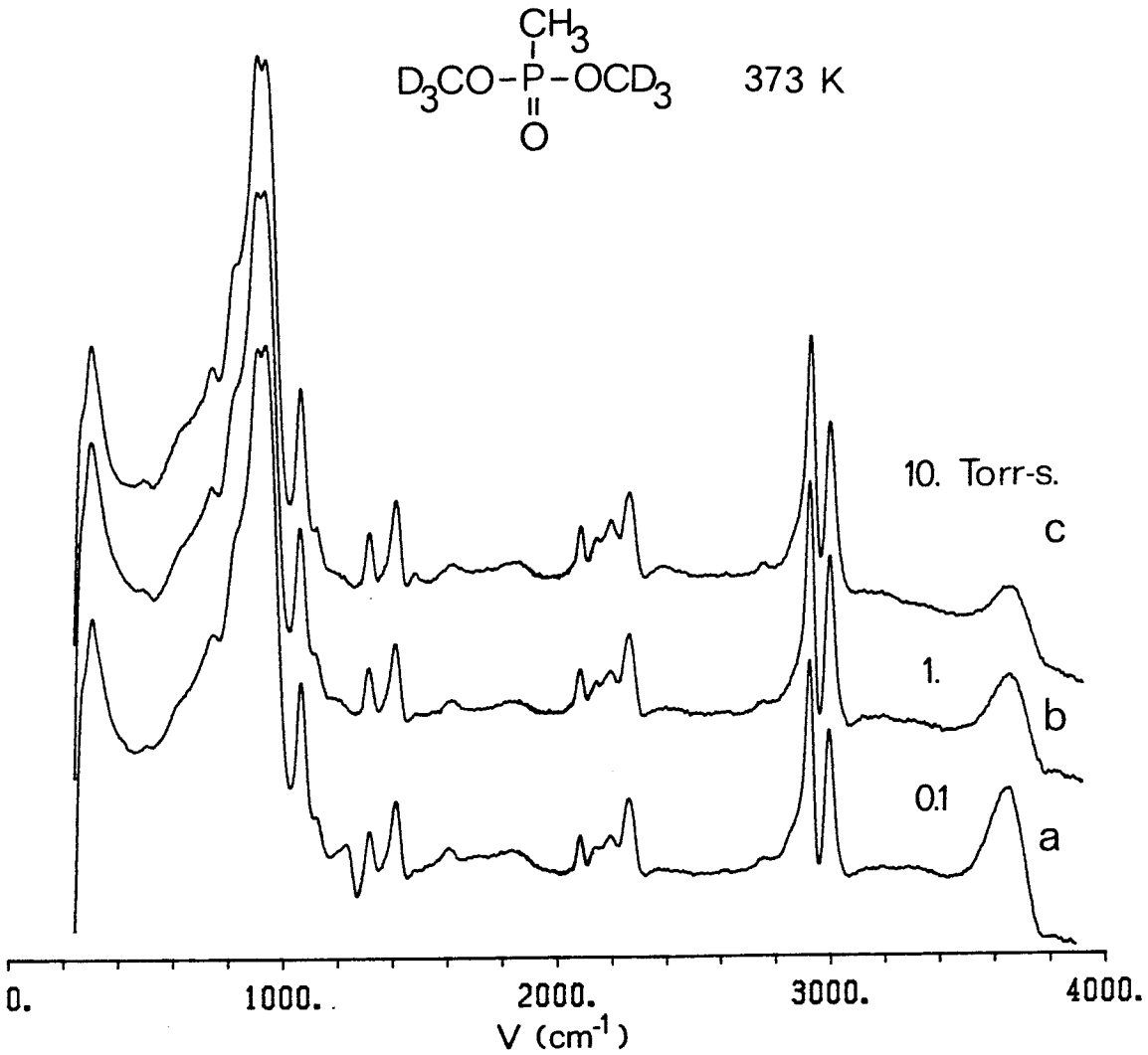
CH3
D3CO-P-OCD3
O
373 K
10. Torr-s.
c
1.
b
0.1
a
0.
1000.
2000.
3000.
4000.
V (cm-1)

Figure III-9

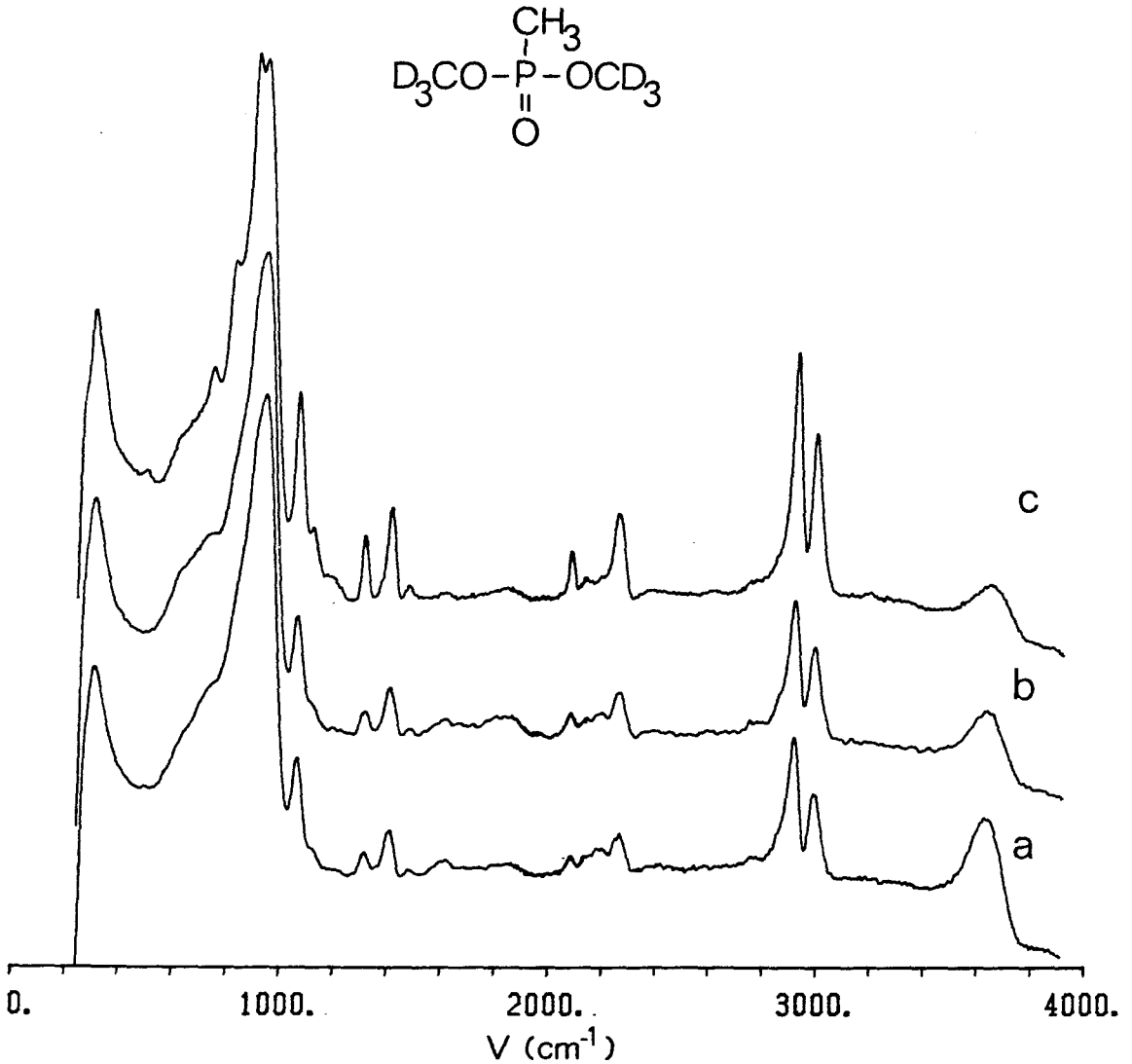

Figure III-10

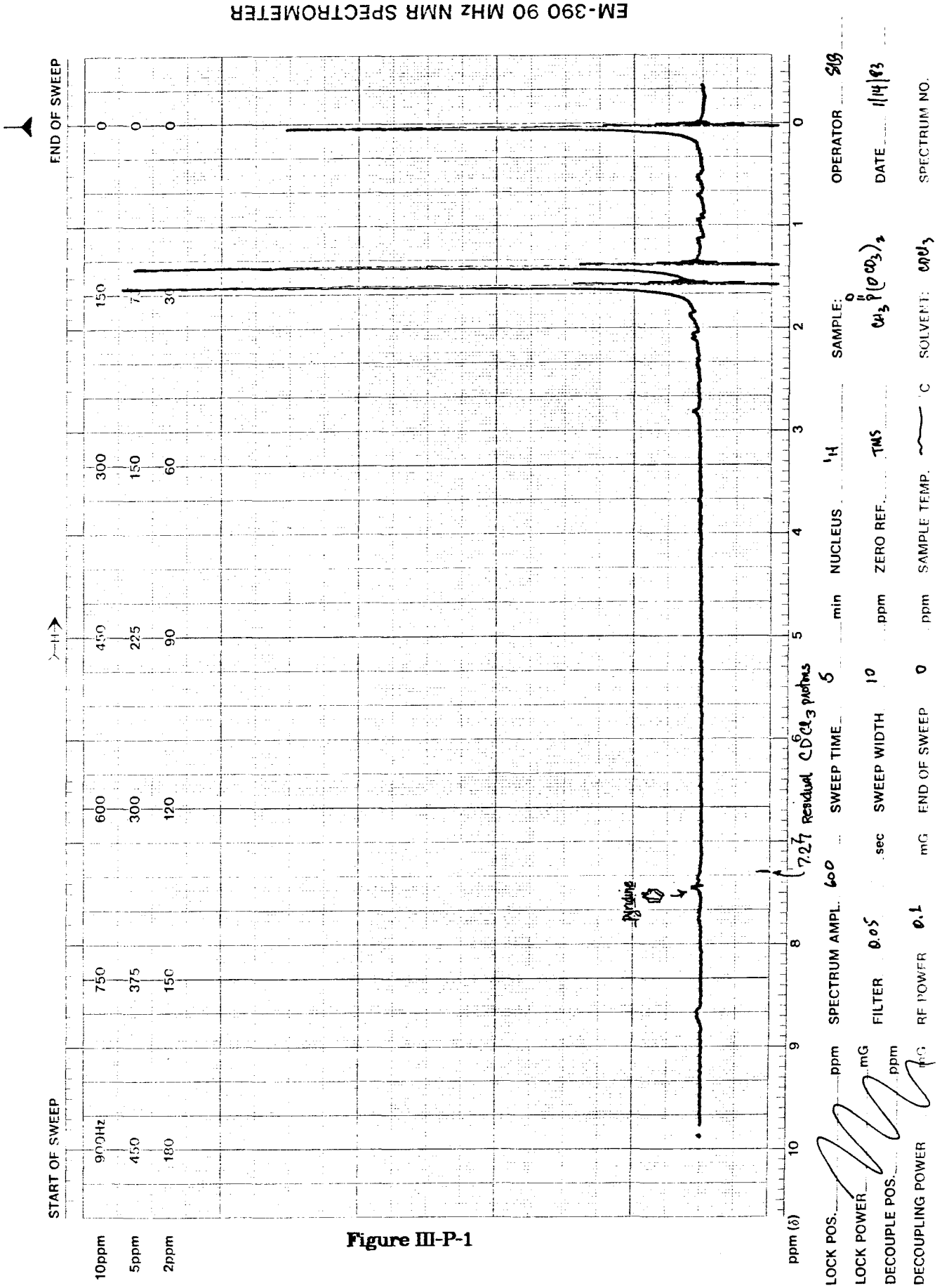

Figure III-P-1

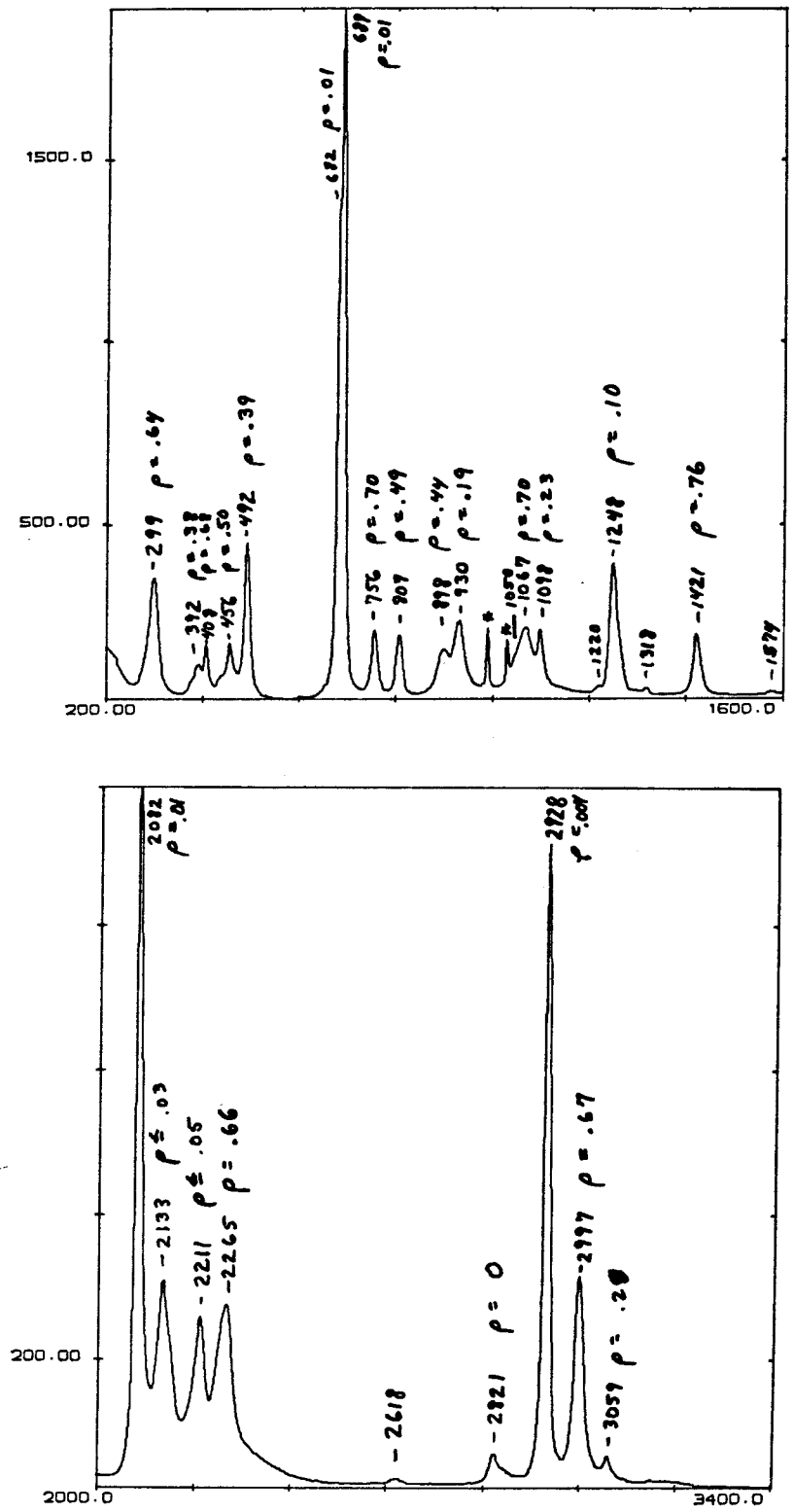

Figure III-P-2

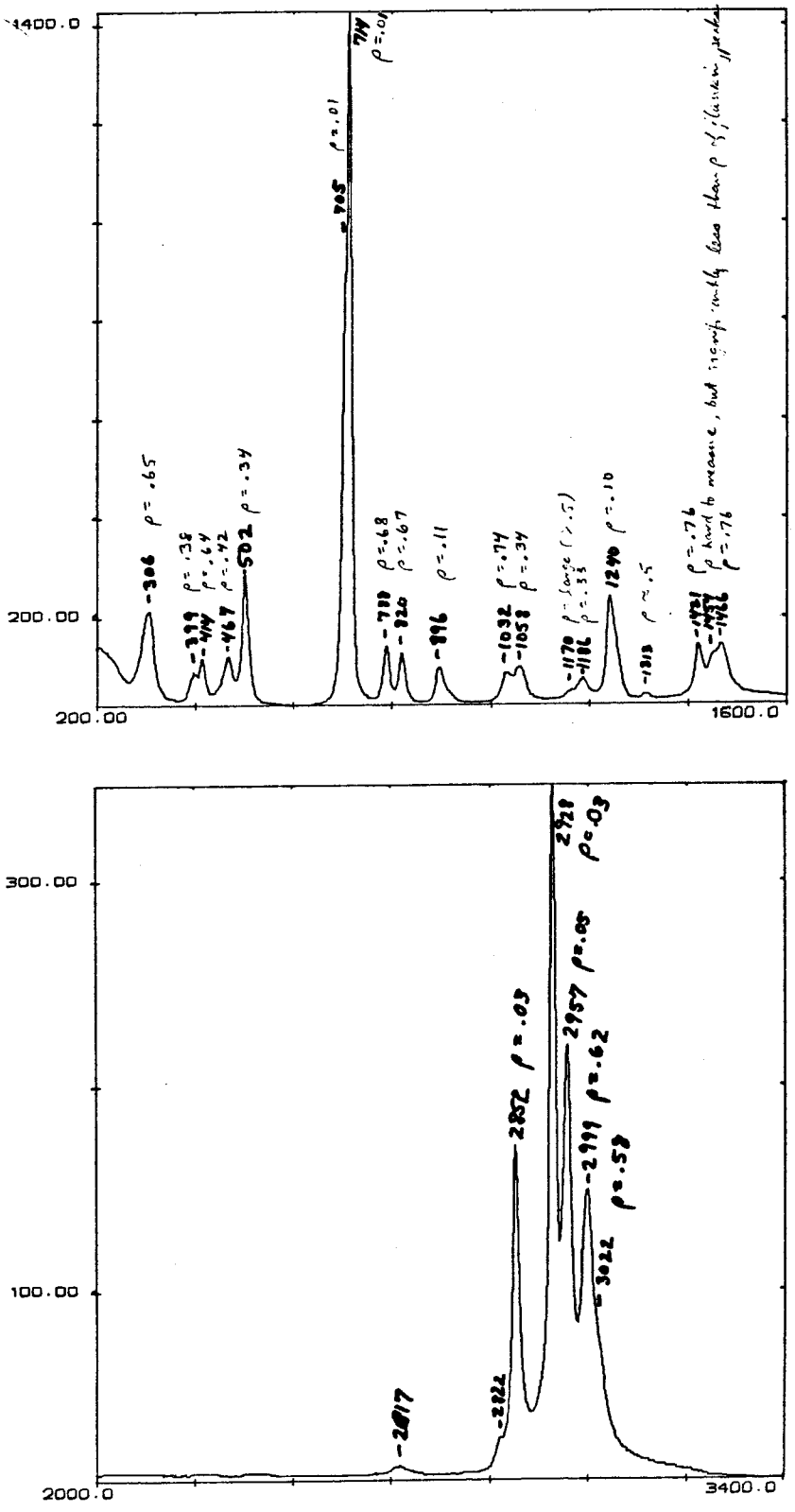

Figure III-P-3

EM-390 90 MHz NMR SPECTROMETER

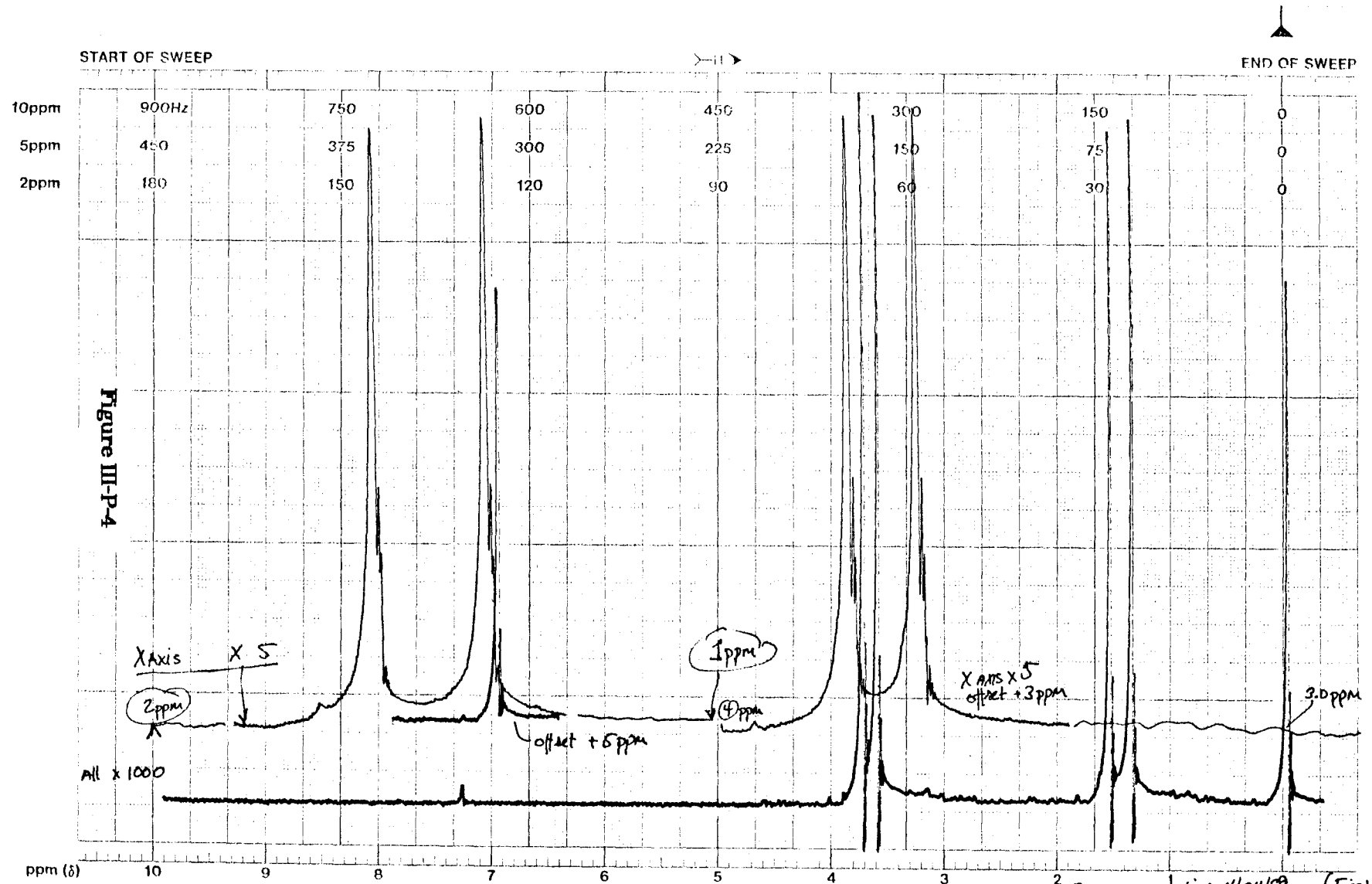

Figure III-P-4

2nd Batch purified 4/24/83 (First Fraction)

LOCK POS. ppm SPECTRUM AMPL. SWEEP TIME min NUCLEUS SAMPLE: ✓ $CH_3P(O)(OCH_3)(OH)$ OPERATOR MKT

LOCK POWER mG FILTER sec SWEEP WIDTH ppm ZERO REF. DATE 4/25/83

DECOUPLE POS. ppm

DECOUPLING POWER mG RF POWER mG END OF SWEEP ppm SAMPLE TEMP. C SOLVENT $CDCl_3$ 1% TMS SPECTRUM NO.

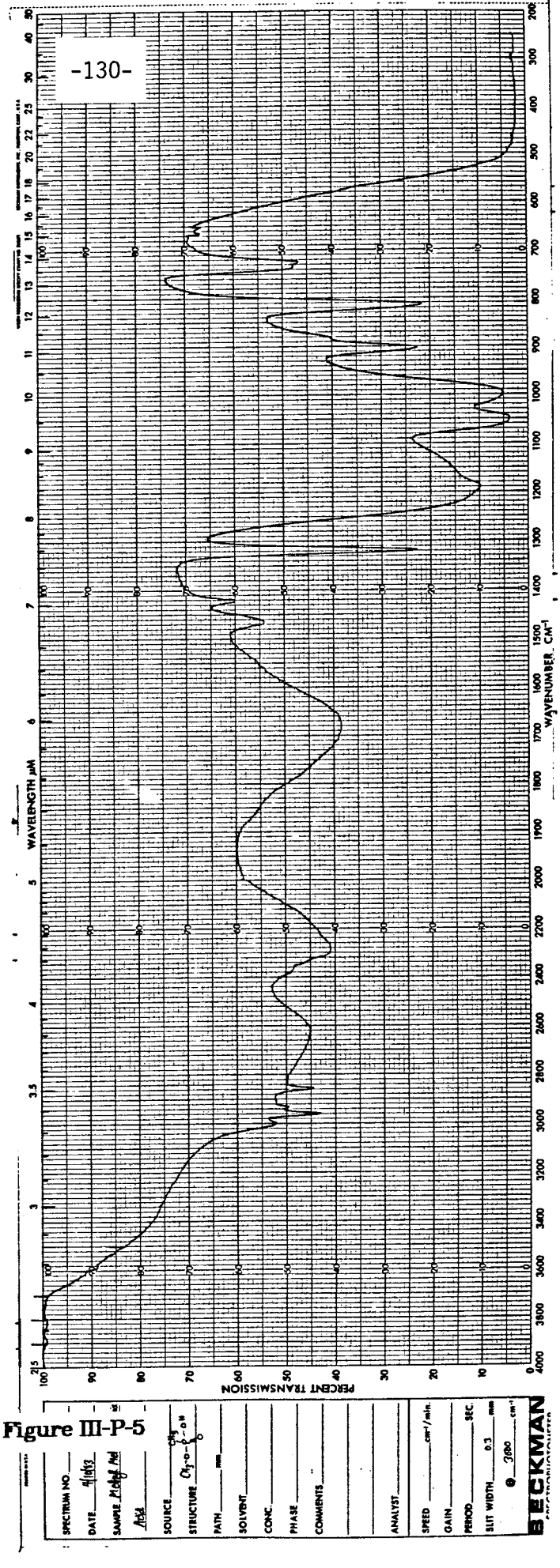

Figure III-P-5

Table 1

DMMP(*l*) Raman	DMMP/Al_2O_3 200K; IETS	Assignments DMMP/DDMMP	DDMMP/Al_2O_3 200K; IETS	DDMMP(*l*) Raman	MMPA/Al_2O_3 295K; IETS
3022		$\nu_a[(O)CH_3]$			
2999	2981	$\nu_a[(P)CH_3]$	2980	2997	2983
2957P		$\nu_s[(O)CH_3]$			
2928P	2912	$\nu_s[(P)CH_3]$	2912	2928P	2917
2852P	2843	$\nu_s[(O)CH_3]$			2840
				2821w	
			2252	2265	
			2195	2211P	
			2137	2133P	
			2074	2082P	
1466/1454	1452	$\delta_a[(O)CH_3]$			1453
1421		$\delta_s[(O)CH_3]$			
1421	1409	$\delta_a[(P)CH_3]$	1408	1421	1409
1313	1308	$\delta_s[(P)CH_3]$	1310	1318vw	1307
1240P		ν[P-O]	1217	1248P	
1186P	1177	$\rho[(O)CH_3]$			1162sh
1170	1166				1162
				1098	
				1067	
1058	1048	ν[C-O(P)]	1059	1050	1048
1032	1048				
			929	930P	
896P	900	$\rho[(P)CH_3]$	899	898P	901
820	830	ν[(C)O-P]	820	807	822
788	830sh			756	
714P	736sh	ν[P-C]	720sh	689P	749
705P	721	ν[P-C]	695	682P	
	630vw	ν[Al-O(P)]			
502P	501		492	492P	488vbr
467P	469		455	456P	
414	413		404	408	
306P	310		302	299	312
	257				269sh

Table 2

CD_3OD/Al_2O_3 200K (IETS)		Assignments				
Relative Intensity	Position cm^{-1}	CH_3O	CD_3O	H C O O	H C O O	Misc.
10	3650					ν(OH)
11	3003sh			ν(CH)		
17	2971	$\nu_a(CH_3)$				
37	2880			$A_1\nu$(CH)		
30	2860sh	$\nu_s(CH_3)$				
11	2738			ν(CH)		
8	2700					ν(OD)
2	2360					
36	2204		$\nu_a(CD_3)$			
28	2180sh				$A_1\nu$(CD)	
16	2131				ν(CD)	
21	2062		$\nu_s(CD_3)$			
8	1605			$B_2\nu_a$(OCO)		
20	1469	$\delta_a(CH_3)$				
15	1406sh			$A_1\nu_s$(OCO)		
23	1389	$\delta_s(CH_3)$		$B_2\delta$(CH)		
13	1355				$A_1\nu_s$(OCO)	
07	1248					
100	1118	$\rho(CH_3)$	$\delta_a(CD_3)$			
95	1058	ν(O–CH_3)	$\delta_s(CD_3)$	$B_1\delta$(CH)	$B_2\delta$(CD)	
74	941					ν(Al-O)
50	906				$B_1\delta$(CD)	
3	682			$A_1\delta_s$(OCO)		
3	619					
30	293					
30	261					

Table 3

$CH_3PO_3^{-2}Na_2^{2+}$ IR Aqueous Soln.[15]		$CH_3P(O)(OH)_2/Al_2O_3$ 295K IETS Major Species		Minor Species		$CH_3P(O)(OH)_2Na$ IR Powder [48]		Assignments	
				3630	m,vbr				ν(AlO-H)
2985	vw	2985	vs			2989	w	$\nu_a(CH_3)$	
2920	vw	2915	vs			2921	w	$\nu_s(CH_3)$	
		2820	w			2800	s	fermi res	
				2710	vw				
				2605	vw				
				2440	m,vbr	2450	m		ν(PO-H)
						2300	s		
				1805					ν(Al-H)
						1680	m		ν(PO-H)
				1550					
1429	w	1418	s			1419	w	$\delta_a(CH_3)$	
						1314	m	$\delta_s(CH_3)$	
1304	m	1308	s			1310	m		
						1234	s		δ(PO-H)
1085	vs,vbr	1145	w,sh,vbr			1160	s	$\nu(PO_3)$	
						1093	m	$\rho(CH_3)$	
1050		1035	w,sh			1038	s	$\nu(PO_3)$	
972	m							$\nu(PO_3)$	
				940	s,vbr				ν(Al-O)
						930	s	$\nu(PO_3)$	
						920	s		
880	vw	902	s			868	m	$\rho(CH_3)$	
750	w	809	vs			765	s	ν(P-C)	
515	w	497	m,vbr			524	s	$\delta_s(PO_3)$	
480	vw,sh					478	s	$\delta_a(PO_3)$	
						461	m		
336	m	310				330	m	$\rho(PO_3)$	
						300	m		
						240	m		

Chapter IV

The Decomposition of Phosphonate Esters Adsorbed on Aluminum Oxide

Abstract

Inelastic electron tunneling spectroscopy was used to examine the adsorption and reaction of three phosphonate esters on aluminum oxide surfaces which were synthesized by the plasma oxidation of aluminum metal films. The phosphonate esters were diisopropyl methyl phosphonate (DIMP), dimethyl methyl phosphonate (DMMP) and diphenyl methyl phosphonate (DPMP). The adsorption temperatures ranged from 200 to 673 K. The exposures of gaseous DIMP and DMMP were 1.0 Torr-s, while DPMP was exposed to the surface as a 0.025 M solution in hexane. DIMP was found to adsorb associatively in low coverages at 295 K, whereas at 373 K, DIMP was found to adsorb dissociatively in low coverages as isopropyl methyl phosphonate. Above 373 K the isopropyl methyl phosphonate decomposed to the metastable hydroxy methyl phosphonate, which, in turn, decomposed completely to the methyl phosphonate above 573 K. Although the dissociative adsorption temperature was lower (295 K), adsorbed DMMP decomposed similarly through the hydroxy methyl phosphonate to form the methyl phosphonate. However, in this case the hydroxy methyl phosphonate was a short-lived intermediate. DPMP was found to adsorb dissociatively at 295 K, and the adsorbed species formed is stable through 673 K. Consistent with these observations, mechanisms for the adsorption and decomposition of phosphonate esters on aluminum oxide are proposed that involve P-O bond cleavage upon adsorption but O-C bond cleavage upon decomposition of the adspecies.

1.0 Introduction

By studying the interaction of various adsorbates with aluminum oxide, the surface chemistry of this important material may be clarified. Previously, we have examined the interaction of gaseous dimethyl methyl phosphonate with aluminum oxide over a wide range of temperatures (200 to 673 K) and exposures (5×10^{-5} to 10 Torr-s) [1]. The gaseous phosphonate ester adsorbs molecularly at 200 K in high coverages. On the other hand, increasing the temperature of adsorption to 295 K causes the phosphonate ester to adsorb dissociatively in low coverages to form methyl methyl phosphonate. If the temperature of adsorption is increased still further to 573 K, then the dissociatively adsorbed phosphonate ester decomposes to methyl phosphonate.

The previous work emphasized the spectroscopic identification of the various adsorbed species and, in this way, confirmed that the transformations indeed took place. This paper is an extension of the previous work in that it examines the interaction of similar phosphonate esters with aluminum oxide surfaces via tunneling spectroscopy. However, issues concerning the mechanisms for the dissociative adsorption and decomposition of the phosphonate esters on aluminum oxide are emphasized here.

Our conclusions are based on the vibrational spectra of three diesters of methyl phosphonic acid adsorbed on aluminum oxide between 200 and 673 K. The particular phosphonate esters are diisopropyl methyl phosphonate $[(CH_3)_2CHO]_2(CH_3)P(O)$, dimethyl methyl phosphonate $(CH_3O)_2(CH_3)P(O)$ and diphenyl methyl phosphonate $(C_6H_5O)_2(CH_3)P(O)$. These three esters have chemically very different ester moieties. Hence, depending on the reaction mechanism, they can display either very different or very similar reactivities. This feature will be useful in drawing conclusions concerning reaction mechanisms

on the surface.

Aside from our previous work [1], there are few accounts in the literature of the adsorption of phosphonate esters on aluminum oxide. An infrared spectroscopic study of the adsorption of diisopropyl methyl phosphonate on hydroxylated alumina powders at 295 K concluded that although adsorption was predominantly molecular, a small amount of the dissociatively adsorbed phosphonate ester was present [2]. Evidently, the adsorption of diphenyl methyl phosphonate has not been reported on any surface.

2.0 Experimental Procedures

2.1 Adsorbates

Diisopropyl methyl phosphonate (DIMP) was obtained from Alfa Products in 98% purity. Dimethyl methyl phosphonate (DMMP) was obtained from Aldrich Chemical Company in 97%+ purity. Diphenyl methyl phosphonate (DPMP) was synthesized by the reaction of triphenyl phosphite methiodide with ethanol following a previously published procedure [3]. The purity of the final product was confirmed by a comparison between the ^1H NMR spectrum of the product and one reported in the literature [4].

2.2 Tunnel Junction Fabrication Procedure

The tunnel junction fabrication and measurement procedures have been documented elsewhere [1]. Nevertheless, it is important to emphasize the nature of the aluminum oxide surfaces being studied here. They are formed by oxidizing the surfaces of evaporated aluminum metal films with a glow discharge in approximately 0.2 Torr of O_2 (99.999% purity). The similarity of this surface oxide to γ-alumina has been demonstrated with XPS [5].

The procedure for dosing the surfaces varies depending upon the vapor pressure of the adsorbate. For DIMP and DMMP, the surfaces were contacted with the gaseous adsorbate. With this procedure the surface temperature during exposure could be varied arbitrarily. On the other hand, the vapor pressure of DPMP is approximately 10^{-7} Torr at 295 K [6]. Consequently, a 0.025 M solution of DPMP in spectral grade n-hexane was freshly prepared for each of the experiments with DPMP. A few drops of this solution were then pipetted onto the surface at room temperature and atmospheric pressure. The solvent evaporated in a few minutes, and then the surface was returned to vacuum where it could be heated arbitrarily. Again, more detailed specifications for these procedures are found elsewhere [1].

3.0 Results and Discussion

3.1 Dissociative Adsorption

DMMP, in exposures of 1.0 Torr-s, adsorbs dissociatively on aluminum oxide between 295 and 473 K [1]. A key factor in determining this was the positions of the P-O stretching vibrations of the adsorbed species, since from these it is possible to easily distinguish dissociative from associative adsorption. Therefore, selectively deuterium labeled dimethyl methyl phosphonate (DDMMP) was used extensively in these experiments, since it was free from modes that occluded the extraordinarily weak P-O stretching vibrations in the unlabeled compound. Without use of similarly labeled forms of DIMP and DPMP, it is doubtful whether the positions of the P-O stretching vibrations could be ascertained. Rather, we will rely on a combination of less direct spectroscopic data and information in the literature to infer that on the one hand, DIMP adsorbs associatively at 295 K, while on the other hand, DPMP adsorbs dissociatively at 295 K. The evidence for this will be discussed below in connection with results for adsorption of these

esters between 373 and 673 K.

Furthermore, these results are also consistent with our proposed dissociative adsorption mechanism for phosphonate esters on aluminum oxide, which is based on previous results with DMMP, and which is depicted in Scheme 1 [1]. At this point, it is convenient to discuss this mechanism, which is similar to nucleophilic substitution occurring in phosphonate esters under neutral and alkaline conditions [6,7]. A somewhat similar mechanism has been proposed previously for the dissociative adsorption of isopropyl methyl phosphonofluoridate [2]. The mechanism consists of adsorption of the neutral phosphonate ester on a coordinately unsaturated aluminum site [Scheme 1a]. This destabilizes the phosphorus center and leads to nucleophilic attack by a lattice oxygen at the phosphorus to form the penta-coordinate intermediate [Scheme 1b]. This is followed by the transfer of a proton from the surface to the leaving group oxygen and elimination of the alcohol [Scheme 1c].

This mechanism is supported by all available data. The initial step of the mechanism is consistent with the similarity between the number of coordinately unsaturated aluminum atoms as determined by titration with gaseous trimethyl phosphine oxide and the surface coverage of the dissociatively adsorbed DMMP [1]. The nucleophilic behavior of the lattice oxygen, as in the second step, has been demonstrated clearly in other reactions on aluminum oxide, such as the conversion of acetaldehyde and dimethyl ketone to acetate [8,9]. Furthermore, several carboxylic acid esters adsorb dissociatively on aluminum oxide [10], and the mechanistic similarity between homogeneous nucleophilic substitution at an acyl carbon and homogeneous nucleophilic substitution at the phosphoryl phosphorus has been emphasized [11].

The dissociative adsorption mechanism (Scheme 1) indicates a bimolecular

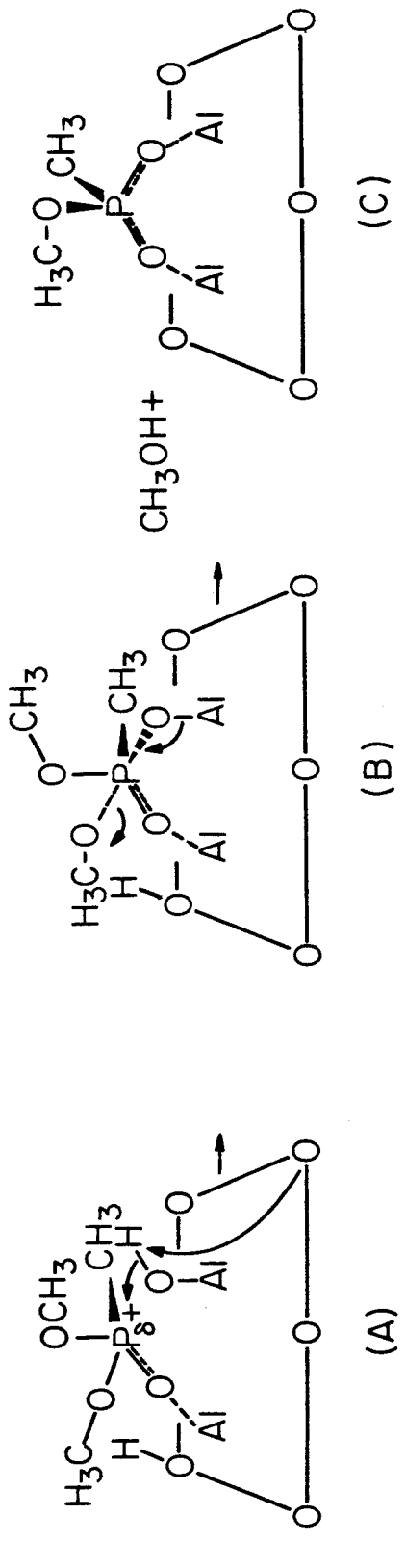

Scheme IV-1

nucleophilic substitution taking place at the phosphorus [S_N2(P)] leading to P-O bond cleavage. As mentioned, this is consistent with the behavior of phosphonate esters under neutral and alkaline hydrolysis [6,7]. For comparison, the preexponential factors and activation energies for homogeneous hydrolysis of the phosphonate esters under study are given in Table 1 [6]. Two principal effects explain the relative ordering of the alkaline hydrolysis rates shown in Table 1 [6,7]. First, because the mechanism is bimolecular and takes place via trigonal bypyramidal transition state, steric hindrance will disfavor the alkaline hydrolysis of DIMP as compared to DMMP and DPMP. Second, because the basicity of the phenoxy, methoxy and isopropoxy anions increases in that order, the hydroxide ion will more easily displace the phenoxy as compared to the isopropoxy, and thus again the alkaline hydrolysis of DIMP is disfavored compared to DMMP and DPMP. Consequently, the combination of these two effects accounts for the two to three orders of magnitude lower rate of alkaline hydrolysis for DIMP versus DMMP and DPMP. Moreover, it is a consequence of this much lower activity toward nucleophilic substitution at the phosphorus that DIMP adsorbs associatively at 295 K, whereas both DMMP and DPMP adsorb dissociatively at 295 K. Rates and activation energies for the alkaline hydrolysis of analogous esters of acetic acid are given in Table 2 [12]. In this case, the hydrolysis mechanism is a bimolecular nucleophilic substitution taking place at the acyl carbon [S_N2(Ac)] [12]. Note the similar activation energies and preexponential factors in comparison with phosphonate hydrolysis. The acid catalyzed hydrolysis of these carboxylic acid esters also takes place by a S_N2(Ac) reaction. The activation energy is expected to be approximately 5 kcal/mole higher [12].

However, as will be important later, phosphonate esters can also be hydrolyzed by nucleophilic substitution at the alkyl carbon of the ester moiety, leading to C-O bond cleavage [6]. This occurs in acidic media. For comparison, the

relative rates and activation energies for the acidic hydrolysis of the phosphonate esters under study are given also in Table 1. The relative ordering of the rates for acidic hydrolysis can be explained in terms of differences in mechanism. Under these conditions, the decomposition of DIMP proceeds by a unimolecular nucleophilic substitution at the alkyl carbon of the ester [$S_N1(Ak)$] [6]. On the other hand, in DMMP it is unfavorable for the methyl of the ester to form a carbo-cation. Consequently, DMMP probably decomposes by a bimolecular nucleophilic substitution at the alkyl carbon of the ester [$S_N2(Ak)$], which is apparently less favorable under these conditions [6]. Even less favorable is the decomposition of DPMP, the difficultly of nucleophilic substitution at the phenyl carbon being well known. Note that the order of increasing relative rates is reversed in going from alkaline hydrolysis to acidic hydrolysis, and that the activation energy for hydrolysis by attack at the phosphorus is approximately half the activation energy for attack at the alkyl carbon.

Esters of carboxylic acids will undergo hydrolysis by unimolecular nucleophilic substitution at the alkyl carbon of the ester only if the resulting carbo-cation formed is sufficiently stable. For example, t-butyl acetate hydrolyzes in water, yielding the Me_3C^+ carbo-cation. The activation energy is 27.5 kcal/mole [16], and this compares favorably with the activation energy for the mechanistically similar hydrolysis of phosphonate esters in acid media (see Table 1).

The phosphonate ester is likely to adsorb dissociatively on the aluminum oxide surface as the bidentate bridging phosphonate (rather than the bidentate chelating), as shown in Scheme 1c. This is attested to by the close match in the frequencies of the ν_s(O-P-O) and ν_a(O-P-O) stretching modes between adsorbed hydroxy isopropoxy methyl phosphonate (1090 cm^{-1} and 1180 cm^{-1} [2]), which produces a surface species identical to dissociatively adsorbed DIMP, and the homogeneous metal complex $Al(IMP)_3$ (1088 cm^{-1} and 1179 cm^{-1} [17]), which is

known to consist largely or entirely of the bidentate bridging homogeneous analogue of dissociatively adsorbed DIMP.

Other work suggests that either the (100) or the (110) planes of γ-alumina are the actual surfaces synthesized [18,19]. Both the (100) and (110) γ-alumina surfaces contain adsorption sites that equally well accommodate the geometry of the bidentate bridging, dissociatively adsorbed phosphonate, as judged from crystallographic determinations of the structure of homogeneous metal phosphinates [20]. However, the adsorption site picture in Scheme 1 is tentatively located on the (100) plane, since this site also provides a more favorable geometry for further decomposition of the adsorbed phosphonate.

3.2 The Adsorption and Decomposition of DIMP

The interaction of aluminum oxide with gaseous DIMP is discussed first since relevant information on this phosphonate ester is available in the literature. An infrared spectroscopic study of the adsorption of gaseous DIMP on aluminum oxide powders concluded that DIMP adsorbs predominantly associatively at 295 K [2]. In addition, a small amount of the dissociatively adsorbed species was present. In view of the proposed mechanism for dissociative adsorption, the low susceptibility of DIMP to homogeneous alkaline hydrolysis supports these conclusions.

On the other hand, the tunneling spectrum of an aluminum oxide surface exposed to 1.0 Torr-s of DIMP at 373 K is shown in Fig. 1a. A comparison between Fig. 1a and the spectrum of DIMP adsorbed associatively at 200 K (not shown) reveals that the relative ratio of the number of isopropyl groups to the number of methyl groups bound to the phosphorus decreases in going from adsorption at 200 K to adsorption at 373 K, as judged from changes in the relative intensities of the appropriate vibrational modes. This is consistent with a

change from molecular adsorption to dissociative adsorption which would ideally cause this ratio to fall from two to one. Thus the associatively adsorbed DIMP must decompose to dissociatively adsorbed species between 295 and 373 K.

The tunneling spectra of aluminum oxide surfaces exposed to 1.0 Torr-s of DIMP at 573 K and 673 K are shown in Figs. 1b and 1c, respectively. From these spectra it is clear that the decomposition of adsorbed DIMP proceeds in a fashion somewhat analogous to the decomposition of adsorbed DMMP [1]. As the adsorption temperature is increased from 373 K [Fig. 1a] to 573 [Fig. 1b], the dissociatively adsorbed DIMP begins to decompose, as evidenced by substantial changes taking place in the shapes of the CH stretching and deformation regions. Increasing the adsorption temperature further to 673 K produces a spectrum [Fig. 1c] that is virtually identical with the tunneling spectrum of DMMP adsorbed at 673 K [1]. Since the latter spectrum has been identified as characteristic of methyl phosphonate adspecies, it is clear that the decomposition of adsorbed DIMP also yields the methyl phosphonate [1].

The gaseous hydrocarbon evolved during the decomposition of adsorbed DIMP is propene. This can be surmised for the following reasons. It was found that isopropyl methyl phosphono fluoroidate (IMPF) adsorbs dissociatively on alumina to form isopropyl methyl phosphonate, which is identical to the species formed when DIMP adsorbs dissociatively on the aluminum oxide [2]. At 295 K, the adsorbed IMPF produced gaseous propene corresponding to a decomposition rate of 2% per week [2]. Heating the adsorbed IMPF intensified the production of gaseous propene [2]. In addition, the pyrolysis of liquid diisopropyl n-hexyl phosphonate begins at approximately 480 K and produces gaseous propene and n-hexyl phosphonic acid [21]. This is in agreement with the tunneling spectra of adsorbed DIMP, which begins to show decomposition of DIMP at 473 K (not shown).

The tunneling spectra of Fig. 1 also indicate the presence of a heretofore unidentified, stable intermediate in the decomposition of adsorbed DIMP to MP. In going from 373 K [Fig. 1a] to 573 K [Fig. 1b], the intensity of the mode at 2440 cm^{-1} increases concomitantly with the increase in the extent of decomposition of the adsorbed DIMP. Then in going from 573 K [Fig. 1b] to 673 K [Fig. 1c] the intensity of this mode declines concomitantly with the increase in surface coverage of MP, which is thermodynamically the most stable species. The 2440 cm^{-1} mode is attributable to the bidentate hydroxy methyl phosphonate adspecies **(1)**.

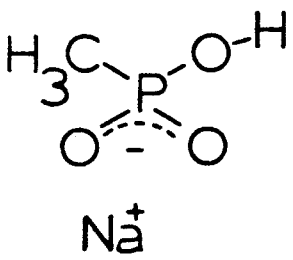

1

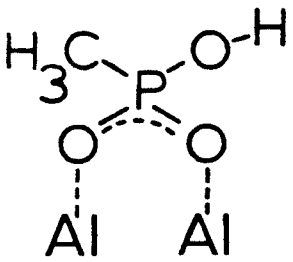

2

This identification is based on a homogeneous analogue of this species, the monobasic sodium salt of hydroxy methyl phosphonic acid **(2)**, which has an OH stretching mode at 2440 cm^{-1} [22]. In addition, the same mode was observed in connection with the incomplete dissociative adsorption of methyl phosphonic acid on aluminum oxide to give adsorbed hydroxy methyl phosphonate [1]. Note that it is difficult to detect the presence of this species by any vibrational mode other than the one at 2440 cm^{-1}, since both this species and methyl phosphonate have strongly overlapping spectral signatures, and we have a mixture of these two species.

From these observations, the decomposition of adsorbed DIMP is proposed to proceed as in Scheme 2. At 295 K, DIMP is adsorbed associatively [Scheme 2a]. Increasing the temperature to 373 K results in the decomposition of the

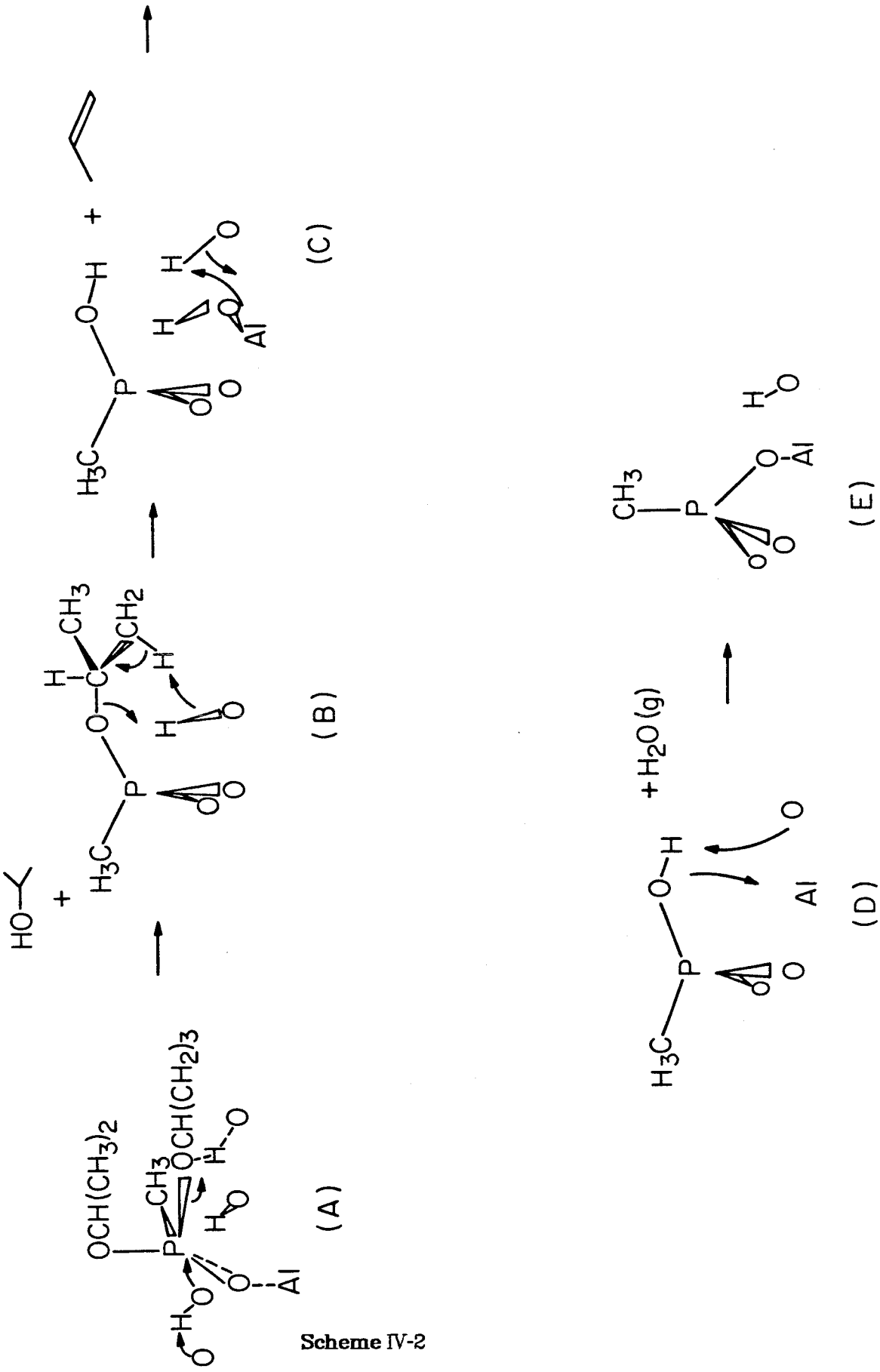

Scheme IV-2

associatively adsorbed DIMP via nucleophilic substitution at the phosphorus atom by a surface oxygen, to produce isopropyl methyl phosphonate and gaseous propyl alcohol [Scheme 2b]. This is a very reasonable occurrence in view of the alkaline hydrolysis rates given in Table 1. At 373 K the alkaline hydrolysis rate of DIMP is comparable to the alkaline hydrolysis rate of DMMP at 295 K. Since DMMP adsorbs dissociatively at 295 K, it follows that this latter rate is an approximate measure of the dissociative adsorption threshold. (Admittedly, this assumes that the nucleophilic reactivity of the surface does not decrease upon heating to 373 K. This is a reasonable approximation in view of the limited dehydroxylation occurring at these temperatures [19].) The decomposition of the isopropyl methyl phosphonate proceeds further at 473 K by the surface catalyzed elimination of propene [Scheme 2b] to produce the hydroxy methyl phosphonate [Scheme 2c]. The mechanism indicated [Scheme 2b] for this transformation is only tentative and is similar to mechanisms proposed for the dehydration of alcohols [23]. On the other hand, the pyrolytic elimination of propene in liquid diisopropyl n-hexyl phosphonate, which begins above 480 K [21], may proceed as depicted in Scheme 3 analogously to pyrolytic eliminations of alkenes in carboxylic acid esters and xanthate esters [24].

Although the six-membered ring transition state is common to both Schemes 3 and 2b, it is impossible to carry over all the aspects of the former mechanism to the latter. Although base catalyzed elimination mechanisms are observed in the dephosphorylation of some phosphate esters, such mechanisms cannot be operative here since they would result in a methyl phosphonate anion rather than the hydroxy methyl phosphonate that is observed [7,25]. In addition, the decomposition mechanism shown [Scheme 2b] is much favored over mechanisms involving a nucleophilic attack at the phosphorus by lattice oxygen, as occurs in the dissociative adsorption mechanism (Scheme 1). These latter

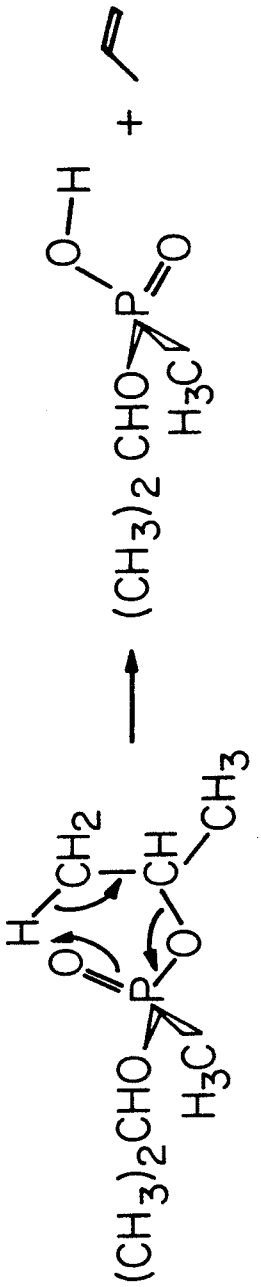

Scheme IV-3

mechanisms are improbable for the following two reasons. First, compared to the neutral phosphonate ester, the IMP adspecies now has more negative charge on the phosphorus which makes it a poorer electrophile [26]. For example, the alkaline hydrolysis of phosphonate esters only proceeds through formation of the monoester [27]. Second, because IMP is constrained by two points of attachment to the surface, it would be difficult for the phosphorus center to accommodate the trigonal-bypryamidal transition state needed for a bimolecular nucleophilic substitution. The hydroxy methyl phosphonate [Scheme 2c] persists on the surface until further dehydroxylation of the surface [Scheme 2c] produces a neighboring coordinately unsaturated aluminum [Scheme 2d]. The hydroxy methyl phosphonate then reacts with this site [Scheme 2d] to form a methyl phosphonate and a surface hydroxyl [Scheme 2e]. A direct reaction between a surface hydroxyl and the hydroxy methyl phosphonate would be unfavorable because of the relatively low acidity of the hydroxy methyl phosphonate proton ($pK_A \approx 7.9$ [28]), in comparison to surface hydroxyls on the partially dehydroxylated surface ($pK_A > 7.2$ [29]).

Decomposition of the MP adspecies is expected to occur only above 750 K, since aluminum phosphinate polymers do not decompose below this temperature [30]. However, this temperature regime was inaccessible due to the physical limitations of our experiments.

3.3 The Adsorption and Decomposition of DMMP

The identification of a probable mechanism for the decomposition of adsorbed DIMP was facilitated by some knowledge of the gaseous products of decomposition. For DMMP, this information is presently unavailable. Nonetheless, we will still be able to delineate substantially the possible decomposition mechanisms.

The dissociative adsorption and decomposition DMMP on aluminum oxide has been studied previously [1]. Like DIMP, the stable surface species resulting from the adsorption of DMMP at 673 K is the methyl phosphonate [1]. However, unlike dissociatively adsorbed DIMP, which shows significant signs of decomposition at 473 K and is virtually completely decomposed at 673 K, dissociatively adsorbed DMMP showed significant signs of decomposition beginning only at 573 K, and only 50% of the total adspecies population was estimated to consist of MP at 673 K [1].

Figure 2a is the tunneling spectrum of 1.0 Torr-s of DMMP adsorbed on the aluminum oxide surface at 573 K. Of particular significance is the near absence of a mode at 2440 cm^{-1} in Fig. 2a as compared with the spectrum of DIMP adsorbed under similar conditions [Fig. 1b]. Since this mode is characteristic of the hydroxy methyl phosphonate, this implies that this species is a much less stable intermediate in this case compared to the decomposition of DIMP. That the hydroxy methyl phosphonate is in fact present in the decomposition of DMMP is verified by the tunneling spectrum of an aluminum oxide surface that is exposed to 1.0 Torr-s of DMMP at 373 K, and then heated in vacuuo to 573 K [Fig. 2b]. Following this treatment, the hydroxy methyl phosphonate is clearly present on the surface, as evidenced by the considerable intensity of the mode at 2440 cm^{-1}.

Although the presence of the hydroxy methyl phosphonate is not surprising, it is somewhat surprising that there is a pronounced and reproducible difference between heating the dissociatively adsorbed species to its decomposition temperature versus adsorbing the DMMP at the decomposition temperature. Furthermore, aside from the absence of the 2440 cm^{-1} mode in Fig. 2a, there do not appear to be any significant differences between Figs. 2a and 2b, with the possible exception that the surface hydroxyl stretching mode is of

stronger intensity in the former than in the latter. Thus the alteration of the preparation procedure perturbs the final surface species distribution only slightly. Consequently, we would argue that the hydroxy methyl phosphonate in Fig. 2b was produced not by a completely new reaction pathway, but rather by a subtle perturbation in the already existing reaction pathway for the decomposition of DMMP, following adsorption directly on the surface at 573 K [Fig. 2a]. This leads to the conclusion that the hydroxy methyl phosphonate is a transient species in this latter reaction [Fig. 2a], and that the effect of the alternative preparation procedure [Fig. 2b] was to somehow quench the further decomposition of this species.

The homogeneous chemistry of phosphonate esters gives several important clues as to how the decomposition mechanism proceeds. As discussed earlier in connection with the decomposition of adsorbed DIMP, the phosphorus center of the dissociatively adsorbed DMMP will not be susceptible to nucleophilic substitution. However, unlike the isopropoxy moiety of dissociatively adsorbed DIMP, the methoxy moiety of dissociatively adsorbed DMMP cannot undergo facile elimination to form gaseous alkene. Therefore, the only reasonable possibility is for decomposition to proceed by nucleophilic substitution at the alkyl carbon of the ester moiety, as occurs in the hydrolysis of phosphonate esters under acidic conditions (see Section 3.1). Furthermore, this must be a bimolecular nucleophilic substitution since the methyl group of the ester moiety unfavorably forms a carbo-cation. This leads us to propose a mechanism for the decomposition of DMMP which is consistent with these observations (Scheme 4). Scheme 4a depicts the base catalyzed nucleophilic substitution by a lattice oxygen at the alkyl carbon center of the dissociatively adsorbed DMMP to form the hydroxy methyl phosphonate intermediate and a surface methoxide (Scheme 4b). The hydroxy phosphonate and methoxide eliminate rapidly to form gaseous methyl

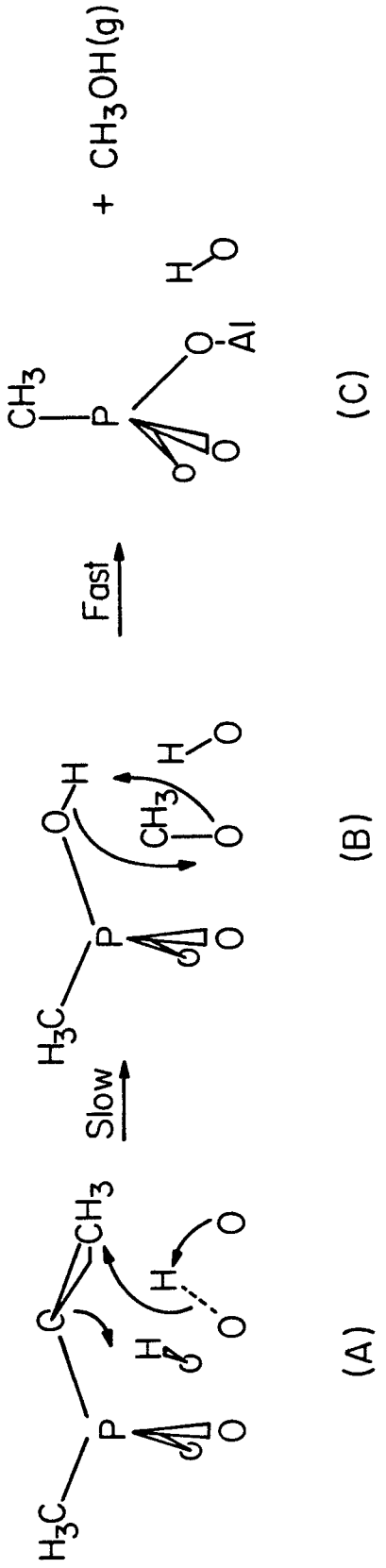

Scheme IV-4

alcohol and methyl phosphonate, as shown in Scheme 4c. This last step is tentative, but it is in accordance with the observation that additional hydrocarbons do not accumulate on the surface during the decomposition of adsorbed DMMP. At the decomposition temperature, the surface methoxide is unstable and would be oxidized to a formate. However, the formate so produced would be exceedingly difficult to remove from the surface and would therefore be indicated in the spectra. Since it is not, the reaction depicted in Scheme 4b seems to make the best sense. Data on the gaseous decomposition products could confirm this, but unfortunately they are currently unavailable. Nevertheless, we feel that Scheme 4 correctly shows an important feature of the decomposition in that it must proceed not by nucleophilic attack at the phosphorus but by nucleophilic attack at the methoxy carbon.

The Adsorption and Decomposition of DPMP

The tunneling spectra of diphenyl methyl phosphonate (DPMP) adsorbed on aluminum oxide at 295 K and heated to 373, 573 and 673 K are shown in Figs. 3a, b, c and d, respectively. The interpretation of these spectra is facilitated by recognizing the three majority surface species present: surface hydroxyls, adsorbed phenol and dissociatively adsorbed DPMP (i.e., phenyl methyl phosphonate). The adsorbed phenol is the byproduct of the dissociative adsorption of DPMP.

The relative surface coverages of these three species can be assessed independently from different regions of the tunneling spectrum. The surface hydroxyl coverage can be monitored by the peak at approximately 3630 cm^{-1} which is due to the (Al)O-H stretching vibration. The adsorption of phenol on thermally pretreated alumina powders was studied with infrared spectroscopy [31]. Adsorption between 420 and 573 K produced a surface phenoxide

coordinated to a surface aluminum [31]. A similar conclusion was reached concerning the nature of phenol adsorption at 295 K in a tunneling spectroscopic study [32]. The adsorption conditions and instrumental technique in the latter study are similar to those employed here. A comparison between the tunneling spectrum in Fig. 3a and the tunneling spectrum of adsorbed phenol in this previous work [32] indicates that the prominent low energy shoulder at approximately 2850 cm^{-1} in Fig. 3a is due to a surface phenoxide. The phenoxide of the phenyl methyl phosphonate will not contribute to this mode since each of its CH stretching modes should lie above 3000 cm^{-1}, in analogy with the spectrum of liquid phenol [32]. Finally, the mode at 2925 cm^{-1}, which is due to the $\nu_s[(P)CH_3]$ vibration, can be used to characterize the surface coverage of the phenyl methyl phosphonate. However, care must be taken in judging the intensity of this mode since it is partially superposed on the broad surface phenoxide mode appearing as a shoulder at 2850 cm^{-1}.

The tunneling spectra in Fig. 3 are consistent with these assignments. In going from the spectrum of DPMP adsorbed at 295 K [Fig. 3a] to the spectrum of DPMP adsorbed at 295 K and heated to 373 K [Fig. 3b], the relative intensities of all CH modes remain virtually unchanged (the absolute intensity difference between Figs. 3a and 3b is attributed to a difference in the initial adsorbate concentrations). This is consistent with the dissociative adsorption of DPMP at 295 K, because if there had been a large concentration of molecularly adsorbed DPMP on the surface at 295 K, the subsequent heating to 373 K would have caused some of this to desorb, or decompose, which would have then resulted in a change in the CH stretching mode intensities. Rather, only the hydroxyl mode is observed to decrease in intensity, probably due to the desorption of associatively bound water. The complete dissociative adsorption of DPMP is also in accord with the extremely high rates of homogeneous alkaline hydrolysis for

DPMP compared with DMMP, since DMMP adsorbs dissociatively, and the dissociative adsorption and homogeneous alkaline hydrolysis reactions may be mechanistically very similar.

In going from the spectrum of adsorbed DPMP heated to 373 K [Fig. 2b] to the spectrum of adsorbed DPMP heated to 573 K [Fig. 2c], the changes observed are due to increasing dehydroxylation caused by the higher temperature and to the desorption of some of the surface phenoxide as gaseous phenol, which accompanies this more extensive dehydroxylation. These changes are most clearly visible in terms of the decrease in the amplitude of the low energy shoulder at 2850 cm^{-1} in going from Fig. 3b to Fig. 3c. Since the intensity of this shoulder is proportional only to the surface phenoxide coverage, this coverage must be decreasing. However, the decrease in surface phenoxide coverage also causes all of the other phenyl-related modes to decrease in intensity, and this causes the overall spectrum to change shape somewhat. For example, the CH stretching modes at 3004 and 3055 cm^{-1} also decrease in intensity. However, since the latter is purely due to a phenyl vibration, it decreases more substantially than the former, which has a partly alkyl character. Nevertheless, all changes observed in going to the higher temperature can be related to either the desorption of the surface phenoxide as gaseous and/or further dehydroxylation.

These same trends persist in going to the spectrum of adsorbed DPMP heated to 673 K [Fig. 3d]. Specifically, the spectrum does not reflect the appearance of the methyl phosphonate, which would be evident from the appearance of a mode at 750 cm^{-1} that is not observed. In addition, the intensities in the 1300 to 1500 cm^{-1} spectral region are properly accounted for by assuming only the presence of phenyl methyl phosphonate. Thus it appears that the phenyl methyl phosphonate is stable on the surface at 673 K and does not decompose to the methyl phosphonate. This is consistent with the mechanisms that were proposed

earlier for the decomposition of adsorbed DIMP and adsorbed DMMP (Schemes 2 and 4). In analogy with these, the DPMP must necessarily decompose by nucleophilic substitution at the phenyl carbon. This is an unfavorable reaction, as discussed earlier in connection with the homogeneous hydrolysis of DPMP in acidic media (Section 3.1). Thus, the lack of reactivity of the phenyl methyl phosphonate is strong confirmation that decomposition of adsorbed phosphonate esters proceeds either by elimination (DIMP) or nucleophilic attack at the alkyl carbon of the ester (DMMP) resulting in C-O bond cleavage, rather than P-O bond cleavage.

4.0 Conclusions

This work represents important conceptual and instrumental achievements. Most previous studies employing tunneling spectroscopy to study chemisorption and surface reactions can be categorized as survey studies, where several different compounds are adsorbed at 295 K. Although important, this type of work represents only the first step in studying surface and catalytic chemistry, since much of this occurs at significantly higher temperatures. When considered as a whole with the previous study of DMMP [1], this study perhaps represents a milestone in the application of tunneling spectroscopy to study the chemistry of adsorption and reaction, because, unlike survey studies, we have focused in detail on the adsorption of one phosphonate ester, DMMP, over a wide temperature range, 200 to 673 K. This in turn has led to significant general conclusions concerning the chemistry of phosphonate esters on oxide surfaces. It was shown that the appropriate homogeneous reaction chemistry could explain the observed decomposition reactions of phosphonate esters on aluminum oxide. This is a consequence of localized bonding interactions that occur on oxide surfaces. Two important reactions were identified: (1) nucleophilic sub-

stitution at the phosphorus atom, and (2) nucleophilic substitution at the alkyl carbon of an alkoxy. The relative ease of C-O bond cleavage in isopropoxy, methoxy and phenoxy on the aluminum oxide was found to decrease in that order. Finally, these ideas were incorporated into mechanisms for surface reactions. It is hoped that this success with tunneling spectroscopy will stimulate further work with this promising vibrational spectroscopic technique.

References

1. M. K. Templeton and W. H. Weinberg, in preparation.

2. A. E. T. Kuiper, J. J. G. M. van Bokhoven and J. Medema, J. Catal. **43**, 154 (1976).

3. S. R. Landauer and H. N. Rydon, J. Chem. Soc. **1953**, 2224.

4. M. L. Honig and E. D. Weil, J. Org. Chem. **42**, 379 (1977).

5. H. E. Evans and W. H. Weinberg, Appl. Surface Sci. **5**, 258 (1980).

6. R. F. Hudson and L. Keay, J. Chem. Soc. **1956**, 2463.

7. R. F. Hudson, *Structure and Mechanism in Organo-Phosphorous Chemistry*, Academic Press, 1965, p. 260.

8. H. E. Evans and W. H. Weinberg, J. Chem. Phys. **71**, 1537 (1979).

9. A. V. Deo, T. T. Chuang and I. G. Dalla Lana, J. Phys. Chem. **75**, 234 (1971).

10. A. Bayman, P. K. Hansma and L. H. Gale, Surface Sci. **125**, 613 (1983).

11. B. I. Istomin, M. G. Voronkov and Yu. I. Sukhorukov, Zhurnal Obsch. Khim. **52**, 292 (1982).

12. E. K. Euranto, Ch. 11 in *The Chemistry of Carboxylic Acids and Esters*, S. Patai, Ed., John Wiley, 1969, p. 505.

13. A. Koivisto, Ann. Acad. Sci. Fennicae, Ser. AII, No. 73 (1956).

14. E. Tommila and S. Maltamo, Suomen Kemistilehtz **28B**, 118 (1955).

15. A. Skrabal and A. M. Hugetz, Monatsch. Chem. **47**, 17 (1926).

16. K. R. Adam, I. Lauder and V. R. Stimson, Australian J. Chem. **15**, 467 (1962).

17. C. M. Mikulski, N. M. Karayannis and L. L. Pytlewski, J. Inorg. Nucl. Chem. **36**,

971 (1974).

18. B. C. Lippens and J. J. Steggerda, Ch. 4 in *Physical and Chemical Aspects of Adsorbents and Catalysts*, B. G. Linsen, Ed., Academic Press, 1970, p. 171.

19. H. Knözinger and P. Ratnasamy, Catal. Rev. Sci. Eng. **17**, 31 (1978).

20. R. Cini, P. Colamarino, P. L. Orioli, L. S. Smith, P. R. Newman, H. D. Gillman and P. Nannelli, Inorg. Chem. **16**, 3223 (1977).

21. A. E. Canavan, B. F. Dowden and C. Eaborn, J. Chem. Soc. **1962**, 331.

22. B. Dupuy and C. Garrigou-Lagrange, J. Chimie Phys. **65**, 632 (1968).

23. W. H. Saunders and A. F. Cockerill, *Mechanisms of Elimination Reactions*, John Wiley, 1973, p. 262.

24. Ibid, p. 380.

25. A. Lapidot, D. Samuel and B. Silver, Chemistry and Industry **1963**, 468.

26. R. F. Hudson, *Structure and Mechanism in Organo-Phosphorus Chemistry*, Academic Press, 1965, p. 268.

27. H. Cristol, M. Levy and C. Marty, J. Organometallic Chem. **12**, 459 (1968).

28. J. Emsley and D. Hall, *The Chemistry of Phosphorus*, Harper and Row, 1976, p. 307.

29. K. Tanabe, in *Catalysis Science and Technology*, Vol. 2, J. R. Anderson, M. Boudart, Eds., Springer-Verlag, 1981, p. 232

30. E. E. Flagg and D. L. Schmidt, J. Polymer Sci. A-1 **8**, 1 (1970).

31. D. R. Taylor and K. H. Ludlum, J. Phys. Chem. **76**, 2882 (1972).

32. W. M. Bowser and W. H. Weinberg, Japan J. Appl. Phys., Suppl. 2, Pt. 2, 863 (1974).

33. A. Hidalgo and C. Otero, Spectro. Acta **16**, 528 (1960).

Figure Captions

Figure 1: Inelastic electron tunneling spectra resulting from the exposure of 1.0 Torr-s of diisopropyl methyl phosphonate to aluminum oxide at various temperatures: (a) 373 K, (b) 573 K and (c) 673 K.

Figure 2: (a) Inelastic electron tunneling spectrum resulting from the exposure of 1.0 Torr-s of dimethyl methyl phosphonate to aluminum oxide at 573. (b) Inelastic electron tunneling spectrum resulting from the exposure of 1.0 Torr-s of dimethyl methyl phosphonate to aluminum oxide at 373 K, followed by heating the surface in vacuuo to 573 K.

Figure 3: Inelastic electron tunneling spectra of aluminum oxide surfaces exposed to a 0.025 M solution of diphenyl methyl phosphonate at 295 K, and subsequently heated in vacuuo to various temperatures: (a) 295 K, (b) 373 K, (c) 573 K and (d) 673 K.

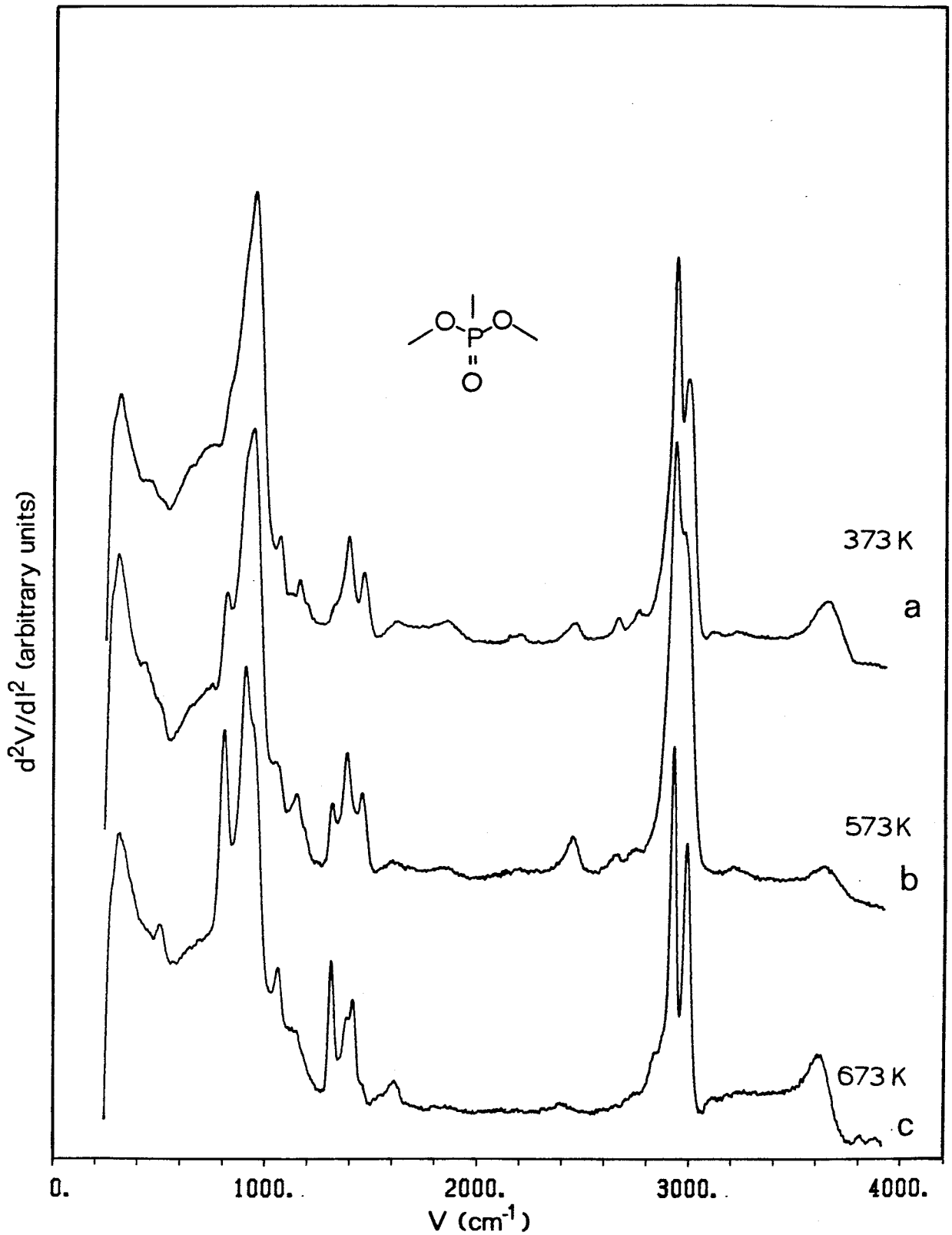
373 K
a
573 K
b
673 K
c
d^2V/dI^2 (arbitrary units)
0.
1000.
2000.
3000.
4000.
V (cm^{-1})

Figure IV-1

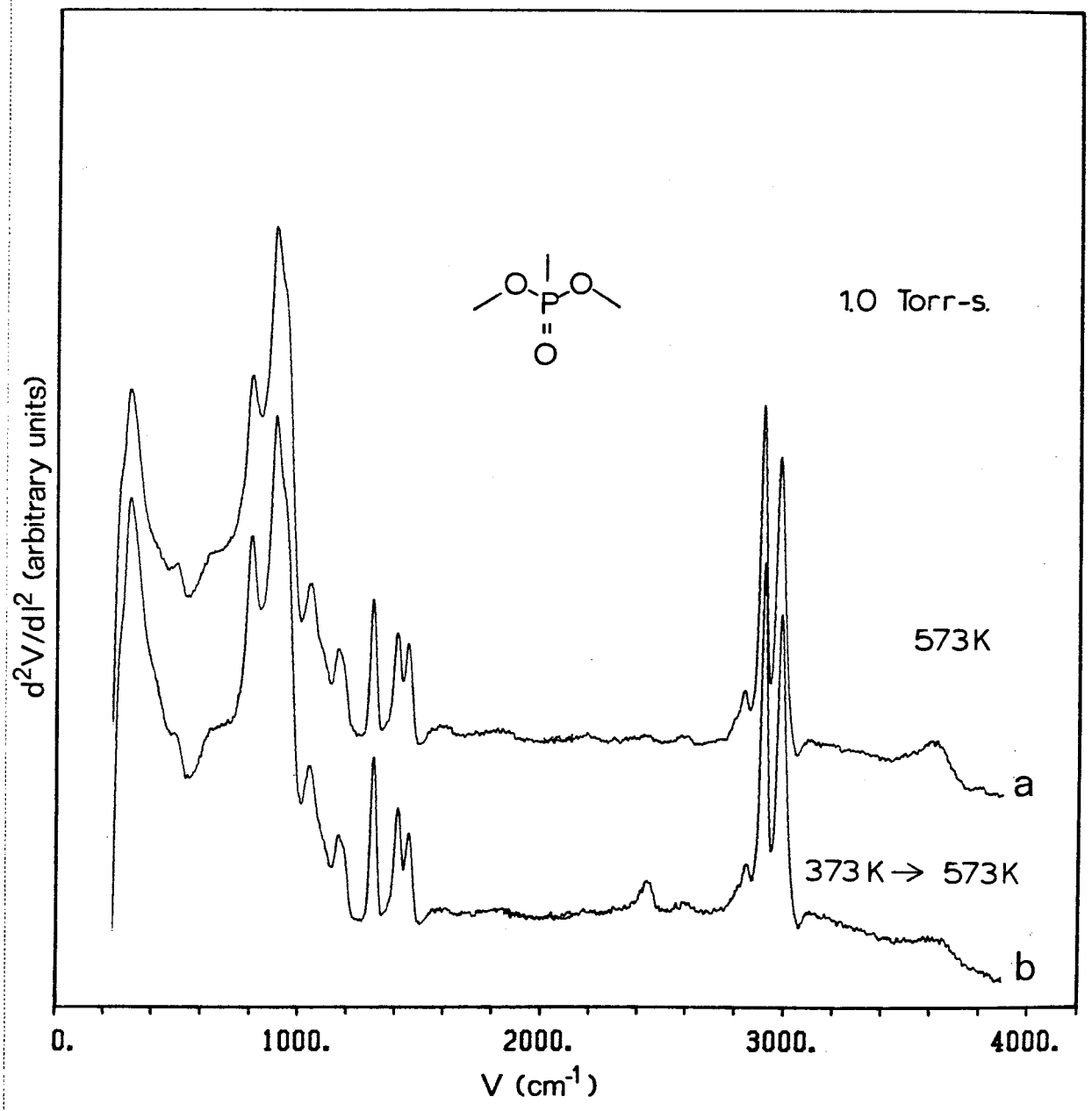
1.0 Torr-s.
573K
a
373K → 573K
b
d^2V/dl^2 (arbitrary units)
0.
1000.
2000.
3000.
4000.
V (cm^{-1})

Figure IV-2

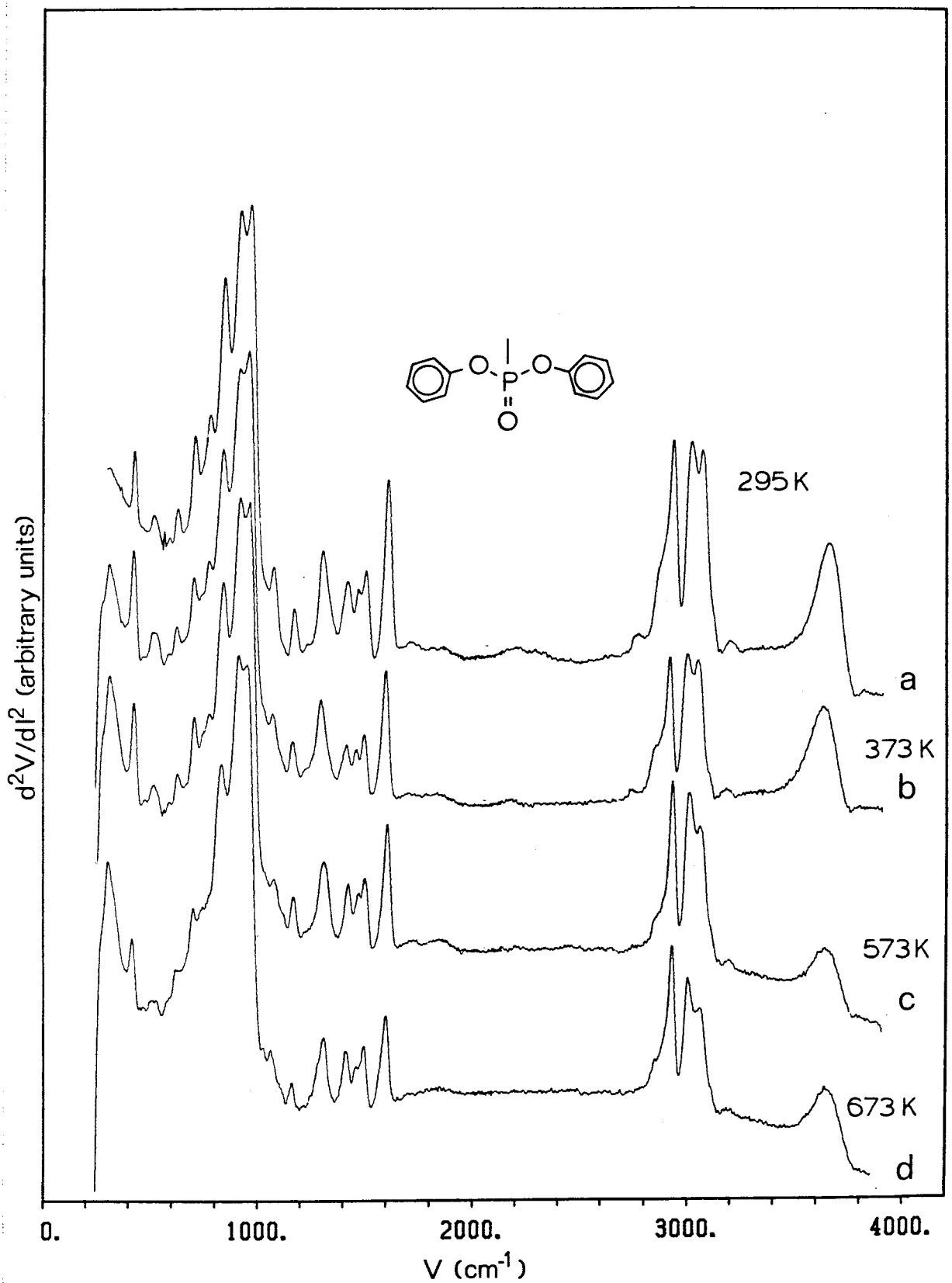
295 K
373 K
573 K
673 K
a
b
c
d
d^2V/dl^2 (arbitrary units)
0.
1000.
2000.
3000.
4000.
V (cm^{-1})

Figure IV-3

Table 1 [6]:

Alkaline Hydrolysis, 353 K			Acid Hydrolysis, 383 K	
Ester	E_a(kcal-mole^{-1})	A(l-mole^{-1}-sec^{-1})	E_a(kcal-mole^{-1})	A(sec^{-1})
$(CH_3)_2CHO(CH_3)P(O)$	14.9	2.24×10^5	25.6	1.83×10^{11}
$(CH_3O)_2(CH_3)P(O)$	13.5	1.75×10^7	26.7	4.23×10^{10}
$(C_6H_5O)_2(CH_3)P(O)$	12.4	4.66×10^7	26.0 (assumed)	2.62×10^8

Table 2 [12]:

Alkaline Hydrolysis 298 K			Acid Hydrolysis	
Ester	E_a(kcal-mole^{-1})	A(l-mole^{-1}-sec^{-1})	E_a(kcal-mole^{-1})	A(sec^{-1})
$(CH_3)COO\text{-}CH(CH_3)_2$ [13]	11.1	3.03×10^{6}		
$(CH_3)COO\text{-}CH_3$ [14]	12.2	1.43×10^{8}		
$(CH_3)COO\text{-}C_5H_6$ [15]	11.5 (assumed)	3.28×10^{8}		
$(CH_3)COO\text{-}C(CH_3)_3$ [16]			27.5	1.0×10^{16}

Chapter V:

Conclusions

1. Conclusions

The stable intermediates formed in several heterogeneous reactions with aluminum oxide films have been successfully identified with inelastic electron tunneling spectroscopy (IETS). These reactions included associative and dissociative adsorption, nucleophilic substitution, surface catalyzed elimination, hydrolysis, and hydrogenolysis. Primarily two adsorption systems were studied in great depth. These were the cyclopropane carboxylic acid/Al_2O_3 system and the phosphonate ester/Al_2O_3 system. Attesting to the versatility of tunneling spectroscopy, the adsorption temperature for these systems ranged between 200 and 700 K, and exposures ranged between 6×10^{-4} and 10 Torr-s. The extreme variation in adsorption conditions resulted in the formation of a wide range of stable adsorbate/surface complexes. For the identification of such complexes, the tunneling spectra of model compounds were heavily exploited.

Still much remains to be accomplished before tunneling spectroscopy will take a place among the more traditional techniques of infrared and Raman spectroscopies. The introduction of reasonably priced Fourrier transform infrared spectrometers into the market place has dealt a blow to IETS. Furthermore, the sensitivity of Raman spectroscopy has steadily developed to a point where adsorbates in submonolayer coverages on single crystal surfaces can now be characterized. Still, this thesis has emphasized the potential of IETS to probe the structure of adsorbed species. With few resources we have been able to greatly clarify several heterogeneous reactions on aluminum oxide films. And with continued attention, there is every reason to suspect that IETS may yet lead to startling discoveries in the field of surface chemistry.

Appendix A:

Computer Software for Spectral Analysis

A. Computer Software for Spectral Analysis

A.1 Introduction

IETSPLOT is a general purpose computer program for obtaining high quality plots and peak assignments for data analysis and/or publication. It is particularly suitable for processing digitally recorded IET spectral data. This appendix provides documentation on the use of IETSPLOT and related software.

In any spectroscopy, the importance of obtaining high quality facsimiles of spectral data cannot be overemphasized. In the area of qualitative shape comparison, the visual capabilities of the eye are astounding, and these capabilities are enhanced if data are displayed in a good graphical format (e.g., the background is removed). On the other hand, for precise quantification and reproducibility in the assignment of an energy abscissa to a spectral feature, it makes sense to move to a machine based algorithm. It was with these ideas in mind that IETSPLOT was developed. This computer program is particularly suitable for our tunneling research group since spectral acquisition is done by means of electronics controlled by a PDP 11/10 computer [1], and spectral data are stored in digital form on RT-11 formated floppy disks. Not only does use of the graphics software enhance the reproducibility of peak assignments and reduce publication time (when the plots are directed to a 1623 Zeta Plotter equipped with an India ink pen they need little further drafting for publication), but being relieved of the mundane, the researcher can focus more of his efforts on science.

A.2 Capabilities

The purpose of the IETSPLOT software is to provide important graphical and

analytical services in a flexible framework that allows the user to tailor the graphics to his needs and that accepts a wide latitude of input. Together these capabilities make the software into a versatile tool for handling a wide array of graphic/scientific problems.

The important services that are provided by the software are: (1) to produce high quality graphical output; (2) to assign an accurate energy abscissa based on calibration data and calculated corrections for finite modulation effects on the Pb superconducting band gap [2]; (3) to attempt removal of the characteristic sloping background of an IET spectrum; (4) to perform some smoothing of the data to remove gaussian white noise [3]; (5) to accurately locate significant spectral peaks along the energy ordinate and to intelligently print this energy assignment next to its associated peak; (6) and to accurately piece together several high resolution spectra covering different energy ranges to form one continuous spectrum covering the complete energy range.

The value of these services is significantly enhanced when they are incorporated into a flexible program structure. Instead of a specialized tool, they become a virtual "toolkit" for solving a multitude of different problems. Accordingly, the IETSPLOT software is designed to accept data in a large number of formats. It will take input in the form of either one single spectrum or as several spectra. It is capable of producing quality output with as little information about the data as possible. The concept of flexibility also means that the user has a high degree of control over the graphical output. The most apparent examples of this are that there are three distinct plotting formats available, that the amplitude scaling can be adjusted arbitrarily, and that the amount of background removed can also be adjusted.

A.3 Input/Output Structure and Organization of this Document

Data are processed on a VAX/VMS computer system (located at the Dreyfus-NSF Center for Theoretical Chemistry and denoted later as the "CRELLIN_VAX"). This machine is equipped with various input/output devices, including a flexible disk drive. Using the procedure described in Section A.7, POL files can be transferred with a minimum of effort to the user's hard disk area. Presumably these files would consist of the data to be plotted, and they are subsequently referred to as the "data set." The individual file will be referred to as the "RAW DATA" file since it contains the as yet unprocessed data.

Three programs constitute the software "package." Each program generates a slightly different graphical output. These differences are described in Section A.4.

The software acquires instructions and information about the data set through two channels. The primary channel is referred to as the INPUT FILE. This is a file that is created by the user and consists of a compact description of the data set, i.e., a list of the files that form the data set and the portions of the abscissa that each covers, etc.. The attributes of the INPUT FILE are discussed in detail in Section A.5, rules for its format are given in Section A.8, and an example INPUT FILE is shown in Section A.8.1.. Note that, although there are constraints on the format of the INPUT FILE, there are in general several ways to write an INPUT FILE for a given data set, and some ways work better than others.

The other channel of input to the program is by interactive means. The most useful aspects of the interactive channel are that it provides the means whereby the user can tailor the spectral amplitude and the amount of background removed from the spectrum. All of the interactive inputs are discussed

in Section A.6.

The output of the program consists of a file that contains graphic instruction for the Zeta Plotter. The program automatically creates and saves the file in the user's default directory with the same root name as the INPUT FILE, but with the type changed to "PLT." In order to obtain the actual plot, it is necessary that the user direct this file to the Zeta Plotter.

It is suggested that this document be assimilated by first reading Section A.4 through Section A.6, which describe respectively the important aspects of the code versions, the INPUT FILE, and the interactive input. During this time it may be helpful to study the example INPUT FILE in Section A.8.1, and to consult the format rules for INPUT FILE construction in Section A.8. The main purpose of Section A.7 through Section A.9 is to present the software documentation in a streamlined fashion with examples and in much the same way that one would go about making a plot from POL file(s), i.e., first transfer the files to the CRELLIN_VAX, then write the appropriate INPUT FILE, and then run the program. Accordingly, Section A.7 shows by example how to transfer POL files (RT-11) to the CRELLIN_VAX, Section A.8 gives the format rules for the INPUT FILE and an example input file, and Section A.9 shows an example of the interactive responses during an actual run of IETSPLOT and gives a line-by-line description of the input and output. Finally, for the ambitious reader, Section A.10 suggests several areas in which the software might be improved.

The purpose of this document is to supply the reader with the information that will enable him to use the software effectively. A familiarity with the VAX/VMS operating system such as one might get from the VAX/VMS Primer is assumed. It is not intended that this document provide a detailed account of the computational algorithms. Rather, these algorithms are dealt with only

when this understanding is necessary for using the software effectively.

A.4 Versions

There are three versions of the FORTRAN source code in common use. The original source code, IETSPLOT, generates an 11" x 17" plot (Fig. A-1) that is labeled with the experimental parameters, peak positions, and an axis calibrated in millivolts. Typically the Zeta plotter requires 10 minutes to generate such a figure. It is usually necessary to make several plots while iteratively adjusting the background removal parameter and the scaling parameter before an acceptable plot is made (the background removal parameter determines how much of the sloping background is removed, while the scaling parameter allows for adjustment of the amplitude scaling of the spectrum). This would be exceedingly time consuming using IETSPLOT alone. Hence, modified versions of this code were implemented to produce 8.5" x 11" plots as quickly as possible. This allows one to rapidly try different values of background removal and scaling parameters, as well as to check the validity of the INPUT FILE. One of these versions, named SMALPLOT, produces an 8.5" x 11" plot of the spectrum with only the axis labeled in millivolts. The other version, named SMALNUM, produces the same 8.5" x 11" plot as does SMALPLOT, but with the addition of the peak assignments printed on the plot (in wave numbers). Examples of the graphical output of IETSPLOT, SMALPLOT, and SMALNUM using the same data set are shown in Fig. A-1 through Fig. A-3, respectively. The author has found both SMALPLOT and SMALNUM to be exceedingly useful, and they have almost completely superseded the use of IETSPLOT. The 8.5" x 11" format is more convenient than the larger plot, and the plots are quickly made. In addition, the spectral features are still easily discernible on these small plots. Furthermore, since the peak amplitude runs perpendicular to the folds of the plotting paper, it is possible to scale the

peak amplitude arbitrarily large (Fig. A-4)and thus enhance small amplitude changes, something that is not possible with IETSPLOT. This also makes it possible to "build up" a series of spectra in parallel as might be efficacious for a publication figure (Fig. A-5). There is another factor that makes SMALNUM especially useful: although for the most part the source code differs little for the three versions in ways other than scaling parameters, it differs significantly for SMALNUM in the subroutines that assign and label the peaks. It suffices to say that SMALNUM does a much better job of assigning and separating genuine peaks from spurious noise than the other two programs (more about this later). Needless to say, the INPUT FILE setup for all three programs is identical. In the following sections IETSPLOT is referred to in the sense of a generic program; i.e., what is said there is also valid for SMALPLOT and SMALNUM.

A.5 The INPUT FILE

The INPUT FILE functions as the primary channel of communication between the IETSPLOT software and the user. Accordingly, the IETSPLOT software looks in the INPUT FILE to find essential information that it needs in order to construct the plot. By itself, however, the INPUT FILE is nothing more than a file that is created by the user in accordance with rules given in Section A.6. When broken down into its functional parts, the INPUT FILE is seen to consist of:(1) a heading section that contains a description of the data set (e.g., the chemical formula of the compound exposed to the aluminum oxide surface, the temperature of exposure and the extent of exposure); (2) a list of the names of the files that contain the RAW DATA spectra that are to appear in the plot; (3) the energy abscissas that are to be associated with each of these files; (4) and some optional information that indicates how the files in the list are to be scaled relative to one another. Thus the INPUT FILE can be thought of as a compact

description of the data set that is to be plotted.

However it is also necessary to realize that the *order* in which the information appears in the INPUT FILE is just as important as the *content* of the information. Although the formal rules for constructing the INPUT FILE are presented in Section A.8, because of the large latitude of flexibility that the software is designed to accommodate, there are often many different ways in which to construct an INPUT FILE for a given data set, some of which will produce less than optimal results. It is the purpose of this section to introduce the basic concepts governing the structure and content of the INPUT FILE as well as to point out the nuances that differentiate between an acceptable INPUT FILE and one that leads to a graphical disaster. When reading this section, it may be helpful to consult both the example INPUT FILE and the formal rules for the INPUT FILE given in Section A.8.1 and A.8, respectively

The INPUT FILE is designed to accommodate up to 9, 70 column lines of descriptive information about the data set. The user must specify on the first line of the input file, at the far left hand side, a number n between 1 and 9. Accordingly, n-1 lines following the first line will be reserved for descriptive information. This information then appears only on plots generated by IETSPLOT. More importantly, however, this information also serves to provide the user with documentation on the data set covered by that particular INPUT FILE. Furthermore, the lines are printed at a vertical spacing of every half line on the graphical output. Consequently, every other line provides for subscripting the previous line. If subscripts are not to be employed, then every other line should be left blank. Thus, there are in effect provisions for a maximum of 4 full lines of descriptive information with 4 lines of subscripts.

Following the optional descriptive information, the parameters used for the

plasma oxidation must be entered on one line. That is the plasma oxidation time, the oxidation voltage, and the oxidation current must appear on this line separated by commas. Again this information only appears on the plots generated by IETSPLOT.

For a high resolution study, it is better to take the tunneling spectrum in several parts. This allows one to optimize the lock-in amplifier sensitivity for best signal-to-noise and to change the modulation voltage over each portion of the spectrum. IETSPLOT is designed to take these individual pieces or "narrow scans" and recombine them into a plot covering the entire spectrum. For this purpose, a list of the names of the appropriate files that are to be "assembled" into one complete spectrum is included in the INPUT FILE following the oxidation parameter information. This list is subsequently referred to as the "file name" list. Note that these files consist of the POL files that have been transferred to the CRELLIN_VAX by the procedure given in Section A.7, and that each entry in the file name list actually consists of two lines of information for the first two entries of the file name list and three lines for each subsequent entry. The first line of the entry consists of the file name enclosed between grave accents (`). The second line contains numerical information about the file. This information consists of the following parameters separated by commas: (1) the number of data points in the file minus one; (2) the voltage, in millivolts, that corresponds to the second point in the file; (3) the voltage, in millivolts, that corresponds to the last point in the file; and (4) the root mean square of the modulation amplitude in millivolts. A third line is included only beginning with the third entry of the file name list. As explained in detail below, this line contains the value of the coefficient RELSCALE.

The number of files that IETSPLOT can combine into one spectrum is unlimited. The RAW DATA files are plotted sequentially in the order in which they

appear in the INPUT file. However, *under no circumstances is the second RAW DATA file plotted.* This is because the RAW DATA file appearing in the second position is attributed special importance; IETSPLOT uses this file as the CALIBRATION spectrum.

The CALIBRATION spectrum is used only for the purposes of determining the scaling factors that are to be applied to each of the "narrow scans." In order to fully understand the function of the CALIBRATION spectrum it is necessary to examine how IETSPLOT manages to recombine the "narrow scans" into a plot covering the entire spectrum. It is able to do this in two ways: (1) if a wide scan is available that covers most of the spectrum, IETSPLOT can use this wide scan to determine the appropriate relative scalings of the individual parts by matching the intensity of each individual part to its corresponding region of the wide scan; or, (2) IETSPLOT will take a value for the relative scaling that has been determined by the user and placed in the INPUT FILE. In other words, in case (1), IETSPLOT tries to determine the best values of the coefficients "RELSCALE" and "OFFSET" in the equation:

$$Y(v) = \text{RELSCALE} \times \text{YREF}(v) + \text{OFFSET} ,$$

where Y is one of the individual spectra, and YREF is a rescaled version of the the wide scan spectrum or CALIBRATION spectrum. In case (2), the coefficient "RELSCALE" is supplied by the user, and IETSPLOT need only determine OFFSET. Note that, in either case, a CALIBRATION spectrum must be supplied. However, in case (2), since only an offset needs to be determined, it is only necessary that the abscissas for YREF and Y overlap slightly (if they do not, an acceptable spectrum is usually still obtained because IETSPLOT "forces" an overlap). The temptation for option (1) lies in its convenience; nothing needs to be provided other than a list of the files containing the pieces of the digitally encoded spectrum and a wide spectral scan. However, it has been found in practice that the

method used by the code for determining the appropriate scalings for the individual sections (e.g.,coefficients RELSCALE and OFFSET) is only satisfactory, and that a much better match between contiguous portions of the spectrum can be obtained by providing a value for the relative scaling. This value is usually 1.0 because the sections of the spectrum usually are recorded with the same modulation voltage and on the same sensitivity scale of the lock-in. Note that when supplying a value for the fixed relative scaling, often the best result is obtained if the CALIBRATION file is identical to the first RAW DATA file; this works well when there is some overlap in the abscissas between this file and and the files that are to be subsequently plotted.

The optional relative scaling coefficient (RELSCALE) is to be included by itself on a third line for each entry in the file name list beyond three. If the value of the relative scaling coefficient is non-zero, then IETSPLOT will set RELSCALE equal to the supplied value. On the other hand, if zero is entered on the third line, then IETSPLOT will use the more complex scale matching alogrithm to determine a value for RELSCALE. It is unnecessary to supply a value of RELSCALE for the first entry in the file name list for the reason that the amplitude of this file forms the standard against which all other files are scaled. Moreover, the CALIBRATION file is automatically rescaled by the program so that the overlapping region between it and the first file of the file name list have the same amplitude. Consequently it is unnecessary to supply a value of RELSCALE for this file, the second file of the file name list. The RELSCALE coefficient that should be used with a file is simply equal to the factor that the amplitude of this file should be divided by so that its amplitude scaling is equivalent to the amplitude scaling for the first file of the file name list. For example, if the first file was recorded with a lock-in sensitivity of 1 microvolt, and the third file was recorded with a lock-in sensitivity of 2 microvolts, then the value of RELSCALE

used for the third file should be 0.5 .

Although in principle the files to be plotted can be listed in any order in the INPUT FILE, there are two important considerations that should be kept in mind when formulating the list. First IETSPLOT scales the plot to the plotting page based on the maximum amplitude range of the RAW DATA file that is plotted first (i.e., that appears first in the INPUT FILE). Second, as discussed later, the background removal routine works by taking a portion of the first RAW DATA file as the baseline. Unless some optional baseline region is specified, as discussed later, IETSPLOT uses the section of the first RAW DATA file that overlaps with the 210 to 330 millivolt region as the baseline region, and the effectiveness of the automatic background removal procedure is directly proportional to the linearity of this region.

A.6 Interactive Input

Interactive input provides a second channel through which the graphical output of IETSPLOT can be tailored. In particular, interactive inputs allow the user: (1) to specify which INPUT FILE is to be processed; (2) to specify the beginning of the region of the spectrum that the background subtraction algorithm is to key on; (2) to specify the end of the region of the spectrum that the background subtraction algorithm is to key on; (4) to adjust the amount of background that is to be subtracted from the spectrum; and (5) to adjust the amplitude scaling of the spectrum. In each case the program prompts the user for each of the five inputs by printing an appropriate message on the terminal. This section describes in detail the manner in which each of the interactive inputs affects the data processing. They are discussed in the sequential order in which they are needed as input to the program.

In order to begin processing of the spectral data, IETSPLOT needs to know

the name(s) of the RAW DATA files in which the spectral data are stored. Since this information is conveniently located in the INPUT FILE, IETSPLOT will ask for the name of this INPUT FILE by printing the message "INPUT SOURCE DATA FILE." In response to this, the user should enter the name of the INPUT FILE enclosed between grave accents (`). Note that the program automatically creates a file in which to store the graphical output. The name of this file consists of the type name of the INPUT FILE with "PLT" appended as the file type. Note that valid name for INPUT FILES cannot have type specifications, and that the name of the entered INPUT FILE must end with a period and contain only one period. For example, valid names are like `abc080.` but not like `abc080` ,`abc080.dat`, or `[mkt.sub1]abc080.`.

The second and third inputs to the program determine the starting and ending positions of the portion of the spectrum that is to be used to determine the baseline. The program then determines the appropriate linear function of energy that it must subtract from this baseline region to make this region flat. The same linear function of energy is then applied over the entire spectrum to remove the background. The idea behind the algorithm is that regions of the tunneling spectrum that are free from molecular vibrations are better regions for judging the extent of the sloping elastic contribution to the inelastic tunneling spectrum. IETSPLOT uses the region of the spectrum from 1690 cm^{-1} to 2660 cm^{-1}, since adsorbed, unlabelled hydrocarbons usually do not have vibrational modes there. However, if this region has large absorptions, an alternative region of the spectrum may be specified for determining of the baseline. This is simply done by inputing the starting and ending positions of the desired region in millivolts on separate lines, in response to the message "INPUT VSTART AND VEND." Otherwise, the *default option is invoked by returning zeros as input.* It should be noted that the region specified must overlap with the *first* RAW DATA

file specified in the INPUT FILE, as IETSPLOT uses *only the intersection of this region with the first* RAW DATA *file as the baseline region.*

With the fourth input to IETSPLOT, the amount of background removed from the spectrum can be adjusted. If in response to the message "INPUT ASCALE(=X)," zero is entered as input, IETSPLOT uses the computed value for background removal. Otherwise, the value of the non-zero input is used for the background subtraction. Usually IETSPLOT does a very good job at computing the amount of background that needs to be removed from the spectrum to make the baseline look flat. IETSPLOT prints out the computed value immediately before inquiring for the input. Usually adjustments of less than ten percent in this parameter will produce efficacious results. If the baseline still has *too much positive slope*, then the computed value *plus* a small amount is returned as input, and, conversely, for too much negative slope.

The fifth and last input to IETSPLOT allows the amplitude scaling of the spectrum to be adjusted. This feature is really only useful when using SMALPLOT and SMALNUM since the spectral amplitude runs perpendicular to the paper folds. Hence, if the spectrum is too large for one page, it is automatically continued onto the next page. In connection with these two programs this feature is useful for adjusting the relative scaling between two separate plots so that a comparison between relative amplitudes is facile. With IETSPLOT on the otherhand, if the spectral amplitude is too large, then plotter errors will result. *If zero is returned as input in response to the message "CHANGE YSCALE?," then the default scaling is enacted.* The default scaling adjusts the amplitude scale so that 130 percent of the maximum amplitude variation of the *first* spectrum to be plotted corresponds to the space allotted to the amplitude scale. The space allotted to the amplitude scale is 9.5 inches with IETSPLOT and 4.75 inches with SMALPLOT and SMALNUM. The default scaling represents an input of 1.3,

and in the case of SMALPLOT and SMALNUM produces plots that use only 4.75 inches of the available 8.5 inches in the 8.5" x 11" format. The parameter of 4.75 inches was chosen so that the plots from SMALPLOT and SMALNUM would be exact one-half scale replicas of plots generated by IETSPLOT. Nevertheless, one can get around this limitation simply by returning a number smaller than 1.3 as input for this parameter. Typically, values of 1.0, which correspond to making the maximum amplitude variation correspond to 100 percent of the of the available amplitude space, make super looking plots that show better detail.

A.7 Procedure for Transferring Files to the CRELLIN_VAX

As previously mentioned, the current measurement electronics for taking d^2V/dI^2 curves is interfaced to a PDP 11/10 digital computer, and spectra are recorded on flexible disk media under the POL operating system [5]. The IETSPLOT software resides on the CRELLIN_VAX. Therefore, to make use of this software, it is necessary to put the RAW DATA files recorded in the RT-11 format onto the CRELLIN_VAX in a form compatible for this computer. The availability of flexible disk drives directly connected to the CRELLIN_VAX and of DEC proprietary software for translating RT-11 format files to Files-11 structured files has facilitated this transfer. The following procedure is used to transfer files recorded on flexible disks under the POL operating system to the CRELLIN_VAX in Files-11 format. The left hand column contains user responses in lower case and operating system responses in upper case. In the right hand column are comments that explain each response.

$ allocate dy:	Allocate the flexible disk drive.
_DYA1: ALLOCATED	VAX responds that drive 1 has been allocated. Put the disk in the indicated drive.

$ mount/foreign/write dya1:	Now mount the disk.
%MOUNT-I-MOUNTED,	mounted on _DYA1:
$ run sys$system:fix	Run the file transfer utilities package
FLX>drb1:/rs/im:2=dy1:abc080.lda/rt/im:2[1]	Tell the VAX to transfer POL file abc080 to the default directory in image mode format putting a carriage return after every 2 16 bit bytes.
FLX> <ctrl>Y	When all files have been transferred in the above manner, exit from FLX.
$ dismount dya1:	Dismount the drive.
$ deallocate dya1:	Deallocate the drive.

A.8 INPUT FILE Format Description

The following describes the format structure necessary for the INPUT FILE. It may be helpful to refer to the example INPUT FILE in section A.8.1 while assimilating this material.

1. TITLCRD(1)
   FORMAT(A70)

   TITLCRD(1) - Total number of title cards. Values between 1 and 9 allowed. Must be left adjusted.

2. DO 2 I=2,TITLCRD(1)
   TITLCRD(I)
   FORMAT(A70)

   TITLCRD(I) - These title cards contain descriptive information about the data set. These cards only appear on the plots generated by IETSPLOT. Here the cards are *printed at half-line spacings*. Thus the odd cards (3,5,7,9) allow one to put subscripts on the even cards. If subscripts are not desired, the odd cards, up to the number specified in TITLCRD(1), should be left blank.

3. OXTIME,OXVOL,OXCUR
   FREE FORMAT

1 The ADAC System 1000 files need to be transferred in units of 4 16 bit bytes, since the data points in these files are recorded as I*4 numbers. Therefore substitute **im:4** for **im:2**.

OXTIME	-	Oxidation time in seconds.
OXVOL	-	Oxidation voltage in volts.
OXCUR	-	Oxidation current in milliamps.

4. DATFILE
FREE FORMAT

DATFILE	-	Name of the file containing the digitally encoded spectrum that is to be plotted first. Must be enclosed in quotation marks. IETSPLOT will determine how much baseline to subtract from the entire spectrum as well as match the spectrum amplitude to the page size from this spectrum. Therefore, when plotting two or more files, a judicious choice of the first file will save aggravation.

5. NDATA,VI,VF,VMOD
FREE FORMAT

NDATA	-	Number of points in the spectrum - 1.
VI	-	The voltage, in millivolts, which corresponds to the second point in the spectrum.
VF	-	The voltage, in millivolts, which corresponds to the last point in the spectrum.
VMOD	-	RMS value of the modulation voltage in millivolts.

6. CALIBNAME
FREE FORMAT
IF NONE THEN END

CALIBNAME	-	The calibration file name. If a calibration file is given, IETSPLOT will recognize that several files are to be joined to form one plot. The calibration file name should be the name of the digitally encoded spectrum that is to be used to match up the individual pieces of a composite plot (see 10. for exception).

7. NCDATA,CVI,CVF
FREE FORMAT

NCDATA	-	Number of data points in the calibration file - 1.
CVI	-	The voltage, in millivolts, which corresponds to the second point in the spectrum.
CVF	-	The voltage, in millivolts, which corresponds to the last point in the spectrum.

8. DATFILE
FREE FORMAT

DATFILE - Name of the file containing the digitally encoded spectrum that is to be plotted next. Must be enclosed in quotation marks.

9. NDATA,VI,VF,VMOD
FREE FORMAT

NDATA - Number of points in the spectrum - 1.
VI - The voltage, in millivolts, which corresponds to the second point in the spectrum.
VF - The voltage, in millivolts, which corresponds to the last point in the spectrum.
VMOD - RMS value of the modulation voltage in millivolts.

10. RELSCALE
FREE FORMAT

RELSCALE - The relative scaling between this file and the Calibration file if using the fixed relative scaling option. IF RELSCALE is set equal to zero, then IETSPLOT will determine, to the best of its ability, the appropriate relative scaling for this file.

11. IF MORE THEN GO TO 8
ELSE END

A.8.1 Example INPUT FILE

The following INPUT FILE was used in conjunction with IETSPLOT, SMALPLOT, and SMALNUM to generate Fig. A-1 through Fig. A-3, respectively.

```
6
Adsorbate          Exposure          Temperature

(CH O) (PO)CH   0.25 Torr-s      295 K
   3  2      3
fab 8/26/82     mes 8/27/82     33.153 ohms
   100.,    1100.,   16.
'[mkt.red3]dlv080.lda;1'
  1199,   249.727,   484.17,   1.5
'[mkt.red3]dlv080.lda;1'
  1199,   249.727,   484.17
'[mkt.red3]dlx080.lda;1'
  1199,   29.357,   263.851,   1.5
  1.0
```

A.9 Example Interactive Execution of SMALPLOT

The following is an example of an interactive run of SMALPLOT. The file listed above is used as the INPUT FILE. Below, it is referred to as the file named 295ep25hr. The plot generated is shown in Fig. A-4. The user's input is underlined. The line numbers on the far left refer to the comments given below the sample run.

```
 1 $ run SMALPLOT
 2 INPUT SOURCE DATA FILE
 3 '295ep25hr.'<cr>
 4 INPUT VSTART & VEND
 5 0<cr>
 6 0<cr>
 7 OUTPUT SUM FROM TSCHEBYSHEV:     333.5932
 8 INPUT ASCALE (= 8.315394
 9 7.7<cr>
10 7.700000            0
11 CHANGE YSCALE ? (EXPAND DEF= 1.3)
12 0.65<cr>
13      1199    0.1956953      0.1956953      249.7270      484.1700
14  0.9999842       2.5952315E-2
15 BASELINE INTEGRAL & NP20MV
16  -483.3814            102
17 DET BASELINE INTEG MIN  & MAX PEAK HEIGHT
18   0.733244E+03       0.379996E+04
19 NUM  & NSIG
20                30          3
21                73    0.1956953      0.1957379      249.7270      263.8171
22 BASELINE INTEGRAL & NP20MV
23   188.0067            102
24 DET BASELINE INTEG MIN  & MAX PEAK HEIGHT
25   0.737618E+03       0.227865E+04
26 NUM  & NSIG
27                29          15
```

A.9.1 Comments on the Interactive Run

1. Run SMALPLOT.

2. Program asks for the name of the INPUT FILE.

3. The name of the INPUT FILE is entered. It must be enclosed in single quotes.

4. Program asks for the starting point and ending point, in millivolts, of the region that is to be used for the baseline. Note that the starting point and

ending point are to be input on separate lines.

5. Zero is entered, so the default value of the starting point is used.

6. Zero is entered, so the default value of the ending point is used.

7. Diagnostic output from TSCHEBYSHEV subroutine.

8. Program asks whether ASCALE is to be changed and prints the computed value of ASCALE. ASCALE is the amount of amplitude per millivolt to be removed from the raw spectrum.

9. A new value of ASCALE is entered (7.7). Had the user not wished to change ASCALE, '0' would have been entered.

10. The new value of ASCALE is printed.

11. Program asks whether YSCALE is to be changed and prints the default value of YSCALE (1.3). YSCALE times the maximum amplitude variation in the first spectrum is equal to the space, in inches, allocated for the ordinate.

12. A value of 0.65 is returned for the amplitude scaling. This makes the spectral amplitude larger than the space allotted, but this is allowable since the space allocated for the ordinate is only 4.75 inches of the full 8.5 inch page. If 0 were entered as input, the default scaling of 1.3 would have been effected.

13. Diagnostic output from INTERPOL subroutine.

14. Variables 'C' and 'E' are printed. These correspond respectively to the scaling and offset that need to be applied to the CALIBRATION SPECTRUM to match it to the FIRST SPECTRUM. In this case, since the two spectra are identical, ideally C and E should be 1.0 and 0.0, and in fact they are close to these values.

15. Diagnostic output from BASELINE subroutine.

16. Diagnostic output from BASELINE subroutine.

17. Diagnostic output from BASELINE subroutine.

18. Diagnostic output from BASELINE subroutine.

19. Diagnostic output from SORTPEAK subroutine. The SORTPEAK subroutine determines which of the peaks in the spectrum should be labeled. The total number of peaks located is given by the variable NUM, while the number of these peaks that are "significant" is given by the variable NSIG.

20. Diagnostic output from SORTPEAK subroutine: the variables NUM and NSIG are printed. Note that only 3 of the 30 peaks have been judged to be suitable for labeling.

21. - 27. The printed output repeats itself from line 11, only this time applied to the second file to be plotted.

A.10 Suggested Improvements

A number of simple modifications would enhance the utility of these programs. The peak discrimination algorithm is one area where important contributions could be made. Currently, two rather crude tests are used to determine the "significance" of a peak, e.g., whether it should be labelled. These tests are applied by the peak sorting subroutine (SORTPEAK) to the list of peaks determined by the peak location subroutine (PEAKLOC). A peak is significant if: (a) the height of the peak is 10 percent above the baseline, and (b) the absolute value of the second derivative is sufficiently high when smoothed by a 16 point fit to a cubic polynomial. Because both of these methods are not based on evaluating the local signal to noise, they are rather crude. Although these methods perform sufficiently well, it is suggested that the discrimination routine be replaced by a method that truly reflects the statistical significance of a peak, such as an appropriate test of the local autocorrelation function.

It is somewhat unfortunate that SMALPLOT and SMALNUM do not print any of the title card information or the interactive plotting parameters on the plot, since the user eventually ends up adding this himself. Initially the purpose of this was to minimize the time necessary for the Zeta Plotter to make the plot. It turns out that it would take a negligible additional amount of time to print this information with the plotter operating at full speed.

The quality of ink transfer to the page could also be improved by reducing the plotting speed during tracing of the spectrum. This is an especially attractive proposal since this could be done without increasing the time required to make the plot. This is possible because the computer must transfer the plotting information to the plotter in several blocks. When plotting at high speed, the plotter manages to finish printing out the entire block and has to wait inactively for subsequent blocks of information from the computer.

More extensive modifications can also be suggested. The ideas behind many of these modifications are intrinsic to the question, "What is the best way to manipulate and use graphical data?" Complex questions such as this have no unique answers. The author's own ideas of how to optimize the capabilities of graphics software have changed dramatically during the course of implementing and improving these programs. Initially, it was felt that *the machine should and could do everything*. Consequently, the program was designed to "think for itself" and get by with the very least amount of input from the user (initially none). In some cases this was quite successful, as for example in the peak labelling subroutines, where the program does a reasonable job of making the peak assignments. However, in other cases, such as the algorithms for determining both the relative scaling and the offset, this concept was not effective; without going to unreasonable lengths, the code was just incapable of accurately determining the scaling parameters by itself. Consequently this led to substituting

into the program a routine that would use a small amount of user input. So the author gradually came to the conclusion that the way to maximize the usefulness of computer graphics is to strive for that optimum where both man and machine work together.

The author has seen some excellent interactive software for looking at gas chromatography spectra. This makes use of a low resolution graphics terminal for "reviewing" the spectrum. Such an idea might be implemented on a VT-100 with only a modicum of effort. However, most of the major modifications that are envisioned would involve extensive rewrites of the IETSPLOT software, and, in point of fact, it would probably be easier for a software designer who was unfamiliar with this code to start from scratch.

References

[1] B. F. Lewis, M. Mossesman, W. H. Weinberg, Surf. Sci., **41**, 142 (1974).; W. M. Bowser, PhD Thesis, California Institute of Technology, Pasadena, CA, 1980.

[2] J. Kirtley, P. K. Hansma, Phys. Rev. B, **13**, 2910 (1976).

[3] A. Savitzky, M. J. E. Golay, Analyt. Chem., **36**, 1627 (1964).

[4] J. L. Taylor, PhD Thesis, California Institute of Technology, Pasadena, Ca, 1978.

Figure Captions

Fig. A-1 This Figure was made with IETSPLOT using the INPUT FILE shown in the text, and an ASCALE of 7.7 . It is shown reduced by 75 percent.

Fig. A-2 This Figure was made with SMALPLOT using the INPUT FILE shown in the text, and an ASCALE of 7.7 . It is shown at full scale.

Fig. A-3 This Figure was made with SMALNUM using the INPUT FILE shown in the text, and an ASCALE of 7.7 . It is shown at full scale.

Fig. A-4 This Figure demonstrates how it is possible to greatly expand the amplitude scaling with SMALPLOT (or SMALNUM). It was made with SMALPLOT using the INPUT FILE shown in the text, an ASCALE of 7.7, and a YEXPAND of 0.65 . It is shown at reduced scale.

Fig. A-5 With SMALNUM it is possible to build up a series of spectra, as was done to obtain this Figure.

Fig. A-6 Through A-19 list the VAX/VMS Fortran IV source code for IETSPLOT.

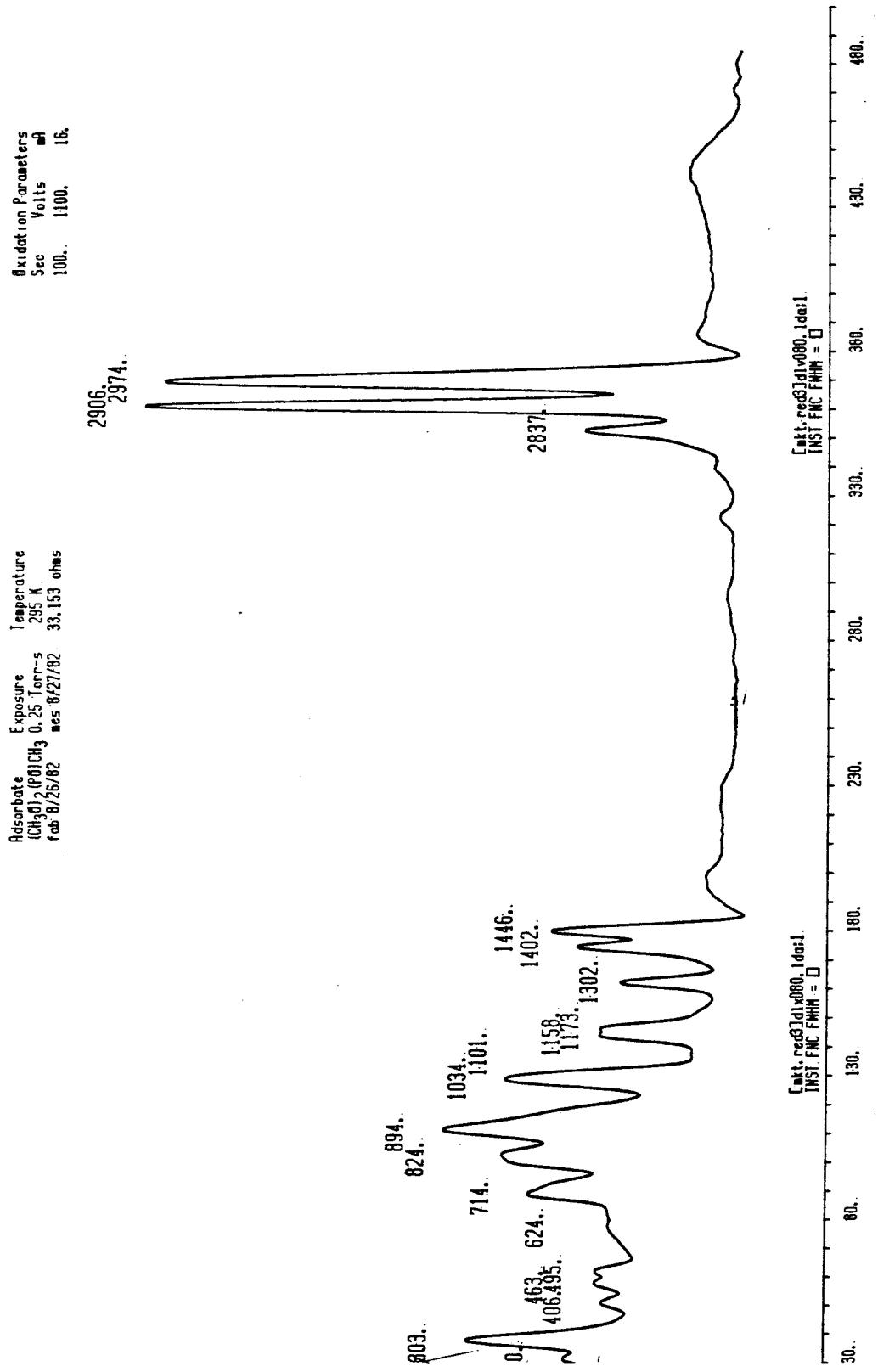
Adsorbate
(CH3O)3(PO)CH3
fab 8/26/02
Exposure
0.25 Torr-s
mes 8/27/02
Temperature
295 K
33.153 ohms
Oxidation Parameters
Sec Volts mA
100. 1100. 16.
2906.
2974.
2837.
1446.
1402.
1302.
1158.
1173.
1101.
1034.
894.
824.
714.
624.
495.
463.
406.
803.
0.
Cakt.red3ld1x080_1da:1
INST FNC FWHM = 0
Cakt.red3ld1y080_1da:1
INST FNC FWHM = 0
30.
80.
130.
180.
230.
280.
330.
380.
430.
480.

Figure A-1

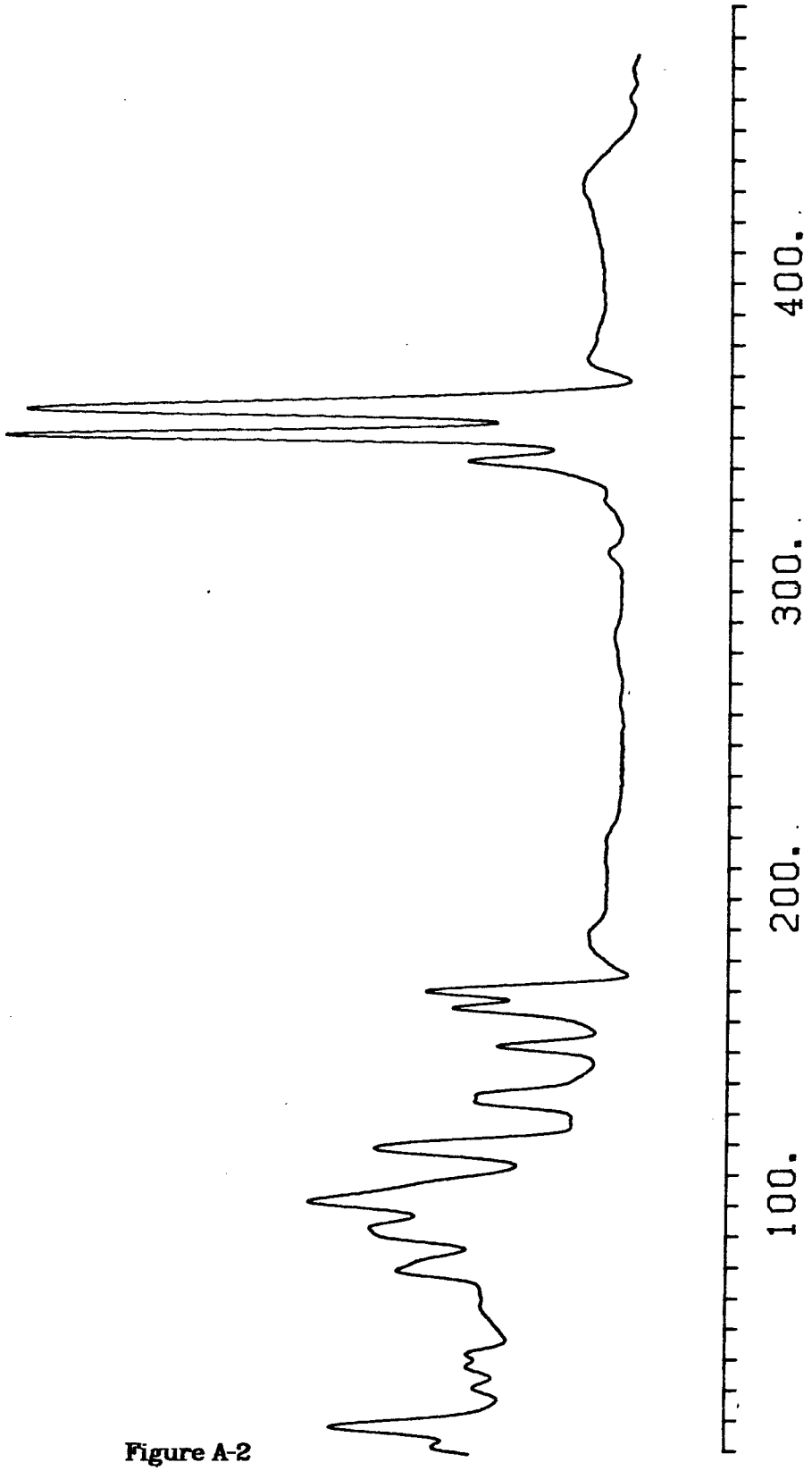

Figure A-2

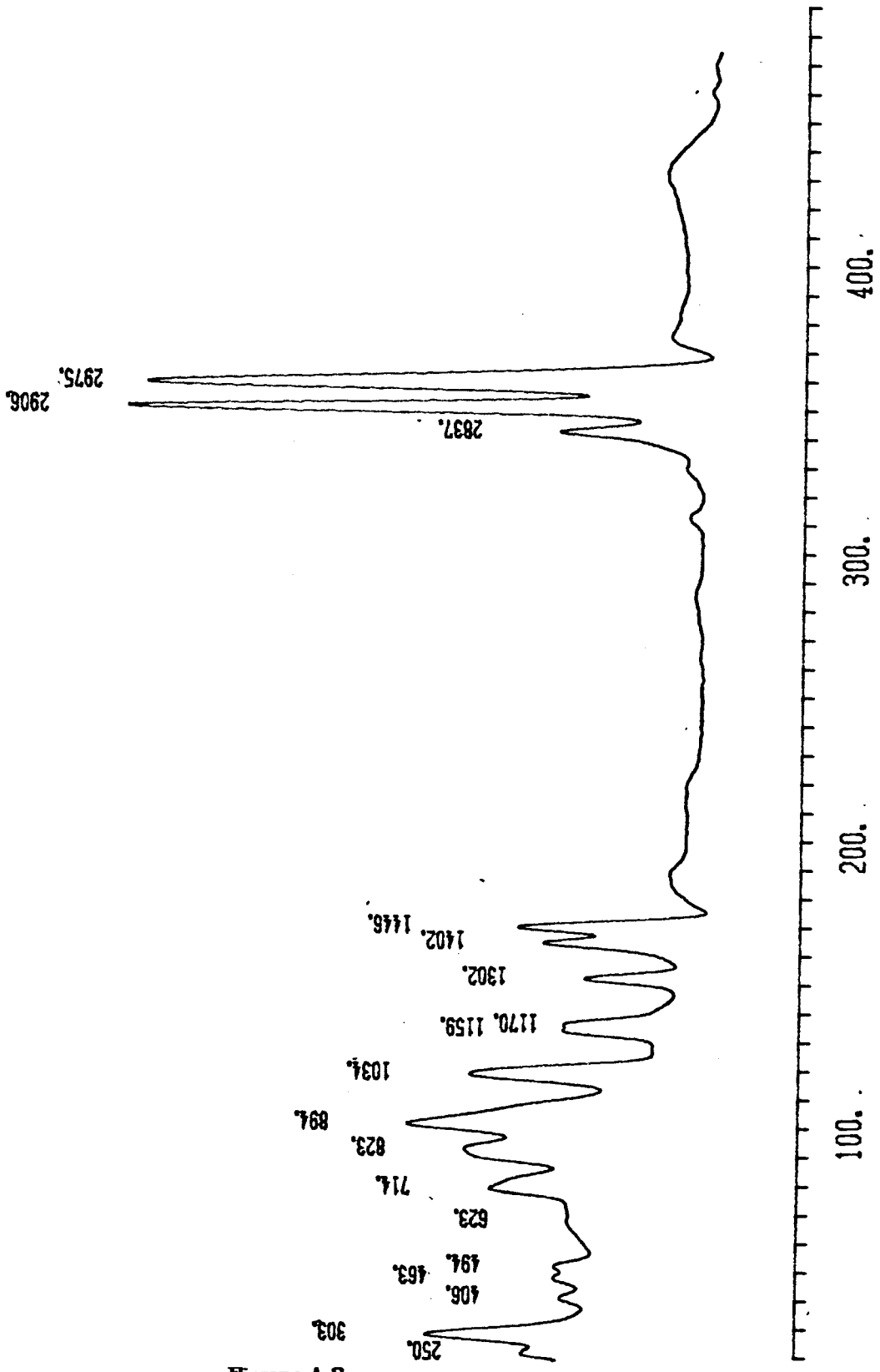
2975.
2906.
2837.
1446.
1402.
1302.
1170.
1159.
1034.
894.
823.
714.
623.
494.
463.
406.
303.
250.
100.
200.
300.
400.

Figure A-3

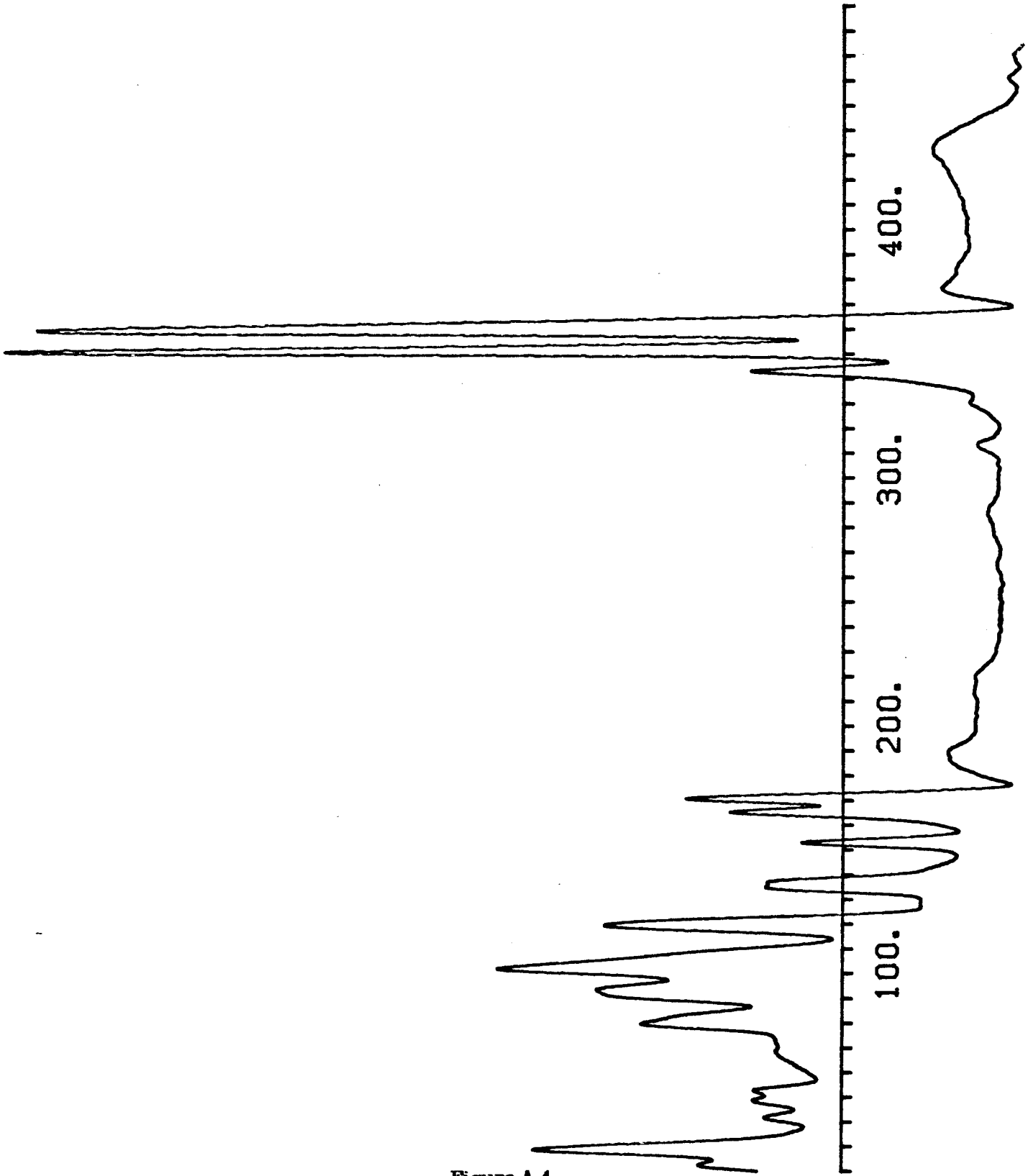

Figure A-4

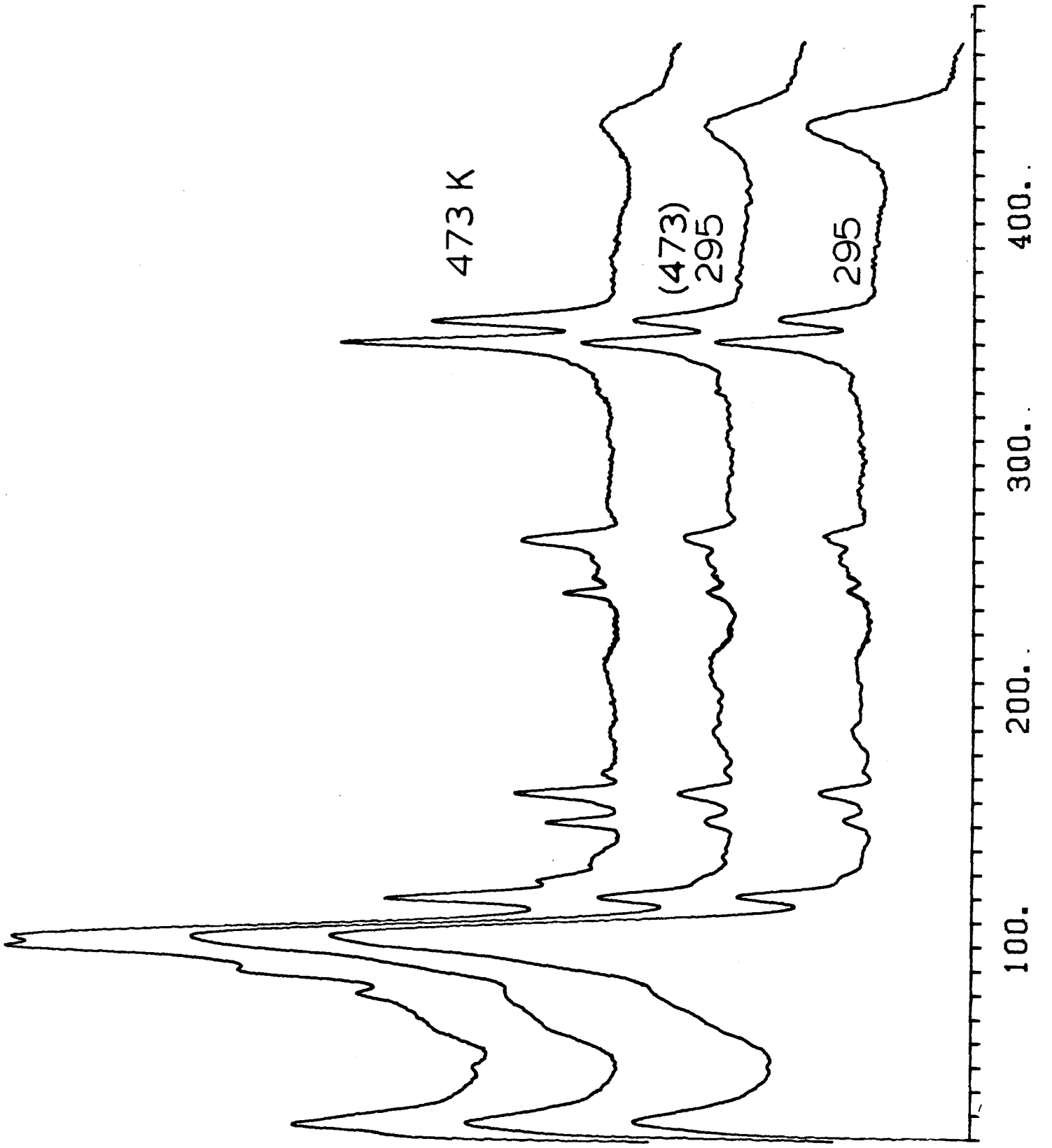

Figure A-5

```
      PARAMETER XSCALE=10.,YSCALE=4.75, VBEGIN=30.0,MVPERIN=55.8
      CHARACTER*30 FNAME,PLOTFILE*35,TITLCRD(9)*70,DATFILE,CALIBNAME
      DIMENSION IFNAME(1),INTSTR(17)
      DOUBLE PRECISION SUM
      DIMENSION X(2010),Y(2010),YS(2010),YD(2010),YBR(2010)
      DIMENSION XPS(100),YPS(100),VXPEAK(100)
      DIMENSION YCALIB(2010),YITRP(2010),XCALIB(2010),XB(2010)
      COMMON /LABARR/XPL(100),YPL(100),AMPVEC(100)
      COMMON /LABDAT/XSPACE,YSPACE
      COMMON /SCALEDAT/EXPAND
C
C          ******* written by MICHAEL K TEMPLETON  ******
C      *******  COPYRIGHT 1984 by MICHAEL K TEMPLETON  ********
C      *******          all rights reserved             ********
C
C     ------------------------------------------------------------
C               ****  inquire TTY for input file  ****
C
      PRINT *, 'INPUT SORCE DATA FILE'
      READ *,FNAME
C
C              create name for plot file
      DO 30 I=1,30
   30 IF(ICHAR(FNAME(I:I)) .EQ. 46 .AND.
     & ICHAR(FNAME(I+1:I+1)) .EQ. 32) GO TO 40
   40 PLOTFILE(1:I-1)= FNAME(1:I-1)
      PLOTFILE(I:I+3)= '.PLT'
C               and open plot file
      OPEN(NAME=PLOTFILE,UNIT=10,TYPE='NEW')
C             now open file with spectra file data
      OPEN(UNIT=8,NAME=FNAME,TYPE='OLD')
C
C              first read in TITLE CARD
      READ (8,22) TITLCRD(1)
   22 FORMAT(A70)
C                  ** now determine how many title cards and read them in  **
      IF (48 .LE. ICHAR(TITLCRD(1)(1:1)) .LE. 57 ) THEN
C
      NCARD = ICHAR(TITLCRD(1)(1:1)) - 48
      DO 23 I= 2,NCARD
   23 READ (8,22) TITLCRD(I)
C             now read in oxidation parameters
      READ (8,*) OXTIME,OXVOL,OXCUR

      ELSE

C             ** otherwise get critical data in obsolete file type **
C             now read in experimental parameters
      READ (8,*) TEMP,EXPSUR,OXTIME,OXVOL,OXCUR
C
      END IF
C
C              read in data file name
      READ (8,*) DATFILE
C               and parameters associated with this file
      READ (8,*) NDATA,VI,VF,VMOD
C           PROGRAM MAIN BODY
C***************************************************
C
C
      CALL FILEREAD(NDATA,DATFILE,Y)
      CALL ABSCISSA(NDATA,VI,VF,X,VINC)
      CALL SMOOTH9PTCUBIC(NDATA,Y,YS)
C
C                   best background subtraction if obtained if
C                    the spectral region is restricted !!

C                     therefore calc. starting and ending subscripts
      PRINT *, 'INPUT VSTART & VEND'
      READ *,VSTART,VEND
      IF(VSTART .EQ. 0.0)  VSTART= 210.
      IF (VEND .EQ. 0.0)  VEND= 330.
      ISTART= MAX(1.,(VSTART-X(1))/VINC + 1)
      IEND= MIN(FLOAT(NDATA),(VEND-X(1))/VINC + 1)
```

Figure A-6

```
      CALL TSCHEBYSHEV(IEND,YS,YBR,ISTART,SUM)
C           ASCALE and XZERO param for later use in X subratction
      ASCALE= 2*SUM/(X(IEND)-X(ISTART))
      PRINT *, 'INPUT ASCALE (=',ASCALE
      READ *,ASCALENEW
      IF(ASCALENEW .NE. Ø.Ø)  ASCALE= ASCALENEW
      PRINT *,ASCALE,NEWASCALE
      PRINT *,'CHANGE YSCALE ? (EXPAND DEF= 1.3)
      READ *, EXPAND
      IF(EXPAND .EQ. Ø.Ø) EXPAND= 1.3
      XZERO= .5*(X(INT((IEND-ISTART)/2.+1))+
     & X(NINT((IEND-ISTART)/2.+1.Ø5)))
C             now implement background removal
      CALL ARESCALE(NDATA,X,YS,YBR,XZERO,ASCALE,1.,Ø.)
C
C            *** QUERY MULTIPLE FILE PLOT ? **
C                  if no more data, skip calibration section by
C                    traping to 6Ø5 and ploting YBR - then to PLOT LEGENDS
C
C
C                     if a CALIBRATION spectra is not used,we must be
C                     sure that YBR has scaling factors when we follow trap
      CALL SCALE(NDATA,X,YBR,VBEGIN,MVPERIN,YUNPIN,YMIN,YMAX,Ø.)
C
      READ (8,*,END=6Ø5) CALIBNAME
      READ (8,*) NCDATA,CVI,CVF
C                 this wll be calib file data
C
C
C                *** now that we have YBR calculate YCALIB
C
      CALL FILEREAD(NCDATA,CALIBNAME,YCALIB)
      CALL ABSCISSA(NCDATA,CVI,CVF,XCALIB,CVINC)
C
      CALL OVERLAP(X(1),X(NDATA),XCALIB(1),XCALIB(NCDATA),
     & ALOVER,AHOVER)
C
C
C              now generate interpolation file.
C                    File that limits start of overlap will be reference.
C                      Now which file do we interpolate with?
      IF(ALOVER .EQ. XCALIB(1)) THEN
      CALL INTERPOL(ALOVER,INT((AHOVER-ALOVER)/CVINC)*CVINC
     & +ALOVER,CVINC,VINC,X,YS,YITRP,NPTS)
      CALL MATCH3(NPTS,YCALIB,YITRP,INT(.1*NPTS),C,E)
C
      ELSE
C
      CALL INTERPOL(ALOVER,INT((AHOVER-ALOVER)/VINC)*VINC+ALOVER,
     & VINC,CVINC,XCALIB,YCALIB,YITRP,NPTS)
      CALL MATCH3(NPTS,YITRP,YS,INT(.1*NPTS),C,E)
C
      END IF
C
      PRINT *, C, E
      CALL RESCALE(NDATA,XCALIB,YCALIB,XZERO,ASCALE,1/C,-E/C)
      CALL SCALE(NCDATA,XCALIB,YCALIB,VBEGIN,MVPERIN,YUNPIN,
     & YMIN,YMAX,Ø.)
      CALL SCALE(NDATA,X,YBR,VBEGIN,MVPERIN,YUNPIN,YMIN,YMAX,1.)
 6Ø5  CALL PEAKLOC(NDATA,YBR,X,VXPEAK,NUM)
      CALL BASELINE(VI,VF,VINC,YBR,YMIN,BSINMN,YMAX1)
      CALL SORTPEAK(VXPEAK,NUM,XPS,NSIG,YBR,VINC,VI,BSINMN,
     & YMAX1)
      CALL LABELPOS(YBR,XPS,NSIG,
     & YUNPIN,YMIN,MVPERIN,VBEGIN,VI,VINC)
C
C
C                          now plot out data
      CALL PLOTS(53,Ø,1Ø)
      CALL ORIGIN(.5,1Ø.,1)
      CALL PLOTDATA(NDATA,X,YBR,NSIG,XPS,YSCALE,MVPERIN,
     & VBEGIN,VF,DATFILE,VMOD)
```

Figure A-7

```
C
C                       now get data for next file (other wise trap to 61Ø)
C                       (first store 1st spectrum parameters for fixed
C                          relative scale option)
      NRDATA= NDATA
      RVI= VI
      RVF= VF
      RVINC= VINC
C
      READ(8,*,END=61Ø) DATFILE
      READ (8,*) NDATA,VI,VF,VMOD
C                  option for fixed rescaling is invoked when RELSCALE is read
C                       first initialize RELSCALE to zero (trap value), so
C                       execution flows properly when RELSCALE is not available

      RELSCALE= Ø.Ø
      READ(8,*,END=41Ø) RELSCALE
C                        with fixed relative scaling, use overlap of spectra to
C                        to fix baseline (offset). Therefor exchange YCALIB
C                        with YBR
C                       But first change ncdata to ndata etc.
      NCDATA= NRDATA
      CVI= RVI
      CVF= RVF
      CVINC= RVINC
      DO 4Ø5 I= 1,NCDATA
      XCALIB(I)= X(I)
  4Ø5 YCALIB(I)= YBR(I)
C                     initialize C so MATCH3 works properly w/wo rel scaling
C                   Subroutine Match3 will either find slope & baseline, or
C                        just baseline if a RESCALE value has been supplied
C                          (e.g. C .ne. Ø).
      C= RELSCALE
  41Ø CONTINUE
      IF(RELSCALE .EQ. Ø.Ø) C= Ø.Ø

C                       remove x comp from YCALIB
      CALL RESCALE(NCDATA,XCALIB,YCALIB,XZERO,-ASCALE,1.,Ø.)
C                  read in new data file
      CALL FILEREAD(NDATA,DATFILE,Y)
      CALL ABSCISSA(NDATA,VI,VF,X,VINC)
      CALL SMOOTH9PTCUBIC(NDATA,Y,YS)
      CALL OVERLAP(X(1),X(NDATA),XCALIB(1),XCALIB(NCDATA),
     & ALOVER,AHOVER)
C                       now which file do we interpolate with?
      IF(ALOVER .EQ. XCALIB(1)) THEN
      IF(ALOVER .GE. AHOVER) ALOVER= AHOVER-1Ø
C           *** this is patch for non overlaping files - forces
c                  comparison of 1Ø mv overlap.
      CALL INTERPOL(ALOVER,INT((AHOVER-ALOVER)/CVINC)*CVINC
     & +ALOVER,CVINC,VINC,X,YS,YITRP,NPTS)
      CALL MATCH3(NPTS,YCALIB,YITRP,INT(.1*NPTS),C,E)
C
      ELSE
C
      IF(ALOVER .GE. AHOVER) ALOVER= AHOVER-1Ø
C                                *** this is patch for non overlap, again ***
      CALL INTERPOL(ALOVER,INT((AHOVER-ALOVER)/VINC)*VINC+ALOVER,
     & VINC,CVINC,XCALIB,YCALIB,YITRP,NPTS)
      CALL MATCH3(NPTS,YITRP,YS,INT(.1*NPTS),C,E)
C
      END IF
C
      CALL RESCALE(NDATA,X,YS,XZERO,ASCALE,C,E)
C                   ** now plot out data again **
      CALL SCALE(NDATA,X,YS,VBEGIN,MVPERIN,YUNPIN,YMIN,YMAX,1.)
      CALL PEAKLOC(NDATA,YS,X,VXPEAK,NUM)
      CALL BASELINE(VI,VF,VINC,YS,YMIN,BSINMN,YMAX1)
      CALL SORTPEAK(VXPEAK,NUM,XPS,NSIG,YS,VINC,VI,BSINMN,
     & YMAX1)
      CALL LABELPOS(YS,XPS,NSIG,
     & YUNPIN,YMIN,MVPERIN,VBEGIN,VI,VINC)
```

Figure A-8

```
      CALL PLOTDATA(NDATA,X,YS,NSIG,XPS,YSCALE,MVPERIN,
     & VBEGIN,VF,DATFILE,VMOD)
C
  61Ø CONTINUE

C                      first plot axes
       CALL AXIS(Ø.Ø,Ø.Ø,3HMEV,-1,47Ø./MVPERIN,-9Ø.,999.,
      & 1Ø./MVPERIN)
       DO 63Ø I= 1,INT(47Ø/1ØØ)
       XLOC= (-VBEGIN+I*1ØØ)/MVPERIN
       YLOC= -Ø.4
       AXISMV= I*1ØØ
  63Ø CALL NUMBER(YLOC,-XLOC,.15,AXISMV,-9Ø.,Ø)
C
C
       CALL ORIGIN(-.5,-1Ø.,1)
       CALL PLOT(8.5,Ø.,999)
       CLOSE(UNIT=1Ø)
       END
```

Figure A-9

```
      SUBROUTINE PLOTDATA(NDATA,X,Y,NSIG,XPS,YSCALE,MVPERIN,
     & VBEGIN,VF,FNAME,VMOD)
      REAL MVPERIN
      CHARACTER *(*) FNAME
      COMMON /LABARR/XPL(100),YPL(100),AMPVER(100)
      DIMENSION X(2010),Y(2010),XPS(100)
      DIMENSION XJ(2010),YJ(2010)
      DIMENSION IFNAME(1)
C
C
C
      CALL SPEED(15)
      DO 147 I=1,NDATA+1
  147 X(I)= -X(I)
      CALL LINE(Y,X,NDATA,1,0,2)
      DO 148 I=1,NDATA+1
  148 X(I)= -X(I)
      RETURN
C                     ** shading **
C                ** ** NEW SHADING ROUTINE  ** **
      DIST= .01
      DO 343 I= 2,NDATA-1
      IF(ABS(Y(I+1)-Y(I-1)) .LT. 1.0E-6) SLOPE = -SIGN(1.0E+6,
     & Y(I+1)-Y(I-1))
      IF(ABS(Y(I+1)-Y(I-1)) .GE. 1.0E-6) SLOPE =
     & (X(I-1)-X(I+1))/(Y(I+1)-Y(I-1))
      BCEPT= Y(I) - SLOPE*X(I)
      XINC= DIST/((1/X(NDATA+2))**2+(SLOPE/Y(NDATA+2))**2)**.5
      XINC= SIGN(XINC,SLOPE)
      XJ(I)= X(I)+XINC
      YJ(I)= SLOPE*XJ(I)+ BCEPT
  343 CONTINUE
      XJ(1)= X(1)
      XJ(NDATA)= X(NDATA)
      XJ(NDATA+1)= X(NDATA+1)
      XJ(NDATA+2)= X(NDATA+2)
      YJ(1)= Y(1)
      YJ(NDATA)= Y(NDATA)
      YJ(NDATA+1)= Y(NDATA+1)
      YJ(NDATA+2)= Y(NDATA+2)
      CALL LINE(XJ,YJ,NDATA,1,0,2)
C
  311 CONTINUE
C               ** NOW PLOT OUT LABELS **
C                              first calculate energy shift and FWHM
      CALL CORRECT(VMOD,SHIFT,FWHM)
C
  580 CALL ASPECT(.6)
      DO 575 I= 1,NSIG
C                  if label if off page, shift it to defualt position if psbl
      IF(YPL(I) .GT. YSCALE +.75 .OR. YPL(I) .LT. 0.0) YPL(I)= 1.0
      CALL NUMBER(YPL(I),-XPL(I)-.062,.1,(XPS(I)-SHIFT)*8.06548,
     & 0.0,0)
  575 CONTINUE
C
C
      RETURN
C             now plot FWHM, and DATFILE NAME
C
C
      J= LEN(FNAME)
      PRINT *,FNAME
      DO 670 I=1,J
      IFNAME(1)= ICHAR(FNAME(I:I))
  670 CALL SYMBOL((VF-VBEGIN)/MVPERIN-5.+(I-1)*.15*.6,.3,.15,
     & IFNAME,0.0,0)
      CALL SYMBOL((VF-VBEGIN)/MVPERIN-5,.1,.15,16HINST FNC FWHM =
     & ,0.0,16)
      DO 55 I= 1,2
      CALL PLOT((VF-VBEGIN)/MVPERIN-5+.6*.15*16,.1,3)
      CALL PLOT((VF-VBEGIN)/MVPERIN-5+.6*.15*16 + FWHM/MVPERIN,.1,2)
      CALL PLOT((VF-VBEGIN)/MVPERIN-5+.6*.15*16 + FWHM/MVPERIN,.25,2)
      CALL PLOT((VF-VBEGIN)/MVPERIN-5+.6*.15*16,.25,2)
      CALL PLOT((VF-VBEGIN)/MVPERIN-5+.6*.15*16,.1,2)
   55 CONTINUE
      RETURN
      END
```

Figure A-10

```
      SUBROUTINE CORRECT(VMOD,SHIFT,FWHM)
C               this subroutine calcualtes the proper energy shift (in mev)
C                to correct Pb energy gap @ 4.2 K for modulation effects
C                 Kirtley & Hansma Phys Rev B 13__,2910 (1976)




C                  In addition, FWHM value is determined for modulation
C                   (see Kirtley's review article)
C                ** VMOD meV rms **
C                      .5 < vmod/delta < 2.
      SHIFT= -1.414*VMOD*.14 + 1.13
C                     1 < vmod < 2 meV
      FWHM= 1.49*VMOD + 0.30
      RETURN
      END



      SUBROUTINE FILEREAD(NDATA,FILENAME,Y)
      INTEGER*4 M,IH,IL
      DIMENSION Y(2010)
      CHARACTER*(*) FILENAME
      OPEN(ACCESS='DIRECT',NAME=FILENAME,TYPE='OLD',
     & UNIT=6,RECORDTYPE='FIXED')
C
C
C        READ IN FIRST SIX(3) PARAMETERS
      DO 50 I=1,3
      READ(6'I) M
C      WRITE(7,200) M
  200 FORMAT(I20)
   50 CONTINUE
C        THROW AWAY FIRST DATA POINT?
      READ(6'4)M
C          NOW READ IN WORKING DATA SET
      DO 100 I=1,NDATA
      READ(6'(I+4)) IL
      Y(I)= IL
  100 CONTINUE
C
C            NOW CLOSE OUT INPUT FILE
C
      CLOSE(UNIT=6)
C
      RETURN
      END



      SUBROUTINE ABSCISSA(NDATA,VI,VF,X,VINC)
      DIMENSION X(2010)
C
C
C            ** NOW GENERATE ABSCISSA **
C
C                        ** VINC= mv/point
      VINC= (VF-VI)/(NDATA-1)
      DO 110 I= 1,NDATA
      X(I)= VI + VINC*(I-1)
  110 CONTINUE
      RETURN
      END
```

Figure A-11

```
      SUBROUTINE SMOOTH9PTCUBIC(NDATA,Y,YS)
      DIMENSION Y(2Ø1Ø),YS(2Ø1Ø),YHOLD(2Ø1Ø)
C
C          NOW SMOOTH DATA (9PT CUBIC/QUADRATIC)
C
      DO 12Ø I=5,NDATA-4
      YHOLD(I)= (-21*(Y(I-4)+Y(I+4))+14*(Y(I-3)+Y(I+3))
     & +39*(Y(I-2)+Y(I+2))+54*(Y(I-1)+Y(I+1))+59*Y(I))/231.
C      YHOLD(I)= ( -3*(Y(I-2)+Y(I+2)) + 12*(Y(I-1)+Y(I+1))
C     & +17*Y(I) )/35.
  12Ø CONTINUE
      DO 125 I=1,4
      YHOLD(I)= Y(I)
      YHOLD(NDATA-I+1)= Y(NDATA-I+1)
  125 CONTINUE
C               now transfer from YHOLD to YS
      DO 13Ø I= 1,NDATA
  13Ø YS(I)= YHOLD(I)
      RETURN
      END
```

```
      SUBROUTINE TSCHEBYSHEV(NDATA,YS,YBR,ISTART,SUM)
      DIMENSION YS(2Ø1Ø),YBR(2Ø1Ø)
C             TSCHEBYSHEV ROUTINE TO REMOVE SLOPE
C
      SUM= Ø.Ø
      DELTA=.5/1ØØØ
      DELTAX= (2.-DELTA)/(NDATA-ISTART)
C               calc exact numerical center
      CENTR= (NDATA+ISTART)/2.
C                now locate proper points to start integration correcting
c                           for odd/even # of pts.
      NCPOS= INT(CENTR + .5)
      NCNEG= INT(CENTR)
C
      DO 122 I= Ø, (NDATA-ISTART)/2.-2, 2
C                include shift 1/2 unit for center point
      XTSCH= DELTAX*(I+CENTR-NCNEG)
      STERM= Ø.Ø
C                simpson's rule num. int.;form terms into complimentary sums
      DO 199 K= Ø,2
  199 STERM= STERM + (1-3.*(ABS(K-1.)-1))*
     & (YS(NCPOS+I+K)-YS(NCNEG-I-K))*(XTSCH+K*DELTAX)*DELTAX/
     & (3.*(1-(XTSCH+K*DELTAX)**2)**.5)
  122 SUM= SUM+STERM
C           for even # of pts, must include intg over cntr region
      IF (CENTR .EQ. NCNEG) GO TO 123
      SUM= SUM+DELTAX**2*(YS(NCPOS)-YS(NCNEG))/4.
C             correction for intervals on either side of cntr pt not even
  123 INTUNI= INT((NDATA-ISTART)/2.)

      IF (INT(INTUNI/2.) .EQ. INTUNI/2.) GO TO 124
      X= INTUNI*DELTAX
      SUM= SUM+.5*(YS(NCPOS+INTUNI)-YS(NCNEG-INTUNI))*DELTAX
     & *X/(1-X**2)**.5
      X= X - DELTAX
      SUM= SUM+.5*(YS(NCPOS+INTUNI-1)-YS(NCNEG-INTUNI+1))*DELTAX
     & *X/(1-X**2)**.5
C                now normalize
  124 SUM = SUM*2/3.14159
      PRINT *,'OUTPUT SUM FROM TSCHEBYSHEV:',SUM
      IF(SUM .LT. Ø.Ø) SUM= Ø.Ø
C
      RETURN
      END
```

Figure A-12

```
      SUBROUTINE SCALE(NDATA,X,Y,VBEGIN,MVPERIN,YUNPIN,YMIN,
     & YMAX,OVERRIDE)
      PARAMETER YSCALE= 4.75
      REAL MVPERIN
      COMMON /SCALEDAT/ EXPAND
      DIMENSION X(2Ø1Ø),Y(2Ø1Ø)
C
C                 if OVERRIDE = 1, then we already know scale parms, so jump
C                  and just shove them in arrays
      IF(OVERRIDE .EQ. 1) GO TO 14Ø
C
C           MAXIMUM,MINIMUM & SCALE
      YMIN= 1.E+6
      YMAX= -1.E+6
      DO 13Ø I= 1,NDATA
      IF (Y(I) .GT. YMAX) YMAX=Y(I)
      IF (Y(I) .LT. YMIN) YMIN=Y(I)
  13Ø CONTINUE
C                  we want to slightly reduce to scale so everyting fits
C                    ** plotter y-scale: y-units per inch
      YUNPIN= EXPAND*(YMAX-YMIN)/YSCALE
      YMIN= YMIN-(EXPAND-1.)*(YMAX-YMIN)/2.
      IF(YMIN .LT. Ø.Ø) YMIN= 1.1*YMIN/.92
  14Ø CONTINUE
C
C           ADD SCALE PARAMETERS INTO ARRAYS
      Y(NDATA+1)= YMIN
      X(NDATA+1)= VBEGIN
      Y(NDATA+2)= YUNPIN
C                   ** plotter scale mv per inch
      X(NDATA+2)= MVPERIN
      RETURN
      END




      SUBROUTINE PEAKLOC(NDATA,YBR,X,VXPEAK,NUM)
      DIMENSION YBR(2Ø1Ø),YD(2Ø1Ø),X(2Ø1Ø),VXPEAK(1ØØ)
C




C           TRY AND LOCATE PEAK POSITIONS
C
C           FIRST TAKE 1ST DERIV(9PT CUBIC/QUARTIC)
      CALL DERIV9PTQAD(NDATA,YBR,YD)
C        NOW LOCATE NODES
C                 reset peak number counter
      NUM= Ø
      DO 15Ø  I=5,NDATA-6
      IF (YD(I) .GE. Ø.Ø) GO TO 15Ø
      IF (YD(I-1) .LT. Ø.Ø) GO TO 15Ø
      XPEAK= X(I)-YD(I)*(X(I)-X(I-1))/(YD(I)-YD(I-1))
      NUM= NUM + 1
C                          vector of all peaks!
      VXPEAK(NUM)= XPEAK
  15Ø CONTINUE
      RETURN
      END
```

Figure A-13

```
      SUBROUTINE BASELINE(VI,VF,VINC,YBR,YMIN,BSINMN,YMAX1)
      DIMENSION YBR(2Ø1Ø)
C
C            LOCATE THE SIGNIFICANT PEAK POSITIONS: XPS
C
C                       first must establish baseline
C
C                        YMAX1= max height of spect. w. bkgrnd removed
      YMAX1= -1E+6
C                    zero min baseline integral(intgrate over 2Ø mv)/(2Ø mv).
C                  Initilization  to -YMIN will essentially shift correct & invt. s
c                    to the proper place for correct bsline determination
      BASEINT= -YMIN
C                    # of points IN 2Ø mv region
      NP2ØMV= 2Ø./VINC
      DO 2Ø5 I=INT((MAX(VI,5Ø.)-VI)/VINC + 1),INT((MAX(VI,5Ø.)-VI)/
     & VINC + 1) + NP2ØMV - 1
  2Ø5 BASEINT= BASEINT + YBR(I)/NP2ØMV
      PRINT *,'BASELINE INTEGRAL & NP2ØMV'
      PRINT *,BASEINT,NP2ØMV
C
C                       now serch for the min baseline integral over spectrum
C
C                         first initialize baseline integral minimum
      BSINMN= 1.E+6
      DO 21Ø I=INT((MAX(VI,5Ø.)-VI)/VINC + 1),INT((MIN(VF-25.,4ØØ.)-VI)/
     & VINC + 1)
      BASEINT= BASEINT + (YBR(I+NP2ØMV)-YBR(I))/NP2ØMV
      IF(BASEINT .GT. BSINMN) GO TO 11ØØ
      BSINMN= BASEINT
 11ØØ IF(YBR(I) .GT. YMAX1) YMAX1= YBR(I)
  21Ø CONTINUE
C                    now reshift BSINMN  to original positions
      BSINMN= BSINMN + YMIN
      PRINT *,'DET BASELINE INTEG MIN  & MAX PEAK HEIGHT '
      PRINT 5Ø1,BSINMN,YMAX1
  5Ø1 FORMAT(4E16.6)
      RETURN
      END
```

```
      SUBROUTINE SORTPEAK(VXPEAK,NUM,XPS,NSIG,YBR,VINC,VI,BSINMN,
     & YMAX1)
      DIMENSION YBR(2Ø1Ø)
      DIMENSION VXPEAK(1ØØ),XPS(1ØØ)
C                        (re)initialize sorted peak counter
      NSIG= Ø
C                   now that baseline is established(BSINMN),sort through VXPEAK
C
      DO 24Ø I= 1,NUM
      IF(YBR((VXPEAK(I)-VI)/VINC+1) .LT. .1*(YMAX1-BSINMN) + BSINMN)
     &  GO TO 24Ø
      CALL SND16PTDRV(YBR,VXPEAK(I),VINC,VI,SNDDRV16PT)
      IF(-SNDDRV16PT/VINC**2 .LT. (YMAX1-BSINMN)*5./5ØØ.) GO TO 24Ø
      NSIG= NSIG + 1
      XPS(NSIG)= VXPEAK(I)
  24Ø CONTINUE
      PRINT *,'NUM  & NSIG'
      PRINT *,NUM,NSIG
      RETURN
      END
```

Figure A-14

```
      SUBROUTINE LABELPOS(YBR,XPS,NSIG,
     & YUNPIN,YMIN,MVPERIN,VBEGIN,VI,VINC)
      REAL MVPERIN
      DIMENSION YBR(2Ø1Ø)
      DIMENSION XPS(1ØØ),YPS(1ØØ)
      DIMENSION SECMAX(1Ø),AMXLBL(1Ø)
C               need commons for calling LABOV
C
      COMMON /LABARR/XPL(1ØØ),YPL(1ØØ),AMPVEC(1ØØ)
      COMMON /LABDAT/XSPACE,YSPACE
C
C
C
C             **  LABEL POSITIONING ROUTINE  **
C
C                     XSPACE= x-length of label(inches)
      XSPACE= .125
C                     YSPACE= y-length of label(inches)
      YSPACE= .3
C
C
C
C             NOW ASSIGN Y LOCATION TO XPS
C
      DO 25Ø I= 1,NSIG
C*****************************************
  25Ø YPS(I)= YBR(INT((XPS(I)-VI)/VINC +1))
C
C             ESTABLISH CENTER POSITION FOR LABEL CORRESP. TO XPS
C                NOTE: WORK IN DIRECT PLOTTER UNITS(INCHES)
C
C                   set intial label .5 inches over peak




      DO 26Ø I= 1,NSIG
      YPL(I)= (YPS(I)-YMIN)/YUNPIN + .5
      XPL(I)= (XPS(I)-VBEGIN)/MVPERIN
  26Ø CONTINUE
C
C             ** NOW DO LABELS OVERLAP SPECTRUM **
C
C                    we can shift label up to +- 2 sectors(=.5xspace)
C
C                           figure out #of points in sector-length(s1=.25xspace)
      NSECTOR= INT(.25*XSPACE*MVPERIN/VINC)
      DO 3ØØ K= 2,NSIG
C                           now scan sectors(8) to det. max height
      DO 27Ø J= 1,8
C               RESET SECMAX(J)
      SECMAX(J)= -1E+6
C                           calculate peak subscript
      NPEAK= (XPS(K)-VI)/VINC +1
      DO 27Ø I= NPEAK+(J-5)*NSECTOR,NPEAK+(J-4)*NSECTOR
C*****************************************
  27Ø SECMAX(J)= MAX(SECMAX(J),YBR(I))
C
C                    now det. maximum over label region and min posib. dist.
C
      AMINPOS = 1E+6
      DO 28Ø J= 1,5
      AMXLBL(J)= MAX(SECMAX(J),SECMAX(J+1),SECMAX(J+2),SECMAX(J+3))
C                              use NLBMIN later to decide #sectors to shift
      IF(AMINPOS .GT. AMXLBL(J)) NLBMIN= J
  28Ø AMINPOS= MIN(AMINPOS,AMXLBL(J))
      AMPVEC(K)= (AMXLBL(3) - YMIN)/YUNPIN
      AMINPOS= (AMINPOS-YMIN)/YUNPIN
C
```

Figure A-15

```
C
C                    now check to see if initial placement ok
C
      IF(AMPVEC(K) .LT. YPL(K)-.125) GO TO 300
C          ** LABEL blocking plot  **
C                 assign default position if we can't gain by shift
      YPL(K)= AMPVEC(K)+.25
C                  if label can be put less than 1.5in. above orig peak, o.k.
      IF(AMPVEC(K) .LT. YPL(K)+1.0) THEN
      YPL(K)= AMPVEC(K) + .25
C                 else since we must move it up more than 1.5in., will a shift
C                       help us that much,otherwise use default shift above pk.
      ELSE IF(AMPVEC(K)-AMINPOS .GT. .25) THEN
C                   yes we gain by shifting
      YPL(K)= AMINPOS + .125
      XPL(K)= XPL(K) + (NLBMIN-3)*NSECTOR*VINC/MVPERIN
      AMPVEC(K)= AMINPOS
      END IF
  300 CONTINUE
C
C             **  MUST GET RID OF LABEL OVERLAP  **
C
      DO 350 I= 2,NSIG
      CALL LABOV(I,I-1)
  350 CONTINUE
C
      RETURN
      END
```

```
      SUBROUTINE LABOV(I,J)
C                 CHECKS FOR OVERLAP BETWEEN TWO LABEL BLOCKS J,K AND SHIFTS
C
      PARAMETER CLEARANCE=.03
      COMMON /LABARR/XPL(100),YPL(100),AMPVEC(100)
      COMMON /LABDAT/XSPACE,YSPACE
      IF(ABS(XPL(I)-XPL(J)) .GT. XSPACE+CLEARANCE) RETURN
      IF(ABS(YPL(I)-YPL(J)) .GT. YSPACE+CLEARANCE) RETURN
      YPL(I)= YPL(J) + SIGN(YSPACE+CLEARANCE,YPL(I)-YPL(J))
C                 check to see if shift moved label too close to spectrum
      IF(YPL(I) .GT. AMPVEC(I) + .125) RETURN
C                       then by default label must be shifted up
      YPL(I)= YPL(J) +YSPACE+CLEARANCE
      RETURN
      END
```

```
      SUBROUTINE DERIV9PTQAD(NDATA,YS,YD)
      DIMENSION YS(2010),YD(2010)
C
C          FIRST TAKE 1ST DERIV(9PT QUADRATIC)
      DO 140 I=5,NDATA-4
      YD(I)= (-4*(YS(I-4)-YS(I+4))-3*(YS(I-3)-YS(I+3))
     & -2*(YS(I-2)-YS(I+2))-1*(YS(I-1)-YS(I+1)) )/60.
  140 CONTINUE
      RETURN
      END
```

Figure A-16

```
      SUBROUTINE SND16PTDRV(YS,VXPEAK,VINC,VI,SNDDRV16PT)
      DIMENSION YS(2Ø1Ø)
C
C           TAKE SECOND DERIVITIVE (16 PT CUBIC/QUAD)
      I= NINT((VXPEAK-VI)/VINC)
      NP= 1
      IF(VINC .LE. Ø.3) NP=2
      SNDDRV16PT= (91*(YS(I-7*NP)+YS(I+7*NP))+52*(YS(I-6*NP)+
     &   YS(I+6*NP)) +19*(YS(I-5*NP)+YS(I+5*NP)) +
     &  -8*(YS(I-4*NP)+YS(I+4*NP))-29*(YS(I-3*NP)+YS(I+3*NP))
     & -48*(YS(I-2*NP)+YS(I+2*NP))-53*(YS(I-1*NP)+YS(I+1*NP))
     & -56*YS(I))/(6188.*NP**2)
  14Ø CONTINUE
      RETURN
      END



      SUBROUTINE DERIV9PT(NDATA,YS,YD)
      DIMENSION YS(2Ø1Ø),YD(2Ø1Ø)
C
C          FIRST TAKE 1ST DERIV(9PT CUBIC/QUARTIC)
      DO 14Ø I=5,NDATA-4
      YD(I)= (86*(YS(I-4)-YS(I+4))-142*(YS(I-3)-YS(I+3))
     & -193*(YS(I-2)-YS(I+2))-126*(YS(I-1)-YS(I+1)) )/1188.
  14Ø CONTINUE
      RETURN
      END
```

```
      SUBROUTINE OVERLAP(XA1,XAEND,XB1,XBEND,ALOVER,AHOVER)
C
C              DETERMINE OVERLAP
      ALOVER= MAX(XA1,XB1)
      AHOVER= MIN(XAEND,XBEND)
      RETURN
      END
      SUBROUTINE INTERPOL(ALOVER,AHOVER,VRINC,VYINC,X,Y,YITRP,NPTS)
      DIMENSION Y(2Ø1Ø),X(2Ø1Ø),YITRP(2Ø1Ø)
C               first calculate # of pts. in interpolation
      NPTS= INT((AHOVER-ALOVER)/VRINC +1)
C               now do linear interpolation on Y
      PRINT *,NPTS,VRINC,VYINC,ALOVER,AHOVER
      DO 1ØØ I= 1,NPTS
      XREF= ALOVER + (I-1)*VRINC
C                   where VRINC is the reference file voltage inc
C               if the two x values are close enough, use Y with no interp
      IF( NINT(1ØØ*XREF) .EQ. NINT(1ØØ*X(I))) THEN
      YITRP(I)= Y(I)
      ELSE
      ICL= INT((XREF-X(1))/VYINC + 1)
      ICH= ICL + 1
      YITRP(I)= Y(ICL)+(Y(ICH)-Y(ICL))*(XREF-X(ICL))/(X(ICH)-X(ICL))
      END IF
  1ØØ CONTINUE
      RETURN
      END
```

Figure A-17

```
      SUBROUTINE MATCH3(NPTS,YREF,Y,ISTART,C,E)
      DIMENSION YREF(2Ø1Ø),Y(2Ø1Ø)

C
      IF(C .EQ. Ø.Ø) THEN
C
C             This subroutine determines coefficients in the expansion
C
C                          Y = C*YREF  + E
      LOOP= Ø
CC              initialize C,E
      C= Ø.Ø
      E= Ø.Ø
      CALL XINTEGRAL3(NPTS,YREF,YREFINT,ISTART)
      CALL XINTEGRAL3(NPTS,Y,YINT,ISTART)
C                     REM derivitive vectors not good over range 1 - NPTS
C                now determine C and E from YREF
      DO 1ØØ I= MAX(5,ISTART),NPTS-4
      IF(ABS(YREF(I)-YREFINT) .LT. 2Ø.) GO TO 1ØØ
      LOOP = LOOP + 1
      C1= (Y(I) - YINT)/(YREF(I) - YREFINT)
      E1= YINT-C1*YREFINT
      C= C+C1
      E= E+E1
  1ØØ CONTINUE
      C= C/LOOP
      E= E/LOOP
      RETURN
C
      ELSE
C
C                 determines E only!  Traps here if C .NE. Ø.Ø
      E= Ø.Ø
      DO 2ØØ I= 1,NPTS
      E= E+ (Y(I)-C*YREF(I))/NPTS
  2ØØ CONTINUE
      RETURN
      END IF
      END
```

```
      SUBROUTINE XINTEGRAL3(NDATA,Y,YINTEGRAL,ISTART)
      DIMENSION Y(2Ø1Ø)
C           assumes a region of extent 1 on integral limits
      DELTAX= 1.Ø/(NDATA-MAX(1,ISTART))
C           initialize integral
      YINTEGRAL= Ø.Ø
      DO 1ØØ I= MAX(1,ISTART),NDATA-1
C           use trapezoidal rule
  1ØØ YINTEGRAL= YINTEGRAL+DELTAX*(Y(I)+Y(I+1))/2.
      RETURN
      END
```

Figure A-18

```
      SUBROUTINE ARESCALE(NDATA,X,Y,YOUT,XZERO,SCALE,C,E)
      DIMENSION X(2Ø1Ø),Y(2Ø1Ø),YOUT(2Ø1Ø),YHOLD(2Ø1Ø)
      DO 1ØØ I=1,NDATA
      XX= (X(I)-XZERO)
1ØØ   YHOLD(I)= (Y(I)-E)/C - XX*SCALE
      DO 2ØØ I=1,NDATA
2ØØ   YOUT(I)= YHOLD(I)
      RETURN
      END


      SUBROUTINE RESCALE(NDATA,X,Y,XZERO,SCALE,C,E)
      DIMENSION X(2Ø1Ø),Y(2Ø1Ø)
      DO 1ØØ I=1,NDATA
      XX= (X(I)-XZERO)
1ØØ   Y(I)= (Y(I)-E)/C - XX*SCALE
      RETURN
      END
```

Figure A-19

Appendix B:

A Temperature Controller for Tunneling Spectroscopy

B. A Temperature Controller for Tunneling Spectroscopy

B.1 Introduction

The technique developed by BOWSER and WEINBERG [1] is used in our laboratory for substrate heating. This involves resistively heating an aluminum film while simultaneously using the temperature coefficient of resistance of the aluminum film to determine the film temperature. Although the absolute temperature accuracy is limited to ten percent because of variations in the temperature coefficient of resistance of the aluminum film, this method has the supreme advantage of simplicity. Furthermore, since in most instances the temperature accuracy needed falls within ten percent, this method proves to be the one of choice. However, because of the unique measurement configuration used with this method, standard designs for temperature controllers are not applicable. Usually most commercial schemes are based on the feedback of a thermocouple reference voltage, whereas with this method it is necessary to feedback a resistance. One could of course solder a thermocouple to the aluminum film, but doing so defeats the simplicity of the method, and perhaps perturbs the simple geometry sufficiently so that the thermocouple voltage may not in fact truly reflect the film temperature over the junction area. Hot wire anemometry employs some schemes for temperature control that could be applicable in this instance. However, these methods do not make use of a four-wire probe measurement in the feedback loop, and therefore would be expected to provide only crude temperature control in this instance, where lead-in wire resistances are significant. Consequently, an instrument (Fig. B-1) was custom designed and developed to monitor and control the thin film temperature by using the temperature coefficient of resistance of the aluminum film as the control variable.

The temperature controller has two channels (one for each of the two substrates in this system) and two modes of operation on each channel which are designated "measurement" and "control." In the measurement mode, the instrument acts as a four-wire probe for measuring the resistance of the aluminum film (see Section B.3 for a detailed description of how the circuit elements of the controller function to make this measurement). The measurement mode can be used to monitor metal film temperatures below room temperature, as well as at any time when heating current is not being supplied (e.g., cool during down). On the other hand, the control mode is used to heat the metal film. In the control mode, the instrument is configured in essentially the closed loop form of the measurement mode. The setting of a potentiometer directly sets the resistance of the metal film; the controller automatically supplies the proper current to the film such that its resistance (and thus temperature) remains at the set point value. In addition, the controller has provisions for automatically going from one steady state to another steady state in a gradual manner. This instrument greatly alleviates the tedium of manual control, and it is more precise.

Some considerations for the design of the temperature controller are discussed in the following section (Section B.2). Then in Section B.3, a brief description of the workings of the temperature controller in the measurement mode will be given. This should provide the user with enough rudimentary knowledge of the workings of the circuit to enable him to use the temperature controller, and to follow the instructions in Section B.4 for setting up and using this instrument. Those requiring a more thorough understanding of the instrument and its design are encouraged to read Section B.5 on the dynamics of the temperature controller. This section explains how the transient response of the circuit is analyzed and how this transient response is used to change set points

in a gradual manner. It should be emphasized that this section is not an analysis of the stability of the feedback loop, which is beyond the scope of this document.

B.2 Design Considerations

A resistance controller must do three basic things: (1) it must be able to measure the four-wire resistance of the aluminum film;(2) it must be able to determine and supply the required amount of current to the aluminum film so that the film's resistance will correspond to the calculated film resistance at the desired temperature;(3) and finally, it should have provisions for changing the substrate temperature from one desired value to another in a continuous manner, i.e., sharp discontinuities in the surface temperature may produce thermal shock phenomena that are likely to result in cracking of the oxide barrier and hence tunneling barriers with unsatisfactory electrical characteristics.

Of course, all three tasks are related, but of the three, the measurement problem is the simplest. This is because it is unnecessary to operate the device in a feedback configuration, and consequently phase shifts produced by the elements in the feedback loop cannot cause unstable behavior. Yet in spite of this simplicity, an understanding of the open loop behavior provides all the quintessential details that are necessary for understanding the performance of the temperature controller. Such an analysis is given in Section B.4.

Slightly more complicated than this is to use the circuit as a controller since it is then necessary to operate the circuit in a feedback configuration. A steady state, linear analysis of this configuration, not taking into account the detailed frequency response of the operational amplifiers, is only slightly more complicated than an analysis of the open loop circuit. This type of analysis is

carried out in Section B.5.3 where it naturally follows from the steady state solution to the dynamic equations that describe the controller behavior. However a detailed analysis taking the frequency response of the feedback loop elements into account can be troublesome and sometimes shows that the circuit may need some modification, if it is to remain stable and not to oscillate wildly. For the temperature controller, it turns out that it was necessary to add the small feedback capacitor on Operational Amplifier 2 to eliminate this kind of oscillation (see Fig B-1).

A significantly more complicated problem than the steady-state, linear analysis is that of "dynamically" operating the circuit so that it will provide for a gradual change of the set point. There are a number of ways in which this might be done. One of these, in common use today, is to insert digital control into the feedback loop. Essentially this involves using a computer to measure what is happening to the substrate temperature and then to determine how to adjust the heating current to produce the desired result. This corresponds to continuously operating the controller at steady-state, since changes in the set point made by the computer occur on a time scale which is large compared to the dynamic response of the circuit. Although this method is an excellent approach to control when response times of no less than milliseconds are required (as in this case), it has the drawback of expense (although this is rapidly being removed) and an added layer of hardware complexity. It is the author's feeling that this would be the method to choose over the long run as it enhances reproducibility and ease of use tremendously. However, instead of this approach, the author decided upon a small modification of the controller circuit so that its transient response could be exploited for this purpose. In other words, the circuit is slightly altered so that its settling time in going from one steady-state to another steady state is on the order of minutes rather that hundreds of

microseconds. Since this larger settling time is now similar to the desired rate for heating or cooling of the junctions, it can be conveniently used for this purpose. This leads to the use of the external capacitor bank and a dimensionless table (Table B-1) for roughly producing the desired result. The assumptions and calculations that went into this scheme for temperature control are discussed in the section on controller dynamics, Section B.5.

B.3 Basic Principles of Operation

The measurement circuit works on the same basic principles employed by nearly all four-wire measurement circuits, i.e., a fixed current is injected into the aluminum film through one pair of wires and the resulting voltage drop is measured on a different pair of wires. The principles behind the operation of the measurement circuit can be easily analyzed as follows. Let the unknown resistance of the aluminum film be denoted as R, and let R_{ref} be the value of the precision resistor (known) in series with the aluminum film, as shown in the simplified schematic in Fig. B-3. Suppose i is the current injected by the current source into the the precision resistor. Then by Ohm's law the voltages measured across these resistances by Amplifier 1 and Amplifier 2 are just iR_{ref} and iR, respectively. Amplifier 1 is simply a unity gain amplifier and so its output is just iR_{ref}. Amplifier 2 is a unity gain inverting amplifier and so its output is just $-iR$. Note that the ratio of these two outputs is independent of the current i; this is the fundamental design principle that the circuit will exploit. Amplifier 3 is a variable gain inverting amplifier. As shown in Fig. B-3, this amplifier is formed from an operational amplifier and two resistors R_{fb} and R_I [2]. All this amplifier does is to multiply the voltage coming from Amplifier 1 of iR_{ref} by $-R_{fb}/R_I$, where R_{fb} is the 10 kilohm precision potentiometer that the operator adjusts, and R_I is

a 10 kilohm precision resistor. Thus, after being amplified by Amplifier 3, a voltage of $-iR_{ref}R_{fb}/R_I$ is now applied to one input of the Comparitor, while the signal $-iR$ is applied to the other input of the Comparitor. As the name implies, the Comparitor simply compares the two voltages on its two inputs. The comparitor gives a null signal when the voltages on its inputs are identical, which in this case is when

$$iR_{ref}R_{fb}/R_I=iR\ ,$$

which reduces to

$$R_{fb}/1000=R$$

when the component values are introduced. Hence, by adjusting R_{fb} until the comparitor changes sign (it is impossible to null the comparitor exactly), the value of R has been determined and is equal to the value of R_{fb} divided by 1000.

B.4 Procedures of Operation

The following describes the operating procedure for using the temperature controller to measure the resistances of, and to heat, the aluminum films.

1. Turn off the deposition monitor. The radio frequency interference caused by this instrument confuses the temperature controller electronics.
2. Set the mask in the vacuum chamber to the "open" position. Otherwise there is a danger that the copper leads, which are soldered to the substrates, will be shorted against the mask.
3. Set-up the temperature controller with the connections shown in Fig. B-1 and Fig. B-2; i.e., connect the power supply leads, the electrical feedthroughs to the vacuum chamber, and cables to oscilloscope channels 1 and 2.
4. Set switches SW1 and SW2 down, and switches SW3 and SW4 down. This puts

the temperature controller in "measure mode," and switches out the unnecessary feedback capacitances, respectively.

5. *Before* turning on the power, make a note of the current meters on the Power Supply for the temperature controller. Now turn on the Power Supply. **If the currents drawn by the temperature controller are more than 50 milliamps immediately turn off the Power Supply**, since something is not connected properly or the switches are not in the proper positions (see items 3 and 4). The Oscilloscope should be set to "chop" mode, AC line trigger, with a gain of 5 volts per division on each channel, and a sweep rate of about 0.05 seconds per division.

6. Allow the oscilloscope and the controller to warm up for about five minutes. At this time, if two horizontal traces fail to appear on the oscilloscope, something is wrong with the oscilloscope connections or settings.

7. Determine the resistance of the aluminum film that forms the aluminum electrode of junction 1 (subsequently this resistance is referred to simply as "the resistance of J1"). This is done by first setting potentiometer P1 to zero (turn fully ccw) and rotary switch RSA to zero (turn fully ccw). Then RSA is turned clockwise one position at a time until the oscilloscope trace for J1 (channel 1 of the oscilloscope) changes from about -15 volts to +15 volts. Then turn RSA back one position (the trace should fall back to -15 volts) and record how many positions RSA has been advanced. Now advance the precision 10 turn potentiometer P1 until again the trace for J1 just changes from about -15 volts to +15 volts. Leave P1 set so that the trace has just changed to the +15 volt position, since this will avoid the pitfall of a certain equipmental quirk. Conversely for J2, set P2 so that the trace has just become approximately -15 volts. The four-wire resistance of J1 has then been deter-

mined and is equal to

$$R_{J1} = 5 \times N_{RSA} + R_{P1} / 1000 \ ,$$

where R_{J1} is the resistance of the aluminum film of junction 1, N_{RSA} is the number of positions that RSA has been advanced, and R_{P1} is the resistance of the potentiometer P1. A similar procedure is used to determine the resistance of J2, only this time RSB and P2 are used, and the scope trace changes sign from approximately +15 volts to -15 volts.

8. The aluminum films can now be heated. First it is necessary to compute the resistance that the film will have when it is at the desired temperature. This is done as discussed by Bowser and Weinberg [1].

9. Rapidly heating the aluminum film. If it is desired to heat the aluminum film to the desired temperature *rapidly*, the following can be done. First, from the above expression (in Item 7), back-calculate the values for P1 and RSA that will give the desired value of the film resistance at high temperature. Second, dial in the calculated values of P1 and RSA and then switch SW1 all the way up (this puts the temperature controller into control mode). That is all there is to it.

10. Manually raising the temperature slowly. In the control mode the controller will supply whatever current is necessary to bring the aluminum film resistance to match the corresponding resistance that is set by P1 and RSA. Consequently, if the operator wishes to raise the temperature slowly, this can be done manually by first switching the controller mode to control and then raising P1 and RSA slowly. However, make sure that the oscilloscope trace for J1 is measuring approximately +15 volts before raising SW1 (conversely for J2).

11. Automatically raising the temperature slowly. The manual procedure for

raising the temperature slowly can be rather tedious if a slow temperature progression is desired. Consequently, it is more convenient to use the provisions for automatically raising and lowering the temperature. First decide to what temperature the film is to be heated and back-calculate the values of RSA and P1 as described in Item 9. Second, look in the column under $\Delta T(^{o}C)$ in Table B-1 and find the closest value for the temperature change that the aluminum film will experience, i.e., the difference between the temperature of the aluminum film when it is hot and at room temperature. It is better to use the row of the entry that overestimates rather than underestimates this value. Follow the row of this entry across to the entry under the column $\bar{R}(I)= TI^2 + 1$. Record this number. This is the dimensionless time τ that is required for the controller to heat a dimensionless resistance $\bar{R}$ to 90 percent of a dimensionless temperature difference ΔT. The dimensionless time τ is equal to:

$$\tau = t/R_{fb}C_{fb} ,$$

where t is the time period in seconds that is needed to raise the temperature of the aluminum film from its initial temperature to 90 percent of its final temperature; R_{fb} is the feedback resistance in ohms and is equal to the sum of the resistances RSA and P1 that will be used for the new set point; C_{fb} is the as yet unknown value of the feedback capacitance in Farads. Once a value for the time period t has been decided upon (good choices are 300 or 600 seconds), C_{fb} (in microfarads) should be calculated from the above expression since τ, t, and R_{fb} are now all determined. Once C_{fb} has been calculated, the appropriate switches on the capacitor bank must be set. This is done by advancing RSC one position counter-clockwise for each 100 MFD of C_{fb} and advancing RSD one position counter-clockwise for each 1000 MFD of C_{fb}. The exact same procedure is used if the aluminum film of J2 is to be

heated, only this time the values used in the above expression are those appropriate for this film, and switches RSE and RSF are set.

12. Switching the capacitances into the controller circuit. Once the feedback capacitances have been set, it is necessary to switch them into the controller circuit, and let the controller circuit come to steady state. First make sure that the channel being used for automatic heating is switched into "measurement mode"; e.g., for J1 make sure SW1 is down. Then switch SW3 into the up position. This switches the feedback capacitances into the circuit. In the present configuration, the circuit voltages and currents equilibrate with a time constant of t/τ seconds. Therefore, in approximately $4t/\tau$ seconds the voltages and currents come to within ninety-eight percent of steady-state. This can be determined visually. If the trace for J1 was reading +15 volts before throwing SW3, then upon throwing SW3 the trace for J1 should change to read -15 volts; when the circuit has equilibrated, the J1 trace will again read +15 volts, so simply watching for the J1 trace to change sign will indicate that the circuit has equilibrated. Note that if after the time estimated above the trace has not changed sign, increase P1 very slowly until the trace does so. Usually no more than a 0.05 kilohm increase in P1 is sufficient. A similar procedure is applicable when setting the capacitances for the aluminum film of J2.

13. Begin heating the aluminum film for J1 by switching the controller into control mode (raise SW1), and then as quickly as possible dial in the appropriate values of P1 and RSA for the high temperature set point.

14. Cooling the aluminum film. When the heating period is over, the aluminum film for J1 may be cooled gradually to room temperature simply by resetting P1 and RSA to their original values. When the current drawn by the positive

power supply falls to a low value, the junctions are reasonably cool, and the controller can be switched back into measure mode by setting SW1 down and then SW3 down. Note that the film will cool within the shorter time governed by the relationship

$$t_{cooling} = \frac{R_{fb_{cold}}}{R_{fb_{hot}}} t_{heating}$$

Warning: Do not reset the mask position when the controller is in the control mode since this may cause damagingly high currents to flow through the aluminum films. When doing the Pb evaporation it important to have the controller power supply off.

B.5 Dynamics of the Temperature Controller

This section presents an analysis of the dynamics of the temperature controller circuit which are dominated by the feedback capacitance C_{fb} as shown in Fig. B-3. As discussed earlier in Section B.2, this capacitance was originally introduced into the closed loop circuit to prevent it from oscillating wildly. However, the analysis presented in this section indicates that the feedback capacitance can be exploited to provide a means for automatically raising the temperature of the aluminum film at any desired rate. This turns out to be a feasible prospect for two reasons. The first reason is that the dynamics of the temperature controller itself are suitable for this task. By suitable, it is meant that the dynamics of the controller can be easily adjusted by adjusting the value of the feedback capacitance, and that the dynamic response is a smooth, monotonic function of time. Second, fortuitous results make the dynamics of the controller only a function of one dimensionless group and independent of the rate of heat transfer between the aluminum film and the surroundings. The dimensionless

group essentially represents a dimensionless temperature. Consequently, the dynamic response can be easily scaled to accommodate different values of the aluminum film resistance as naturally occurs through the course of making junctions, and one can neglect effects on the dynamics that might result from positioning the substrate differently.

Section B.5 is divided into six parts. In Section B.5.1, a schematic is introduced, and most of the physical variables that will subsequently be used throughout Section B.5 are defined. Then, in Section B.5.2 the equations governing the relationships between the physical variables are given. In Section B.5.3, this set of equations is reduced to one differential equation in terms of the variables representing time, current through the aluminum film, and the resistance of the aluminum film. Also, following from the steady-state simplification of this differential equation, it is shown that the steady-state closed loop response of the controller will produce the desired temperature in the aluminum film. In Section B.5.4, dimensionless variables are introduced into the differential equation governing the dynamic response, and it is shown that this response depends on only one dimensionless group. Up to this point, the dependence of the resistance of the aluminum film on the current flowing through it has not been expressed explicitly. In Section B.5.5, this topic is discussed, and models for the temperature dependence of the aluminum film on the current flowing through it are presented. In Section B.5.6, numerical solutions to the dimensionless dynamic response are presented. It is from these solutions that Table B-1 was developed.

B.5.1 Idealized Schematic

Shown in Fig. B-4 is an idealized schematic of the temperature controller in the

closed loop configuration. Where possible, this schematic has been simplified by lumping together groups of circuit elements to form idealized amplifiers. The resistance of the precision reference resistor and the resistance of the aluminum film are denoted respectively by R_{ref} and R. Note that while R_{ref} is a constant, R is strictly a function of the temperature of the aluminum film T. Accordingly, R will sometimes be expressed as R(T) to explicitly show this dependence. Note that $R_o = R(T_o)$, where T_o is the initial steady-state temperature. The current flowing though these resistive elements is denoted by i. The voltages across the differential inputs to Amplifier 1 and Amplifier 2 are given respectively by V_1 and V_2, and the amplifier gains are symbolized respectively by G_1 and G_2. The feedback resistance and feedback capacitance of Operational Amplifier 3 are denoted respectively by R_{fb} and C_{fb}. The resistance in series with the inverting input (-) of Operational Amplifier 3 is denoted by R_I . The voltages at the inputs to the Comparitor are denoted by V_+ and V_- . The output voltage of the Comparitor is denoted by V_{out} , and the open loop voltage gain of the comparitor is denoted by G_c. The current gain of the transistor is given by β.

B.5.2 Network Equations and Relations

The following relations are determined by using an elementary network analysis of Fig. B-4 and rudimentary operational amplifier theory in some cases.

$$V_1 = iR_{ref} \tag{1}$$

$$V_2 = iR(T) \tag{2}$$

$$V_+ = V_2G_2 = G_2iR(T) \tag{3}$$

$$\frac{V_1 G_1}{R_I} = \frac{i R_{ref} G_1}{R_I} = -\left\{C_{fb}\frac{dV_-}{dt} + \frac{V_-}{R_{fb}}\right\} \tag{4}$$

$$\left\{V_+ - V_-\right\} G_c = V_{out} \tag{5}$$

From the simplified model of a transistor in Fig. B-5, where R_β is the base-to-emitter resistance and i_β is the base-to-emitter current of the transistor,

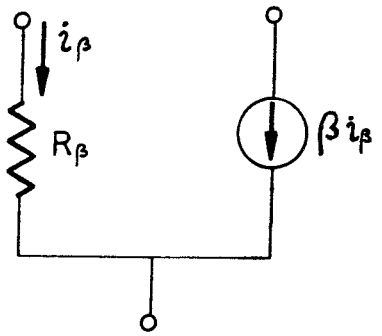

Figure B-5. Direct current, small signal model for an ideal transistor.

it follows that

$$\frac{V_{out} - (1+\beta) i_\beta [R_{ref} + R(T)]}{R_\beta} = i_\beta \quad . \tag{6}$$

Using the relation that $i = (1+\beta) i_\beta$, Equation (6) simplifies to

$$V_{out} = i\left\{\frac{R_\beta}{1+\beta} + R_{ref} + R(T)\right\} \quad . \tag{6a}$$

Strictly speaking, the resistance of the aluminum film is only a function of temperature [1]; i.e.,

$$R(T) = R_o\left[1 + b(T - T_o)\right] \quad .$$

The film temperature in turn is coupled to the controller dynamics through the current in the thermal energy balance

$$AC_p \frac{\partial T}{\partial t} = i^2 R(T) - H(T - T_s) \quad ,$$

where A is the area of the aluminum film, C_p is the heat capacity of the film per unit area, H is the heat transfer coefficient between the aluminum film and the substrate, and T_s is the temperature of the substrate. In addition the temperature of the substrate will be governed by a thermal energy balance:

$$V_s C_{p_s} \frac{\partial T_s}{\partial t} = H(T - ts) - H'(T_s - T_a) \quad ,$$

where V_s is the volume of the substrate, C_{p_s} is the heat capacity per unit volume of the substrate, H' is the heat transfer coefficient between the substrate and the ambient, and T_a is the ambient temperature. Using these equations it is possible to express the temperature of the aluminum film T in terms of the current i, the time t, and other physical parameters; i.e.,

$$R(T) = R[T(i,t)] = R(i,t) \quad .$$

If the film temperature is slowly raised, then the thermal energy balances will be in pseudo steady-state with respect to the controller dynamics. An approximate worst case calculation reveals that this is probably true. In view of the much slower controller dynamics, it will be possible to ignore the dynamics of the heat transfer problem, and to express R as a function only of the current i; i.e., at pseudo steady-state

$$R(i,t) = R(i) \quad ,$$

where now the time dependence of R is implicit in the variable $i(t)$. For the present, the dependence of R on i will not be given in explicit form. This task is

dealt with in Section B.5.5.

B.5.3 Simplification of the Network Relations

The goal is to solve the network equations in terms of i , t , and $R(i)$. These are the natural variables to work with since $R(i)$ will be given an explicit dependence upon i in Section B.5.5. Note the equations are nonlinear if i is considered to be the dependent variable, and t is the independent variable. For example, in Equation (6a), if as the simplest case $R(i)$ is assumed to behave as $R = R_o+ni$, then terms such as iR are parabolic in i. Fortunately however, if t is viewed as the dependant variable, the equations will turn out to be linear.

Substituting Equation (3) and Equation (6a) into Equation (5) yields

$$\left\{G_2 iR - V_-\right\} G_c = i\left\{\frac{R_\beta}{1+\beta} + R_{ref} + R\right\} \quad . \tag{7}$$

The principle of operational amplifier design relies heavily on the approximation that the open loop gain G_c of the device is approximately infinity. In this case, assuming that G_c is very large yields

$$\left\{-G_2 iR - V_-\right\} = \frac{i}{G_c}\left\{\frac{R_\beta}{1+\beta} + R_{ref} + R\right\} \approx 0 \quad , \tag{7a}$$

or

$$V_- \approx G_2 iR \quad . \tag{7b}$$

Taking the derivative of Equation (7b) with respect to time gives

$$\frac{\partial V_-}{\partial t} = G_2 \frac{\partial iR}{\partial t} \quad . \tag{7c}$$

Remember that this is valid only when $\frac{i}{G_c}\left\{\frac{R_\beta}{1+\beta} + R_{ref} + R\right\} \approx 0$. Substituting Equa-

tion (7b) and Equation (7c) into Equation (4) gives an equation in terms of i and t only, namely

$$\frac{R_{ref}}{R_I} G_1 i = -\left\{ C_{fb} G_2 \frac{\partial i R}{\partial t} + \frac{G_2 i R}{R_{fb}} \right\} .$$

After simplification this yields

$$-\frac{\partial i R}{\partial t} = iR\left\{ \frac{1}{C_{fb} R_{fb}} + \frac{G_1}{G_2} \frac{R_{ref}}{R_I} \frac{1}{RC_{fb}} \right\} . \qquad (8)$$

This equation clearly shows that the steady-state design criterion is satisfied; setting the time derivative in Equation (8) equal to zero gives, upon rearrangement,

$$\frac{R}{R_{ref}} = -\frac{G_1}{G_2} \frac{R_{fb}}{R_I} . \qquad (9)$$

Recalling that R_{ref} is fixed at 10 ohms, R_I is fixed at 10 kilohms, and the amplifier gains are adjusted so that $\frac{G_1}{G_2} = -1$, Equation (9) simplifies to the trivial equation $R = \frac{R_{fb}}{1000}$. This shows that setting R_{fb} will set the resistance of the aluminum film R , independent of the functional form of $R(i)$.

B.5.4 Dimensionless Representation

At this point it would be inefficient to integrate Equation (8) to determine the dynamic response of the controller. This is because the results of such an integration would be valid for only one point in the parameter space defined by R_{fb}, C_{fb}, and R. So instead, we now consider a more fruitful method for spanning the parameter space.

Define a dimensionless resistance $\bar{R} \equiv \frac{R}{R_o}$, where R_o is some appropriate

resistance, say for example, characteristic of the initial aluminum film resistance without any current flowing. Similarly define a dimensionless time $\tau \equiv \frac{t}{C_{fb}R_{fb}}$ and a dimensionless current $I \equiv \frac{i}{I_o}$, where I_o is a characteristic current and $C_{fb}R_{fb}$ is a characteristic time (in this case it is the time constant of the open loop integrator). Substituting these dimensionless variables into Equation (8) yields

$$-\frac{\partial I\bar{R}}{\partial \tau} = I\bar{R}\left\{1+\frac{G_1}{G_2}\frac{R_{ref}R_{fb}}{R_I R_o}\frac{1}{\bar{R}}\right\} \quad . \tag{10}$$

Note that one dimensionless group appears regardless of how the relation $R = R(i)$ is prescribed, or how I_o is specified. This group

$$\frac{R_{ref}}{R_I}\frac{R_{fb}}{R_o}$$

essentially represents the dimensionless temperature difference between the hot and cold states of the aluminum film. Therefore, one expects solutions of Equation (8) to look similar as long as the difference between the initial and final temperatures of the aluminum film are the same. However, since $\tau = \frac{t}{C_{fb}R_{fb}}$ will be different for films of differing initial resistance, the real time rate for heating will be scaled appropriately in time for each film. The connection between the dimensionless parameter and the dimensionless temperature difference can be shown more explicitly; it is known that the aluminum film temperature T is given by [1]

$$b(T-T_o) = \frac{\Delta R}{R_o} \quad .$$

Adding unity to both sides gives

$$b(T-T_o+\frac{1}{b}) = \frac{R_o+\Delta R}{R_o} = \frac{R_{fb}}{R_o}\frac{1}{1000} \quad .$$

After redefining T_o in terms of a new variable T_o' ,

$$b(T-T_o') = \frac{R_{fb}}{R_o}\frac{1}{1000} \quad ,$$

which more directly shows the relationship between the dimensionless parameter and the dimensionless temperature difference. The linear relationship between the dimensionless temperature and $\frac{R_{fb}}{R_o}$ is preserved only for temperatures where terms greater than first order in the expansion

$$R = R_o[1+b\Delta T+c(\Delta T)^2+\ldots\ldots\ ]$$

are unimportant.

B.5.5 Functional forms for R(i)

In order to solve for the controller dynamic response, it is necessary to provide some explicit form for the dependence of the resistance R of the aluminum film on the current i . As discussed in Section B.5.2, the pseudo steady-state assumption allows one to neglect the dynamics of the heat transfer problem. However, a bothersome aspect of the heat transfer problem still remains. Since the heat transfer from the aluminum film is highly dependent upon the positioning of the substrate in relationship to ambient surfaces, the parameters in the heat transfer equation will be different for every substrate. Thus it is clear that unless the controller dynamics are independent of the parameters in the heat transfer equations, insurmountable difficulties may arise. For example, suppose one models the function R(i) as

$$R(i) = R_o + ni \quad ,$$

where n is a constant that depends on the physical geometry. Unless the dynamic response is independent of n (or approximately independent of n), it will be impossible to circumvent the problem of variations in the thermal contact between the substrate and the ambient surfaces. (Ignore for the moment the question of whether this is a sufficiently good model for $R(i)$.) Surprisingly, the dynamic response turns out to be independent of n, as will now be shown. This outcome is not clear even though the dimensionless equation (Equation 10) is independent of such constants. First an appropriate characteristic current I_o is needed to convert the above expression into dimensionless form. Since the constant n has the dimensions of resistance/current, it will be used to form I_o; i.e.,

$$I_o = \frac{R_{ref}R_{fb}}{R_I n} \quad .$$

This leads to

$$R(i) = n\left\{\frac{R_{ref}R_{fb}}{R_I n}\right\}\frac{i}{I_o} + R_o \quad ,$$

and

$$\bar{R}(i) = \frac{R(i)}{R_o} = \frac{R_{ref}R_{fb}}{R_I R_o} I + 1 \quad , \qquad (11)$$

where I is the dimensionless current and $\bar{R}(i)$ is the dimensionless resistance of the aluminum film. Thus it can be seen that this choice for I_o was especially good because the dimensionless parameter of importance in Equation (11) is the same as the dimensionless parameter that appears in Equation (10). This is not generally true. However, as long as it is possible to model $R(i)$ in terms of

the current i raised to some power, then this result will certainly be true. Other functional forms for the dependence of R on i , such as a polynomial in i, are not clearly independent of all parameters other than the dimesionless temperature.

The other important topic in this section concerns how R(i) should be modeled. Although the linear choice suggested above is simplest, physical considerations suggest that an i^2 dependence would be better. In the absence of significant radiative heat transfer and in accordance with Newton's law of cooling, the thermal energy balance at pseudo steady-state becomes:

$$H(T-T_a) = i^2R(T) \quad . \tag{12}$$

Using Equation (12), it is possible to reformulate the direct relationship between R and T [1] into an expression involving R and i. This expression is given by

$$R = R_o\left\{\frac{1}{1-\frac{R_o b}{H}i^2}\right\} \quad . \tag{13}$$

For sufficiently small values of $\frac{R_o b}{H}i^2$, this expression can be expanded in a Taylor series; i.e.,

$$R = R_o\left\{1+\frac{R_o b}{H}i^2+\left\{\frac{R_o b}{H}i^2\right\}^2+ \ . \ . \ . \ .\right\} \quad . \tag{14}$$

The first term of the series is proportional to i^2 , which indicates that a physically more plausible model for R(i) would be based on the relation

$$R = R_o+ni^2 \quad . \tag{15}$$

Although this model would appear to be good to third order in i, one would like to know something more quantatative about its validity. Equation (13) can be

rearranged with the help of Equation (12) to give

$$R = R_o\left\{\frac{1}{1-\frac{b\Delta T}{1+b\Delta T}}\right\} \quad . \tag{16}$$

From a comparison of Equation (16) and Equation (13) it is clear that

$$\frac{R_o b}{H} i = \frac{b\Delta T}{1+b\Delta T} \quad . \tag{17}$$

Since the right hand side of Equation (17) is only a function of temperature, it allows us to evaluate approximately the terms in the Taylor series expansion, Equation (14). For an aluminum film heated to 300 °C , the terms of the Taylor series in Equation (14) become

$$1.594 = 1.00+0.373+0.139+0.052+ \ . \ . \ .$$

From this it is seen that the first two terms in the Taylor series account for 82 percent of the exact value of R(i) for this simple heat transfer model. Certainly the inaccuracies introduced by the simple heat transfer model used in this analysis are more extensive. Thus a parabolic model, as in Equation (15), will be a reasonable approximation to the dynamics of the physical problem. A final point is that a simple comparison between the observed dynamics and the predicted dynamics will indicate much about the validity of the model.

B.5.6 Solutions to the Dynamic Equation for Selected Models of R(i)

Solutions to the dimensionless dynamic equation [Equation (10)] for selected models of R(i). are presented in this section.

B.5.6.1 The Linear Model If $R(i)$ is modeled as:

$$R(i) = R_o + ni \quad ,$$

as shown in the previous section, this leads to

$$\bar{R}(i) = \frac{R_{ref}R_{fb}}{R_I R_o} I + 1 \quad .$$

Defining $\bar{T} \equiv \frac{R_{ref}R_{fb}}{R_I R_o}$, Equation (10) becomes

$$\frac{\partial}{\partial \tau}\left\{\bar{T}I^2 + I\right\} = I(\bar{T}I+1)\left\{1 + \frac{G_1}{G_2}\frac{\bar{T}}{\bar{T}I+1}\right\} \quad .$$

or

$$\frac{\partial I}{\partial \tau} = I\,\frac{\bar{T}I+1}{2\bar{T}I+1}\left\{1 + \frac{G_1}{G_2}\frac{\bar{T}}{\bar{T}I+1}\right\} \quad . \tag{18}$$

This equation can be integrated analytically by separation of variables and then expanding the result in partial fractions. However, for the generation of the family of solution curves, we prefer numerical integration. Fig. B-6 gives solution curves for I versus τ for various values of the dimensionless temperature parameter $\bar{T}$. Fig. B-7 gives similar solution curves except that the ordinate is I divided by the steady-state value of I rather than just I.

B.5.6.2 The Parabolic Model In this section, $R(i)$ is modelled as a parabolic function of current; i.e.,

$$R(i) = n'i^2 + R_o \quad .$$

Again defining a characteristic current of $I_o \equiv \left[\frac{R_{ref}R_{fb}}{R_I n'}\right]^{\frac{1}{2}}$ leads to

$$R(i) = n'\left\{\frac{R_{ref}R_{fb}}{R_I n'}\right\}\left\{\frac{i}{I_o}\right\}^2 + R_o \quad .$$

which upon simplification yields

$$\bar{R}(i) = \frac{R_{ref}R_{fb}}{R_I R_o} I^2 + 1 \quad .$$

Substituting this expression into Equation (10) gives

$$\frac{\partial I}{\partial \tau} = I\frac{\bar{T}I^2+1}{3\bar{T}I^2+1}\left\{1+\frac{G_1}{G_2}\frac{\bar{T}}{\bar{T}I^2+1}\right\} \quad . \tag{19}$$

Again this equation is numerically integrated. Fig. B-8 gives solution curves for I versus τ for various values of the dimensionless temperature parameter $\bar{T}$. Fig. B-9 gives similar solution curves except that the ordinate is I divided by the steady-state value of I rather than just I.

References

[1] W. M. Bowser, W. H. Weinberg, Rev. Sci. Inst., 47, 583 (1976).

[2] *Handbook of Operational Amplifier Applications*, 4th Edition, Burr-Brown Corporation, 1963 (or any book on elementary operational amplifier theory).

Figure Captions

Fig. B-1 Detailed schematic of the temperature controller electronics.

Fig. B-2 Front panel layouts for the temperature controller:(a) the main electronics module; (b) the capacitor bank module.

Fig. B-3 Idealized schematic of the measurement mode configuration for the temperature controller.

Fig. B-4 Idealized schematic of the closed loop configuration for the temperature controller.

Fig. B-5 Direct current, small signal model for an ideal transistor.

Fig. B-6 Solution family of the controller dynamic equation (Equation 18) for values of the dimensionless temperature parameter $\overline{T}$ when the resistance of the aluminum film is assumed to be linearly proportional to the current flow. The ordinate is the dimensionless current I and the abscissa is the dimensionless time τ.

Fig. B-7 Solution family of the controller dynamic equation (Equation 18) for values of the dimensionless temperature parameter $\overline{T}$ when the resistance of the aluminum film is assumed to be linearly proportional to the current flow. For each curve the ordinate is the dimensionless current I divided by the dimensionless steady state current. The abscissa is the dimensionless time τ.

Fig. B-8 Solution family of the controller dynamic equation (Equation 19) for values of the dimensionless temperature parameter $\overline{T}$ when the resistance of the aluminum film is assumed to be proportional to the square of the current flow. The ordinate is the dimensionless current I and the abscissa is the dimensionless time τ.

Fig. B-9 Solution family of the controller dynamic equation (Equation 19) for values of the dimensionless temperature parameter $\overline{T}$ when the resistance of the aluminum film is assumed to be proportional to the square of the current flow. For each curve the ordinate is the dimensionless current I divided by the dimensionless steady state current. The abscissa is the dimensionless time τ.

Table B-1 Dimensionless time τ required to attain 90 % of the steady-state current with the linear and parabolic resistance models for values of the dimensionless temperature parameter $\overline{T}$.

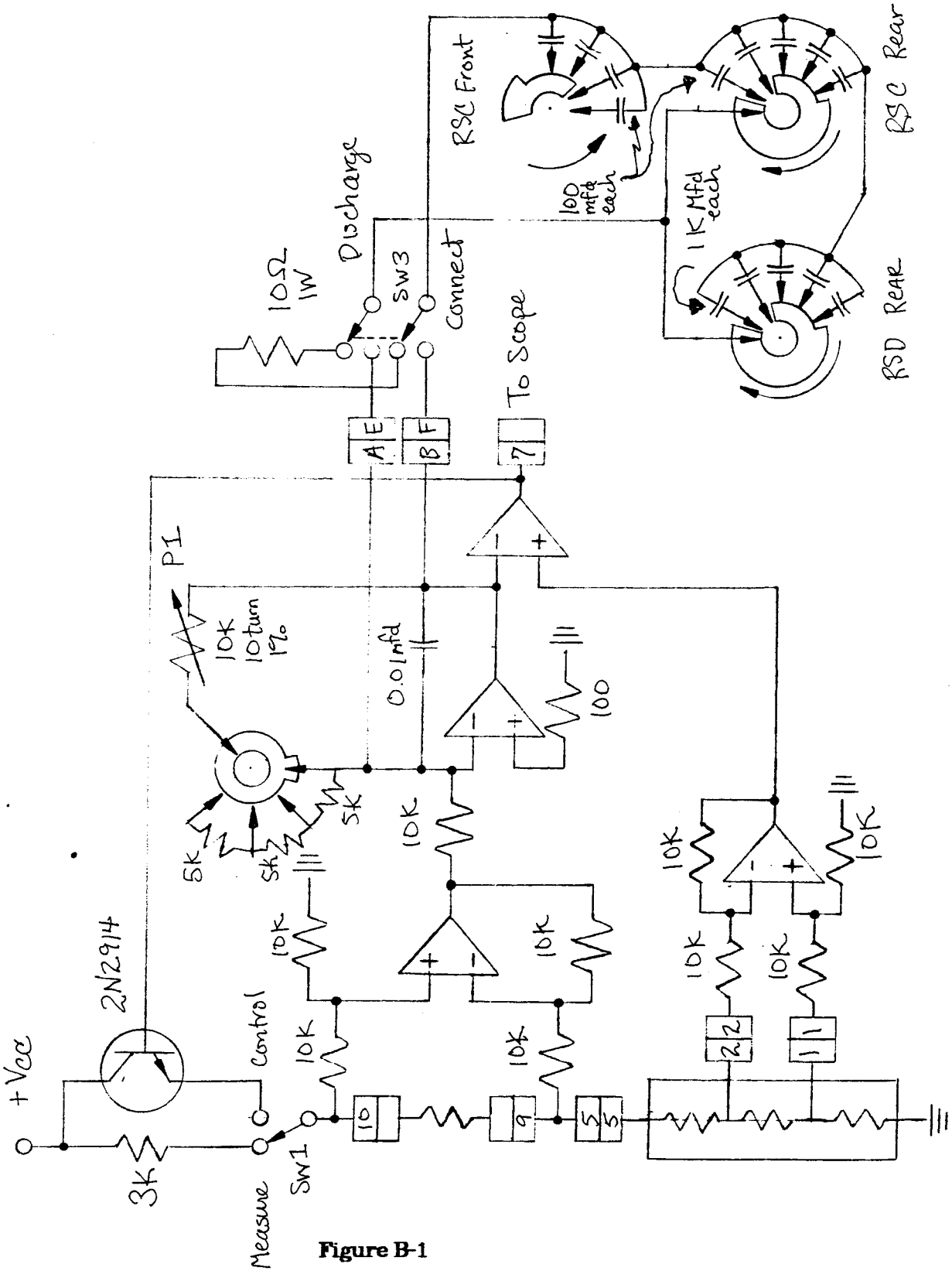
+Vcc
2N2914
3K
Measure
Control
SW1
10K
10K
10K
10K
10K
10K
10K
10K
10K
10K
10K
5K
5K
5K
P1
10K 10turn
0.01mfd
100
10
9
5
5
2
2
1
1
A
E
B
F
7
To Scope
Connect
SW3
Discharge
10Ω 1W
RSC Front
100 mfd each
1K Mfd each
RSC Rear
RSD Rear

Figure B-1

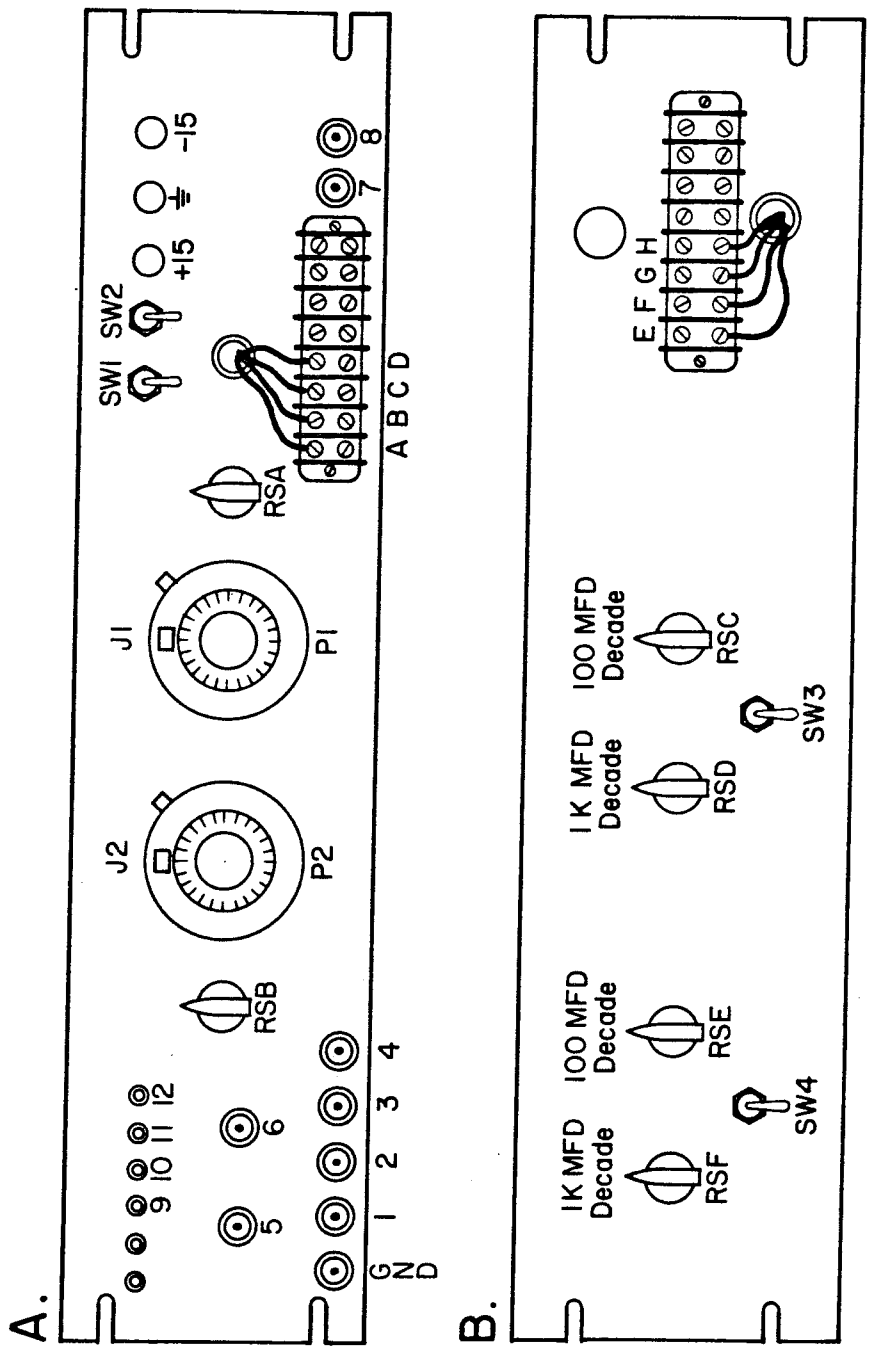
A.
B.
GND
1
2
3
4
5
6
7
8
9
10
11
12
RSB
J2
P2
J1
P1
RSA
SW1
SW2
+15
-15
A B C D
E F G H
RSF
1K MFD Decade
RSE
100 MFD Decade
SW4
RSD
1K MFD Decade
SW3
RSC
100 MFD Decade

Figure B-2

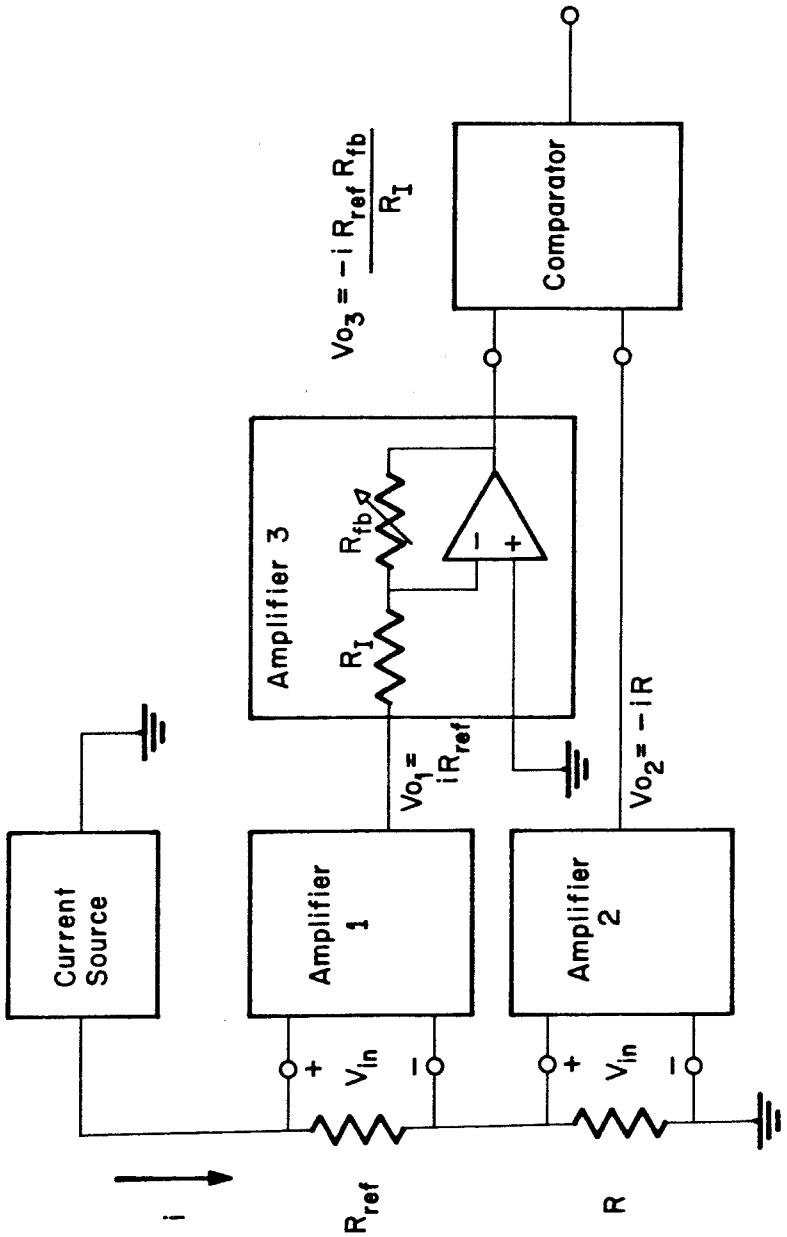
Comparator
$V_{o_3} = -i\,\frac{R_{ref}\,R_{fb}}{R_I}$
Amplifier 3
R_{fb}
R_I
$V_{o_1} = iR_{ref}$
$V_{o_2} = -iR$
Current Source
Amplifier 1
Amplifier 2
+ V_{in} −
+ V_{in} −
i
R_{ref}
R

Figure B-3

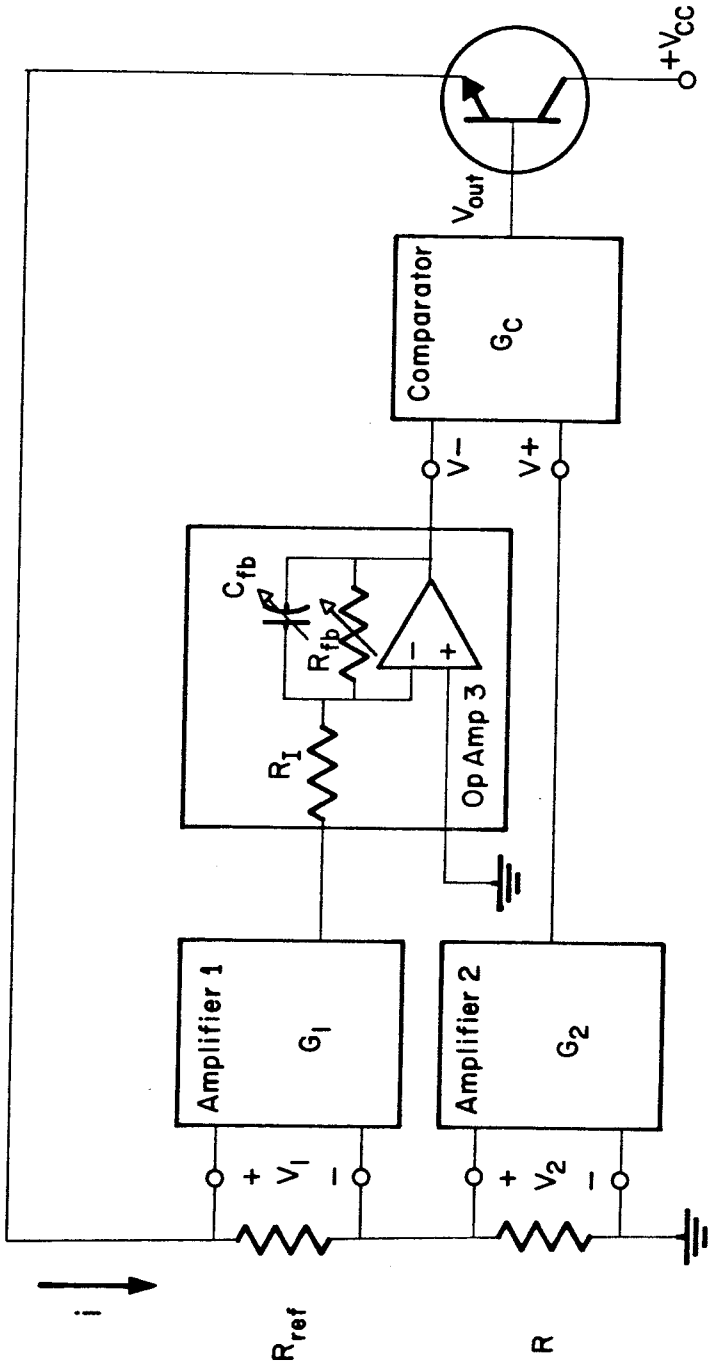
+Vcc
Vout
Comparator
Gc
V−
V+
Cfb
Rfb
R1
Op Amp 3
Amplifier 1
G1
Amplifier 2
G2
+ V1 −
+ V2 −
i
Rref
R

Figure B-4

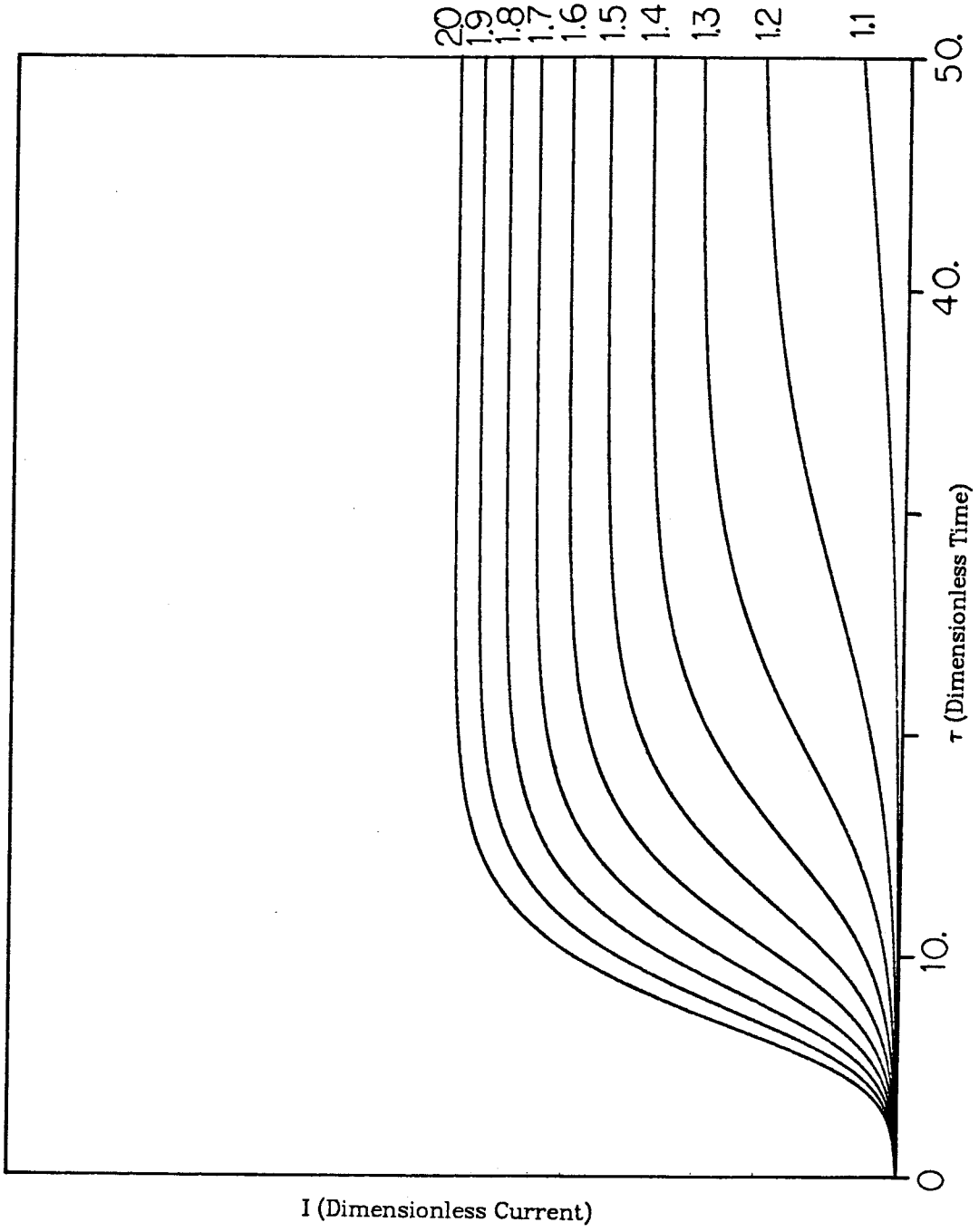
2.0
1.9
1.8
1.7
1.6
1.5
1.4
1.3
1.2
1.1
50.
40.
10.
0
τ (Dimensionless Time)
I (Dimensionless Current)

Figure B-6

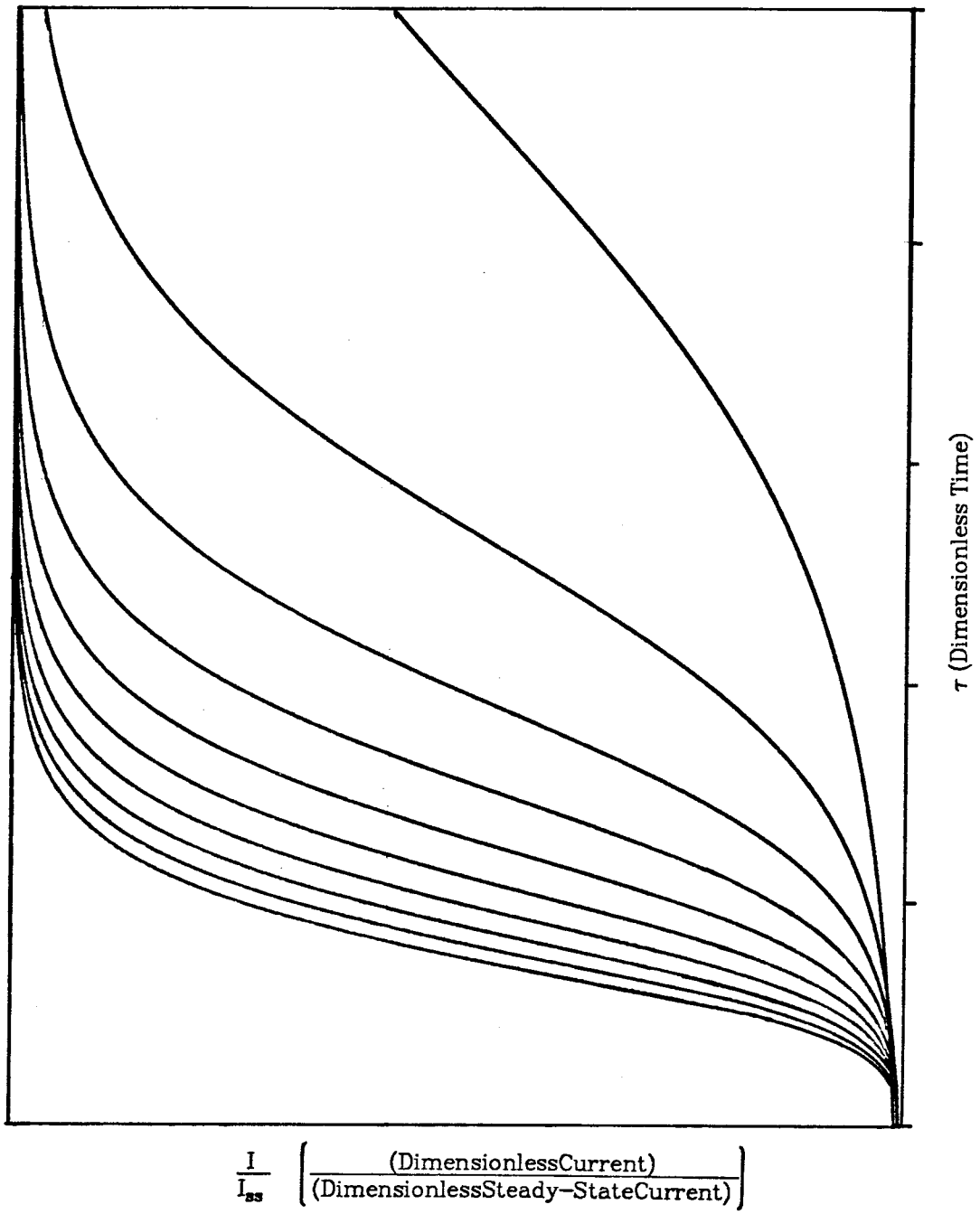
τ (Dimensionless Time)
I/I_ss (DimensionlessCurrent)/(DimensionlessSteady-StateCurrent)

Figure B-7

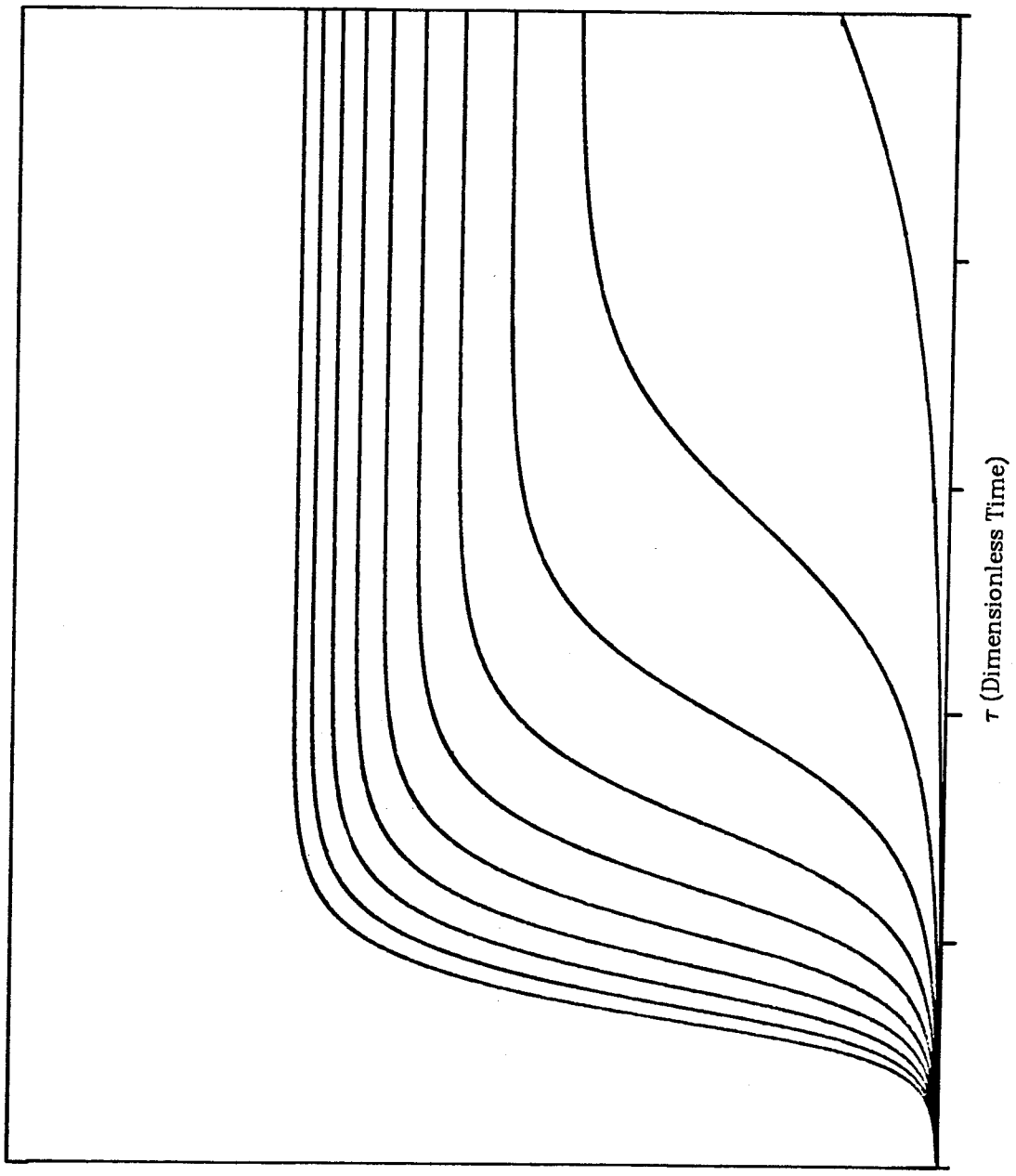

Figure B-8

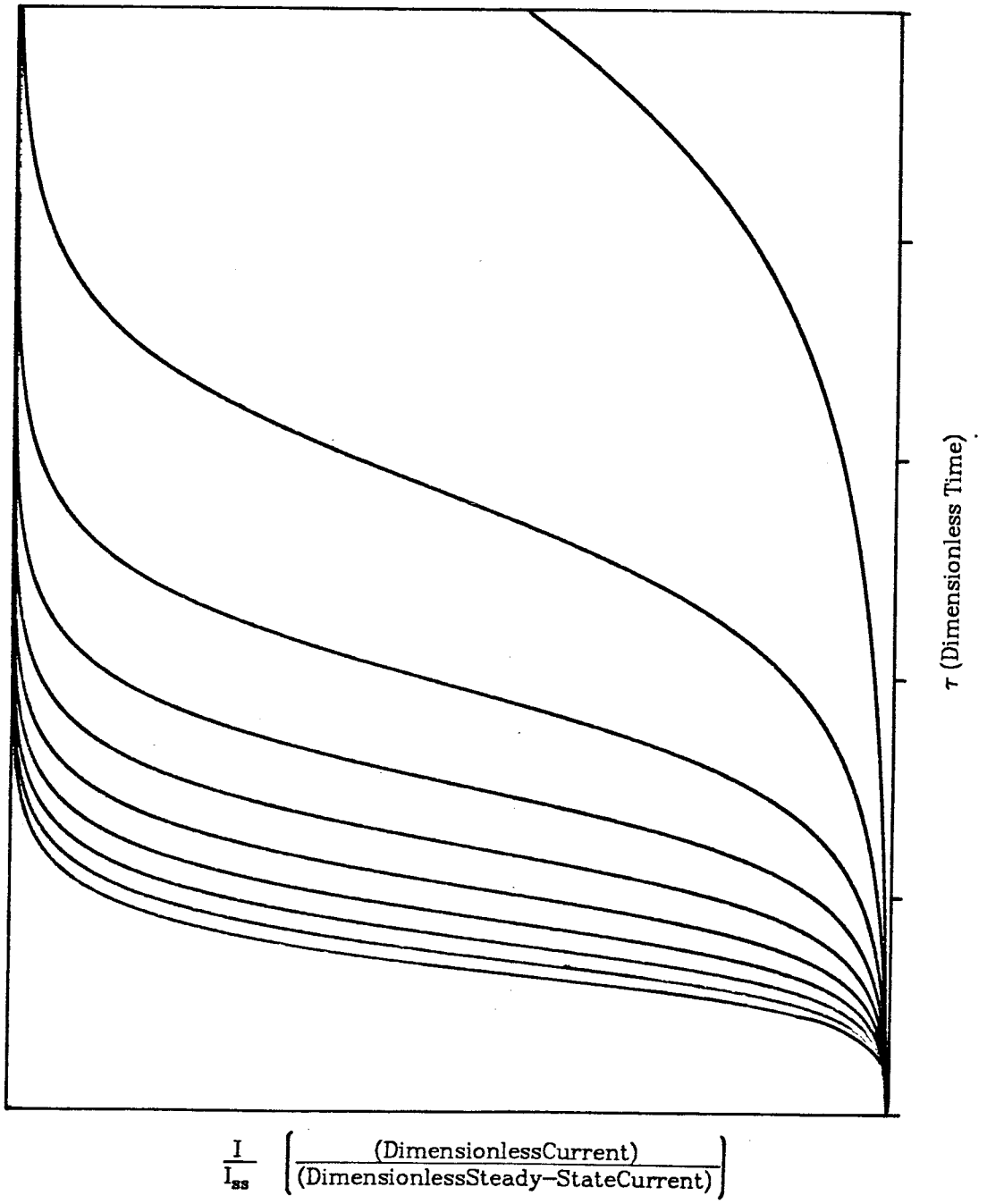
τ (Dimensionless Time)
I/I_ss ((DimensionlessCurrent)/(DimensionlessSteady–StateCurrent))

Figure B-9

$\bar{T}$	$\bar{R}(i) = \bar{T}I+1$	$\bar{R}(i) = \bar{T}I^2+1$	$\Delta T(°C)$
1.1			50
1.2	49.87	41.62	100
1.3	36.37	29.62	150
1.4	30.00	24.00	200
1.5	25.50	19.87	250
1.6	22.50	18.37	300
1.7	20.62	15.75	350
1.8	19.12	14.25	400
1.9	17.62	13.12	450
2.0	16.50	12.37	500

Appendix C:

A Versatile Tunnel Junction Fabrication System

C. A Versatile Tunnel Junction Fabrication System

C.1 Introduction

A versatile tunnel junction fabrication system has been developed by the author. It includes provisions for the study of adsorption and reaction between 200 K and 673 K and between atmospheric pressure and 1 x 10^{-9} Torr. An ancillary manifold handles gaseous dosing of the surface with a wide variety of materials, including those with vapor pressures as low as 100 microns. In addition, the instrument easily handles liquid solution dosing. This instrument was used to fabricate all of the tunnel junctions discussed in this thesis.

Intended for future users, this appendix is to serve as both maintenance/operating guide and a forum for suggested improvements. However, the subtle nuances of all the diverse methods for fabricating tunnel junctions are not discussed. Some attention has been given to them previously [1-3]. In a concession to this point, the parameters and procedure for orchestrating a plasma oxidation in this system are discussed in Section C.6. This is a critical step that lies at the center of success in tunneling. In general, however, features such as layout and design of the system are documented.

To this end, Section C.2 presents an abbreviated description of the system. Section C.3 discusses some of the design objectives and the importance of these in retrospect. Section C.4 provides important maintenance information and layout documentation for the subsystems of the bell jar. These include the general layout of the main chamber (Section C.4.1), the system plumbing (Section C.4.2), the electrical interconnections for the substrates and deposition monitors (Section C.4.3), the plasma oxidation electrode assembly and high voltage hookup (Section C.4.4), and the evaporation sources (Section C.4.5). Section C.5

suggests both simple and more elaborate modifications to improve the versatility of the instrument. Finally, Section C.6 gives the procedures for bringing the system to atmospheric pressure, down to high vacuum, and for carrying out a plasma oxidation. At this point, we would like to acknowledge the work by Bill Bowser [4] in designing the top plate assembly of the fabrication system. This includes the mask, shutter, substrate assemblies and the differentially pumped o-ring seal. Details concerning these items have been reported elsewhere [4].

C.2 System Description

The UHV compatible tunnel junction fabrication chamber consists of a 50-liter stainless steel bell jar of cylindrical shape (see Fig. C-1). The bottom is permanently closed. The top is closed by a removable circular stainless steel plate that seals down on the bell jar by means of a differentially pumped set of viton o-rings. Two tunnel junction substrate holders are mounted on cold (or hot) fingers, which are flanged to the top plate. The top plate also supports the shutter and mask assemblies, electrical feedthrough, auxiliary cold finger and two deposition monitors (one positioned close to the auxiliary evaporation source, the other in the plane of the substrates). Rough pumping is accomplished with two molecular sieve cryo-sorption pumps. Handling gas pressures in the 200 micron to 10^{-5} Torr (the higher end is typical of the oxygen pressure for plasma oxidation), is facilitated with a 2" cryo-trapped oil diffusion pump mounted on a 1½" feedthrough port. For attainment of UHV, a 500 l/sec ion pump (with throttle valve) is used. Three common cathode metal evaporation sources are positioned beneath the tunnel junction substrates in the bottom half of the bell jar; a 20 kva supply provides power. Oxidation electrode (cathode) and shield (anode) are symmetrically positioned with respect to the substrates against the bell jar side wall; the shield eliminates line-of-sight ion

trajectories between the naked cathode and the substrates. At this stage, the system is equiped to introduce adsorbates only as gases and with vapor pressure in excess of 100 microns. However, excellent results with air stable solids are achieved through solution dosing with the chamber opened to air. UHV and Millitorr ionization gauges, and a capacitance manometer gauge is used for Bayard-Alpert pressure measurement of reactive gases. A quadrupole mass spectrometer monitors the residual gas composition.

C.3 Design Objectives

The overriding design consideration for this tunnel junction fabrication system was UHV compatibility. This was emphasized because it would allow a number of new approaches incompatible with high speed oil diffusion pumped systems. Primarily, the ultralow background gas pressure of the UHV environment opens up the field of reactive group VIII transition metals for study, presumably in the form of evaporated metal clusters or partially decomposed/anchored organometallic complexes supported on the Al_2O_3 tunnel junction barrier. Secondly, the lower outgasing properties of UHV compatible materials and lower seal leakage rates make mass spectrometry feasible. A quadrupole mass spectrometer could possibly be used in identifying desorption products, not only of steady-state catalytic reactions, but also transient species following chemisorption or surface species transformation. In addition, thermal desorption spectroscopy from smooth oxide films would be within technical reach, providing adsorbate surface binding energies for some systems, as well as important desorption product mass data in thermally activated decomposition reactions.

In practice, neither of these ends was achieved. The reasons for this lay partly in Paul Hansma and co-workers' success or lack success in studying CO chemisorption on virtually every group VIII transition metal: Fe, Co, Ni, Ru, Rh,

Pd and Pt [5]. Surely they would have examined Ru, Ir and Os also, had it not been for the extreme experimental difficulties encountered evaporating these three metals [6]. Of all metals, osmium has the strongest metal-metal bond and consequently requires enormously high evaporation temperatures, as does Ir. However, aside from not leaving any easy experiments, one extremely troubling point of Hansma's studies were the low intensities observed for the CO stretching modes. This same problem was also apparent in tunneling studies of Al_2O_3 supported organometallic complexes [7,8]. Whether these results are a manifestation of a fundamental limitation, such as the geometry associated with the large size of the supported clusters, or are due to simple technical problems such as low coverage and/or insufficiently high vacuum is currently unknown.

In addition, work with supported metals would be tedious. Unlike UHV single crystal work, tunneling requires breaking vacuum after every experiment. Thus, an unreasonable amount of time would be expended between experiments just baking out the fabrication system to achieve UHV. (Although the lowest pressure thus far attained has been approximately 1×10^{-9} Torr, it was reached with only a mild bake and so the system does appear to be capable of UHV.) Furthermore, the system would need rebaking after the plasma oxidation since this unavoidably introduces considerable amounts of water into the chamber. Finally, as if this is not discouraging enough, Hansma and co-workers made use of a thermal oxide, which was grown at high temperature in atmosphere, for their supported metal experiments [3]. Their plasma grown oxides performed unsatisfactorily, and whether ours would perform acceptably remains to be seen.

The use of a residual gas analyzer to monitor surface reactions was of little success. Because probabilities of adsorption are low on oxides, high dosing pressures are needed which cause severe background problems. An attempt was

made to study thermal desorption from low area oxide surfaces. An aluminum film of approximately 1 cm^2 area was evaporated onto a pyrex substrate. An oxide layer was grown with an oxygen plasma. The surface was cooled to ~200 K and dosed extensively with H_2O. The film was then heated rapidly by passing a large current through it, while the residual gas analyzer was set to monitor gaseous H_2O (the base pressure was ~1 x 10^{-8} Torr). Two problems were associated with this setup: (1) Although there was a small but noticeable change in the H_2O pressure, it was too small to provide workable data, and (2) The metal films microfractured at high heating rates. The project was subsequently abandoned, partly because spatial limitations did not allow easy trial of alternatives.

In retrospect, even though the attainment of UHV proved insignificant, the most useful aspects of the fabrication system are a consequence of adherence to a UHV design philosophy during its construction. This is reflected in the single most important feature of the system, which is the ion pump. It means that the system stays under vacuum. Consequently, experiments can be done without waiting for a two-hour pumpdown, as with the diffusion pumped systems. The UHV design principles also translate into cleanliness; only traces of hydrocarbon contamination are present in the fabrication system. It can be baked repeatedly. This is especially important when changing adsorbates. These factors contribute to the overall quality and ease of interpreting the spectra. Finally, lower residual H_2O pressures can be obtained in the UHV environment. This is important for experiments examining adsorption at 200 K or the effects of thermal pretreatment.

Many other remaining features of this fabrication system alleviated the tediousness experienced with the old IETS system [1,4]. Mask positioning and substrate loading and unloading are easier than previously. The evaporation sources require less maintenance. Leaks are found easily with a quadrupole

mass spectrometer. The cryo-trap can go seven hours without refilling. The main chamber, manifold and controls are arranged ergonomically. A temperature controller is present for substrate heating. It is often the attention to details that delineates success from failure.

There are two final important features. The ability to perform solution dosing easily with little observable contamination and with good repeatability, proved crucial to the success of the work with dimethyl methyl phosphonate, and will continue to be an extremely useful procedure. In addition, the extremely leak-free manifold gave excellent results when working with low vapor pressure compounds.

In summary, although our initial objectives were not achieved, they still lead to the construction of a very versatile instrument for tunnel junction fabrication.

C.4 Specifications

C.4.1 Layout of the Main Chamber

A frontal outside view of the main chamber is shown in Fig. C-1. The inside space is partitioned into three sections. The top section (Section 1) consists of all hardware attached to the top plate. This includes the mask, shutter and substrate holders, which are documented elsewhere [1]. It also includes an electrical feedthrough and connections to the substrates and deposition monitors, which are discussed later. Below is Section 2 which consists of 10 2-3/4" conflat ports and their associated feedthroughs and instruments. Figure C-2 depicts slice through Section 2 and gives the function of each feedthrough port. About 10 inches below Section 2 is Section 3. This section consists of the evaporation sources. Spanning between Sections 2 and 3 are OFHC copper conductors that

supply current to the evaporation sources.

C.4.2 Fabrication System Plumbing

The fabrication system plumbing is shown in Fig. C-3. It can be divided into three subassemblies: (1) the diffusion pump and foreline [Fig. C-3a], (2) the roughing line and cryo-sorption pumps [Fig. C-3b], and (3) the dosing line and manifold [Fig. C-3c]. Interconnections between these assemblies are minimal, but contribute to the overall flexibility and ease of use. In some cases they necessitate extra care. For example, the case of the diaphram gauge, which resides on the manifold, is kept evacuated through the diffusion pump foreline. Therefore, the foreline should not be subjected to high pressures without first isolating this gauge from the foreline by closing valve F4. Similarly, the case should not be pressurized from the manifold side without first closing F4. Also note the connection to the old IETS manifold [1]; both the high purity nitrogen and research grade oxygen are obtained through this connection.

The diffusion pump and foreline assembly [Fig. C-3a] consist of a Varian M2 diffusion pump and cryo-trap, a pneumatically controlled foreline isolation valve (F2), and a dedicated mechanical pump with a molecular sieve trap. A 1½" polyamide sealed right-angle valve (F1) connects the diffusion pump to the main chamber. Although every effort was made to maximize the conductance of this connection, it is estimated to be only between 10 and 20 liters per second. The foreline pressure is monitored by thermal couple gauge TCF.

Since the foreline is at maximum vacuum during operation of the diffusion pump, it is also convenient to install two other systems requiring continuous evacuation on the foreline. Valve F3 couples the foreline to the differential pumping section of the top plate o-ring seal. In addition, the case of the diaphram gauge is kept evacuated through valve F4.

A 1½" viton sealed right-angle valve (R1) isolates the main chamber from the roughing line by cryo-sorption pumps [Fig. C-3b]. One of these is sufficient for the entire roughing task at any one time. A thermocouple gauge (TCR) monitors the pressure in roughing line. Valve R2 functions as the atmospheric pressure vent valve. It connects the roughing line to the high purity nitrogen cylinder through the old IETS manifold.

A compact and versatile manifold is connected to the main chamber through a minimum length dosing line [Fig. C-3c]. The dosing line passes sequentially from the manifold through a backing valve (M2) and a metering valve (M1) into the main chamber. The line passes into the chamber through a 1/4" O.D. stainless steel tube welded into a double-sided conflat flange. The line continues inside the chamber via a 10" flexible stainless steel tube, the end of which terminates approximately 5" below the substrates and is directed at them. Stainless steel cajon VCR glands with OFHC copper gaskets and welded connections are used throughout the dosing line.

The manifold is comprised of both a glass section and a metal section. To prevent breakage, a flexible metal-to-glass transition tube connects the two sections. The metal section can be isolated from the glass section by closing valve M7. A dedicated mechanical pump with a molecular sieve trap furnishes the vacuum through valve M8. A thermocouple gauge (TCM), which is connected to the glass section, and a sensitive differential diaphram gauge (Wallace and Tiernan model #FA145), which is connected to the metal section via valve M4, monitor the pressure in the manifold. Special care should be taken when using the diaphram gauge. It should never be subjected to fast pressure changes or differential pressures of over 310 Torr (6.0 psi). For example, before venting the manifold to atmosphere, the isolation valve (M4) for this gauge must be closed. In general, keep M4 closed as often as possible. The valve M4 opens directly on

the capsule of the diaphram gauge. On the other hand, the case of the diaphram gauge is pumped continuously by the foreline mechanical pump through valve F4. The pressures between the capsule and case may be equalized by opening valve M3. In general, this is never done. If this should be done, then the effect of this action on the foreline pressure should be considered carefully. For example, if M3 is opened *without* closing valve F4, then supposing there was a high pressure in the capsule, the pressure in the foreline would increase. If the diffusion pump is running at the time, this action would lead to disastrous consequences. Therefore, exercise extreme caution: DO NOT MISTAKE VALVE M3 FOR VALVE M4.

Stainless steel bellows valves connected by stainless steel cajon VCR glands with OFHC copper gaslets are used throughout the metal section of the manifold. Consequently, it will handle a wide range of materials from ultralow vapor pressure compounds to high pressure gases. When using either of these materials, the glass section of the manifold is closed off with valve M7 to reduce the working volume. The manifold is connected to the old IETS manifold through valve M5. This is important since the sources of high purity nitrogen and research grade oxygen reside on the old IETS manifold. The glass section of the manifold is constructed of heavy wall pyrex tubing and greaseless stopcocks. Connections to this section are made via either 3/8" ultratorr-type connectors are type M o-ring connectors.

C.4.3 Electrical Connections on the Top Plate

A single 8 pin UHV electrical feedthrough provides connection to the substrates and deposition monitors. The feedthrough is rated at 7 amps per wire and 700 V DC. Viewed from inside the main chamber, the connections between the feedthrough and the substrates are shown in Fig. C-4. Table C-1 enumerates the

pinouts to the feedthrough in terms of the 4-wire connections for substrate heating, as indicated by Bowser and Weinberg [9]. The identification numbers of the cables mating with the appropriate feedthrough pins are also listed in Table C-1. These cables connect the feedthrough to the temperature controller as described in Appendix B. Two deposition monitors are also connected to the top plate. One of these is mounted in the plane of the substrates, and is connected to the feedthrough as shown in Fig. C-4 and listed in Table C-1. The second deposition monitor is mounted so as to be much closer to the auxiliary evaporation source, which is principally used for depositing monolayer and submonolayer thick films. Because of the much closer position, the deposition rate as measured by this monitor is approximately 25 times the true rate at the substrate surface. There are an insufficient number of pins on the octal feedthrough to accommodate a connection to the second monitor. Therefore, in order to use this monitor, a second electrical feedthrough must be installed on the "spare" top plate feedthrough, which currently is mounted with an auxiliary cold finger.

C.4.4 Plasma Oxidation Electrode Assembly

The plasma oxidation electrode assembly is shown as viewed from inside the main chamber in Fig. C-5. It consists of an UHV/low vacuum high voltage electrical feedthrough, cathode electrode, anode electrode (discharge shield) and anode electrode holder. The electrode assembly is positioned symmetrically with respect to the substrates, against the main chamber wall. The novel design of the high voltage electrical feedthrough is partly responsible for the success of the unit. Standard commercial UHV high voltage feedthroughs function inadequately in this application. This is because most UHV compatible feedthroughs are designed to carry high voltages at UHV and not at pressures of 200 microns.

This novel feedthrough is made in the following way. A metal-to-glass transition tube is inserted through a clearance hole in a blank conflat flange and welded so that the metal-to-glass transition will be on the vacuum side. A long tungsten wire is inserted into the tube so that it extends out both ends. The end of the glass tube is then melted to form a UHV seal around the tungsten wire which becomes the high voltage conductor. The sealed glass tube is then bent to the desired shape.

The cathode consists of a 4" long, 2 mm diameter aluminum rod of 99.99% purity. It is fastened to the high voltage feedthrough by means of a hollow shaft with two set screws. On the other hand, a hexhead cap screw clamps the anode into the holder. The holder assembly clamps to the current feedthrough for the Pb source. Thus it is important to ground this feedthrough on the atmosphere side when running the plasma oxidation.

Cleaning the anode (discharge shield) is unnecessary. The only periodic maintenance need by the assembly is to readjust or replace the aluminum cathode, since during the course of months this electrode droops. This can be seen through the viewing port. Usually it can be straightened by gently lifting the drooping end with a gloved finger. After many such straightenings it will be necessary to replace the aluminum cathode. To gain access to the cathode assembly, it is necessary first to remove the anode. To do this, loosen the hex-head cap screw fastening the anode. Never loosen any other screws, since this may permanently change the geometry and consequently also the oxidation parameters. Carefully lift out the anode once it is loose. Now the cathode can be disassembled. With a 1/32" Allen key, carefully loosen the set screw holding the hollow shaft to the high voltage feedthrough. Carefully slide the shaft off the high voltage feedthrough. Unloosen the other set screw in the hollow shaft; pull out the old anode and replace it with a new one. Align it carefully in the

hollow shaft and tighten the set screw. Reassemble in the reverse order. A general word of caution: *be extremely careful to avoid stressing the high voltage feedthrough. If it breaks, restoring it will consume many hours.* Before using it in experiments, the new anode should be "burned in" with a preliminary glow discharge for about 30 minutes. The procedure given in Section C.6 should be followed in this endeavor.

The high voltage connection to the plasma oxidation electrical feedthrough is shown in Fig. C-7. The current during the oxidation is monitored by measuring the voltage drop across a resistance of 2.5 K ohms. The oxidation is typically run with a 40 V drop, which corresponds to a current of 16 milliamperes. *During the oxidation, the Simpson meter floats at high voltage. Therefore, to avoid shock, do not touch any of the leads.*

C.4.5 The Evaporation Sources

The evaporation sources assembly is shown in Fig. C-7. It consists of three common cathode sources. The overall design geometry maximizes access for loading and maintenance in the restricted environment deep within the bell jar. The modular construction minimizes heat transfer between the individual sources and simpifies fabrication. The sheet metal parts of the design were executed in 0.008" stainless steel to minimize the weighting on the supporting feedthroughs. The chimneys on the covering boxes provide additional collimation. The front most source presently contains an isolated hot zone 4" x 3/4" x 0.005" Mo boat, which is used to evaporate Pb. Because of its large size, it need be replenished only every four or five evaporations. The center source accommodates a coiled W filament consisting of four strands of 0.030" W wire. The binding posts in this center source are designed especially to accommodate this type of filament. When changing this filament it is especially important to replace the ½" x 0.005"

Mo shielding rings completely over the post. Failure to do so will allow aluminum metal to plate the filament hold-down screw of the binding posts, which will cause the hold-down screws to jam. The far most source is an auxiliary source. Aside from changing filaments, the only periodic maintenance needed by the sources is an occasional cleaning by soaking in a concentrated KOH solution to remove thick metal deposits. This is required more frequently for the source covers, which are designed to accumulate most of the deposits, than for the source pan. In order to remove the pan, first remove all filaments then undo the two 4-40 pan fastening screws which are located next to the cathode binding post of the center source. Reassemble in the reverse order.

C.5 Improvements

Based on considerable experience, a number of worthwhile modifications to the fabrication system can be suggested. The most important of these would be to increase the number of substrates. This number could be doubled from two to four with only a modicum of effort. The gain would represent a very significant increase in system throughput. The envisioned modification would consist of extending each substrate holder to accommodate two substrates rather than one. The top of the mask table would also need to be redesigned somewhat to accommodate this change. However, if it is decided upon this improvement, then it might be more efficient in the long run to completely redesign the top plate. Although some excellent design principles are exploited therein, it still has a number of shortcomings. For example, there are too few feedthroughs on the system, and several more may be designed into the new top plate. Another extremely nagging point is the tendency of the o-rings to fall out of their grooves. Dovetailing or semi-dovetailing the o-ring grooves in a new top plate would remedy this.

Oxides seem to be intrinsically less "sticky" than metals. Therefore, it would be especially attractive to be able to study surface reactions on oxides at much higher pressures. Due to the large volumes present, this is infeasible with the current system. However, it is possible to modify the current system in the way shown in Fig. C-8 to incorporate a small, insolatable high pressure section into which the substrate could be withdrawn. This design is quite similar to instruments currently used for studying the properties of metal surfaces subjected to reactions at high pressures.

C.6 Procedures

C.6.1 Up to Atmosphere

1. Set the mask and shutter to the center position. Turn off both ionization gauges.
2. Make certain the popett valve to the ion pump and the diffusion pump isolation valve (F1) are closed.
3. Close the valve to the differentially pumped section of o-ring seal (F3).
4. Check to make sure backing valve (M2) on the dosing line is closed, metering valve (M1) on the dosing line is open and the valve from the manifold to the old IETS manifold (M5) is closed.
5. Fill the old IETS manifold with approximately 760 Torr of high purity N_2.
6. Open roughing line isolation valve (R1).
7. Open the up-to-air valve (R2) on the roughing line. This vents the main chamber to the old IETS manifold and will cause the pressure there to decrease to a few Torr. Continue pressurization of the main chamber by admitting more N_2 to the old IETS manifold until the chamber is at one

atmosphere.

C.6.2 Evacuation

1. Wipe the o-ring surface and the sealing surface of the chamber with ethanol.
2. Carefully close up the main chamber. Make sure the o-rings stay in their grooves. If they fall even partly out of the grooves, open the chamber fully and reposition them in the grooves.
3. Chill a vacsorb pump. Check the foreline pressure (TCF). It should be below 30 microns. Then make sure the foreline isolation valve (F2) is open. Fill the cryo-trap with LN_2 and only then turn on the diffusion pump.
4. Close the up-to-air valve (R2) on the roughing line and full open the roughing line isolation valve (R1).
5. After a sufficient cooling period, open the isolation valve to the chilled vacusorb pump. During this step, it is essential for the top plate to form a good deal with the main chamber. To form such a seal it is usually necessary to press down on the top plate. Alternatively, two 'C' clamps can be used to apply pressure evenly. Then, once the vacuum develops, the clamps may be removed.
6. After the chamber pressure has fallen below 1 Torr, the differential pumping section of the o-ring seal should be evacuated. Special care must be exercised in doing so because this is done through the diffusion pump foreline while the diffusion pump heater is on. In addition, the case of the diaphram gauge should not be subjected to a high pressure. Therefore, both the foreline isolation valve (F2) and the valve to the case of the diaphram gauge (F4) should be closed prior to opening the valve to the differential pumping section (F3). On opening this valve (F3), the foreline pressure will shoot above 2

Torr. If it fails to do so, then the inner o-ring is improperly seated. In this case, bring the chamber back up to atmosphere and start again at Step 1. Assuming this is not the case, a few minutes after the valve to the differential pumping section (F3) has been opened, the foreline pressure will again fall below 30 microns. The valve to the case of the diaphram gauge (F4) and the foreline isolation valve (F2) should be reopened. ***Failure to do the latter could result in irreparable contamination to the chamber in Step 8.***

7. When the pressure falls below 100 microns, the millitorr gauge can be used to monitor further pressure decreases.

8. When the pressure falls below 10 microns, the pumping should be switched to the diffusion pump. To do this, first close the roughing line isolation valve (R1). Then close the vacsorb isolation valve. Check to see that the diffusion pump is hot (warm-up time is approximately 20 minutes), and that the cold trap is full of liquid nitrogen. The diffusion pump isolation valve should be opened very slowly while monitoring the foreline pressure, and the system pressure. The former should not be allowed to rise above 60 microns, and the latter should begin moving slowly downwards.

9. When the diffusion pump isolation valve is fully open, the bakeout heaters may be turned on. The heaters consist of heating tapes powered by variable voltage transformers. These are preset so the temperature near the differential o-ring seal remains at a safe level. In addition, since the poppet valve is closed, its viton seal is kept below 125°. Do not switch all the bake-out heaters on simultaneously. The sudden inductive load will trip the circuit breaker.

10. The main chamber bakeout is continued for three to six hours under the

diffusion pump. At this point the pressure is below 2 x 10^{-5} Torr, and it is desirable to switch over to the ion pump. With the UHV ionization gauge turned off, the poppet valve is very slowly cracked. The seal should turn freely but the ion pump should remain closed. It is important to do this slowly as there is usually a high pressure gas pocket trapped in the seal. Fully close the diffusion pump isolation valve and then fully open the poppet valve. This will cause a rather dramatic pressure decrease. Fill the cryo-trap with liquid nitrogen if further use of the diffusion pump is planned. Otherwise, turn it off. The bakeout is continued for one to three hours under the ion pump. Switching the bakeout off when the pressure reaches 1 x 10^{-7} Torr will result in a system pressure of approximately 1 x 10^{-8} when cool. This is adequate for most applications.

C.6.3 Plasma Oxidation

1. *Preliminary Setup:* Set the mask in the center position and close the shutter. Turn off the UHV ionization gauge. Begin chilling a vacsorb pump. Set up the diffusion pump in accordance with Item 3 of the evacuation procedure. Set up the Simpson meter as shown in Fig. C-6. Make sure the connections do not short to ground. Set the meter range to 50 V dc. Turn the high voltage power supply to standby. Set the voltage for -1100 volts.

2. *Preparing the Mixture:* Make sure the backing valve on the dosing line (M2) is closed. Close the metering valve (M1). Check the pressure in the manifold. It should be about 60 microns. Open the valve to the diaphram gauge (M4). Purge the manifold several times by repeatedly opening and closing the valve to the distilled H_2O flask in conjunction with opening and closing the mechanical pump isolation valve (M8). Then fill the manifold with 2.0 Torr of H_2O. Move to the old IETS manifold. Purge it with a small amount of

research grade O_2. Then fill it to approximately 450 Torr of O_2. Move back to the manifold and slowly fill it to a pressure 4.0 psia (207 Torr) with O_2 by slowly opening the valve to the old IETS manifold (M5) for the required length of time.

3. *Running the Oxidation:* Isolate all pumps from the main chamber. Open the backing valve on the dosing line (M2) and by slowing opening the metering valve (M1) fill the main chamber with approximately 100 microns of the manifold mixture. Turn the millitorr gauge off and unplug the connectors at the heads of the millitorr and UHV ionization gauges. Turn the high voltage power supply to high voltage and simultaneously start the timer. *Keep away from the Simpson meter.* It should be registering approximately 30 V, which indicates an oxidation current of 12 milliamperes. Over a period of about 30 seconds, continue increasing the pressure in the main chamber until the Simpson meter is registering 40, which indicates a current of 16 milliamperes. Keep the Simpson meter at this level by opening or closing the metering valve. When the timer reaches 60 seconds, fully open the shutter. When the total oxidation time expires, turn the high voltage power supply to standby and close the shutter.

4. *Evacuation:* Close the backing valve on the dosing line (M2) and then fully open the metering valve (M1). Open the isolation valve to the chilled vacsorb pump and then open the roughing line isolation valve (R1). Monitor the pressure decrease with either the millitorr or Barritron gauges. Switch over to the diffusion pump as described in Item 8 of the Evacuation Procedure.

References

[1] H. E. Evans, PhD Thesis, California Institute of Technology, Pasadena, California, 1980, p 204.

[2] P. K. Hansma, Phys. Reports **30**, 145 (1977)

[3] R. M. Kroeker, P. K. Hansma, submitted to Catalysis Rev. Sci. Eng..

[4] W. M. Bowser, PhD Thesis, California Institute of Technology, Pasadena, California, 1980, p 268.

[5] R. M. Kroeker, in *Tunneling Spectroscopy*, Plenum Press, New York, 1982, p 353.

[6] *Thin Film Equipment Catalogue*, Sloan Technology Corporation, 1973, p 150.

[7] W. M. Bowser, W. H. Weinberg, J. Amer. Chem. Soc. **103**, 1453 (1981).

[8] Ibid., 102,4720 (1980).

[9] W. M. Bowser, W. H. Weinberg, Rev. Sci. Instrum. **47**, 583 (1976).

Figure Captions

Figure C-1 Front view of the main chamber delineating Sections 1, 2 and 3.

Figure C-2 Slice through Section 2 of the main chamber. (**a**) capacitive manometer, (**b**) Millitorr ionization gauge, (**c**) Bayard Alpert gauge, (**d**) high current feedthrough to evaporation source common, (**e**) diffusion pump isolation valve, (**f**) high voltage feedthrough to plasma discharge cathode, (**g**) plasma discharge anode (at ground potential), (**h**) vacuum line to manifold, (**i**) dosing line nozzle, (**j**) viewing port, (**k**) Pb evaporation source, (**l**) Al evaporation source, (**m**) auxillary evaporation source, (**n**) quadrupole mass spectrometer.

Figure C-3 Fabrication system plumbing. (a) Diffusion pump and foreline. (b) Roughing line and cryo-sorption pumps. (c) Dosing line and manifold.

Figure C-4 Electrical connections to substrates and deposition monitors as viewed from inside the main chamber.

Figure C-5 Plasma oxidation electrode assembly as viewed from inside the main chamber.

Figure C-6 High voltage connections to the plasma oxidation electrical feedthrough.

Figure C-7 Exploded view of the evaporation sources.

Figure C-8 Modifications for the integrated high pressure reactor.

Table C-1 Pinout and Functions for top plate electrical feedtrough.

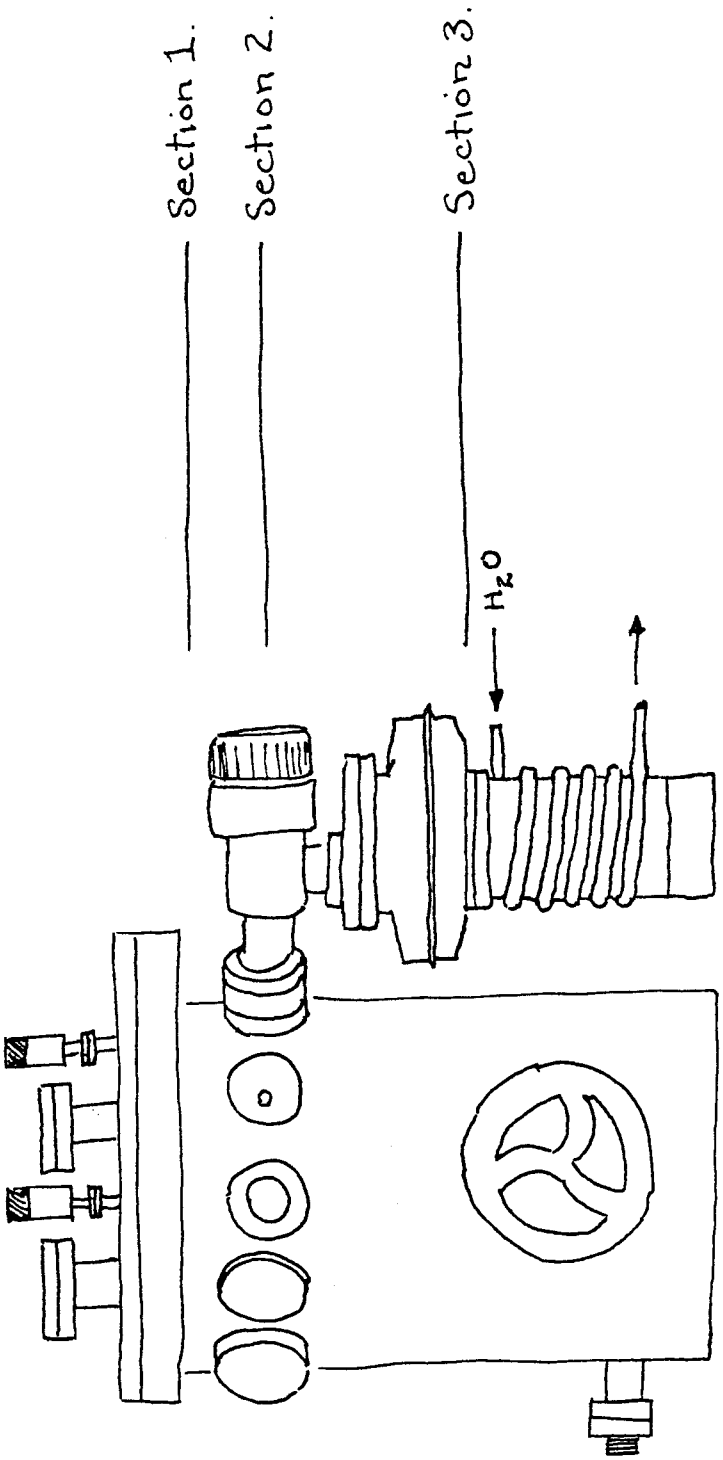

Figure C-1

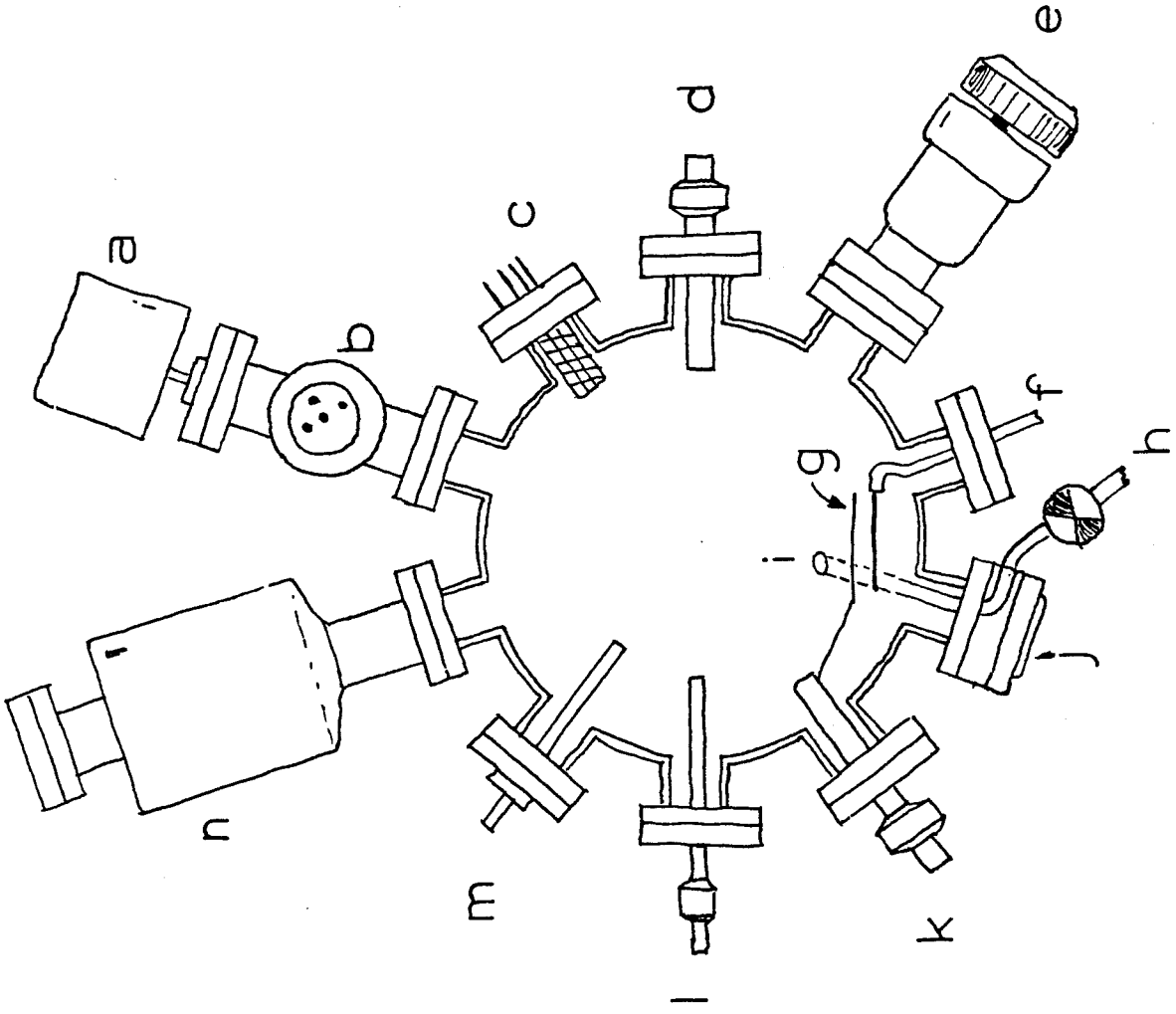

Figure C-2

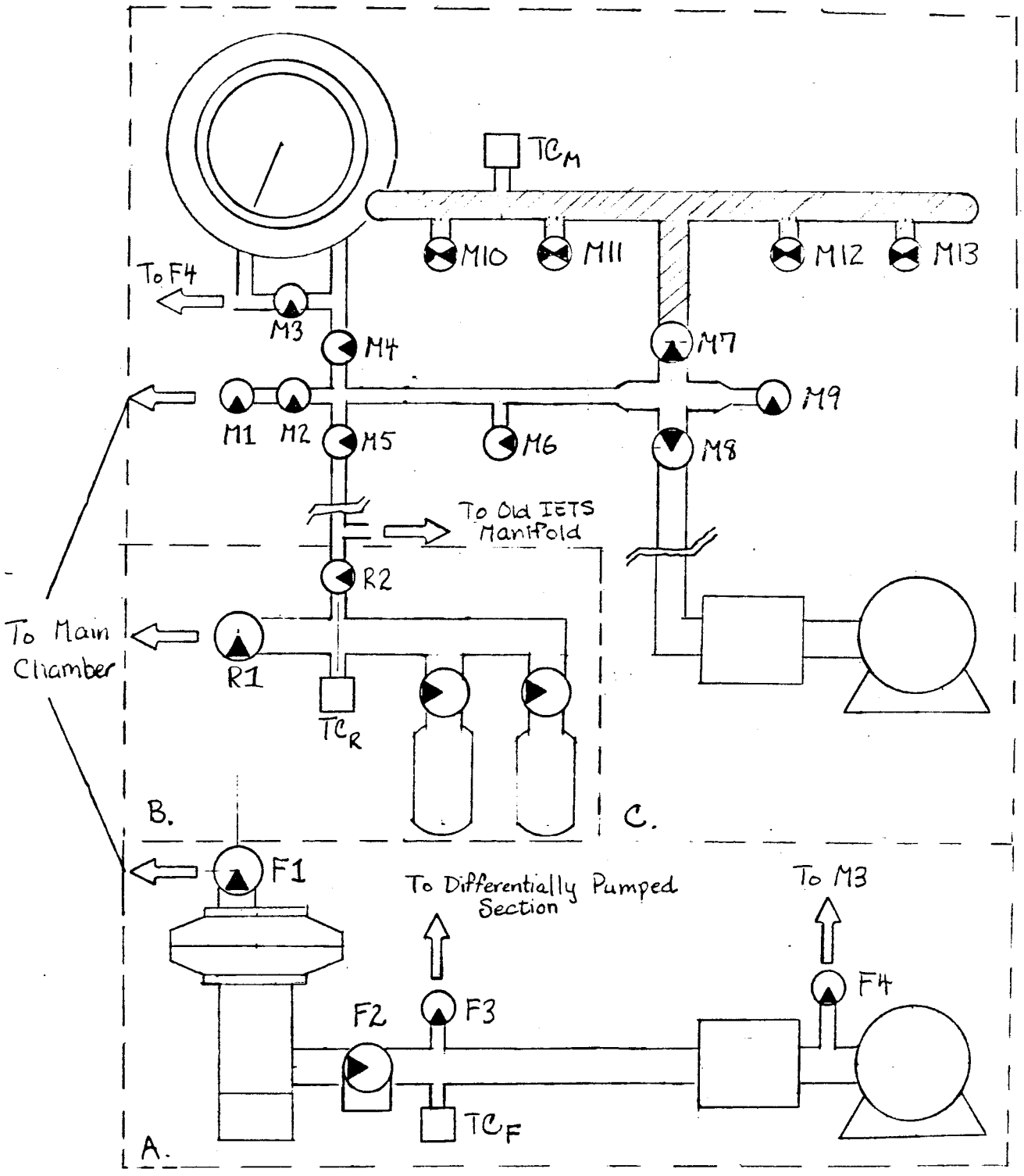
TC_M
M10
M11
M12
M13
To F4
M3
M4
M7
M9
M1
M2
M5
M6
M8
To Old IETS Manifold
R2
To Main Chamber
R1
TC_R
B.
C.
F1
To Differentially Pumped Section
To M3
F4
F2
F3
TC_F
A.

Figure C-3

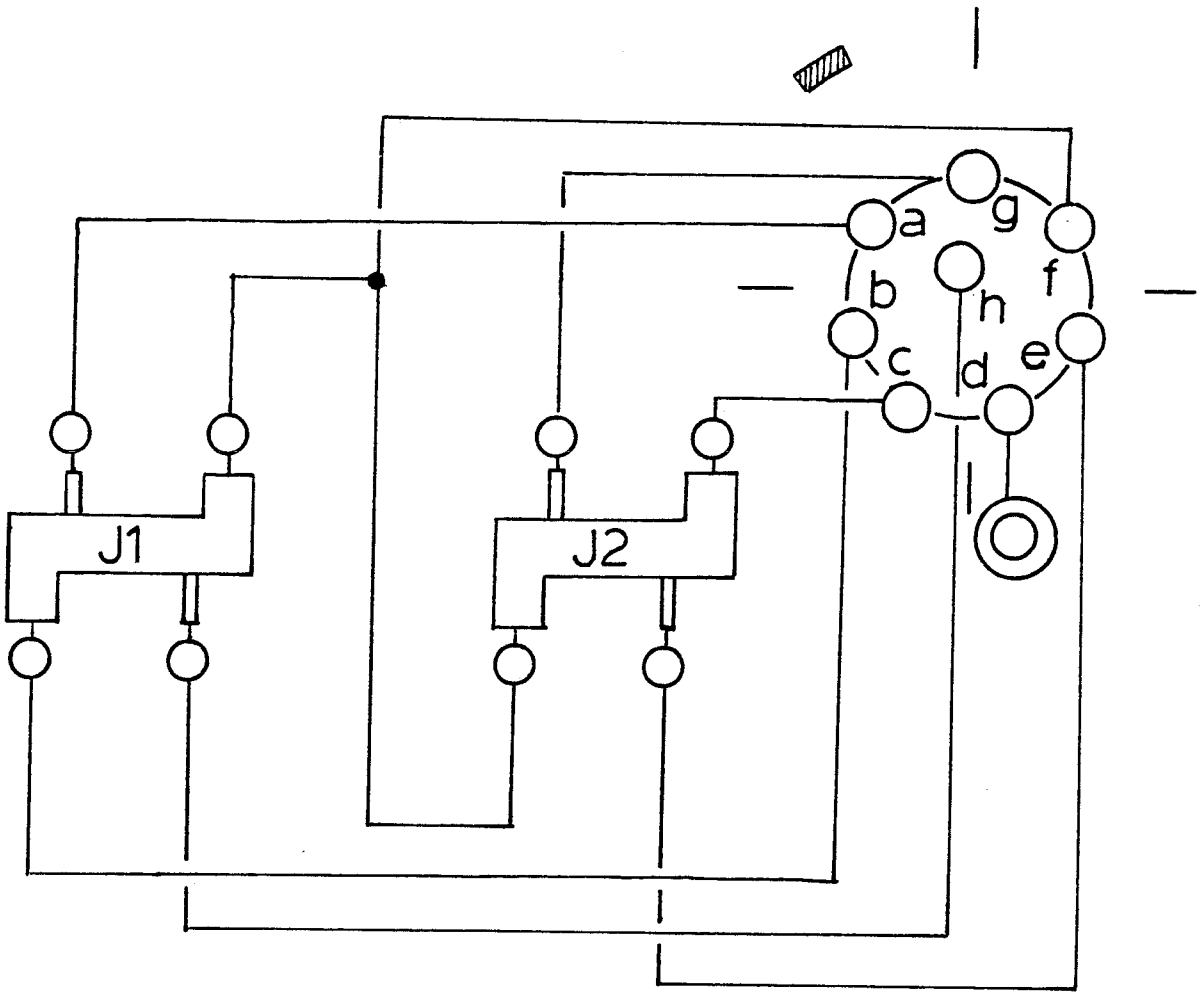

Figure C-4

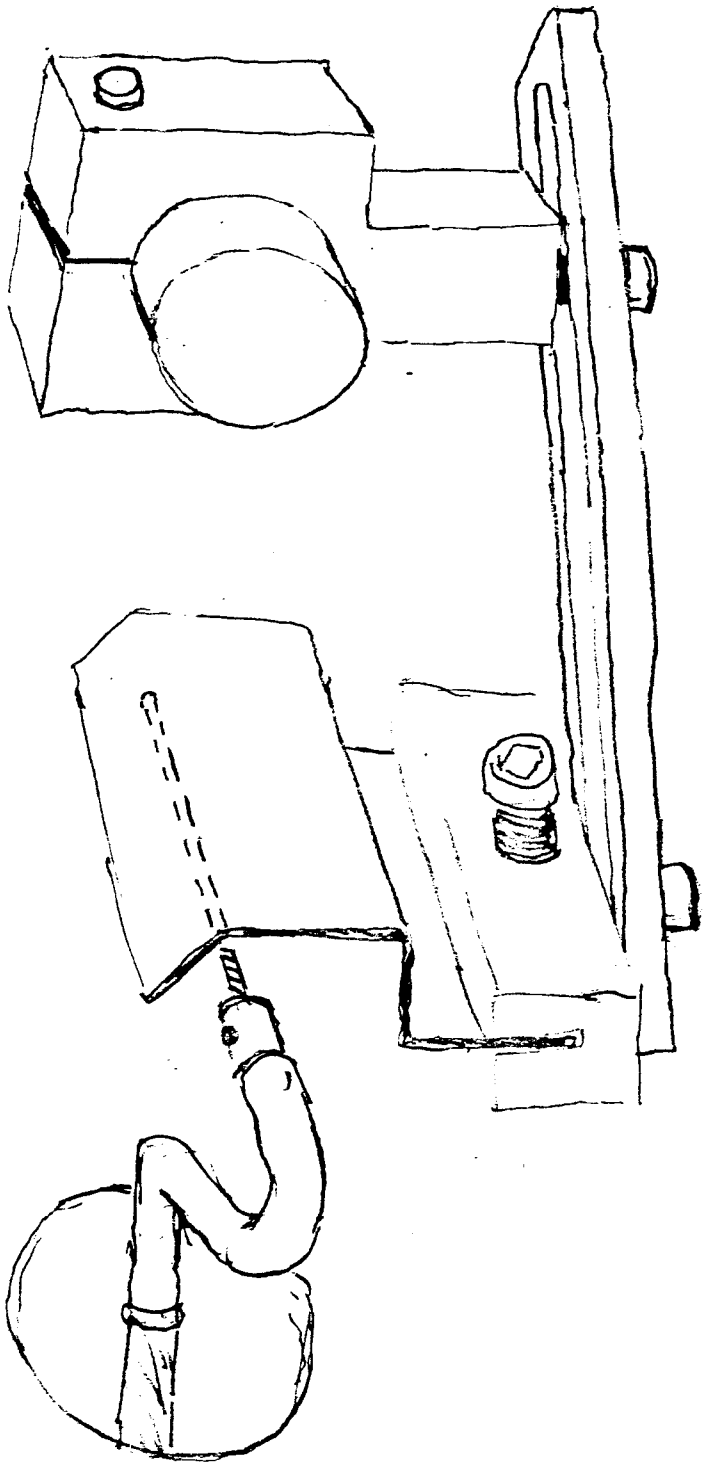

Figure C-5

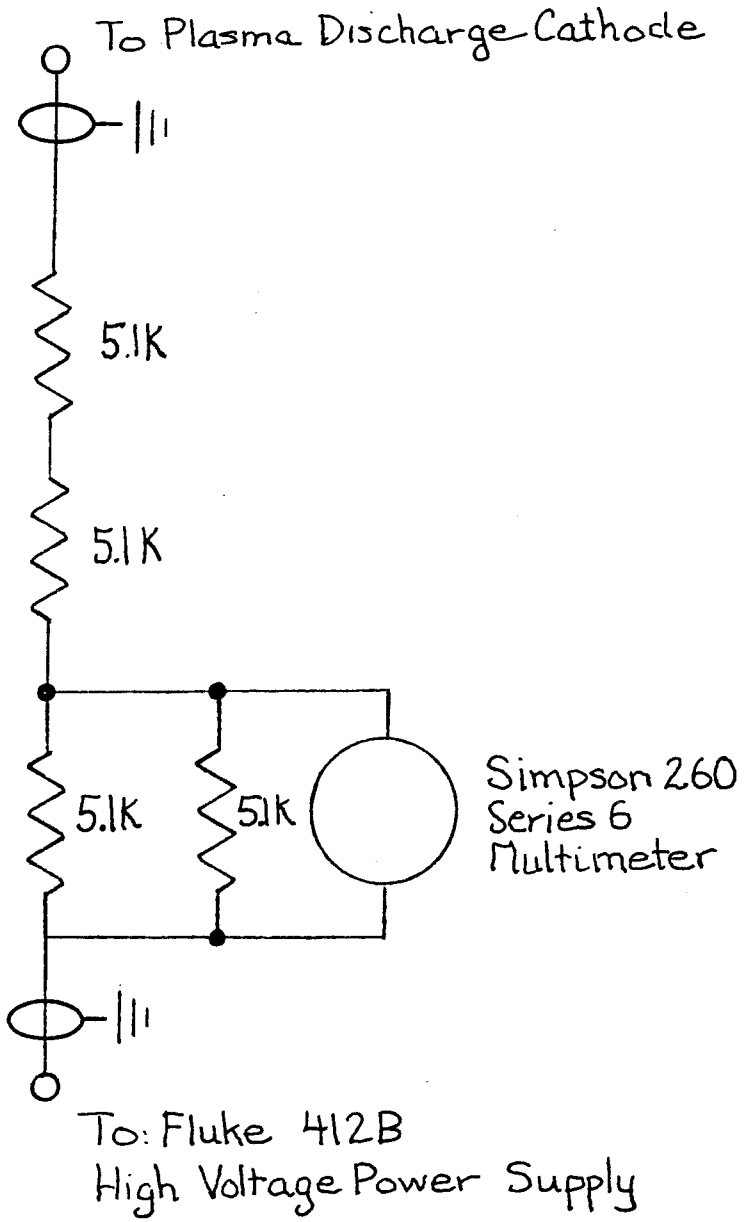
To Plasma Discharge Cathode
5.1K
5.1K
5.1K
5.1K
Simpson 260
Series 6
Multimeter
To: Fluke 412B
High Voltage Power Supply

Figure C-6

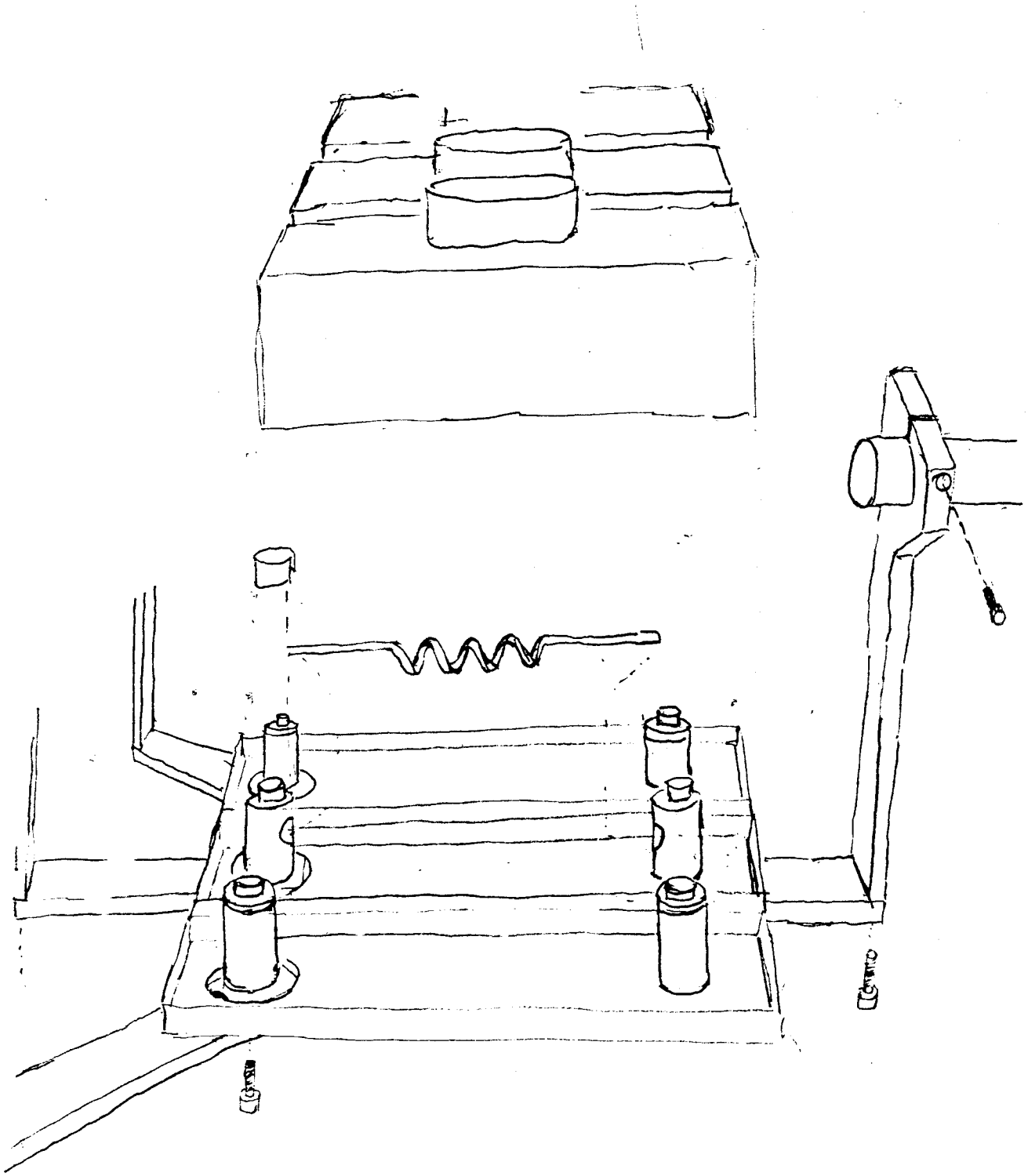

Figure C-7

Figure C-8

Current specifications:

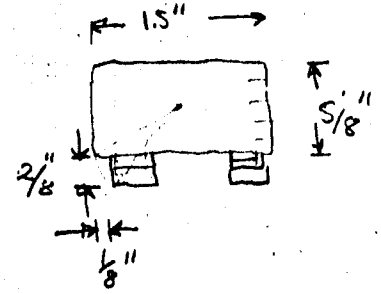

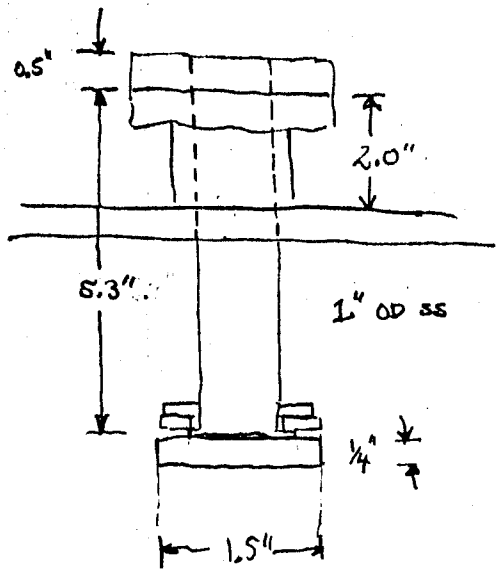

2 3/4" CF minimum ID
= 1.5" !

∴ size must be trimmed down!

Proposed Modification

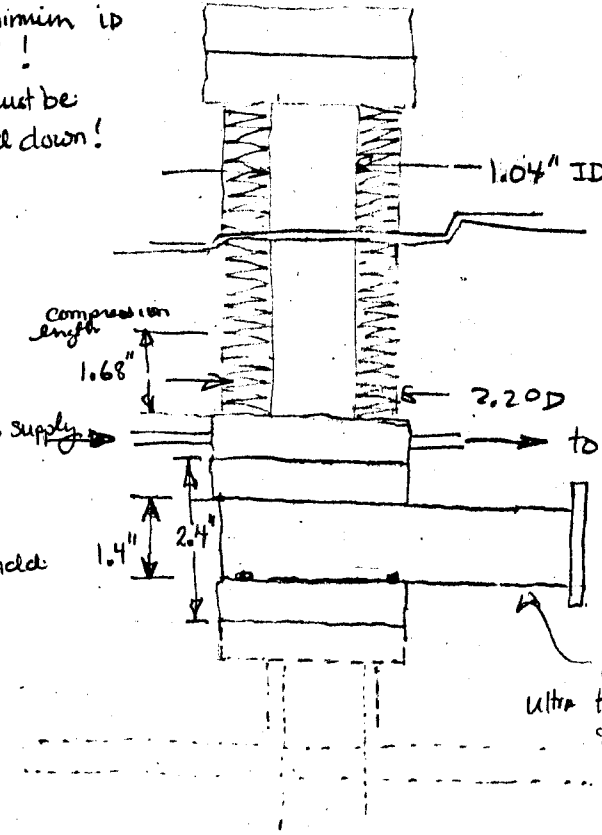

Huntington Model 247-15 welded Bellows $350
10.12" stroke

Jenna has one of these
$840 MDC 1982

∴ Minimum Stroke necessary to clear gate valve
= 0.25 + 5.3 + 0.5 + 1.4 = 7.45"

Really want bellows ~8" stroke 1.75 ID 2.50 OD
1.4 + 1 + 1.68 + 1 → holder tube + 5.08"

use LF type arrangement
① Redesign END CAP
② Electrical connections!

Table 1
Top Plate Electrical Feedtrough: Pinout and Functions

Coaxial Cable	Amphenol 24-6S	Function
5	B	J1 Power
2	A	J1 High Sense
1	H	J1 Low Sense
Orange	F	J1 and J2 ground
6	C	J2 Power
4	E	J2 High Sense
3	G	J2 Low Sense
14	D	Deposition monitor